



# MONASH University

## **Understanding atmospheric circulation leading to anomalously high Australian spring maximum temperatures**

Roseanna Jean Colles McKay

BSc. (Hons), University of Tasmania (2012)

Grad. Dip. Meteorology, Bureau of Meteorology Training Centre (2013)

A thesis submitted for the degree of Doctor of Philosophy at

Monash University in 2022

Faculty of Science, School of Earth, Atmosphere and Environment

## **Copyright notice**

© Roseanna Jean Colles McKay (2022)

I certify that I have made all reasonable efforts to secure copyright permissions for third-party content included in this thesis and have not knowingly added copyright content to my work without the owner's permission.

## Abstract

The magnitude of Australian-average maximum temperatures in spring (September-October-November) may not reach that of summer, but anomalously high maximum temperatures can negatively impact people, agriculture, and infrastructure. Australian spring temperatures are also rapidly increasing in response to anthropogenic climate change. As such, there is a strong need to understand how anomalously high maximum temperatures develop in today's climate. However, studies generally focus on drivers of spring rainfall rather than temperature. Further, as spring lies in the transition from the winter to summer seasons, there are many seasonal changes to the large-scale drivers of variability and atmospheric circulation that may impact anomalously high maximum temperature evolution that require further investigation. The atmospheric teleconnection from the Indian Ocean Dipole to Australia develops through winter to peak in spring before rapidly decaying in early summer. This thesis aims to fill these gaps in our knowledge by exploring the drivers, particularly in relation to the tropical Indian Ocean, of the atmospheric circulation and dynamical heat mechanisms that contribute to anomalously high Australian maximum temperatures through spring.

We address this aim by analysing atmospheric circulation anomalies and dynamical heat mechanisms in reanalyses and in a seasonal prediction model, POAMA. We explore three of Australia's most extreme month- and two-month- long spring heat events and identify atmospheric circulation features that were key during each event. We then compare the influence of the tropics and extratropics on the monthly atmospheric circulation and dynamical heat mechanisms associated with high Australian maximum temperature through spring. Finally, we run a suite of experiments with POAMA to explore the relative influence of the tropical Indian Ocean on Australia's spring-average maximum temperatures and compare these results to hindcasts of three other subseasonal prediction systems.

Overall, this thesis helps isolate the atmospheric circulation patterns and the roles of the tropics and extratropics that drive high maximum temperatures in Australia during spring. We find that a combination of a quasi-stationary Rossby wave train comprised of an upper-tropospheric anticyclone over southern Australia and barotropic cyclone near New Zealand, as well as a second equivalent barotropic cyclone to Australia's southwest support high maximum temperature development through spring. We also find that there is a shift through spring from extratropical to tropical forcing of these atmospheric circulation features, heat mechanisms, and the consequent development of Australian high maximum temperatures. The atmospheric circulation over the Indian Ocean appears important for helping set up heat-conductive conditions over Australia, highlighting the role of the tropical Indian Ocean in Australia's spring climate. However, we identify biases in how quickly Indian Ocean initial conditions decay in POAMA, resulting in weaker tropical Indian Ocean teleconnections than found in reanalysis. As such, future work could build on

the findings of this thesis to fully assess the role of the tropical Indian Ocean in Australian spring maximum temperature variability.

## **Publications during enrolment**

**McKay, R. C.**, Arblaster, J. M., Hope, P., and Lim, E.-P. (2021). Exploring atmospheric circulation leading to three anomalous Australian spring heat events. *Climate Dynamics*, 56(7–8), 2181–2198. <https://doi.org/10.1007/s00382-020-05580-0>

**McKay, R. C.**, Arblaster, J. M., and Hope, P.: Tropical influence on heat-generating atmospheric circulation over Australia strengthens through spring Weather Clim. Dynam. Discuss. (accepted) <https://doi.org/10.5194/wcd-2021-63>, (accepted)

Hope, P., Zhao, M., S. Abhik, Tolhurst G., **McKay R. C.**, Rauniyar, S. P., Bettio, L., Ramchum, A., Lim, E.-P., Pepler, A.S., Cowan, T., Watkins, A. B., Sub-seasonal to seasonal climate forecasts provide the backbone of a near real-time Event Explainer service, *Bull. Amer. Meteor. Soc.*, (accepted)

**McKay, R. C.**, Boschat, G., Rudeva, I., Dowdy, A., Rauniyar S., Gillett Z., Purich A., Pepler, A., Hope P, (2021) “A review of the observed changes in the Southern Hemisphere circulation and their links to rainfall changes in south-eastern Australia” *Bureau Research Report No. 54*

Rudeva, I., Boschat, G., **McKay, R.C**, Pepler, A., Dowdy, A., Hope P., (2021) “Weather systems related to wet and dry extremes” *Bureau Research Report No. 53*

Merryfield, W. J., Baehr, J., Batté, L., Becker, E. J., Butler, A. H., Coelho, C. A. S., Danabasoglu, G., Dirmeyer, P. A., Doblas-Reyes, F. J., Domeisen, D. I. V., Ferranti, L., Ilynia, T., Kumar, A., Müller, W. A., Rixen, M., Robertson, A. W., Smith, D. M., Takaya, Y., Tuma, M., ... **McKay, R. C.**,... Yeager, S. (2020). Current and Emerging Developments in Subseasonal to Decadal Prediction. *Bulletin of the American Meteorological Society*, 101(6), E869–E896. <https://doi.org/10.1175/BAMS-D-19-0037.1>

## Thesis including published works declaration

I hereby declare that this thesis contains no material which has been accepted for the award of any other degree or diploma at any university or equivalent institution and that, to the best of my knowledge and belief, this thesis contains no material previously published or written by another person, except where due reference is made in the text of the thesis.

This thesis includes one original paper published in a peer reviewed journal and one submitted publication. The core theme of the thesis is the atmospheric circulation leading to anomalously high Australian maximum temperature in spring. The ideas, development and writing up of all the papers in the thesis were the principal responsibility of myself, the student, working within the School of Earth, Atmosphere and Environment under the supervision of Prof. Julie Arblaster and Dr. Pandora Hope.

The inclusion of co-authors reflects the fact that the work came from active collaboration between researchers and acknowledges input into team-based research.

In the case of Chapters 2 and 3, my contribution to the work involved the following:

Thesis Chapter	Publication Title	Status	Nature and % of student contribution	Co-author name(s) Nature and % of Co-author's contribution	Co-author(s), Monash student
2	Exploring atmospheric circulation leading to three anomalous Australian spring heat events	Published	80% Concept, methodology, analysis and writing	1) Julie Arblaster, concept, methodology and writing 10% 2) Pandora Hope Methodology and writing 5% 3) Eun-Pa Lim, writing 5%	No (all)
3	Strengthening tropical influence on heat generating circulation over Australia through spring	Accepted	90% Concept, methodology, analysis and writing	1) Julie Arblaster, concept, methodology and writing 5% 2) Pandora Hope Methodology and writing 5%	No (all)

I have not renumbered sections of submitted or published papers in order to generate a consistent presentation within the thesis.

**Student name:** Roseanna Jean Colles McKay

**Student signature:**

**Date:**

I hereby certify that the above declaration correctly reflects the nature and extent of the student's and co-authors' contributions to this work. In instances where I am not the responsible author I have consulted with the responsible author to agree on the respective contributions of the authors.

**Main Supervisor name:** Julie Arblaster

**Main Supervisor signature:**

**Date:**

## Acknowledgements

This research was supported by an Australian Government Research Training Program (RTP) Scholarship, with additional support from the ARC Centre of Excellence for Climate Extremes (CE170100023), the Australian Government's National Environment Science Program (NESP), the Victorian Water in Changing Climate (VicWaCl), and with a Top-up Scholarship provided by the Bureau of Meteorology. This research was undertaken with the assistance and resources provided by the National Computing Infrastructure (NCI), which is supported by the Australian Government.

This research would not have been possible without the assistance and support of many people. I express my sincere gratitude to everyone who has helped me over the past few years; you are all amazing.

In particular, I would like to thank my supervisors, Prof. Julie Arblaster and Dr. Pandora Hope. Your guidance, feedback, and empathy have made me into the scientist I am today and I could not have completed this thesis without your support. I have greatly benefitted from your scientific expertise and I highly value your advice: academic, personal and professional. I deeply appreciate all the time and effort you have put into getting me to this point, particularly as you had to juggle the added stresses associated with the Covid-19 pandemic and the IPCC report. I am in awe of both of you and how much you are able to achieve whilst helping me.

I also want to thank several individuals whose wisdom and scientific insight improved my research. Firstly, Dr. Eun-Pa Lim for her patience with my endless questions about coding, science and the bigger picture of my thesis; thank you. Drs. Matthew Wheeler, Ghyslaine Boschat, George Kiladis and one anonymous reviewer for their advice and feedback that greatly improved chapter 2 (as published). I also thank Zoe Gillet and Drs Harry Hendon and Andrew Marshall, and two anonymous reviewers for their comments on my third chapter, submitted for publication. I thank Dr. Thea Turkington for supplying the tropical-tripole index used in chapter 3. I would also like to thank Ghyslaine, Harry, as well as Dr. Guomin Wang for their support, scientific discussions and, particularly in Guomin's case, significant help with coding that underpinned much of the analysis of this thesis. Thank you to Dr. Debra Hudson and Mikhael Tolstyk for your help understanding the HMCR model. Thank you also to Dr. Irina Rudeva for her helpful feedback on my final discussion chapter. I also want to thank my colleagues and friends at the Bureau of Meteorology for all your guidance and scientific knowledge.

Thank you to my fellow students Zoe Gillet, Donxia Yang, David Hoffman, Cass Rogers, Scott Clark, Peter van Rensch, Pia Freisen, Angie Weis, and many, many more at Monash University and CLEX. I have learnt and gained so much from sharing the PhD experience with you.

To my friends and family, your emotional support and encouragement over the years means the world. Mum, our weekly phone calls are a great source of comfort. Sam and Naomi, our regular online stitching sessions are a great joy, and I cannot thank you enough for the invaluable comments you made on my earlier thesis drafts. James, your big-brotherly advice on how to deal with the realities of a PhD has been immensely reassuring and helpful. Roen, Aviva, Tom, Hugh, dad and all my friends and family in Hobart, Melbourne and further afield. Thank you.

To our cat Tanooki, thank you for the immense source of comfort and joy you bring just by being you.

Finally, and most importantly, to my partner Luke. You are source of comfort, love, encouragement, and support. I am so lucky I found you in my time as a PhD student.

# Table of Contents

<b>1</b>	<b><i>Introduction to thesis</i></b> .....	<b>1</b>
1.1	<b>Thesis aim:</b> .....	<b>3</b>
1.2	<b>Australian spring temperature in the context of the global atmospheric circulation</b> .....	<b>3</b>
1.2.1	Australian maximum temperature climatology.....	3
1.2.2	Heat mechanisms on sub-seasonal and seasonal time scales .....	4
1.3	<b>Spring Teleconnections to Australia</b> .....	<b>5</b>
1.3.1	Remote drivers of variability.....	5
1.4	<b>Rosby wave teleconnections</b> .....	<b>10</b>
1.5	<b>Seasonal prediction systems as a tool to understand teleconnections</b> .....	<b>13</b>
1.6	<b>Australian spring temperatures in the context of a changing climate</b> .....	<b>15</b>
1.7	<b>Research questions and thesis outline</b> .....	<b>17</b>
<b>2</b>	<b><i>Exploring Atmospheric Circulation Leading to Three Anomalous Australian spring Heat Events</i></b> .....	<b>19</b>
2.1	<b>Abstract</b> .....	<b>19</b>
2.2	<b>Introduction</b> .....	<b>19</b>
2.3	<b>Method and Data</b> .....	<b>23</b>
2.3.1	Observational and Reanalysis Data.....	23
2.3.2	POAMA model forecasts.....	24
2.3.3	Comparing reanalysis and POAMA forecasts.....	25
2.3.4	Linear Rossby wave theory .....	26
2.4	<b>Results</b> .....	<b>27</b>
2.4.1	Temperature anomalies.....	27
2.4.2	Australian maximum temperatures and southern Australian 200hPa geopotential height.....	31
2.4.3	September 2013 .....	33
2.4.4	October-November 2014.....	36
2.4.5	October 2015 .....	38
2.5	<b>Discussion</b> .....	<b>42</b>
2.6	<b>Conclusion</b> .....	<b>44</b>
<b>3</b>	<b><i>Strengthening tropical influence on heat generating circulation over Australia through spring</i></b> .....	<b>46</b>
3.1	<b>Abstract</b> .....	<b>46</b>
3.2	<b>Introduction</b> .....	<b>46</b>
3.3	<b>Methods and data</b> .....	<b>49</b>
3.3.1	Indices and datasets .....	49
3.3.2	Rosby wave analysis .....	50
3.3.3	Statistical analysis .....	51
3.4	<b>Results</b> .....	<b>52</b>
3.4.1	SON maximum temperatures, circulation patterns and associations with drivers .....	52
3.4.2	Monthly circulation patterns and associations with drivers.....	55
3.4.3	Connection between subtropical jet and atmospheric circulation.....	60
3.4.4	Mechanisms and drivers of monthly maximum temperatures through spring.....	61
3.5	<b>Discussion and conclusions</b> .....	<b>68</b>
<b>4.</b>	<b><i>Tropical Indian Ocean Influence on Australian Spring Circulation and Maximum Temperatures in Numerical Dynamical Forecast Models</i></b> .....	<b>73</b>

<b>4.1</b>	<b>Introduction .....</b>	<b>73</b>
<b>4.2</b>	<b>Datasets and methods overview .....</b>	<b>76</b>
4.2.1	Observational data.....	76
4.2.2	Subseasonal-to-seasonal (S2S) models.....	77
4.2.3	POAMA system (version A).....	78
4.2.4	Reconstructed and seasonal forecasts of spring .....	79
<b>4.3</b>	<b>S2S hindcast tropical Indian Ocean relationships .....</b>	<b>81</b>
4.3.1	Regression analysis .....	81
4.3.2	Comparison with reanalysis.....	81
4.3.3	Relationships to the IOD in the S2S Models .....	83
4.3.4	S2S Summary .....	92
<b>4.4</b>	<b>Indian Ocean Dipole experiments .....</b>	<b>93</b>
4.4.1	Comparison of reanalysis and POAMA hindcast composites .....	94
4.4.2	IOD experiment design .....	96
4.4.3	IOD experiment results.....	98
4.4.4	IOD experiment summary.....	106
<b>4.5</b>	<b>Confined ocean variability experiments .....</b>	<b>107</b>
4.5.1	Ocean variability experiment design .....	107
4.5.2	Ocean variability experiment results .....	108
4.5.3	Ocean variability experiment summary.....	116
<b>4.6</b>	<b>Discussion and chapter conclusion.....</b>	<b>116</b>
<b>5</b>	<b><i>Thesis Conclusions and Discussion .....</i></b>	<b>121</b>
<b>5.1</b>	<b>Addressing the research questions.....</b>	<b>121</b>
<b>5.2</b>	<b>Thesis synthesis .....</b>	<b>122</b>
<b>5.3</b>	<b>Implications, caveats and future work .....</b>	<b>123</b>
5.3.1	Other heat drivers and mechanisms not considered.....	124
5.3.2	Limits to Rossby wave theory .....	127
5.3.3	Restrictions associated with numerical modelling .....	129
5.3.4	Impact of anthropogenic climate change .....	131
<b>5.4</b>	<b>Thesis conclusion .....</b>	<b>132</b>
<b>6</b>	<b><i>References .....</i></b>	<b>133</b>

## Table of Figures

Figure 1-1 Australian spring temperature anomalies.....	2
Figure 1-2 Maximum temperature SON climatology and standard deviation .....	4
Figure 1-3 IOD and ENSO ocean, atmosphere, and land impacts .....	7
Figure 1-4 Drivers of Australian rainfall variability .....	9
Figure 1-5 SON linear regression of DMI (a) and partial DMI (Niño3.4 index linearly removed; b) onto OLR.....	11
Figure 1-6 SON IOD and ENSO atmospheric wave trains.....	12
Figure 1-7 SON climatological total wave number .....	13
Figure 1-8 Central-tropical Indian Ocean wave train.....	15
Figure 2-1 Australian maximum temperature anomalies during three spring heat events.....	29
Figure 2-2 Australian maximum temperature standard deviation during September, October, and November .....	30
Figure 2-3. Observed monthly spring relationships of 200Z vs Australian maximum temperature .	31
Figure 2-4 POAMA monthly spring relationships of 200Z vs Australian maximum temperature .....	32
Figure 2-5 Ensemble-member forecasts 200Z vs Australian maximum temperature for each event .....	33
Figure 2-6. September 2013 low- and upper-level atmospheric circulation.....	35
Figure 2-7 October-November 2014 low- and upper-level atmospheric circulation .....	37
Figure 2-8 October 2015 low- and upper-level atmospheric circulation.....	40
Figure 3-1 Australian-averaged maximum temperature regressed onto gridded maximum temperature .....	52
Figure 3-2 SON circulation and maximum temperature linear regressions onto circulation and gridded maximum temperature .....	54
Figure 3-3 Time series of observed and statistically reconstructed spring maximum temperature	55
Figure 3-4 Spring-monthly regressions of maximum temperature onto with low-level circulation.	56
Figure 3-5 As with Fig 3-4 but for upper-level circulation .....	57
Figure 3-6 Regional Australian maximum temperature regressions onto atmospheric circulation .	59
Figure 3-7 Climatological monthly total wave number and wave activity flux .....	60
Figure 3-8 Spring monthly extratropical and tropical regressions to maximum temperature and statistical time series reconstruction .....	62
Figure 3-9 As with Fig 3-8 g-i, but reconstructed with different combinations of climate modes of variability.....	63
Figure 3-10 As in Fig. 3-8(g-i) but from circulation features and heat mechanisms .....	64
Figure 3-11 MLR of circulation features onto Australian maximum temperature.....	65
Figure 3-12 As with Fig. 3-11, but regressed onto dynamical heat mechanisms .....	66
Figure 3-13 Monthly correlations between circulation features and heat mechanisms .....	68
Figure 3-14 Upper-level circulation regressions onto dynamical heat mechanisms.....	70
Figure 3-15 As in Fig. 3-10 d-f but with antecedent moisture included as a predictor .....	71
Figure 4-1 Observed (ERA5) spring relationship between the IOD and partial IOD to the atmospheric circulation .....	82
Figure 4-2 As with Fig. 4-1 but for Australian spring maximum temperature and precipitation.....	83
Figure 4-4 Bootstrap estimates of linear regressions of S2S model reconstructed spring DMI onto atmospheric circulation .....	84
Figure 4-4 As in Fig. 4-3, but with Niño3.4 first linearly removed.....	84
Figure 4-6 As with Fig. 4-3 but for reconstructed spring maximum temperature (°C) and precipitation (mm/day).....	85
Figure 4-6 As in Fig. 4-5, but with Niño3.4 first linearly removed.....	85
Figure 4-7 Observed and reconstructed S2S model SON DMI and Niño3.4 index.....	87

Figure 4-8 HMCR, UKMO, KMA, POAMA (ver. A) HC daily west-pole of the DMI .....	89
Figure 4-9 As in Fig. 4-6 but for the east-pole of the DMI .....	90
Figure 4-10 As in Fig. 4-6 but for Niño3.4 SSTs .....	91
Figure 4-11 Observed IOD composite atmospheric circulation and SST .....	94
Figure 4-12 As in Fig. 4-11 but for POAMA (version A) hindcast .....	95
Figure 4-14 As in Fig. 4-12, but for composite anomalies of Australian maximum temperature (°C) and precipitation (mm/day) from the AWAP dataset. ....	96
Figure 4-14 As in Fig. 4-12 but for lead-1 reconstructed spring POAMA hindcast (ver. A). ....	96
Figure 4-15 Experiment ocean initial condition boundaries.....	97
Figure 4-16 Reconstructed spring SST anomalies from POAMA IOD experiments .....	99
Figure 4-17 IOD experiment lead-1 reconstructed spring forecast atmospheric circulation anomalies (relative to climatology experiment).....	101
Figure 4-18 As with Fig. 4-17, but differences are between the enhanced IOD and single composite anomalies experiments.....	102
Figure 4-19 As with Fig. 4-17, but for maximum temperature (°C) and precipitation (mm/day) ...	103
Figure 4-21 Ensemble-member daily west- and east-pole indices from the positive IOD experiments .....	104
Figure 4-21 As with Fig. 4-20, but for negative IOD experiments .....	104
Figure 4-22 Confined-variability experiment lead-1 seasonal-spring SST regressions onto DMI and partial DMI .....	110
Figure 4-24 As in Fig. 4-22 but for seasonal spring DMI regressed onto circulation anomalies. ....	111
Figure 4-24 As in Fig. 4-23 but with seasonal Niño3.4 index first linearly removed. ....	111
Figure 4-25 As in Fig. 4-22 but for maximum temperature (°C) and precipitation (mm/day) .....	112
Figure 4-26 Lead-1 seasonal spring DMI and Niño3.4 time series for the different constrained variability experiments .....	113
Figure 4-27 Daily values of west- and east- DMI poles and Niño3.4 indices from the confined variability experiments .....	114
Figure 4-28 As with Fig. 4-27 but for the ACCESS-S2 hindcast (from 1981 to 2018).....	115
Figure 4-29 Chapter summary of relationships in observations and models.....	118

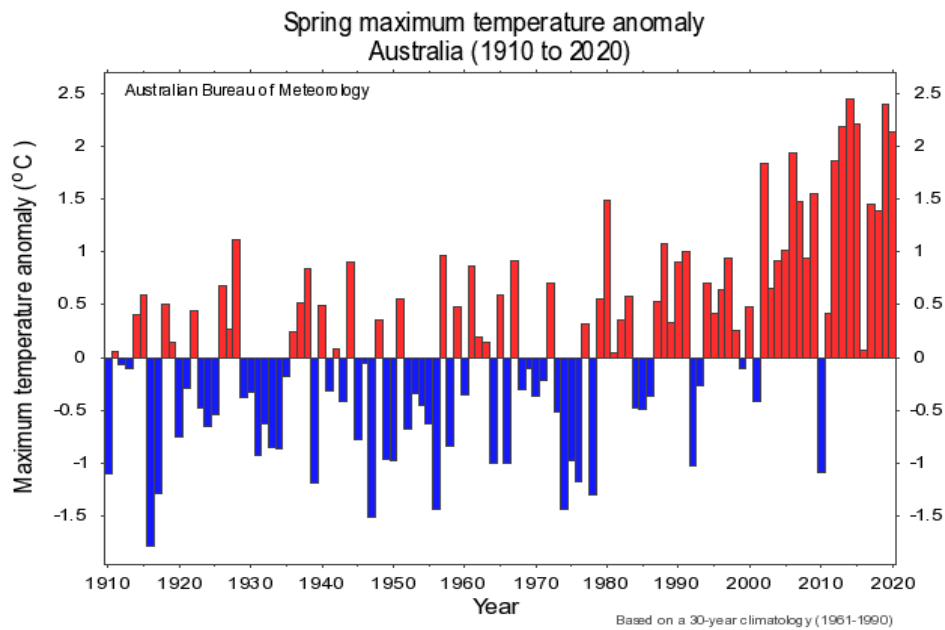
## Table of Tables

Table 2-1 Summary of drivers attributed to heat events - synthesis from literature .....	23
Table 3-1 Correlation and partial correlations between circulation features and dynamical heat mechanisms .....	58
Table 4-1 Summary of Models .....	80
Table 4-2 IOD, ENSO correlations in S2S models and observations .....	86
Table 4-3 IOD events used in POAMA experiments .....	93
Table 4-4 IOD experiment ICs for August 1, September 1, October 1 initialisations. ....	98
Table 4-5 Average values for IOD experiments .....	100
Table 4-6 Confined ocean variability experiment initial conditions .....	108
Table 4-7 Correlation between indices in Fig. 4-29 .....	118

# 1 Introduction to thesis

Anomalous heat outside the tropics in Australia during spring (September-October-November) may not reach the magnitudes of a summer (December-January-February) heatwave, but can still have devastating impacts. Particularly in association with the ongoing warming trend associated with anthropogenic climate change (Collins et al., 2013; Eyring et al., in press), anomalous and increasing high spring maximum temperatures in Australia are linked to decreases in length of the pasture growing season (Cullen et al., 2009), lower wheat crop yields (Taylor et al., 2018), earlier ripening and shorter harvesting season of wine grapes (Jarvis et al., 2019), an increase in fire weather danger in spring (Dowdy, 2018) and pre-conditioning of the summer wildfire season (Abram et al., 2021). Anomalously high spring maximum temperatures can also adversely impact human health due to lack of acclimatisation following winter (Loughnan et al., 2014; Nairn & Fawcett, 2014). Temperatures in spring have been increasing (e.g. Bureau of Meteorology & CSIRO, 2020; Fig. 1-1) and maximum temperatures in recent springs have exceeded historical records (e.g. Arblaster et al., 2014; Hope et al., 2015, 2016; Gallant and Lewis, 2016). It is likely that more extreme heat records will fall as the background warming trend continues (Alexander & Arblaster, 2009, 2017; Power & Delage, 2019; Fischer et al., 2021). However, despite the potentially devastating impacts, Australian spring maximum temperatures have received relatively little attention as most studies assessing variability and trends in spring have focused on rainfall.

Australian rainfall and maximum temperature are inversely correlated (e.g. Hope & Watterson, 2018), and Australia's tropical and extratropical remote modes of variability generally promote either wetter and cooler or drier and hotter conditions in spring (e.g. Jones & Trewin, 2000; Risbey et al., 2009a; Min et al., 2013). However, studies often focus on the statistical relationships between remote drivers and Australia's spring climate. Further, studies that do attempt to physically explain these relationships by exploring atmospheric teleconnections between the remote drivers and Australia generally do so to understand spring rainfall, not temperature. While, we can expect atmospheric teleconnection pathways that promote high rainfall to also drive low temperatures, it is inappropriate to assume from this statistical relationship that the teleconnections are identical without verification. As such, there is a clear need to better understand what drives interannual changes in the atmospheric circulation that are conducive to anomalous high Australian maximum temperatures in spring.



**Figure 1-1 Australian spring temperature anomalies**  
 Australian area-averaged spring (SON) maximum temperature anomalies (°C) during the period 1910 to 2020, relative to a 1961-1990 climatology. From the Bureau of Meteorology: [www.bom.gov.au/climate](http://www.bom.gov.au/climate), accessed on 27 August, 2021.

Atmospheric circulation anomalies, e.g. in the form of quasi-stationary Rossby waves, connect remote variability with changes to Australian spring rainfall (e.g. Hendon et al., 2014; Cai et al., 2011a; McIntosh & Hendon, 2018). Rossby waves generated by anomalies in the tropical Indian Ocean have been linked with atmospheric circulation anomalies that contributed to recent extreme spring maximum temperatures (Hope et al., 2015). However, it is not always obvious what drives these atmospheric teleconnections or how they work. Inter-ocean basin interactions make it difficult to isolate the specific influence of individual tropical basins on global teleconnections (e.g. Li, X. et al., 2016; Cai et al., 2019). The seasonal Indo-Pacific subtropical jet (e.g. Koch et al., 2006; Gillett et al., 2021) should prevent Rossby wave teleconnections from the tropical Indian Ocean to the southern hemisphere extratropics in winter, but also spring, (e.g. Hoskins & Ambrizzi, 1993; Simpkins et al., 2014). While multiple studies have progressed our understanding of how these atmospheric teleconnections are able to promote rainfall, the lack of corresponding studies associated with high maximum temperatures is a clear gap in the literature.

In the context of rising maximum temperatures and the associated impacts, it is critical to improve our understanding in the atmospheric circulation that drives high spring maximum temperature. Improving our understanding of the atmospheric teleconnections and mechanisms that lead to anomalous Australian spring heat in the current climate will lead to better preparedness and resilience in the future climate. As such, this thesis has the following aim:

## 1.1 Thesis aim:

To understand the drivers of atmospheric circulation associated with anomalous high maximum temperatures in Australia in spring.

The remainder of this chapter describes the current understanding of atmospheric teleconnections and drivers that lead to high Australian spring maximum temperatures. I highlight gaps in the literature that lead to three research questions that guide this thesis and outline how I will address the aim.

## 1.2 Australian spring temperature in the context of the global atmospheric circulation

This section starts with a description of Australia's spring maximum temperature climatology and then sets up the context for why monthly or seasonal circulation anomalies during spring are relevant for anomalous high spring maximum temperatures.

### 1.2.1 Australian maximum temperature climatology

The Australian continent is in the southern hemisphere and extends from the mid-latitudes into the tropics, resulting in a wide range of climate types that vary across the continent and through the year (e.g. Nicholls et al., 1997). Broadly, the warmer tropical regions are dominated by a cycle between wet (December to March) and dry seasons (April to November). The cooler higher latitudes' climate cycles through summer (December-January-February; DJF), autumn (March-April-May; MAM), winter (June-July-August; JJA), and spring (September-October-November; SON) seasons (e.g. Karoly et al., 1998; see Fig. 1-2a for Australian spring maximum temperature climatology). The transition from winter to summer leads to highly variable spring weather, particularly in the south and southeast of Australia, where the maximum temperature standard deviation is higher than in the north (Fig. 1-2b).

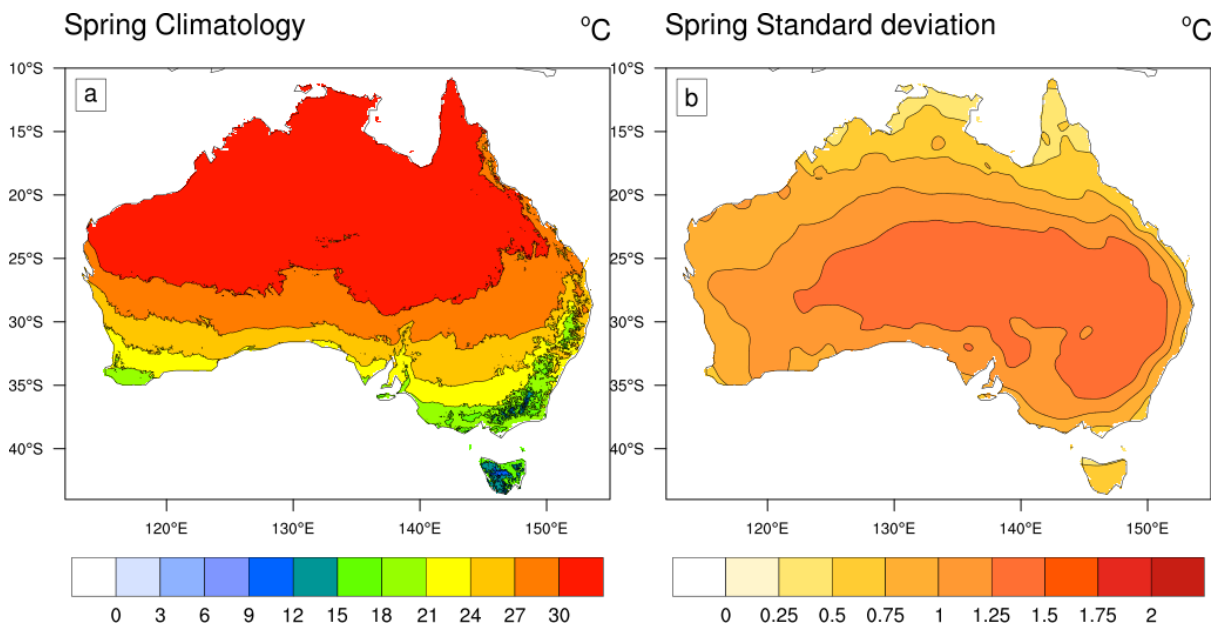


**Figure 1-2 Maximum temperature SON climatology and standard deviation**

*Maps of Australian spring maximum temperature climatology (a) and standard deviation (b). The spring climatology was calculated over a 1981 to 2010 period. Standard deviation was calculated from over linearly detrended 1979-2019 spring anomalies relative to climatology. Australian maximum temperature data from AWAP dataset (Jones et al., 2009)*

On a monthly to seasonal time-scale in spring, temperatures have long correlation lengths: when it is hot somewhere in Australia, it tends to be hot everywhere (e.g. Jones & Trewin, 2000; Winter et al., 2016). The exception is tropical north Australia, which has relatively low maximum temperature variability through September-November (Fig. 1-2b) and can behave differently with different interannual drivers of variability (e.g. Sharmila & Hendon, 2020). Overall, however, the majority of Australian monthly to seasonal spring maximum temperatures behave in concert and can broadly be studied simultaneously. Note that much of the spring maximum temperature signal is dominated by the central and south-east. This thesis is limited to the austral spring season as monthly to spring-season maximum temperatures are coherent across the majority of the country, have received less attention compared to in winter or summer temperatures, and several of the strongest drivers of interannual variability peak in this season.

### 1.2.2 Heat mechanisms on sub-seasonal and seasonal time scales

Monthly to seasonal atmospheric anomaly patterns reflect the synoptic weather systems that occurred during that time, and consequently, should be consistent with the corresponding monthly temperature anomalies (e.g. Hauser et al., 2020). As such, positive height anomalies (or synonymously anticyclonic vorticity) over southern Australia are linked to positive spring temperature anomalies (e.g. Hope et al., 2015; Gallant & Lewis, 2016; Risbey et al., 2018; Lim et al., 2019a). This anticyclone can enhance warming by increasing adiabatic warming via sinking motion and diabatic heating via insolation (e.g. Hendon et al., 2014; Quinting & Reeder, 2017; Lim et al., 2019a, 2021a), or deflect wetting weather systems away from Australia (Cai, et al., 2011a,b; Pook et al., 2013; Timbal & Hendon, 2011; McIntosh & Hendon, 2018; Hauser et al., 2020). At the surface, anomalous northerly winds and warm air advection from the interior of the

continent (e.g. Boschat et al., 2015) would also contribute to higher temperatures, particularly if anticyclonic blocking in the Tasman Sea, directly to the east of southern Australia, is also present (Marshall et al., 2014). Understanding how and why the atmospheric circulation promotes these patterns will lead to better understanding of how maximum temperature develops.

Note that changes to the land-atmosphere heat fluxes associated with dry-conditions also follow sustained periods of warming and drying atmospheric circulations in the lead up to spring can further enhance high maximum temperatures (Arblaster et al., 2014; Loughran et al., 2019; Hirsch & King, 2020). While the importance of the land-surface feedbacks for heat generation is an important factor in spring maximum temperatures, the focus in this thesis is on the component of heat driven by the atmospheric circulation. As such, this thesis focuses primarily on the dynamic, rather than thermodynamic, mechanisms that drive heat and how that relates to the broader atmospheric circulation.

### 1.3 Spring Teleconnections to Australia

This section provides an overview of Australia's key remote modes of variability and how they generate Rossby wave teleconnections that influence Australia's spring climate.

#### 1.3.1 Remote drivers of variability

Tropical variability across the ocean basins can influence the climate in extratropical Australia. El Niño Southern Oscillation (ENSO) in the tropical Pacific, and the Indian Ocean Dipole (IOD) are two of Australia's strongest climate modes of variability (e.g. Meyers et al., 2007; Risbey, et al., 2009a). Both IOD and ENSO are coupled atmosphere-ocean interactions, where changes to the equatorial thermocline enhance or suppress convection in the east and west of each tropical ocean basin that in turn change the zonal Walker Circulation and promote global climatic teleconnections (e.g. Meyers et al., 2007; Fig. 1-3). The positive phase of the IOD and warm phase (El Niño) of ENSO are associated with drier and warmer conditions over north, east and southern Australia in spring (e.g. Risbey, et al. 2009a; Min et al., 2013). Both the IOD and ENSO develop through austral winter, but the IOD's magnitude and influence on Australia's maximum temperature peaks in SON (Saji et al., 2005) and then quickly dies off as the monsoon winds along coast of Java-Sumatra change direction (e.g. Meyers et al., 2007). ENSO, on the other hand, persists through summer and its peak influence on Australian temperature and rainfall is in NDJ (Jones & Trewin, 2000).

ENSO and IOD variability correlate closely (e.g. Meyers et al., 2007; Risbey, et al., 2009a; Min et al., 2013), making it difficult to separate the influence of one from the other. ENSO also strongly influences IOD development (e.g. Klein et al., 1999; Shinoda et al., 2004) and to first order the IOD appears forced by ENSO (Stuecker et al., 2017; Zhao et al., 2019). predominantly via an atmospheric bridge (Klein et al., 1999). ENSO

heating in the Pacific alters the Walker Circulation (grey arrows right-hand column of Fig. 1-3), contributing to cooling or warming of the sea surface temperatures (SSTs) around the Maritime Continent (blue and red shading in Fig 1-3). These changes induce anomalous heat fluxes and winds in the tropical Indian Ocean that promote (SSTs, red and blue shading in left-column of Fig 1-3) and anomalous atmospheric circulation (grey arrows in Fig. 1-3) that then lead to IOD events from JJA to SON (Klein et al., 1999; Shinoda, et al., 2004). This atmospheric bridge also promotes warming across the tropical Indian Ocean basin that continues through summer and acts as a 'capacitor' (Xie et al., 2009) that extends ENSO's influence on regional and global climate beyond an event's lifetime (Taschetto et al., 2011; Guo et al., 2018) or precondition ENSO and IOD events in the following seasons (e.g. Kug et al., 2005; Wang, H. et al., 2019).

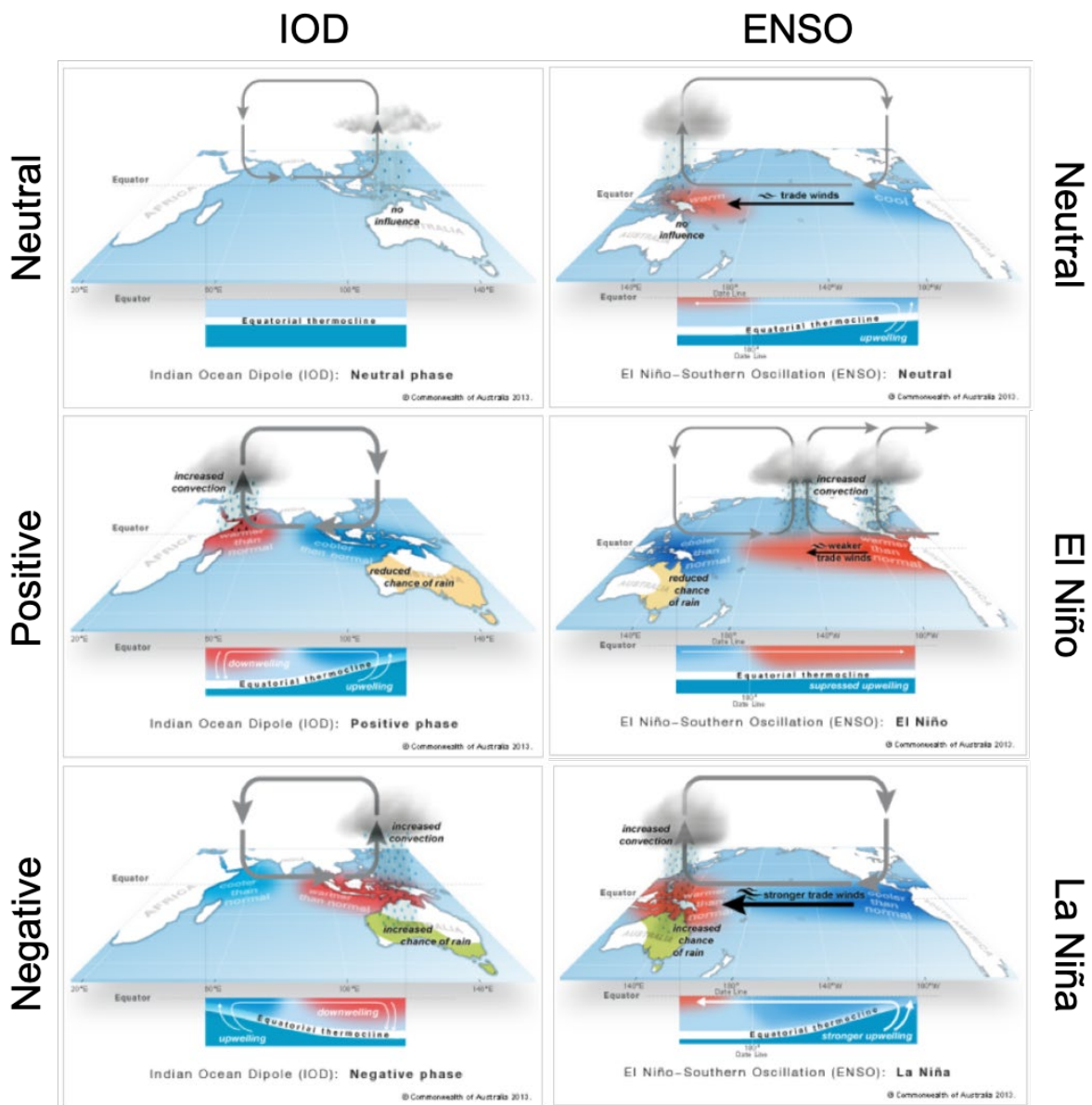


**Figure 1-3 IOD and ENSO ocean, atmosphere, and land impacts**

*Schematic of atmospheric and ocean responses to IOD and ENSO neutral, positive/El Niño, and negative/La Niña phases, and associated rainfall response in Australia. The grey arrows show mean and anomalous Walker Circulation. Anomalously warm SSTs are coloured red, cold SSTs are coloured blue. Orange indicated anomalously low rainfall in Australia and green indicates anomalously high rainfall. Adapted from Bureau of Meteorology ([www.bom.gov.au/climate](http://www.bom.gov.au/climate), accessed on 27 August, 2021).*

However, IOD events can occur independently of ENSO events (e.g. Meyers et al., 2007; Risbey, et al., 2009a) and Australia’s worst droughts are linked with both an absence of La Niña and negative IOD events (Ummenhofer et al., 2009a; King et al., 2020a). The IOD also influences ENSO development and predictability (Kug, 2005; Wu & Kirtman, 2004; Luo et al., 2010; Lim & Hendon, 2017), consistent with the importance of inter-tropical basin relationships (Li X. et al., 2016; Cai et al., 2019) for global teleconnections. Tropical SSTs close to Australia can also influence Australia’s spring rainfall, regardless of

ENSO or IOD phase (van Rensch et al., 2019; Holgate et al., 2020a). The interactions between near and remote tropical oceans are complex and result in complex teleconnections to Australia. However, much of Australia's sub-seasonal and seasonal maximum temperature variability in spring can be linked with the tropical Indian and Pacific Oceans.

The Madden-Julian Oscillation is another remote driver of variability in the tropics that influences Australia's climate. It can be marked by regions of enhanced or suppressed convection across 8 different quadrants (phases) of the tropical Oceans (Wheeler and Hendon, 2004). Phases 2-3 (active convection in the tropical Indian Ocean) are associated with reduced rainfall and higher spring maximum temperatures in Australia (Wheeler et al., 2009; Marshall et al., 2014, 2021a). The MJO operates at a higher frequency (weeks) than the IOD and ENSO (seasons) and is an important source of sub-seasonal predictability (Merryfield et al., 2020; Meehl et al., 2021), though the IOD has also been noted as influencing sub-seasonal climate variability (Shinoda & Han, 2005). Recent work has identified atmospheric circulation teleconnections initiated by the MJO (Wang & Hendon, 2020) in winter that promote cooler minimum temperatures. Further, the MJO can interfere with the influence of ENSO on Australia's spring climate (Lim et al., 2021c). While the MJO plays a role in the atmospheric circulation associated with Australia's spring maximum temperature variability, and merits further investigation, this thesis focuses on the lower frequency contributions of the tropical SST variability.

While tropical ENSO and the IOD are two of the strongest Australian climate drivers (e.g. Meyers et al., 2007; Risbey et al., 2009a; Min et al., 2013), extratropical variability also impacts the Australian climate. The Southern Annular Mode (SAM) (Thompson & Wallace, 2000) is the principal mode of variability in the extratropics and accounts for approximately 10 to 15% of the rainfall and temperature variability in Australia in spring (Hendon et al., 2007). SAM is divided into two phases that correspond to shifts in the eddy-driven jet from stronger and poleward (positive SAM) to weaker and equatorward (negative) (Thompson & Wallace, 2000; Hendon et al., 2007, 2014; Marshall et al., 2012; Fogt & Marshall, 2020). While ENSO and the IOD are coupled processes, SAM is an internally driven atmospheric process that has a decorrelation time of about two weeks. Negative SAM is associated with higher temperatures across central-southern Australia during spring (Hendon et al., 2007; Risbey et al., 2009a; Marshall et al., 2012; Min et al., 2013), that can be promoted and extended through the austral warm seasons due to a strong link with ENSO (e.g. L'Heureux & Thompson, 2006; Hendon et al., 2007; Lim et al., 2019b) and the Southern Hemisphere stratospheric vortex variations (Lim et al., 2018, 2019a, 2021a).

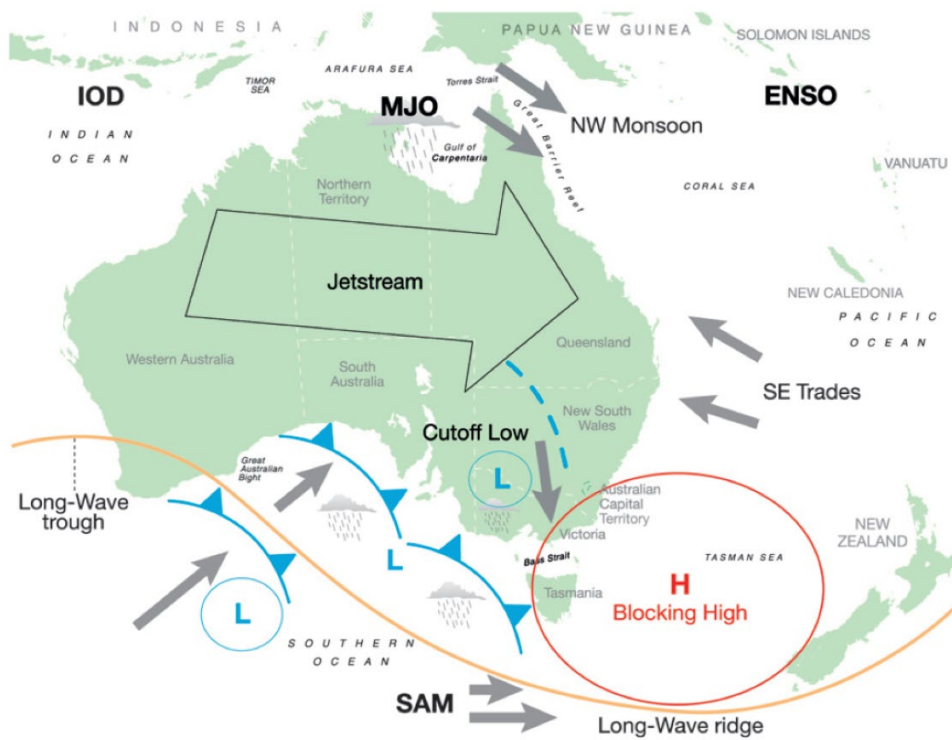


**Figure 1-4 Drivers of Australian rainfall variability**

*Schematic representation of the main drivers of rainfall variability in the Australian region. The dominant features are the IOD, MJO, and ENSO in the tropics, and the SAM and blocking in the extratropics. The influence of the subtropical jet is indicated by the “jet stream” arrow. A schematic cutoff low in a typical position to influence southeast Australian rainfall is shown next to the blocking high. The longwave pattern in the mid-troposphere consistent with the blocking high is also indicated with a trough over Western Australia and a ridge in the Tasman Sea. From Risbey et al. (2009a) © American Meteorological Society. Used with permission.*

A

schematic showing the IOD, ENSO, the MJO, and SAM and how they relate to the large-scale circulation and weather across Australia is shown in Fig. 1-4 (from Risbey et al., 2009a)

Low frequency natural variability modulates the strength of the relationships of the interannual and lower frequency variables on Australia’s climate. In particular, the Interdecadal Pacific Oscillation (IPO) in the tropical to subtropical Pacific Ocean (Power et al. 1999a, 2006; Arblaster et al. 2002; Cai & van Rensch 2012; King et al. 2013; Henley et al. 2015) influences the strength and spatial patterns of ENSO and the IOD, and how they relate to both each other and southeast Australia’s climate (Zhao et al. 2016; Lim et al. 2017). Further, the negative phase of the IPO promotes the positive phase of SAM and associated poleward shift of the eddy driven jet EDJ (Yang et al., 2020). Paleo-records suggest that positive phases of the IPO are associated with megadroughts in eastern Australia (Vance et al., 2015) and variability in the ENSO-IOD relationship over the last millennium (Abram et al., 2020). The IPO and low frequency natural variability are an important factor when considering Australia’s spring climate. However, as this thesis focuses on data from the satellite era, there are too few IPO samples (around four decades) to study its influence on

Australia's spring climate and we restrict this study to interannual influences on sub-seasonal and seasonal times-scales only.

Overall, the relationships as described here with Australian spring temperatures are largely statistical. At best, the slow-variations associated by the remote ocean and atmospheric processes only precondition Australia's climate toward hotter or colder spring maximum temperatures (e.g. Hurrell et al., 2009). To better understand the nuances around how these drivers promote Australian spring maximum temperature variability, it is necessary to understand the Rossby wave teleconnections that connect them to Australia.

#### 1.4 Rossby wave teleconnections

The tropical Oceans have long been argued to influence extratropical climate variability, including Australian maximum temperatures, via the excitation of Rossby waves (e.g. Hoskins and Karoly, 1981). However, most studies that examine these Rossby wave teleconnections to Australia during spring focus on the influence on rainfall.

Hoskins and Karoly (1981) used linearized barotropic wave theory, and assumed zonally symmetric and slowly varying background flow, to demonstrate that the SST heating associated with El Niño generates a quasi-stationary Rossby wave response in the Pacific. This wave, identifiable as a series of a high and low atmospheric height anomalies, arcs poleward and eastward in a great-circle toward the poles where it refracts to return toward the equator and marked a significant step forward in our understanding of tropical to extratropical teleconnections. The dispersion relation for barotropic Rossby waves (equation 1; Hoskins and Karoly, 1981) is as follows:

$$\omega = Uk - \frac{(\beta - U_{yy})k}{K^2} \quad \text{Equation 1.1}$$

Where  $\omega$ , is frequency,  $U$  is the mean-background zonal wind,  $\beta$  is the gradient of planetary vorticity,  $U_{yy}$  is the curvature of the flow and  $K$  and  $k$  are the total and zonal wave numbers, respectively. For a quasi-stationary wave, e.g. the seasonal response to ENSO heating, the frequency,  $\omega$  is zero. Re-arranging equation 1 shows that for a stationary wave,

$$K_S^2 = \frac{\beta - U_{yy}}{U} \quad \text{Equation 1.2}$$

As such, for a real solution, linear Rossby wave theory further requires that the background flow must be westerly and greater than zero (the critical velocity) relative to the Rossby wave propagation, and that the meridional gradient of mean absolute vorticity ( $\beta - U_{yy}$ ) must be positive. These assumptions are restrictive (e.g. the mean flow in the tropics is easterly), though later work eased some of these

requirements by showing that zonal flow can vary slightly (Branstator 1983; Hoskins and Ambrizzi, 1993; Li X. et al., 2015a, b; McIntosh & Hendon, 2018). For a review of the development, benefits and short-falls of linear Rossby wave theory on teleconnections see Liu & Alexander (2007) and Stan et al. (2017), and references therein. Despite its limitations linear Rossby wave theory is successful in explaining much of the teleconnection patterns generated by tropical SST anomalies to the extratropics. This theory is applied throughout this thesis to understand teleconnections to Australia, and though the limits to this theory are acknowledged, it is beyond the scope of this thesis to improve the underlying dynamics.

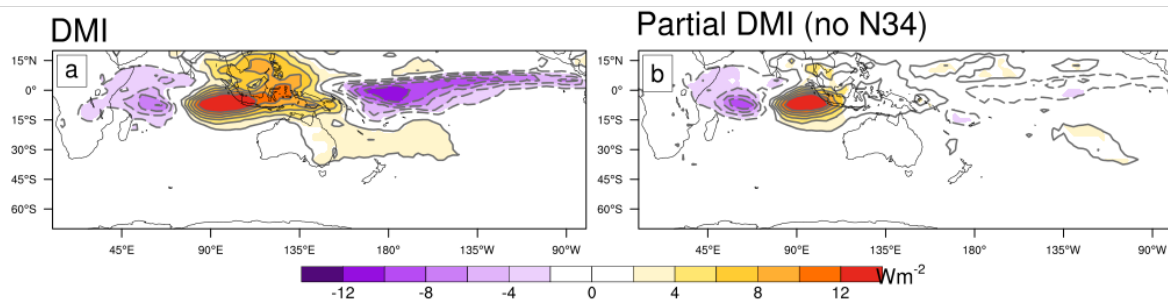


**Figure 1-5 SON linear regression of DMI (a) and partial DMI (Niño3.4 index linearly removed; b) onto OLR**

*Outgoing long wave radiation (OLR) is available for download at [https://psl.noaa.gov/data/gridded/data.interp\\_OLR.html](https://psl.noaa.gov/data/gridded/data.interp_OLR.html). Filled contours show where the regression was statistically significant at the 95% confidence level using a two-sided t-test with 39 independent samples (1979 to 2018).*

The requirement for westerly background flow should prevent Rossby wave formation and propagation from the region of tropical easterlies, however, Sardeshmukh & Hoskins (1988) showed that Rossby wave source (anomalous vorticity) can be remote from the tropical SST heating. The upper-level horizontal wind divergence associated with anomalous tropical convection ‘pushes’ the contours of climatological vorticity poleward until it reaches a region of westerly wind, at which point Rossby wave propagation is possible. Qin and Robinson (1993) linearized the Rossby wave source into two terms; vorticity anomalies generated by either vortex stretching (e.g. convection) or by advection for climatological vorticity by anomalous divergent wind. The latter mechanism results in strong Rossby wave sources west and east of Australia during winter and spring due to the association of the subtropical jet and anomalous outflow generated during IOD and ENSO events (e.g. McIntosh & Hendon, 2018; Wang, G. et al., 2019). As such, linear Rossby wave theory is an effective tool to understand how tropical variability can influence Australia’s climate in spring.

Linear Rossby wave theory has been used to understand teleconnections from the tropical Ocean basins, but it is not always clear how this results in climatic impacts in Australia. The Pacific South American (PSA) pattern associated with ENSO (Karoly, 1989), is ‘down-stream’ (east), and propagates away from Australia.

Cai et al., (2011a) argue that ENSO's influence on Australia comes via the tropical Indian Ocean. During spring, tropical convection driven by IOD, both with and without ENSO enhancement (Fig. 1-5), generates a pair of quasi-stationary Rossby waves from the west and east tropical Indian Ocean. These waves arc poleward and eastward to constructively interfere and generate an anomalous anticyclone south of Australia (positive IOD events; see Fig. 1-6; Saji et al., 2005; Cai et al., 2011a; McIntosh & Hendon, 2018). However, by linear Rossby wave theory, the strong meridional gradient of the zonal wind from the Indo-Pacific subtropical jet (Koch et al., 2006) should effectively prevent any direct propagation of Rossby waves from the tropical Indian Ocean (equation 2; Simpkins et al., 2014; Li X. et al., 2015a; McIntosh & Hendon, 2018). While the tropical Atlantic also generates Rossby wave teleconnections that propagate south of Australia toward Antarctica (Simpkins et al., 2014; Li X. et al., 2014, 2015a,b), it is not clear whether this wave influences Australia's climate. So, while each of the tropical basins generates Rossby waves, questions remain about how they influence Australia's spring climate.

(c) SON, IOD and ENSO

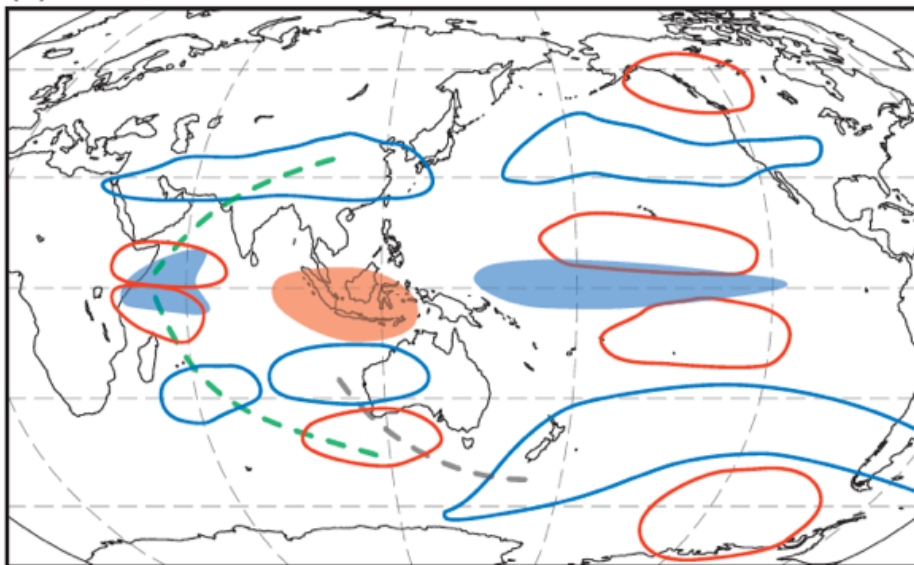


**Figure 1-6 SON IOD and ENSO atmospheric wave trains**

*Schematic illustration of the typical wave trains associated with the IOD and ENSO in SON. This description is for positive phases of the IOD and El Niño. Shaded blue (red) areas indicate regions of increased (decreased) tropical convection. Blue (red) contours indicate anomalously low (high) upper-level heights. The dashed lines trace the prominent wave trains: grey for the east Indian Ocean wave train and green for the west Indian Ocean wave train. The Pacific North and South American (PNA and PSA) wave trains are not marked but visible as the series of high and low height anomalies over the Pacific Ocean. From Cai et al., 2011a © American Meteorological Society. Used with permission.*

The proximity to Australia, as well as the ENSO-IOD co-variability suggest that the tropical Indian Ocean is important for Australia's spring climate, despite the presence of the subtropical jet. Both the subtropical and polar jets act as Rossby waveguides that direct waves along regions of higher K (Hoskins and Ambrizzi

1993; see yellow and turquoise regions in Fig. 1-7). However,  $K$  becomes imaginary on the poleward flank of the subtropical jet (white regions in Fig. 1-7). Hence, any Rossby waves generated by the tropical Indian Ocean should either refract away from or evanesce at this subtropical jet boundary before reaching extratropical Australia (Li, X., et al 2015a,b; McIntosh and Hendon, 2018), despite the strong Rossby wave sources and teleconnection pathways noted above. The solution to this apparent contradiction may be a secondary wave source poleward of the subtropical jet. Eddy-feedbacks between the jet and atmospheric outflow from IOD convection may promote Rossby waves that propagate along the polar waveguide toward Australia (McIntosh & Hendon, 2018). Again, there is some conflict here, as McIntosh and Hendon (2018) also argued that the subtropical jet should have weakened sufficiently by spring to allow direct propagation between tropics and extratropics, despite the persistent regions of imaginary  $K$  (e.g. Li X., et al., 2015a). Regardless, the tropical Indian Ocean appears to be an important, if not fully understood, source of atmospheric circulation variability that influences Australia's spring maximum temperatures.

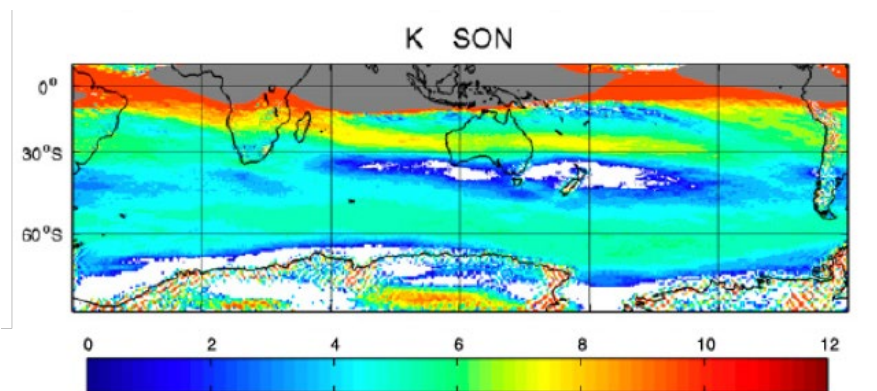


**Figure 1-7 SON climatological total wave number**

*Spring climatological Rossby wave number  $K$  ( $m^{-1}$ ) in ERA-Interim reanalysis data. The white areas indicate the regions where the total wavenumber is imaginary because of a strong meridional gradient of vorticity, while the grey areas indicate the regions where the total wavenumber is imaginary because of the easterly trade wind. The stationary Rossby wave trains will be reflected by the edge of the white region but break when arriving at the grey region. From Li X., et al., 2015a © American Meteorological Society. Used with permission.*

## 1.5 Seasonal prediction systems as a tool to understand teleconnections

Dynamical modelling is often used to extend our knowledge of atmospheric teleconnections beyond what can be achieved with linear Rossby wave theory or observations. As linearized Rossby wave theory has limits, so does dynamical modelling, some of which impact teleconnections from the tropical Indian Ocean in particular. While use of multi-model ensemble can counteract internal model biases or model drift (e.g. Liu et al., 2017), similarities between models can lead to overconfidence in model-mean output (e.g. Abramowitz, 2010; Abramowitz et al., 2019). A common model bias is to simulate overly strong IOD variability (Cai & Cowan, 2013) and positive IOD skew (Li, G. et al., 2015). Confidence in the statistically significant projection of an increase in positive IOD events in the future (Li, G. et al., 2016) is low due to

these model biases, however an increase in positive IOD events has been observed in recent years (e.g. Cai et al., 2014a). As the tropical Indian Ocean is relevant to Australia's spring maximum temperature variability, biases in how the tropical Indian Ocean is simulated may adversely affect our ability to understand Indian Ocean teleconnections.

An alternative approach, that may also help reduce model bias, is to use dynamical seasonal prediction models as a tool to extend our knowledge of atmospheric teleconnections. To apply this successfully requires forecasts that verify well. As the IOD and ENSO are active in spring and combine with Australia's other modes of climate variability, spring in Australia is a season and region with high predictive skill (Shi et al., 2012; King et al., 2020b), and is thus particularly suited to the use of dynamical seasonal prediction systems to help explore teleconnections. Seasonal prediction models are also subject to some biases in how they simulate the tropical Indian Ocean and associated teleconnections (Liu et al., 2017), but they offer some advantages over standard climate models for understanding observed events, their associated circulation and teleconnections, including (list adapted from Wang et al., 2021):

1. Operational use means that these models have been thoroughly tested across multiple real-world events.
2. Relatively short lead-times in forecasts and hindcasts can reduce model drift from observations, compared to standard climate models.
3. These models are typically global, which avoids boundary condition issues, and are fully atmosphere-ocean coupled.
4. Initial conditions are based on atmosphere, ocean, and land observations so that forecasts and hindcasts represent a spread of realistic possible outcomes of real-world events (e.g. Brunet et al., 2010; Meehl et al., 2021)

The Predictive Ocean Atmosphere Model for Australia (POAMA) version 2 (Cottrill et al., 2013; Hudson et al., 2013) is the Australian Bureau of Meteorology's former operational sub- to seasonal prediction system and can also be used as an investigative tool. POAMA provided skilful forecasts of Australian spring conditions (Lim et al., 2009; Hudson et al., 2013) and accurately simulates IOD variability (Zhao & Hendon, 2009). However, POAMA's teleconnection to Australia from the Indian Ocean is weaker than observed and simulates a stronger relationship to ENSO over the IOD (White et al., 2014). Nevertheless, POAMA has successfully been used as an experimental system to explore the impact of carbon dioxide on seasonal forecasts (Hope et al., 2016; Hope et al., 2018; Wang et al., 2021), changing relationships associated with ENSO under continued anthropogenic climate change (Zhao et al., 2016; Lim et al., 2019b), and sensitivity experiments with different ocean initial conditions (e.g. Lim et al., 2015; 2016; Lim & Hendon, 2017). While this thesis is not focused on the predictive skill of Australian spring maximum temperatures, it makes use of POAMA to investigate the teleconnections and atmospheric circulation leading to high temperatures.

## 1.6 Australian spring temperatures in the context of a changing climate

The majority of SON periods in recent decades have recorded Australian-averaged maximum temperatures that were above the long-term average and coincided with several broken temperature records and extreme climate events (Fig. 1-1; see also

[http://www.bom.gov.au/climate/current/statement\\_archives.shtml?region=aus&period=season](http://www.bom.gov.au/climate/current/statement_archives.shtml?region=aus&period=season) ).

Extreme climate events on a seasonal time scale have been intensely studied to attribute the relative contributions of any active drivers of natural variability compared to that of the anthropogenic influence on climate change (e.g. Stone et al., 2013). Different methods are used across different attribution studies, including fractional attributional risk (FAR) (e.g. Gallant and Lewis (2016), statistical regression to reconstruct the event (e.g. Arblaster et al., 2014; Wang et al., 2016), or various modelling techniques (e.g. Arblaster et al., 2014; Lewis & Karoly 2014; Hope et al., 2014;2016, Wang et al., 2016; 2021). The importance to society of understanding the factors that contribute to extreme weather and climate events has led to a recommended procedure for event attribution that highlights the importance of accurate modelling (Phillip et al., 2020; van Oldenborgh et al., 2021). Modelling studies, including using a seasonal prediction system, have the advantage of going beyond statistical relationships to better understand the contributions of both anthropogenic climate change and the remote drivers of variability to the observed atmospheric circulation during events (e.g. Wang et al., 2021)

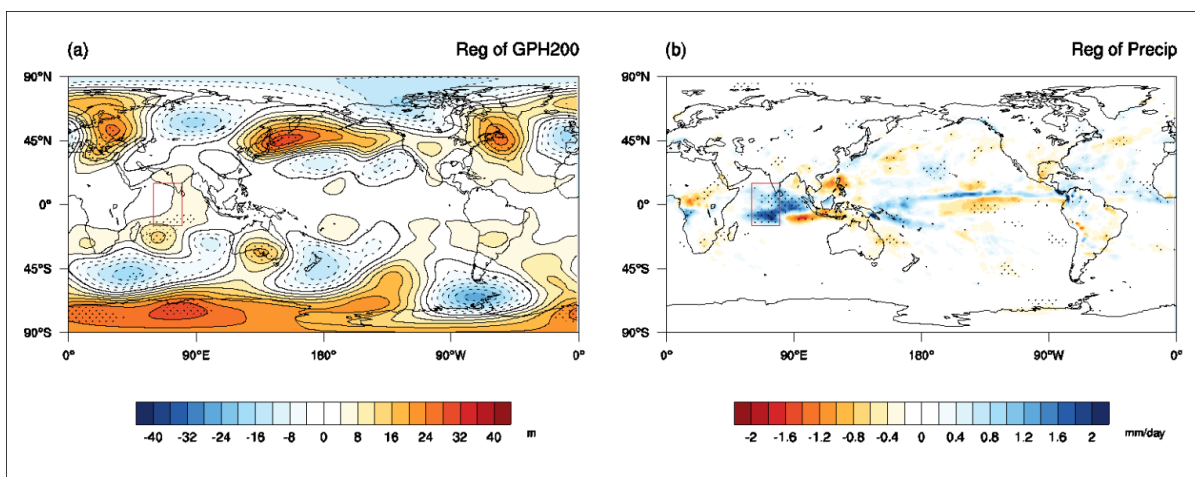


**Figure 1-8 Central-tropical Indian Ocean wave train**

*Partial regression of October-November (a) 200-hPa level geopotential height (m) and (b) precipitation anomaly ( $\text{mm day}^{-1}$ ) onto the rainfall index of tropical central Indian Ocean averaged over  $15^{\circ}\text{S}$ – $15^{\circ}\text{N}$ ,  $60^{\circ}$ – $80^{\circ}\text{E}$  (red box), removing the influence of IOD over the period 1981-2013. Stippling indicates statistical significance greater than 90% confidence level. From Hope et al., 2015 © American Meteorological Society. Used with permission.*

To date, spring of 2014 remains the hottest recorded in Australia and fell in the middle of a set of three anomalously hot springs that each broke several sub-seasonal heat records (Fig. 1-1; See also Bureau of

Meteorology Climate Summaries: <http://www.bom.gov.au/climate/current/season>). Attribution studies of these events agree that much of the observed heat was associated with the background warming trend, with the remainder made up of different contributions from the various modes of variability and heat mechanisms discussed above (e.g. Arblaster et al., 2014; Lewis & Karoly, 2014; Hope et al., 2015, 2016; Gallant & Lewis, 2016). However, subtle differences between the conclusions drawn about the 2014 event highlight that there is more to understand about extreme heat development in spring in Australia. Hope et al. (2015) identified anomalous high geopotential height over southern Australia as a factor in the observed high maximum temperatures during October-November 2014. They argued that this height anomaly was at least partially caused by a quasi-stationary Rossby wave (series of high and low anomalies in Fig. 1-8a) triggered by rapid warming and associated increased convection (red box, Fig. 1-8b) in the central tropical Indian Ocean. Conversely, Gallant & Lewis (2016) downplayed the role of the southern Australian height anomaly in the heat of spring 2014 arguing that the thermal contribution from anthropogenic climate change was far greater. Whether climate change was the bigger contributor to heat in 2014 is not a topic of this thesis; however, better understanding of the Rossby wave train and southern Australian anticyclone may lead to better understanding of heat generation in Australia in spring. An overall improvement in the understanding of the dynamics that lead to extreme heat during spring will feed back into improved understanding of future heat events that occur in conjunction with continued warming.

The background warming trend associated with anthropogenic climate change (Cullen et al., 2013; Eyring et al., in press) was likely a factor in the spring heat events between 2013 and 2015 (e.g. Arblaster et al., 2014; Hope et al., 2015, 2016; Gallant and Lewis 2016) and the more recent dry springs preceding the extreme 2019/2020 fire season (e.g. Watterson, 2020; Abram et al., 2021; Marshall et al., 2021b). Extreme swings of natural atmospheric variability also contributed to the extraordinary conditions in these events (e.g. Abram et al., 2021). Spring 2019 coincided with an extreme positive IOD (Watterson, 2020), strong central Pacific El Niño (Zhang et al., 2021) and a rare and strong sudden stratospheric warming event that promoted sustained and strong negative SAM conditions from mid-spring into summer (Lim et al., 2021a; Lim et al., 2021b), all of which contributed to the hot and dry conditions of 2019/2020. The remote drivers of variability may also be changing under continued anthropogenic climate change (e.g. Hendon et al., 2007; Power et al., 2013; Cai et al., 2014b; Cai et al., 2014c; Chung & Power, 2016; Lim et al., 2019b) with potential consequences for the teleconnections to Australia and spring maximum temperature. As our knowledge of how anomalous heat during recent spring heat events is incomplete, these changes will make it even more difficult to understand what conditions may lead to extreme heat in the future, adding a sense of urgency to our need to better understand spring heat formation.

## 1.7 Research questions and thesis outline

The remote drivers, teleconnections and atmospheric circulation that contribute to anomalous high spring maximum temperature in Australia are relatively under-studied. In particular, spring is a shoulder season when many broad-scale atmospheric changes occur with possible impacts to how heat forms on a sub-seasonal time-scale. Exploring the recent heat events can provide insight into how the atmospheric circulation anomalies lead to anomalous high maximum temperatures, but more is required. The coincidence of Australia's remote drivers of climate variability peaking during spring provides an opportunity for addressing these issues via the use of a sub-seasonal to seasonal model. However, model limitations and biases, combined with limits to Rossby wave theory mean that it is not entirely clear how teleconnections, particularly from the tropical Indian Ocean, contribute to high maximum temperatures.

These gaps in understanding how anomalously high maximum temperature develops in Australia during spring can be summarised into three research questions:

1. What drove the atmospheric circulation that contributed to three of Australia's most extreme spring heat events in observations and POAMA?
2. How do the remote drivers of variability and dynamical mechanisms that promote anomalous Australian maximum temperature vary across the months of spring?"
3. What is the influence of the tropical Indian Ocean on Australian maximum spring temperature development?

The first question will be addressed in chapter 2 by comparing observations of the atmospheric circulation anomalies during three extreme Australian spring heat events to those forecast by the best and worst performing POAMA ensemble members. I will identify several atmospheric circulation features that were important for the heat development. This chapter was published as a journal article in *Climate Dynamics* in 2021.

The second question is addressed in chapter 3. I generalise the findings of chapter 2 by looking at the monthly relationship with the atmospheric circulation and maximum temperatures in Australia during spring. Remote tropical and extratropical forcing of the atmospheric circulation are compared through the months of spring. Heat formation mechanisms and how they relate to the atmospheric circulation across the months will also be examined. This chapter was submitted as a journal article and is under review in *Weather and Climate Dynamics*.

The final research question is addressed in chapter 4. I examine the relative role of the tropical Indian Ocean in Australia's maximum temperature by comparing atmospheric circulation changes across two sets of POAMA experiments with relationships found in other sub-seasonal prediction systems.

The final chapter of this thesis will be a synthesis and discussion of the findings of this thesis and will address the thesis aim.

## 2 Exploring Atmospheric Circulation Leading to Three Anomalous Australian spring Heat Events

This chapter is a reproduction of the paper, “Exploring Atmospheric Circulation Leading to three anomalous Australian spring heat events” published in *Climate Dynamics* by McKay et al., (2021). The section and figure numbers have been adapted to fit the thesis structure, but the text and figures are unchanged. The supplemental figure from the paper is included in the main text of this chapter.

This chapter describes the atmospheric circulation associated with three recent spring month- to two-month long extreme heat events that occurred in Australia. We identify several important atmospheric circulation features common across the events and suggest that the tropical Indian Ocean is important driver behind these feature, particular in the heat events that occurred later in spring.

### 2.1 Abstract

Australian maximum temperatures have reached record values in recent austral springs and are projected to increase further in a warming world. We focus on three record spring heat events in September 2013, October-November 2014 and October 2015, and examine the anomalous atmospheric circulation associated with these events in reanalysis and a sub-seasonal to seasonal prediction system, POAMA, to identify factors contributing to extreme heat over Australia. We find that an anomalous equivalent barotropic cyclonic circulation southwest of Australia and a quasi-stationary wave train formed by an upper-troposphere anticyclonic circulation over southern Australia and barotropic cyclone southeast of Australia are important features in these heat events, though the wave train was only observed in the latter two events. This wave train appears to be linked to the tropics, and particularly the tropical Indian Ocean, suggesting that teleconnections to the tropical Indian Ocean can be important for monthly spring extreme heat formation in Australia. However, the forecast relationship with the tropical Pacific Ocean was over-represented at the cost of the relationship between the Indian Ocean and upper-troposphere anomaly, limiting the ability of POAMA to forecast the full extent of the month- or two month-long heat extremes at zero lead time. This means that the model might underestimate the magnitude of future extreme heat events in spring, a factor that should be assessed in the next generation of seasonal forecast models.

### 2.2 Introduction

In the past decade, the majority of Australian spring (September, October, November) temperatures have been above average e.g. see Monthly Weather Review for September, October, November, 2013 to 2019 produced by the Bureau of Meteorology (<http://www.bom.gov.au/climate/mwr/>). With Australia projected to continue to warm (Alexander and Arblaster 2017), future austral spring temperatures are expected to become more extreme. Spring-time warming trends have been linked to impacts on agriculture, such as reduced pasture growing seasons (Cullen et al. 2009), decreases in wheat crop (Taylor et al. 2018) and

earlier and shorter wine-grape harvesting seasons (Jarvis et al. 2019). Local and global economic consequences are possible as beef, wheat and alcoholic beverages are amongst Australia's top 25 exports (<https://www.dfat.gov.au/about-us/publications/trade-investment/australias-trade-in-goods-and-services/Pages/australias-trade-in-goods-and-services-2016.aspx#exports>). Spring warming trends may also impact human health (e.g., due to a lack of acclimatisation to early season heat, see Nairn and Fawcett 2014) and be linked to an earlier start to the Australian fire season (Dowdy 2018). The impacts of the warming trend and extreme austral spring heat in Australia are an example of what may happen globally as heat extremes become more common as a result of anthropogenic climate change (Collins et al. 2013). Here, we explore three month- to two month- long extreme austral spring heat events to better understand how the heat developed in each event and if those processes were forecast by the Australian Bureau of Meteorology's dynamical seasonal forecast model. September 2013 was the hottest September recorded since 1910 (Australian Bureau of Meteorology 2013); spring 2014 remains the hottest Australian spring to date, with the majority of the heat forming in October and November (Australian Bureau of Meteorology 2014); October 2015 was the hottest October on record, with above average temperatures across much of southern Australia (Australian Bureau of Meteorology 2016).

In austral spring, dry conditions and, by association, high temperatures in Australia (Jones and Trewin 2000; Hope et al., 2009; Gallant and Lewis 2016) have been linked with several remote climate drivers (e.g. Risbey et al. 2009a). El Niño Southern Oscillation (ENSO) and the Indian Ocean Dipole (IOD) can directly impact Australia's climate through subsidence in the tropical north, or indirectly by the initiation and propagation of Rossby waves in the Indian Ocean toward Australia (Cai et al. 2011a; McIntosh and Hendon 2018) that then influence the Australian-region's atmospheric circulation. In particular, the positive phase of the IOD and warm phase (El Niño) of ENSO are associated with drier and warmer conditions over north, east and southern Australia in spring (Risbey, et al. 2009b; Ummenhofer et al. 2009a; Min et al., 2013). Phases 2 and 3 of the Madden-Julian Oscillation (MJO) (Wheeler and Hendon, 2004; Marshall et al. 2014), and the negative phase of the Southern Annular Mode (SAM) (Hendon et al. 2007; Marshall et al. 2012) are also associated with high austral spring maximum temperatures. Negative SAM is associated with anomalous mid-tropospheric subsidence, surface westerly winds, and warmer conditions across much of subtropical eastern and southern Australia in spring (Hendon et al., 2007; Lim et al. 2019a). Although the SAM is known as an internally driven atmospheric process whose decorrelation time is about 2 weeks (Hendon et al. 2007, Marshall et al. 2012), the seasonal mean behavior of the SAM in austral warm seasons demonstrate its association with ENSO (e.g., Zhou and Yu 2004; L'Heureux and Thompson 2006; Lim et al. 2013; Lim et al. 2016a; Lim and Hendon, 2017; Lim et al. 2019b) and the Southern Hemisphere stratospheric vortex variations (e.g., Seviour et al. 2014; Byrne and Shepherd 2018; Lim et al. 2019a), therefore providing predictability to the SAM-driven components of Australian temperatures, rainfall and bushfire risks.

All these climate drivers act on different temporal and spatial scales and can shift the probability distribution toward months or seasons with drier and heat-conducive weather and atmospheric circulation. Anomalously high upper-tropospheric geopotential heights over southern Australia are linked to warm austral springs (Gallant and Lewis, 2016). On shorter time scales, reduced cold front activity (e.g. Cai et al. 2011a,b; Pook et al. 2013), atmospheric blocking in the Tasman Sea (Marshall et al., 2014), advection of warm air poleward (e.g. Boschat et al. 2015), shifts in the heat balance from latent heat (wetter and cooler conditions) to sensible heat (drier and hotter conditions) (Loughran et al. 2019), and increased insolation and subsidence (e.g. Quinting and Reeder 2017) are also linked with warmer conditions. While several of these studies focused on austral summer, many of the processes described are valid for spring, and, in conjunction with the active climate drivers, can be used to understand the heat in the three anomalous spring events.

Australia's different climate drivers provide sources of skilful sub- to seasonal forecasts to the Australian Bureau of Meteorology's former operational system, POAMA (Hudson et al. 2013). POAMA has been found to be skilful at predicting extreme maximum temperatures during austral spring, particularly when climate modes, such as ENSO or the IOD are active (e.g. Hudson et al. 2013; White et al. 2014). The POAMA system began producing operational forecasts from late 2013, including forecasts of the 2014 and 2015 austral heat events. A series of hindcasts run from 1981 to 2013 include the September 2013 heat event. The newer seasonal forecasting system, ACCESS-S1, has increased model resolution and improved model physics compared to POAMA (Hudson et al. 2017) but neither of its hindcasts (1990-2012) or real-time forecasts (2018 to present) include the three extreme spring heat events examined in this study.

Previous studies have explored the potential drivers of each of the three austral spring heat events (see summary in Table 1). The warming influence of anthropogenic climate change has been found to be a factor in the anomalous heat in each event, as well as the extreme heat's otherwise unlikely year-to-year repetition (e.g. Gallant and Lewis 2016; Hope et al., 2016). Anomalously dry conditions in the months preceding spring 2013 were identified as a large factor in the September extreme heat of that year (Arblaster et al., 2014) and were also a factor in the 2014 event (Hope et al. 2015). During the events reduced cold front passage or increased atmospheric blocking in the Tasman Sea occurred for periods across the three events, and further contributed to surface drying and subsequent diabatic heating (e.g. Bureau of Meteorology Monthly Weather Review at <http://www.bom.gov.au/climate/mwr/>). Negative SAM also occurred during each event, but was only a relatively strong contributor to the heat in September 2013 (Arblaster et al. 2014). El Niño and positive IOD events occurred during both the 2014 and 2015 events, but only made small contributions to the sub-seasonal time scale heat event over Australia, despite the extreme amplitude of the 2015 El Niño (Hope et al., 2015; Hope et al. 2016; Black and Karoly, 2016). The MJO may have contributed to the heat in September 2013 and October 2015 (Arblaster et al., 2014;

Hope et al., 2016), but only became active in the eastern tropical Indian Ocean (phase 3) late in November 2014 (see [www.bom.gov.au/climate/mjo/](http://www.bom.gov.au/climate/mjo/)) and may have only influenced the atmospheric circulation around Australia and high maximum temperatures (Wheeler and Hendon, 2004; Wheeler et al., 2009) at the end of the October-November 2014 heat event. An anomalous upper-level anticyclonic circulation was observed over southern Australia in spring 2013 and 2014 and linked to the high maximum temperatures (Hope et al., 2015; Gallant and Lewis 2016). Gallant and Lewis (2016) found that these anticyclonic circulations were not exceptionally strong compared to previous heat events and concluded that the anomalous heat was only due to the thermodynamic warming associated with anthropogenic climate change. Conversely, Hope et al. (2015) argued that the upper-tropospheric anticyclone circulation in the 2014 event had been enhanced through changes in remote sea surface temperatures, and that this further contributed to the high temperatures. These different conclusions highlight a gap in our understanding of spring heat extremes in Australia and the associated atmospheric circulation. A comparison of the upper-tropospheric and surface circulations and associated teleconnection mechanisms across the three heat events in reanalysis and POAMA forecasts, may help us better understand how the heat formed across the three events, and provide clues on what to expect in future heat events.

We build on the short studies that examined each of these austral spring events by comparing the low-level and upper-tropospheric circulation that occurred during those events. We will explore the robustness of the atmospheric circulation patterns suggested in these studies as contributing to the heat development by identifying any patterns that may be common across all three events. We will take advantage of the ensemble spread in the POAMA forecasts to help identify which atmospheric circulation patterns are important for the maximum temperature development during the three events. We discuss several caveats to our findings, including the implication that the atmospheric circulation over the Indian Ocean is poorly predicted in the POAMA model.

Driver	September 2013	October-November 2014	October 2015
ENSO	Weak La Niña Small cooling contribution	Weak El Niño Small, warming contribution	Strong El Niño Small to moderate warming contribution
IOD	Decaying negative Small cooling contribution	Weak positive Small, warming contribution	Strong positive Small to moderate positive contribution
SAM	Strongest negative Large warming contribution	Negative Small, warming contribution	Negative Warming contribution
MJO	Moderate phase 2 (early September) Possible warming contribution	Moderate phase 3 (late November) Contribution not previously studied.	Moderate phase 2 (second half of October) Positive contribution
Tasman Sea Blocking	-	Weak blocking Small warming contribution	Strong blocking (first half of October) Warming contribution.
Antecedent Soil Moisture	Dry antecedent condition Moderate to strong warming contribution	Dry antecedent conditions Small, warming contribution	-

**Table 2-1 Summary of drivers attributed to heat events - synthesis from literature**

*Meta-analysis from Arblaster et al., 2014; Hope et al. 2015; Black and Karoly, 2016; Gallant and Lewis 2016; Hope et al., 2016). Phase and magnitude of MJO (RMM index, Wheeler and Hendon, 2004) are available at <http://www.bom.gov.au/climate/mjo/>*

## 2.3 Method and Data

### 2.3.1 Observational and Reanalysis Data

The ERA-Interim reanalysis (Dee et al. 2011) dataset is used as the observational reference against the POAMA forecasts. Low level circulation is represented by mean sea level pressure (MSLP) and 850hPa wind anomalies for each of the three events examined. Upper-tropospheric circulation anomalies and wave activity flux are calculated at 200hPa using geopotential height, and climatological zonal and meridional wind. 200hPa has been found to be a representative level for upper-tropospheric equivalent barotropic Rossby wave propagation (e.g. Cai et al. 2011a; McIntosh and Hendon 2018). An interpolated Outgoing Longwave Radiation (OLR) dataset is provided by the NOAA/OAR/ESRL PSD, Boulder, Colorado, USA, from their website at [https://psl.noaa.gov/data/gridded/data.interp\\_OLR.html](https://psl.noaa.gov/data/gridded/data.interp_OLR.html) (Liebmann and Smith, 1996).

Observed Australian maximum temperatures over each of the spring events were calculated by taking the weighted areal-average across Australia from the gridded Australian Water Availability Project (AWAP)

dataset (Jones et al. 2009). AWAP has been shown to be consistent with the higher-quality, homogenised ACORN-SAT dataset (Fawcett et al., 2012; Trewin 2013; Gallant and Lewis 2016). However, ACORN-SAT uses only a subset of the available station data (Trewin 2013) and AWAP has been used in earlier studies of the spring heat events (e.g. Arblaster et al. 2013; Hope et al. 2014; 2015), allowing for easier comparison with our results. All anomalies were calculated against a base-state climatology from 1981 to 2010 and all datasets are re-gridded to match the POAMA forecast data.

### 2.3.2 POAMA model forecasts

POAMA (version 2) (Cottrill et al. 2013; Hudson et al. 2013) is a fully coupled dynamical seasonal forecast system, with an atmospheric model at T47 resolution (approximately 250km) and 17 vertical levels, and an ocean model with 25 levels and zonal resolution of 2° and meridional resolution ranging from 0.5° at the equator to 1.5° at the poles. Each forecast is composed of three POAMA model versions, using either standard, modified or bias-corrected physics (see Cottrill et al. 2013 and Hudson et al., 2013 for details), of 11 ensemble members each, to a total of 33 ensemble members. The forecast skill is similar among the different versions of the model, with slight strengths and weaknesses for different variables, times of the year and locations (Lim et al. 2009, 2012). Atmosphere, ocean and land observations are perturbed using a coupled breeding method and used to initialise each ensemble member forecast from the same instant. While the carbon dioxide levels in POAMA are set to 345 ppm, approximately the level in 1985, the use of observations in ensemble-member generation means that the impacts of anthropogenic climate change are felt through the initial conditions. This ensemble-member method produces sufficient spread in atmospheric variables to allow for skilful forecasts from sub-seasonal time scales.

To maximise the atmospheric information going into each sub-seasonal forecast, we use short lead time of 0-2 days POAMA forecasts of each event; forecasts initialised on September 1 for September 2013, September 28 for October-November 2014, and September 27 for October 2015. Earlier initialisation dates of POAMA forecasts began predicting anomalous heat for each event at a two- to three- week lead time with increasing magnitude and skill as the lead time shortened (not shown), consistent with the 1981-2013 POAMA hindcast skill (e.g. White et al., 2013). The peak of the 2014 and 2015 events occurred at least two weeks into the forecast period (see Bureau of Meteorology Temperature archive: <http://www.bom.gov.au/jsp/awap/temp/archive.jsp>), indicating that POAMA can capture processes contributing to the heat beyond persistence (Hudson et al. 2011). After which, only the sub-seasonal month to multi-month predictable component remains in the model, and it is this component that is the focus of this study. September, October-November and October climatologies were calculated from the 1981 to 2010 monthly-mean hindcast initialised on the 1<sup>st</sup> of each respective month (2-month forecast-mean initialised on the 1<sup>st</sup> of October for October-November climatology). Individual member anomalies were

calculated against the relevant model version climatology, and ensemble-mean anomalies were calculated against the ensemble-mean climatology.

A novel aspect of this study is that we use the differences in the atmospheric circulation anomalies in the POAMA ensemble members that forecast the highest and lowest Australian temperatures to further understand the robustness of the circulation associated with the three extreme spring heat events over Australia. The weighted areal-averaged Australian maximum temperature forecast of each heat event was calculated for each ensemble member and ranked hottest to coldest. Composites of the forecast circulation patterns made by the three hottest and coldest ensemble members (approximately the upper and lower 10% of the distribution) were compared to the reanalysis and ensemble-mean patterns. We assume that the common features between reanalysis and the hottest ensemble members, that were not present in the coldest ensemble members, can explain the observed and forecast heat. The 10% threshold was arbitrarily chosen to represent the extremes of the POAMA forecast, but similar results were found using composites of the five hottest and coldest ensemble members (not shown).

### 2.3.3 Comparing reanalysis and POAMA forecasts

The atmospheric anomalies in the reanalysis were found to be greater in magnitude than in any of the POAMA ensemble member forecasts. Therefore, for easier comparison of the circulation patterns between reanalysis and forecast, as well as to gain a measure of significance against previous years, all anomalies were divided by the relevant standard deviation calculated over the 1981 to 2010 climatology period. For the reanalysis and POAMA ensemble mean, the standard deviations were calculated from the reanalysis or ensemble mean detrended timeseries over the climatology period (30 values each). For the hottest and coldest POAMA forecasts, the monthly (or two-monthly for October-November) standard deviation was calculated across all the ensemble members across all years of the detrended 30-year hindcast (990 ensemble member values in total) and scaled by  $1/\sqrt{3}$  (e.g. Swart et al. 2015) to account for the three ensemble members used in each hottest or coldest averaged forecast. This allowed for comparison against the reanalysis values, and also against the variability between ensemble members over the hindcast period. Similar magnitude comparison problems were found when comparing wave activity flux and 850hPa wind vectors in reanalysis and POAMA forecasts, so different scales are used between reanalysis and forecasts across the three events. For clarity, only the largest vectors were plotted (see individual figure descriptions for vector threshold values).

The maximum temperature figures are presented as anomalies (not standardised), with statistical significance calculated from a one-sample two-sided T-test at the 95% confidence level, accounting for the number of ensemble members as described above.

Gallant and Lewis (2016) connected high Australian maximum temperatures with anticyclonic potential vorticity over a region of southern Australia. Here, we adjust their method to test the relationship between southern Australian geopotential height (Z200) and monthly spring maximum temperatures, by plotting the observed September, October, and November Australian area-averaged maximum temperature anomalies against corresponding Z200 anomalies averaged over 120°-150°E and 30°-40°S, (covering southern Australia and the Great Australian Bight), between 1981 to 2015, where each average was weighted by the cosine of the latitude. This process was then repeated for the individual ensemble member forecasts of the three heat events.

#### 2.3.4 Linear Rossby wave theory

Tropical sea surface temperature (SST) anomalies can influence the climate of the extratropics through the initiation and propagation of quasi-stationary equivalent barotropic Rossby waves (e.g. Hoskins and Karoly, 1981). Tropical SST anomalies generate anomalous atmospheric convection that then generates anomalous upper-troposphere divergent flow. This divergent flow distorts the climatological absolute vorticity field outside of the tropics that can then initiate a Rossby wave (Sardeshmukh and Hoskins 1988) that impacts on the extratropical atmospheric circulation and climate. However, the meridional wind-shear around the Australian-region subtropical jet should limit the tropical Indian Ocean's effectiveness as a source of Rossby waves that impact the extratropics through austral winter-spring by blocking direct propagation of waves into higher latitudes (e.g. Hoskins and Ambrizzi, 1993; Simpkins et al. 2014; Li, X. et al. 2015a).

Nevertheless, quasi-stationary Rossby waves, triggered by tropical Indian Ocean SST variations, have been linked to variations in Australia's winter and spring climate (Cai et al., 2011a; Timbal and Hendon 2011; McIntosh and Hendon 2018). During austral winter, when the Southern Hemisphere subtropical jet is strongest (Koch et al. 2006), the tropical Indian Ocean may play an important role in perturbing the mid-latitude stormtrack, which in turn acts as a source of extratropical Rossby waves impacting the southern Australian region (McIntosh and Hendon 2018; Wang and Hendon 2020). The subtropical jet weakens in austral spring (Koch et al. 2006), possibly sufficiently to allow direct Rossby wave propagation toward Australia (McIntosh and Hendon 2018).

The upper-tropospheric circulation associated with quasi-stationary Rossby wave propagation, formation and dissipation is tracked using Rossby wave activity flux (WAF). For conservative, weakly dissipative, slowly varying flow, WAF moves parallel to the Rossby wave group velocity (Plumb 1985) and can therefore be used to analyse the Rossby wave paths occurring concurrently with the spring heat events. We do not incorporate a time lag between the Rossby wave calculation and maximum temperature anomaly as the approximate time for a tropical SST-forced Rossby wave to propagate into the high latitudes is of the order 10 days (e.g. Branstator 2014) and it is assumed that averaging over a month allows sufficient time for

Rossby waves to propagate towards Australia and influence its climate. Here, we use the horizontal component of WAF, computed following Takaya and Nakamura (2000):

$$W = p \cos \phi \left\{ \begin{array}{l} \frac{U}{a^2 \cos^2 \phi} \left[ \left( \frac{\partial \psi'}{\partial \lambda} \right)^2 - \psi' \frac{\partial^2 \psi'}{\partial \lambda^2} \right] + \frac{V}{a^2 \cos \phi} \left[ \frac{\partial \psi'}{\partial \lambda} \frac{\partial \psi'}{\partial \phi} - \psi' \frac{\partial^2 \psi'}{\partial \lambda \partial \phi} \right] \\ \frac{U}{a^2 \cos \phi} \left[ \frac{\partial \psi'}{\partial \lambda} \frac{\partial \psi'}{\partial \phi} - \psi' \frac{\partial^2 \psi'}{\partial \lambda \partial \phi} \right] + \frac{V}{a^2} \left[ \left( \frac{\partial \psi'}{\partial \phi} \right)^2 - \psi' \frac{\partial^2 \psi'}{\partial \phi^2} \right] \end{array} \right\}$$

where  $p$  is the pressure (here, 200hPa) scaled against 1000hPa,  $U$  and  $V$  are the climatological zonal and meridional wind speed magnitudes,  $a$  is the radius of the earth,  $(\phi, \lambda)$  are latitude and longitude,  $\psi' = \Phi' / f$  is the quasi-geostrophic perturbation streamfunction,  $\Phi'$  is the perturbation geopotential, calculated using the 200hPa geopotential height anomaly, and  $f = 2\Omega \sin \phi$  is the Coriolis parameter with the Earth's rotation  $\Omega$ . The wave activity flux is plotted over the standardised 200hPa geopotential height anomalies to represent the upper-troposphere circulation and the associated quasi-stationary Rossby wave activity associated with each heat event.

The source region of Rossby wave trains can be found at regions of divergence of WAF (e.g. McIntosh and Hendon (2018), and can be triggered by regions of anomalous deep tropical convection (Sardeshmukh and Hoskins 1988). We use standardised tropical OLR anomalies (confined to a band within 10° of the equator) as a proxy for the source of convection-driven Rossby wave trains (e.g. Branstator 2014). As the convection forces upper-troposphere divergence out of the tropics, we expect upper-tropospheric anticyclonic circulation (indicated by anomalously high 200hPa; Z200) and wave activity flux divergence poleward and westward of tropical convection. Similarly, we expect cyclonic circulation (anomalously low Z200) and wave activity flux poleward and westward of suppressed tropical convection (Sardeshmukh and Hoskins 1988).

## 2.4 Results

### 2.4.1 Temperature anomalies

Australian maximum temperature anomalies during the three spring heat events of September 2013, October-November 2014, and October 2015, were observed to be extreme and widespread (Fig. 2-1 a-c), with temperatures well above the 1981 to 2010 average (see Australian areal-averaged maximum temperature anomalies in top right corner of each figure). The spatial structure of these heat events was generally well captured by the POAMA forecasts (Fig. 2-1 d-l), although the forecast heat anomaly extended too far westward in September 2013. The magnitude of the ensemble-mean forecast heat was generally underestimated in comparison to the observed heat, particularly in October 2015, though still significant compared to the hindcast climatology. Nevertheless, POAMA demonstrated skill in forecasting the spatial

structure of the three spring heat events, with the hottest ensemble members being closest to the observed magnitude of each of the heat events.

The maps of observed monthly maximum temperature standard deviations from detrended data (Figs. 2-2a, c, e) show lower interannual variability in the north of Australia, with a gradual increase poleward. There is an observed local peak in variability along the subtropical east in November that is simulated well in the POAMA-ensemble mean in November (Fig. 2-2f). POAMA also simulates the same high variability in east Australia in September and October (Fig 2b, d), but that pattern is not evident in the AWAP data in those months (Figs. 2-2a, c). This is consistent with White et al. (2014) who suggested that deficiencies in POAMA forecasts of extreme high temperature extremes may be due to poor simulation of the teleconnection with Indian Ocean SSTs.

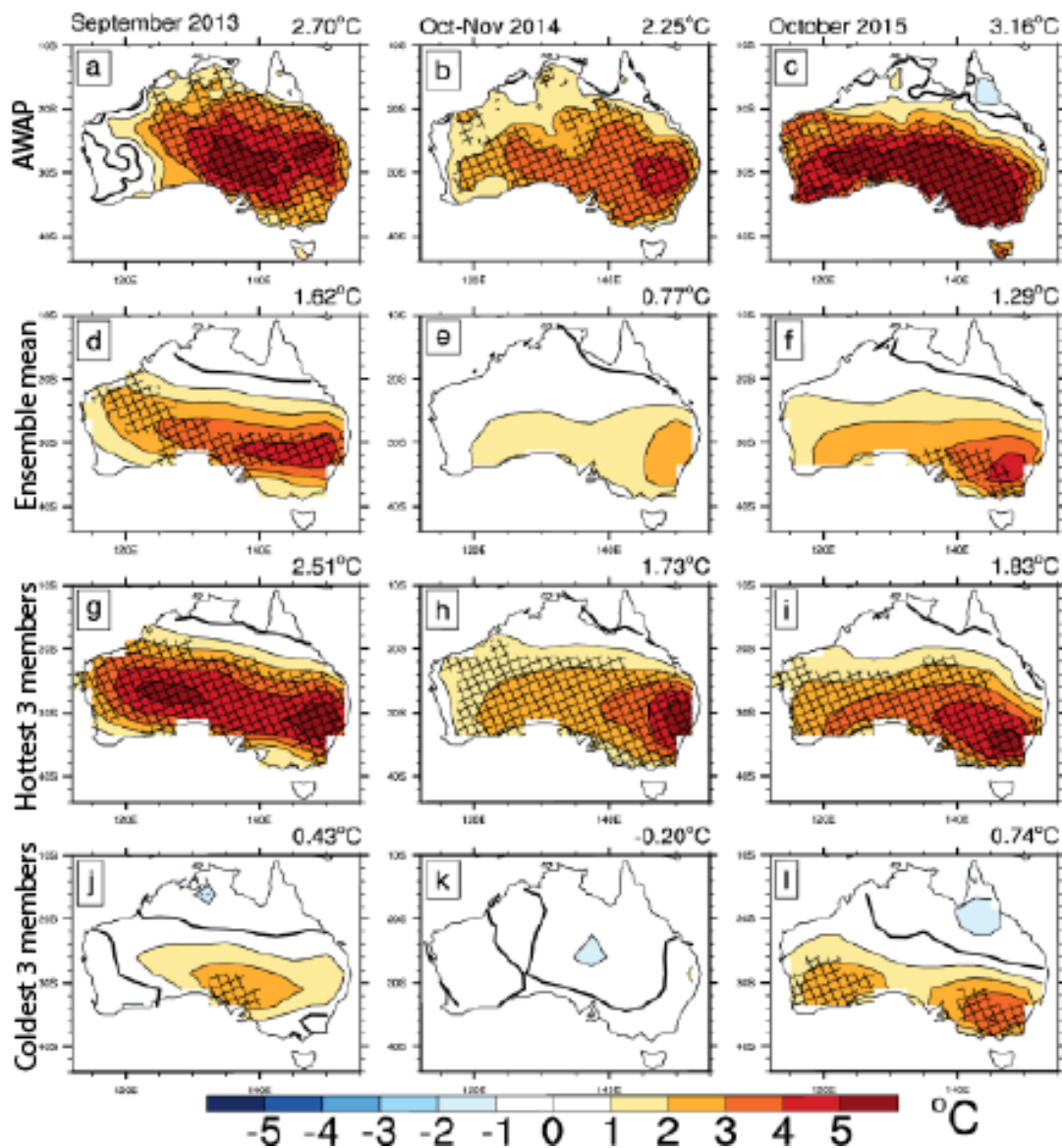


**Figure 2-1 Australian maximum temperature anomalies during three spring heat events**

Maximum temperature anomalies and Australian-averaged anomalies for September 2013, October-November 2014, and October 2015 from the 1981-2010 climatology in observations (a-c), ensemble-mean (d-f) forecast, averaged forecast of hottest 3 ensemble member forecasts (g-i), and coldest 3 ensemble member forecasts (j-l). Cross-hatching indicates anomalies are significant at the 95% confidence interval according to a two-sided T-test, using standard deviation calculated over the 30-year climatology period for the observations and ensemble-mean, and across all 990 ensemble members over the 30-year climatology period for hottest and coldest ensemble member forecasts. The standard deviations used in the hottest and coldest averaged-forecasts were scaled by  $1/\sqrt{3}$  for the T-test calculation.

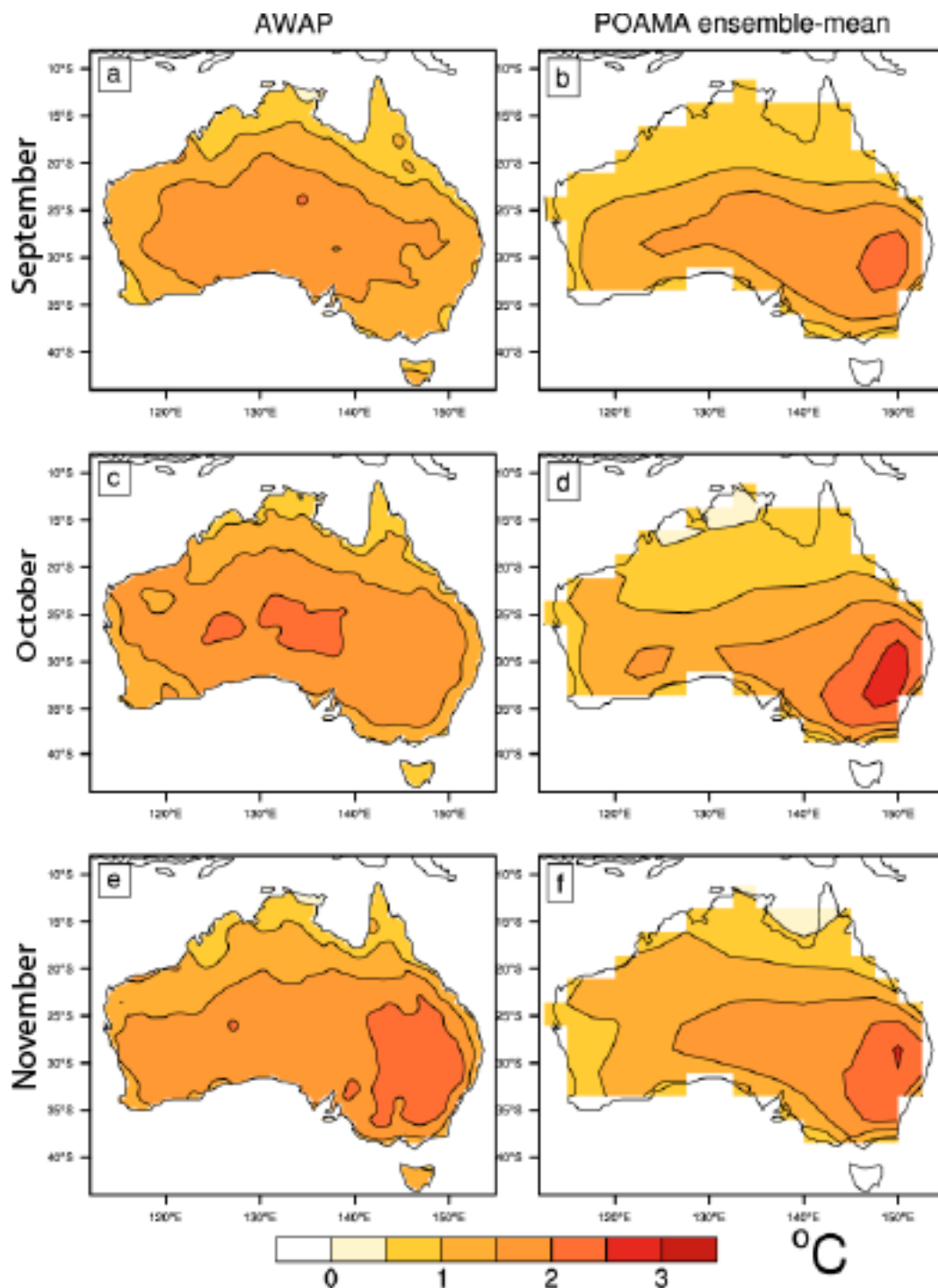


**Figure 2-2 Australian maximum temperature standard deviation during September, October, and November**

Year-to-year variability in Australian maximum temperature as given by standard deviation over the climatology period of 1981 to 2010 in observations from AWAP-dataset (a,c,e) and POAMA ensemble-mean (b,d,f).

## 2.4.2 Australian maximum temperatures and southern Australian 200hPa geopotential height

Consistent with Gallant and Lewis (2016), higher Australian monthly spring maximum temperatures tend to coincide with high (anticyclonic) Z200 over southern Australia (Figs. 2-3a-c). Interestingly, we see that the strength of this relationship between temperature and Z200 increases through spring. There is more spread amongst the observed values in September and a smaller correlation coefficient ( $r=0.47$ ) compared to the latter months, suggesting that high Z200 is not as closely tied to high maximum temperature in September. By October, the spread in observations has decreased and the relationship has strengthened ( $r=0.69$ ), and even more so by November ( $r=0.77$ ). September 2013 was unusual in that it was the hottest September examined, but had only a weak southern Australian Z200 anomaly, whereas Octobers 2014 and 2015, and November 2014 all had coinciding high maximum temperature and Z200 values.

The POAMA ensemble-mean displays a similar historical relationship between maximum temperature and Z200 across the spring months (Fig. 2-4).

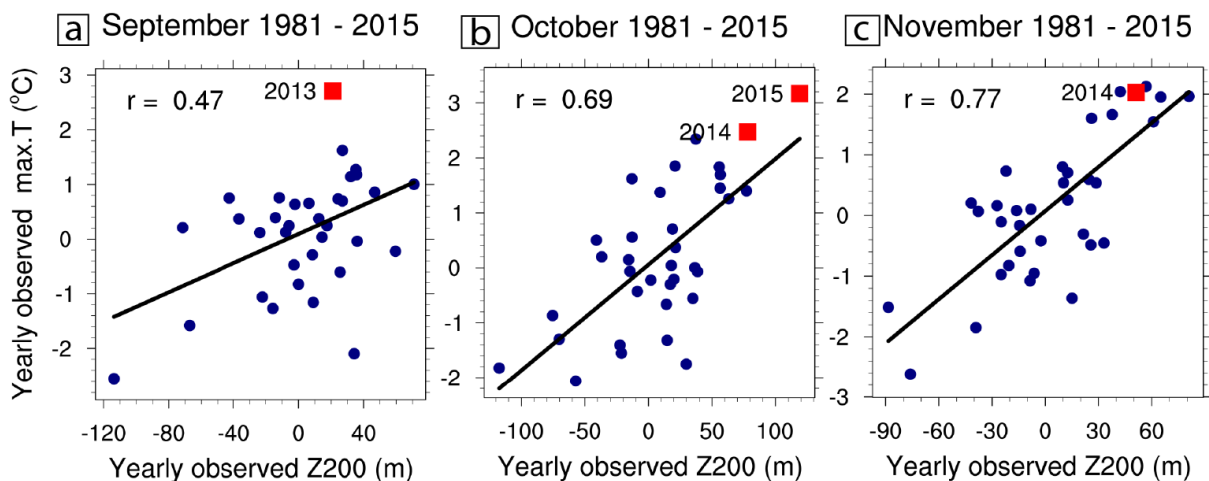


**Figure 2-3. Observed monthly spring relationships of 200Z vs Australian maximum temperature**

Scatter plots with linear regression line and correlation coefficient ( $r$ -value) for observed area averaged Australian maximum temperature anomalies from the AWAP dataset, and the 200hPa geopotential height anomalies averaged over the southern Australia-Great Australian Bight region ( $120^{\circ}$ - $150^{\circ}$ E and  $30^{\circ}$ - $40^{\circ}$ S) for months between 1981 and 2015. Anomalies were calculated against a 1981 to 2010 monthly climatology. Note the different scales between the months.

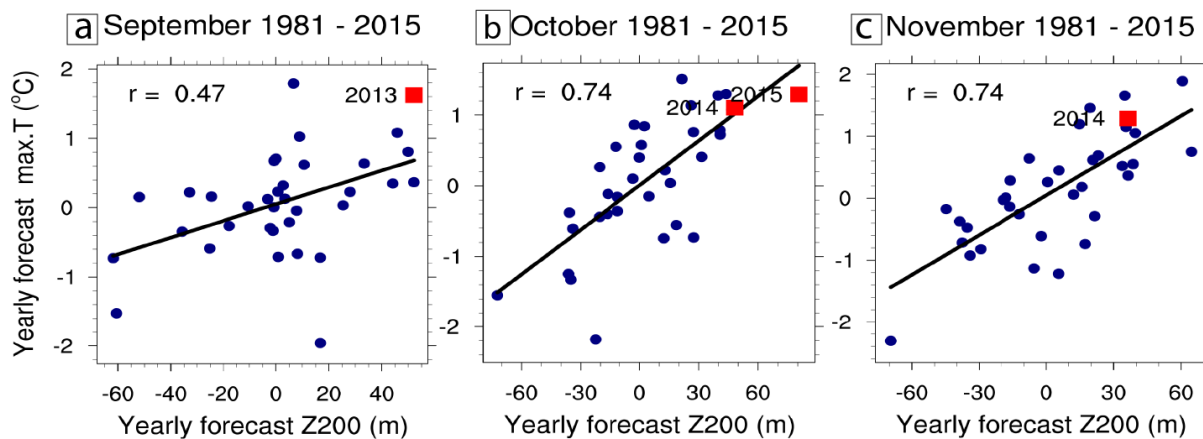


**Figure 2-4 POAMA monthly spring relationships of 200Z vs Australian maximum temperature**

*As in Fig. 2-3, but for the POAMA ensemble-mean.*

The spread across the forecast ensemble members for each event (Fig. 2-5) reveals that higher ensemble member forecast maximum temperatures tend to occur with higher Z200 values in the September 2013 (Fig. 2-5a) and October-November 2014 (Fig. 2-5b) events, with correlation coefficients values of 0.50 and 0.62, respectively. This suggests that those ensemble members that do develop a strong upper-level high over the region also develop warmer conditions across Australia, highlighting its importance as a mechanism to promote anomalously high temperature over Australia in the model. For October 2015, while many of the ensemble members do develop anomalously high 200hPa heights (Fig. 2-5c), the members with highest heights do not necessarily forecast higher maximum temperatures, and the relationship is weaker ( $r = 0.12$ ), indicating that anomalous height over southern Australia is not the only factor in the heat development. While we expect the composites of the warmest ensemble members to reveal anomalously higher anticyclonic 200hPa geopotential heights over southern Australia compared to the coldest members for the September 2013 and October-November 2014 events, it is of interest to further explore a range of factors that help develop the forecast heat across the ensemble members in all the events, and further details of each event are examined in the next section.

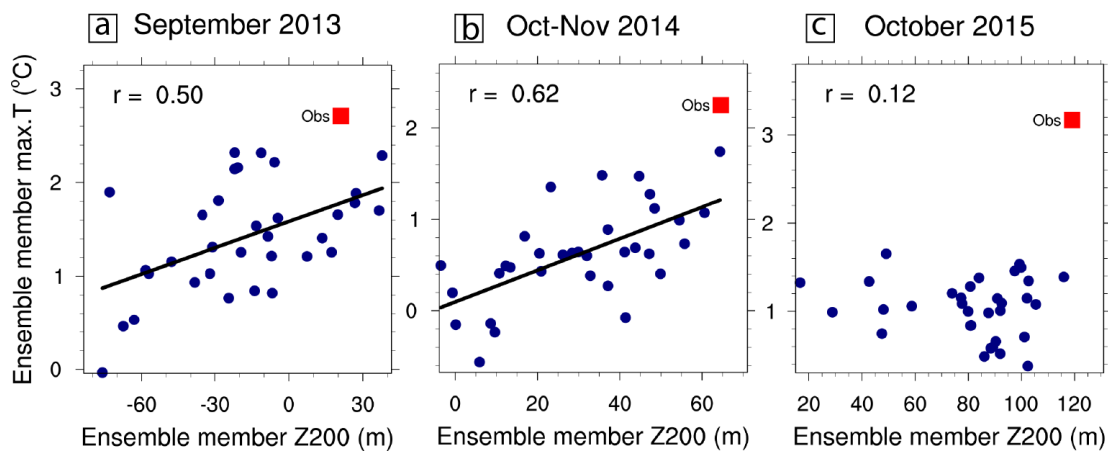


**Figure 2-5 Ensemble-member forecasts 200Z vs Australian maximum temperature for each event**

September 2013, October–November 2014, and October 2015 scatter plots of 33 individual POAMA ensemble member forecasts of Australian areal-averaged maximum temperature anomaly against 200hPa geopotential height anomaly averaged over the region 120°–150°E and 30°–40°S. The line is the approximate relationship given by least-squares regression from the ensemble member forecast values, and the  $r$ -value is plotted in the top left of each figure. The red square shows the observed values of anomalous maximum temperature (AWAP) and 200hPa geopotential height (ERA-Interim reanalysis) for each event. Individual ensemble member anomalies were calculated against a 1981 to 2010 climatology period from the appropriate POAMA model version.

### 2.4.3 September 2013

Gallant and Lewis (2016) identified a moderate upper-tropospheric anticyclone over southern Australia over spring 2013 as a whole. However, the reanalysis of September 2013 has only a weak (within one standard deviation of the mean) upper-anticyclone anomaly over southeast Australia (Fig. 2-6e), also indicated by the area-averaged Z200 anomaly for 2013 in Fig 2.3a. The ensemble–mean and hottest members-averaged (Fig. 2-6 f,g), on the other hand, forecast a strong upper-tropospheric anticyclone over southern Australia around 1.5-2 standard deviations greater than the POAMA climatological mean. The coldest members-averaged forecast (Fig. 2-6d,h) also shows an upper-tropospheric anticyclone, but shifted southeast of Australia. It is possible that the different locations of the upper-tropospheric anticyclone anomaly contributed to the difference in forecast Australian maximum temperature anomaly between the hottest and coldest members-averaged forecasts. However, given the observed high temperature anomaly occurred without the presence of the strong anticyclone over the Great Australian Bight, and the ensemble-mean forecast had an anticyclone but a lower Australian maximum temperature than observed, it is clear that an upper-tropospheric anticyclonic is not a necessary condition for extreme high maximum temperature development in September 2013. We next discuss other aspects of the circulation that may help further explain the September 2013 extreme heat.

The signature of the strong negative SAM noted in Arblaster et al. (2014) is evident in the lower MSLP south of Australia and enhanced MSLP over Antarctica (Fig. 2-6a), and in the corresponding upper-troposphere height anomalies (Fig. 2-6e). POAMA generally has skill at predicting SAM and its teleconnections (Marshall et al. 2012; Lim et al. 2013). However, the POAMA forecasts of low-level (Fig. 2-6 b-d) and upper-tropospheric circulation (Fig. 2-6 f-h) fail to capture the negative SAM-like circulation in September 2013. Consequently, much of the circulation around Australia in the POAMA forecasts does not match the reanalysis. In particular, the reanalysis shows an equivalent barotropic cyclonic circulation anomaly southwest of Australia, a key feature for this heat event noted in Arblaster et al. (2014), but is missing from the POAMA forecasts. Interestingly, the lack of SAM-like pattern in POAMA contrasts with Arblaster et al., (2014), who used a POAMA ensemble mean forecast initialised approximately two weeks earlier that simulated the negative SAM pattern, though POAMA ensemble-mean forecasts before and after the initialisation date used by Arblaster et al., (2014) also failed to capture the negative SAM pattern (not shown). The reanalysis low-level cyclonic circulation anomaly (Fig. 2-6a) is consistent with the passage of low-pressure, cooling weather systems, such as cold fronts, and cool conditions in southwest Australia (Fig. 2-1a). The cyclonic circulation drives westerly low-level wind anomalies in the west of Australia, that then tend to warming (via advection) north-westerly winds towards the east of the continent that would have contributed to the warmer conditions (Fig. 2-1a). An upper-anticyclone over southern Australia, such as in the hottest-averaged forecasts, would have enhanced warming through subsidence, but in reality, it seems that advection, along with other factors not assessed here, such as the antecedent dry conditions (Arblaster et al., 2014) and the thermal warming associated with anthropogenic climate change (Gallant and Lewis, 2016) were important factors in the September 2013 anomalous maximum temperature. As such, it seems that not only the negative SAM circulation, but this south-west cyclonic circulation anomaly was an important factor in the observed extreme maximum temperature development of September 2013 in agreement with Arblaster et al. (2014).

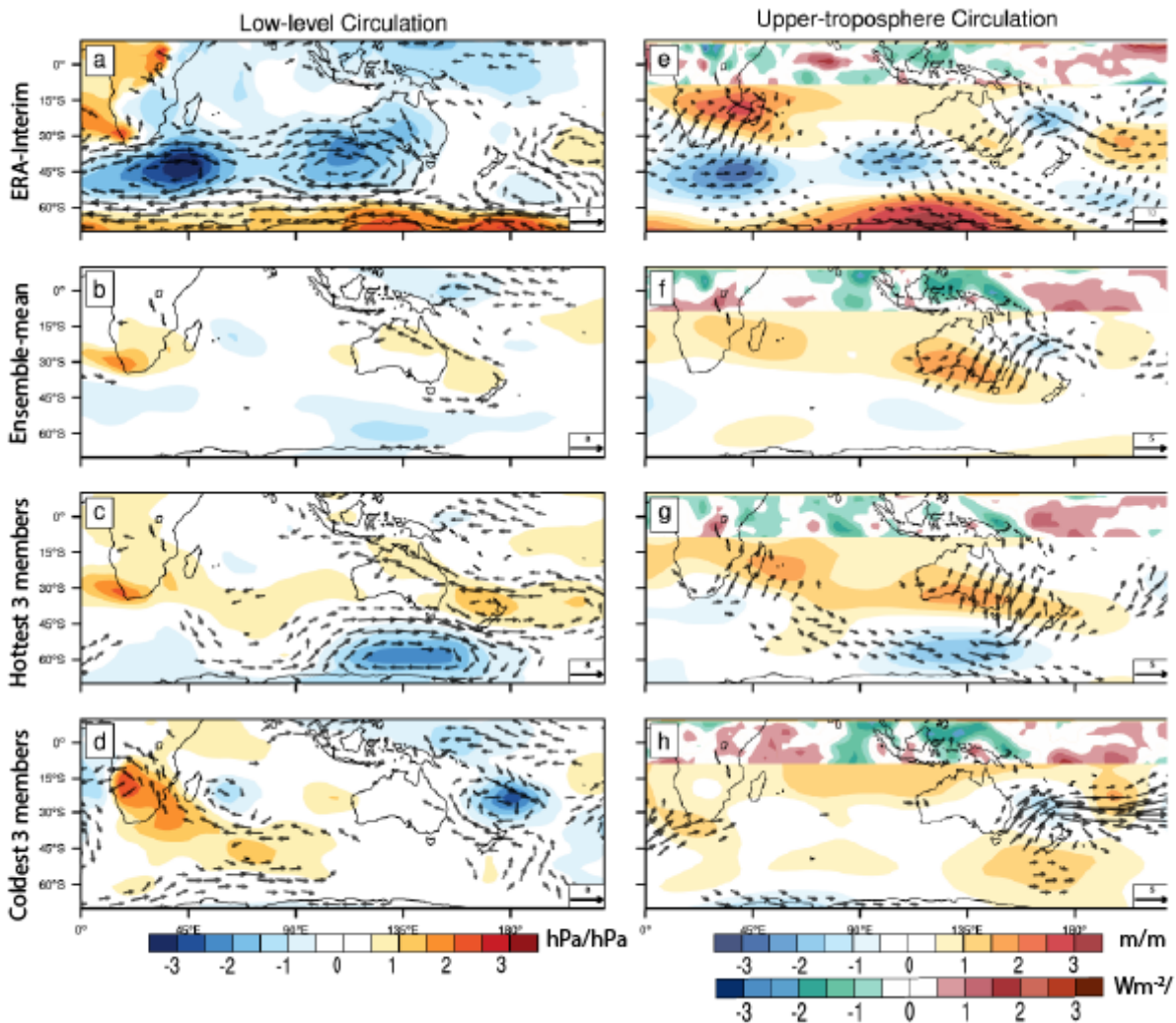


**Figure 2-6. September 2013 low- and upper-level atmospheric circulation**

Low-level circulation (left-column) given by standardised anomalous mean sea level pressure and anomalous 850hPa wind vectors ( $\text{ms}^{-1}$ ), and upper-troposphere circulation (right-column) given by 200hPa standardised geopotential height (south of  $10^{\circ}\text{S}$ ) and standardised OLR anomalies (north of  $10^{\circ}\text{S}$ ), and wave activity flux vectors ( $\text{m}^2\text{s}^{-2}$ ) from observations (a, e), ensemble-mean forecast (b, f), averaged hottest 3 (c, g) and coldest 3 (d, h) ensemble member forecasts. Observed and ensemble-mean anomalies were standardised by dividing by the standard deviation calculated over the 1981 to 2010 climatology period in observations and the ensemble-mean. The hottest and coldest forecasts were standardised by dividing by standard deviation calculated over all 990 ensemble members over the 1981 to 2010 climatology period. For clarity, only 850hPa wind vectors larger than  $2 \text{ ms}^{-1}$  were plotted, and only wave activity flux vectors larger than  $1 \text{ m}^2\text{s}^{-2}$ . Note the difference in reference vector length between observed and forecast vectors.

At the upper-troposphere level, the south-west cyclonic anomaly in reanalysis appears to form part of a Rossby wave train initialised in the central mid-latitude Indian Ocean, as indicated by the wave activity flux

divergence west of this cyclonic anomaly (Fig. 2-6e). This wave activity flux passes through the cyclonic anomaly, then splits to propagate through Australia and Antarctica. There is no clear signal in the tropical OLR anomalies or wave activity flux that could point to a tropical forcing of this wave train. While the hottest-averaged forecast (Fig. 2-6g) does simulate a Rossby wave train, its trajectory is too far poleward. Instead, a second, weak region of wave activity flux divergence is visible out of the east subtropical Indian Ocean in both the hottest-averaged forecasts and the ensemble mean that then propagates through the (forecast) Australian upper height anomaly, though it is not clear whether this activity flux is associated with the negative OLR anomaly forecast in the eastern Indian Ocean. The different wave train trajectories suggest that tropical and subtropical forcing may have played a role in the hotter forecasts, though only extratropical forcing is apparent in the reanalysis of September 2013, indicating that these ensemble members had a warm forecast for the wrong reason.

#### 2.4.4 October-November 2014

In contrast to September 2013, and consistent with the stronger relationship in Figs. 3b and c, October-November 2014 (Fig. 2-7e) has a strong upper-tropospheric anticyclone over southern Australia, just over two standard deviations from the climatological mean. This strong anticyclone is well captured by the hottest-members average forecast (Fig 6g) and ensemble mean (Fig. 2-7f), though shifted westward relative to reanalysis and extended into the tropics. The coldest-members average forecast, on the other hand, has near-neutral height anomalies over Australia (Fig. 2-7h), and weak height anomalies generally across the southern hemisphere. The similarity between the reanalysis 200hPa Australian anticyclone and those in the hotter forecasts suggests that the anticyclone, and the associated warming through subsidence (e.g. Quinting and Reeder, 2017), was an important component in developing the heat of October-November 2014. How this anticyclone relates to the broader circulation pattern may reveal more about how the heat formed during this event.

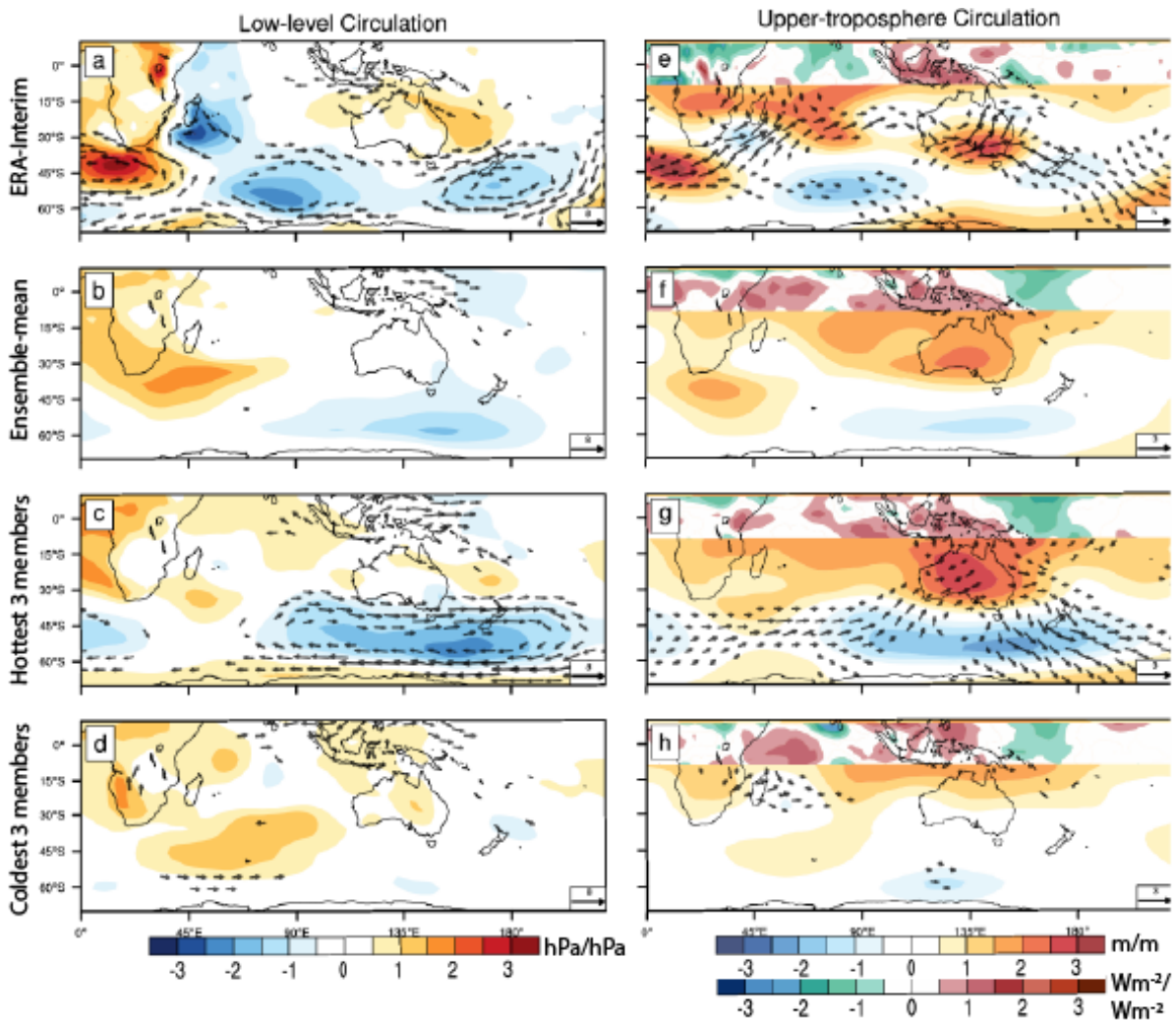


**Figure 2-7 October-November 2014 low- and upper-level atmospheric circulation**  
 As with figure 2.6, but for October-November 2014. For clarity, only 850hPa wind vectors larger than  $2 \text{ ms}^{-1}$  were plotted. Observed wave activity flux vectors were only plotted if greater than  $0.75 \text{ m}^2\text{s}^{-2}$  and forecast vectors were only plotted if greater than  $0.4 \text{ m}^2\text{s}^{-2}$

Unlike September 2013, the October-November 2014 wave train in reanalysis (Fig. 2-7e) does not start near the cyclonic anomaly southwest of Australia, but is a continuation of a wave train that propagates from southwest of Africa. The hottest-average member forecast (Fig. 2-7g) simulates a southern Indian Ocean wave train, but is too zonally oriented relative to reanalysis, and veers strongly to propagate through the Australian upper-tropospheric anticyclone. The reanalysis wave activity flux also displays a second wave train, equatorward of the first, that propagates out of the western subtropical Indian Ocean. Enhanced convection in the central tropical Indian Ocean, and divergence of wave activity flux out of the western subtropical Indian Ocean suggests that this second wave train appears to, at least partly, be driven by a Gill-type response, to anomalously warm tropical Indian ocean SSTs, consistent with Hope et al. (2015). The lower latitude wave train is not represented in the POAMA forecasts. Instead, suppressed convection appears to be driving wave activity flux out of the Maritime Continent in all forecasts. As such, the higher latitude wave train may have been more important to the development of the southern Australian upper-

tropospheric anticyclone in the hottest forecasts. It is possible that the lack of the tropical Indian Ocean forced wave train resulted in under-forecast Australian maximum temperatures (Figs. 1 b, e, h, f) via a weaker forecast Australian upper-anticyclone, and will be explored in future work. In any case, it appears that the atmospheric circulation over the Indian Ocean is an important factor in developing that upper-tropospheric circulation associated with heat in this event.

The October-November 2014 equivalent-barotropic cyclonic circulation (Fig. 2-7a, e) is shifted further southwest from Australia compared to September 2013, and, consequently the observed heat anomaly extends further west than in the previous event (Fig. 2-1b). A second barotropic cyclone is located southeast of Australia and blocking anticyclonic circulation lies in the Tasman Sea and extends along Australia's eastern coast. The surface pressure gradient from these features is insufficient to result in strong low-level flow over Australia, though there is a small northerly component to the flow to the west of Australia (Fig. 2-7a). The weak low-level flow suggests that the warming from advection due to the Tasman Sea blocking (Marshall et al., 2014) may have been only a small component of the observed heat, consistent with Hope et al. (2015), and the contribution through subsidence and enhanced insolation associated with the upper-tropospheric anticyclone, (e.g. Quinting and Reeder, 2017; Lim et al., 2019a) may have played a larger role. The hottest-member average forecast simulates the spatial patterns of the heat (Fig. 2-1 h) and the low-level features better than either the coldest-member average or ensemble-mean forecasts. However, the Tasman Sea anticyclonic circulation in the hottest-member average forecast is weaker and displaced eastward relative to reanalysis by a weak cyclonic trough over southeast Australia and a more zonally elongated cyclonic circulation south of Australia (Fig. 2-7c) such that the low-level wind anomaly is much weaker in northern Australia and much stronger in southern Australia, relative to reanalysis. It is possible that these circulation differences contributed to the under-forecast maximum temperature. The zonally elongated pattern has been previously noted as a bias in the POAMA forecasting system (Marshall et al. 2012). The coldest-members average forecast incorrectly forecast anomalous high Australian MSLP, and, while the ensemble-mean does forecast a weak elongated cyclonic circulation south of Australia, neither it, nor coldest-members average forecast simulate the low-level circulation around Australia found in reanalysis. This reinforces the idea that the total circulation pattern formed by the cyclonic features either side of Australia, the blocking pattern in the Tasman Sea, as well as southern Australian upper-tropospheric anticyclone were important for heat in the October-November 2014 event.

#### 2.4.5 October 2015

An upper-tropospheric anticyclonic anomaly more than three standard deviations greater than the 1981-2010 reanalysis-mean lies over southern Australia in October 2015 (Fig. 2-8e), suggesting that, as in the previous event, warming through subsidence and enhanced insolation were factors in the heat during this

event. As expected from Fig. 2-5c, the POAMA forecasts (Fig. 2-8 f-h) all have high Z200 anomalies, two to three standard deviations greater than the 1981-2010 mean, but place it equatorward relative to the reanalysis position and extend it into the tropics. A similar, though lower in magnitude, Z200 extension from the tropics to extratropics was found in the POAMA forecasts of October-November 2014 (Fig. 2-8 f-h) during a weak El Niño, and this much stronger magnitude Z200 extension from the tropics may be POAMA's response to the strong El Niño occurring in 2015, resulting in each ensemble member forecast being dominated by this driver. Despite the broad extent of high Z200 in the POAMA forecasts, the hottest members-average has a local maximum in Z200 over south-central Australia, reminiscent of a distinct anticyclonic anomaly, though the surrounding gradient in 200hPa geopotential height is weak relative to the reanalysis. This local maximum in Z200 was not present when the compositing was done based on high southern Australian Z200 (not shown), suggesting that it is not just the strength of the height anomaly over southern Australia, but its shape that is important for developing higher temperatures in the POAMA models. While the POAMA forecasts of Z200 appeared to be dominated by the strong El Niño, even the hottest members under-forecast the October 2015 heat (Fig. 2-1i), despite POAMA's demonstrated skill in forecasting extreme heat associated with ENSO during the hindcast period of 1981-2013 (e.g. White et al., 2014). This is consistent with other studies suggesting the weak connection between the strong El Niño and the observed anomalous heat in 2015 (e.g. Black and Karoly, 2016; Hope et al., 2016). Indeed, the impacts of the 2015 El Niño on Australia have been found to be unusual, and global circulation models, such as POAMA, may not have been able to simulate the event well (van Rensch et al., 2019). However, given the hottest-averaged forecasts were also the closest to simulating a distinct upper-tropospheric anticyclone similar to the reanalysis, it is useful to compare what drove the atmospheric circulation in the hottest

forecasts to the coldest forecasts of October 2015.

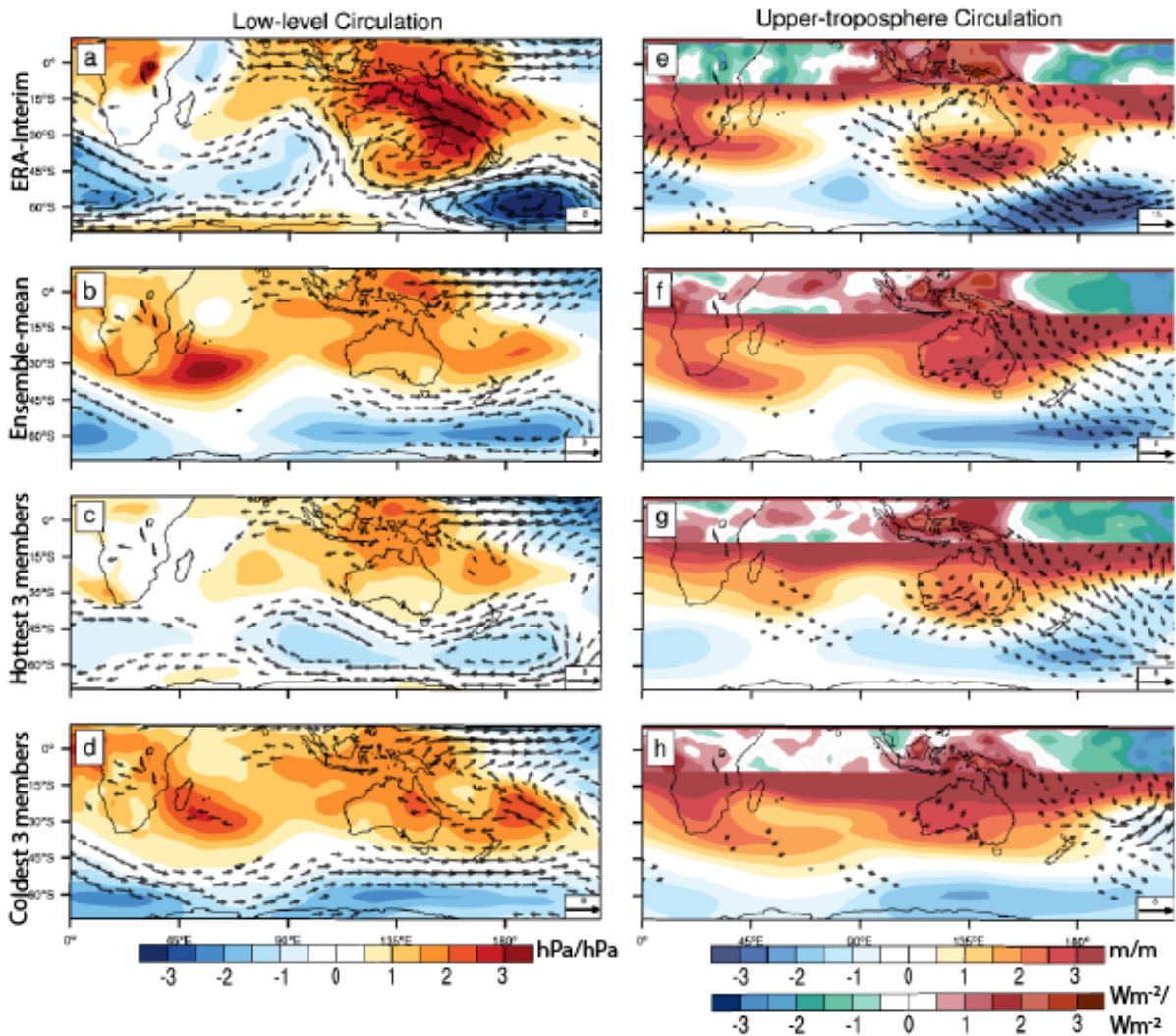


**Figure 2-8 October 2015 low- and upper-level atmospheric circulation**

As with Fig. 2.6, but for October 2015. For clarity, only 850hPa wind vectors larger than  $2 \text{ ms}^{-1}$  were plotted. For clarity, observed wave activity flux vectors were only plotted if greater than  $2.0 \text{ m}^2\text{s}^{-2}$  and forecast vectors were only plotted if greater than  $1.0 \text{ m}^2\text{s}^{-2}$ .

The upper-troposphere wave activity flux in the reanalysis (Fig. 2-8e) is different to both the 2013 and 2014 events. Unlike the previous event, the enhanced convection in the western tropical Indian Ocean is only driving a small amount of wave flux that fails to propagate beyond its source region. Instead, the suppressed convection over the eastern tropical Indian Ocean appears to be triggering a Rossby wave train east of Australia at around  $25^\circ\text{S}$ , as indicated by the wave activity flux divergence over a region of anomalous upper-tropospheric cyclonic circulation west of Australia at around  $25^\circ\text{S}$ . This wave train then propagates through the Australian upper-tropospheric anticyclone, following a similar path to the eastern branch of the ENSO-IOD teleconnection suggested by Cai et al. (2011a). A second region of wave activity flux diverges from the cyclonic circulation southwest of Australia to propagate through the Australian anticyclone. The POAMA forecasts partially simulate this southwest region of wave activity flux divergence,

particularly in the hottest forecasts, but fail to simulate the ENSO-IOD-like wave path to the northwest. However, there are step improvements between the coldest and hottest forecasts; wave activity flux shifts from south-westerly only in the coldest forecasts, to include a stronger westerly component in the ensemble mean, to having north-westerly component in the hottest ensemble members. The hottest ensemble members also have a shallow upper-troposphere trough west of Australia, echoing the cyclonic circulation that forms the first part of the ENSO-IOD-like wave train in reanalysis. It is possible that the better simulated relationship to the tropical Indian Ocean contributed to a better forecast maximum temperature. However, in general, the October 2015 atmospheric circulation over the Indian Ocean was poorly forecast by POAMA. Further, all POAMA forecasts produce large regions of wave activity flux out of the tropical Pacific, downstream of Australia, that is not found in the reanalysis. This suggests again that the POAMA forecasts were dominated by El Niño, and consequently, may have missed atmospheric circulation factors important for the heat development in October 2015.

As in the previous event, the reanalysis has equivalent barotropic cyclones positioned southwest and southeast of Australia and anticyclonic blocking in the Tasman Sea, east of Australia (Figs. 8a,e). However, in October 2015, the southeast cyclone is far stronger and located further poleward; the southwest cyclone is weaker and connected by a trough to the subtropical cyclone west of Australia at the beginning of the ENSO-IOD-like wave train (Cai et al., 2011a); and the Tasman Sea blocking anticyclone is much stronger and extends further west than in the previous event, connecting with high MSLP over Australia, the Great Australian Bight and into the Maritime Continent and western tropical Pacific (Fig. 2-8a). The resulting surface pressure gradient drives onshore easterly flow near the northeast of Australia, matching where the temperature anomaly was cool, (Fig. 2-1c) that quickly tend northerly to advect warm air across the south of the country, where conditions were hottest, suggesting that advection played a large role in developing the heat in this event, along with the subsidence and enhanced insolation associated with the upper-tropospheric anticyclone. However, the POAMA forecasts do not simulate the reanalysis low-level circulation associated with the warm air advection. Instead, a broad region of high MSLP extends from the tropics across Australia, reflecting the pattern in the upper-troposphere forecasts, and a zonally elongated cyclonic anomaly lies far south of Australia. The resulting pressure gradient is generally too weak to produce low-level flow across Australia (Fig. 2-8b-d, f-h). However, as the upper-troposphere circulation, there are step improvements between the more zonally oriented cyclonic circulation anomaly in the coldest forecasts to the hottest forecasts that have isolated cyclonic lobes and a northerly component to the low-level flow over southwest Australia, possibly indicating that better simulation of the southeast and southwest baroclinic cyclonic circulations can contribute to a hotter forecast.

## 2.5 Discussion

While the atmospheric circulation during the three extreme spring heat events examined here was different, there are enough similarities between the reanalysis and POAMA ensemble forecasts across the three events to suggest that the atmospheric circulation pattern created by a combination of barotropic cyclonic circulations either southwest or southeast of Australia, along with the presence of the upper-tropospheric southern-Australian anticyclone and anticyclonic blocking in the Tasman Sea were important for the development of these heat events. How these circulation features affected Australia's maximum temperature and how they were configured around Australia appeared to be influenced by the different climate drivers that were active during each event, and particularly, whether these drivers had origins in the tropics or extratropics. While the impact of other factors not examined here, such as the background warming trend (e.g. Gallant and Lewis, 2016) or dry conditions preceding the events (e.g. Arblaster et al., 2014) must also be remembered, the circulation features discussed here have contributed to our overall understanding of what can drive heat in spring. In particular, the upper-anticyclone in the latter two events appeared to be related to the activity in the tropical Indian Ocean and this could have implications for the predictability of Australian spring heat events.

The upper-anticyclone over southern Australia appeared to be an important component to the heat in the hotter POAMA forecasts of all three events, and the reanalysis of the second two events. This anticyclone would have been conducive to enhanced warming through subsidence (e.g. Quinting and Reeder, 2017), increased insolation (e.g. Lim, et al. 2019), and, combined with the atmospheric circulation associated with the Tasman Sea blocking pattern, warm air advection (e.g. Marshall al. 2014) over eastern Australia. From earlier studies (e.g. Gallant and Lewis, 2016; Hope et al. 2016), and from the springtime climatological relationship between high southern Australian 200hPa geopotential height and high temperature (Fig 2.3a-c), we expected upper-tropospheric anticyclones over southern Australia during each of the three heat events. However, the upper-tropospheric height anomaly in the reanalysis of September 2013 was only weakly positive, indicating that the upper-anticyclone is not the only factor in spring heat development, though it appears that POAMA favours this circulation anomaly as a heat development mechanism. Hence, the importance of the broader circulation pattern to heat development in these spring events has also been considered.

The common presence of barotropic cyclonic circulations southwest or southeast of Australia suggest that these features may have been important factors in developing the heat observed through each event. The latitudinal position of these cyclonic circulations is a reflection of the negative SAM in each event (e.g. Hendon et al., 2007) that has already been linked with the high maximum temperatures (e.g. Arblaster et al., 2014; Hope et al 2015; 2016), though the negative SAM-component of the heat may be due to increased insolation and subsidence than directly associated with the cyclonic circulations (Lim et al.,

2019a), particularly in the latter two events. Low-level warm air advection driven by the southwest cyclonic circulation appears to be a key heat-development mechanism in September 2013, and to a lesser extent in the latter two events in reanalysis, due to the relative positions of the cyclonic features and weaker northerly flow. While the zonally- elongated pressure bias (Marshall et al., 2012) did impact the POAMA forecasts of these 2014 and 2015 cyclonic features, warm air advection associated with the southwest cyclonic circulation may have contributed to the heat in the hottest forecasts as these had the greatest curvature and northerly low-level flow southwest of Australia. The southeast cyclonic circulation, however, does not appear to contribute to northerly flow over Australia and it becomes harder to discern how this feature relates to the high maximum temperatures in the latter two events. It may be that the southeast, and the southwest, cyclonic circulation reflect a greater tendency for cooling low MSLP, synoptic weather systems, such as cold fronts (Hope et al., 2009; Risbey et al., 2009b), to propagate to the southwest or southeast of Australia, rather than penetrate into the continent during the heat events. However, changes to the intensity or frequency of these synoptic weather systems over Australia during these events and the resulting impact on monthly maximum temperatures is beyond the scope of this study. Rather, on the sub-seasonal timescale, the barotropic southeast cyclonic circulation appears to support the surface Tasman Sea blocking pattern that directed warm air advection across eastern Australia, and form a part of the same quasi-stationary Rossby pattern that contributes to the southern Australian upper-tropospheric anticyclone. Consequently, the southeast cyclone may not drive heat development directly but form one part of the overall atmospheric circulation, that includes the southwest cyclonic circulation, that produces the heat. As such, we conclude that the overall circulation pattern around Australia formed by the southeast and southwest cyclonic circulations and the upper tropospheric anticyclone was important for the heat development through each event.

While each event had similar atmospheric circulation patterns associated with the heat, the Rossby wave paths that contributed to the development of these anomalies differed between the events and the POAMA forecasts. In September 2013, the flux was only from the extra-tropics in the reanalysis and the hottest POAMA forecasts; in both October-November 2014 and October 2015 there were contributions from the tropical Indian Ocean, with the hottest POAMA forecasts also simulating the most wave activity flux out of the tropical Indian Ocean. This wave activity flux is likely to be, at least partly, a reflection of the occurrence of El Niño and positive IOD during the 2014 and 2015 heat events. While none of the Rossby wave paths in reanalysis or the POAMA forecasts are identical, on the whole they suggest that the tropical Indian Ocean and high Australian maximum temperatures are linked by the southern Australian upper-tropospheric anticyclone and southeast Australian cyclone quasi-stationary wave pattern. As the relationship between upper-tropospheric anticyclonic circulation over southern Australia and high Australian maximum temperature is weakest in September, and there was no cyclonic circulation southeast of Australia in September 2013, it is also possible that the connection to the tropical Indian Ocean is

weakest in September too. This could be because the relationship between Australia and the tropical climate drivers, ENSO and the IOD, is strongest in later spring (e.g. Jones and Trewin, 2000), or because the decaying subtropical jet is still too strong to allow for direct Rossby wave propagation in September (e.g. McIntosh and Hendon, 2018). While it is not possible to determine if there is a change in the relationship between Australian maximum temperatures and the tropical Indian Ocean over the months of spring from three case studies, further investigation into this relationship would help to clarify the potential predictability of high maximum temperatures over the months of spring.

Comparing the atmospheric circulation in the hottest and coldest POAMA forecasts to the reanalysis of the three events provided additional realisations of each spring heat event to explore. The wave activity flux in the reanalysis and POAMA forecasts shows that the atmospheric circulation over the Indian Ocean, whether tropical or extratropical in origin was important for the three extreme heat events studied here. However, the bias in the POAMA forecasts toward zonally elongated cyclonic circulation to the south of Australia (Marshall et al., 2012) complicated the ability to assess the POAMA realisations of the atmospheric circulation around Australia, particularly with regards to the barotropic cyclones southwest and southeast of Australia seen in the reanalysis. The POAMA forecasts also appeared to favour wave activity flux and atmospheric circulation from the Pacific Ocean, rather than the Indian Ocean. Further, the region of highest interannual temperature variability in POAMA is biased towards south-eastern Australia, which matches the region that correlates most strongly with ENSO (Risbey et al. 2009a; Min et al., 2013), suggesting that POAMA generally over-represents the relationship with the Pacific Ocean at the cost of the teleconnection to the Indian Ocean. This is consistent with earlier studies that examined ENSO and IOD teleconnections to Australia (Zhao and Hendon 2009; White et al. 2014). Despite these biases, the POAMA ensemble members that were closest to the observed temperature anomalies also had the smallest zonal elongation bias or Indian Ocean wave activity flux bias, and were better able to forecast the wave train from the upper-tropospheric anticyclone to the southeast cyclonic circulation. This suggests that better simulation of both the mid-latitude MSLP pattern and the atmospheric circulation over the Indian Ocean could have improved the forecast maximum temperature of the three heat events, as well as forecasts into the future. The bias in the teleconnection from the Indian Ocean to Australia remains an issue in the Bureau of Meteorology's latest seasonal prediction system, ACCESS-S1 (Lim et al., 2016b, Hudson et al., 2017) and long-standing biases over the Indian Ocean are also found in many global climate models (e.g. Li, G. et al. 2015)

## 2.6 Conclusion

This study examined the atmospheric circulation patterns contributing to three extreme spring heat events over Australia, using ERA-Interim reanalysis and the POAMA seasonal prediction system. These events

remain amongst the hottest recorded in Australia to date. While the atmospheric circulation in each of the three heat events varied somewhat, several features stand out as important drivers of the heat across the three events. Barotropic cyclonic circulations southwest of Australia were present in each event, and may be important features for heat development in austral spring. While upper-tropospheric anticyclonic circulation has been linked to austral spring heat generally, a quasi-stationary Rossby wave train comprised of this strong upper-tropospheric anticyclonic circulation over southern Australia and a barotropic cyclonic circulation southeast of Australia, as well as Tasman Sea blocking at the surface, were only present in the second two events, indicating that, while these circulation features were important for the development of heat during these events, it is not a requirement for austral spring heat. Rossby wave activity flux analysis suggests that the anticyclonic circulation appears to be more strongly linked to the tropical Indian Ocean in the reanalysis, however the POAMA forecasts were too dominated by Pacific Ocean influences. This study suggests that improved simulation of extratropical circulation and tropical Indian Ocean teleconnections should be an important focus in order to increase the skill of predictions of unusually high temperatures through spring months in Australia. Atmospheric processes on a sub-seasonal time scale and their predictability are a known gap between the weather prediction and seasonal prediction timescales and, given further increases in the magnitude and frequency of extreme spring temperatures are projected with increasing greenhouse gases, improving our understanding of monthly heat extremes will also help with adaptation.

### 3 Strengthening tropical influence on heat generating circulation over Australia through spring

This chapter is a reproduction of the paper, “Tropical influence on heat-generating atmospheric circulation over Australia strengthens through spring”, accepted for publication in *Weather and Climate Dynamics*. The section and figure numbers have been adapted to fit the thesis structure, and only minor changes have been made to the text and figures. The supplemental figures from the paper are included in the main text of this chapter.

#### 3.1 Abstract

Extreme maximum temperatures during Australian spring can have deleterious impacts on a range of sectors from health to wine grapes to planning for wildfires, but are relatively understudied compared to spring rainfall. Spring maximum temperatures in Australia have been rising over recent decades, and, as such, it is important to understand how Australian spring maximum temperatures develop in the present and warming climate. Australia’s climate is influenced by variability in the tropics and extratropics, but some of this influence impacts Australia differently from winter to summer, and, consequently, may have different impacts on Australia as spring evolves. Using linear regression analysis, this paper explores the atmospheric dynamics and remote drivers of high maximum temperatures over the individual months of spring. We find that the drivers of early spring maximum temperatures in Australia are more closely related to low-level wind changes, which in turn are more related to the Southern Annular Mode than variability in the tropics. By late spring, Australia’s maximum temperatures are proportionally more related to warming through subsidence than low-level wind changes, and more closely related to tropical variability. This increased relationship with the tropical variability is linked with the breakdown of the subtropical jet through spring and an associated change in tropically-forced Rossby wave teleconnections. However, much of the maximum temperature variability cannot be explained by either tropical or extratropical variability. An improved understanding of how the extratropics and tropics projects onto the mechanisms that drive high maximum temperatures through spring may lead to improved sub-seasonal prediction of high temperatures in the future.

#### 3.2 Introduction

Anomalously high Australian spring (September-October-November) maximum temperatures can be highly impactful. High temperatures may negatively impact health due to a lack of acclimatisation (e.g. Nairn and Fawcett, 2014), and agriculture by changing growing season length and crop yields (Cullen et al., 2009; Jarvis et al., 2019; Taylor et al., 2018). Hotter and drier spring conditions have been linked to an earlier start to (Dowdy, 2018) and preconditioning of (Abram et al., 2021) the summer fire season. The trend toward higher temperatures over recent decades (Collins et al., 2013), means that anomalous high maximum temperatures may occur more often (e.g. Alexander and Arblaster, 2009). Several recent springs have

already exceeded historic temperature records, with some spring months breaking records that were set only the previous year (Arblaster et al., 2014; Gallant and Lewis, 2016; Hope et al., 2015; McKay et al., 2021). Much of this observed anomalous heat has been attributed to the background global warming trend (Arblaster et al., 2014; Gallant and Lewis, 2016; Hope et al., 2015; Hope et al. 2016). However, gaps remain in our understanding of what drives anomalous high maximum temperatures in Australia during spring, and particularly on the monthly time-scale that some of these heat events occurred over. As the globe continues to warm, a better understanding of what makes a spring month in Australia hot today will lead to greater resilience against extreme heat in the future.

High spring temperatures have been linked with several remote modes of variability in the tropics and extratropics. In the tropics, the positive phases of El Niño Southern Oscillation (ENSO) in the tropical Pacific and the Indian Ocean Dipole (IOD) in the tropical Indian Ocean are the strongest drivers of high maximum temperatures in Australia in spring, particularly in the south and east (Power et al., 1998; Jones and Trewin, 2000; Saji et al., 2005; Min et al., 2013; White et al., 2014). Many more studies focus on the ENSO and IOD relationships to drier spring conditions (Nicholls et al., 1989; Meyers et al., 2007; Ummenhofer et al., 2009a; Risbey et al., 2009a; Watterson, 2010; Cai et al., 2011a; Min et al., 2013; Pepler et al., 2014; McIntosh and Hendon, 2018; Watterson, 2020) and to more extreme spring fire weather (Harris and Lucas 2019; Marshall et al. 2021b). While, the IOD's influence on Australia's temperature peaks around SON (Saji et al., 2005) compared to around NDJ (November-December-January) for ENSO (Jones and Trewin, 2000), ENSO and the IOD co-vary significantly in austral spring (e.g. Meyers et al., 2007). As such, it can be useful to look at a single index that describes the large-scale tropical SST variability's influence on Australia, such as the tropical tripole index (TPI) (Timbal and Hendon, 2011). While other tropical modes of variability, such as the Madden-Julian Oscillation (MJO), also influence Australia's spring maximum temperatures (e.g. Wheeler and Hendon, 2004; Wheeler et al., 2009; Marshall et al., 2014), we focus on the tropical SST-driven influence on Australia's spring climate.

Variability in the extratropics is also linked to high temperatures in Australia. The negative phase of the Southern Annular Mode (SAM), the primary mode of variability in the extratropics, (Hendon 2007; Risbey et al., 2009a; Min et al., 2013; Marshall et al., 2012, Hendon et al., 2014; Fogt and Marshall, 2020) drives hotter and drier Australian spring conditions, and more extreme spring fire weather (Marshall et al. 2021b). SAM generally varies at a higher frequency than ENSO or the IOD, however, SAM also has lower frequency variations. On a seasonal timescale, El Niño promotes negative SAM, particularly during the warmer months (L'Heureux and Thompson, 2006; Hendon et al., 2007; Lim et al., 2016a; Lim et al., 2019b). Polar stratospheric weakening during austral spring (sometimes associated with sudden stratospheric warming) can also sustain negative SAM (Lim et al., 2018) and higher Australian maximum temperatures from late spring (Lim et al., 2019a). As with ENSO and the IOD, more studies focus on how SAM influences Australian

rainfall than temperature, particularly when examining the teleconnection pathway. While low rainfall correlates well with high maximum temperatures (Simmonds, 1998; Jones and Trewin, 2000; Timbal et al., 2002; Hope and Watterson, 2018), there is a gap in our understanding of how both tropical and extratropical modes of variability impact spring maximum temperature.

Anomalously high geopotential height (or, synonymously, anticyclonic vorticity) over southern Australia is associated with spring high maximum temperatures in Australia (Hope et al., 2015; Gallant and Lewis 2016; McKay et al., 2021). While El Niño, the positive-phase of the IOD, and the negative-phase of the tropical TPI also promote anomalously high geopotential height, it forms further to the south of Australia (e.g. Cai et al., 2011a; Timbal and Hendon, 2011; McIntosh and Hendon, 2018). SAM's negative phase is characterised by an equatorward shift of the eddy-driven jet and bands of anomalously low and high geopotential height in the mid- and high-latitudes respectively (Thompson and Wallace, 2000; Fogt and Marshall, 2020). The altered atmospheric flow associated with the drivers can reduce rainfall, including by deflecting cooling rain-bearing systems (e.g. Jones and Trewin 2000; Hendon et al., 2007; Pepler et al., 2014; van Rensch et al., 2019) away from Australia (Cai et al., 2011a; Risbey et al., 2009b; McIntosh and Hendon, 2018; Hauser et al., 2020). Anomalous heat and dryness is also associated with other mechanisms such as increased subsidence and insolation (Hendon et al., 2014; Lim et al., 2019a; Pfahl et al., 2015; Quinting and Reeder, 2017; Suarez-Gutierrez et al., 2020) or heat advection (Jones and Trewin, 2000; Boschat et al., 2015; Gibson et al., 2017). Understanding the differences between the extratropical and tropical forcing behind some of these heat mechanisms is a goal of this paper.

The mechanisms and atmospheric circulation patterns associated with heat and connections to remote drivers may also vary through spring. McKay et al. (2021) noted that the relationship with the southern Australian upper-anticyclone and maximum temperature is weaker in September than November, and suggested that the anticyclone had greater influence from the tropics in later spring. The impact of SAM in the extratropics on Australia's temperature reverses from winter to spring (Hendon et al., 2007; Risbey et al., 2009a; Marshall et al., 2012; Min et al., 2013; Hendon et al., 2014; Fogt et al., 2020) as the mean zonal winds change with the seasons (Hendon et al. 2007) and the Indo-Pacific subtropical jet (STJ) weakens (Bals-Elsholz et al., 2001; Koch et al., 2006; Ceppi and Hartmann, 2013, Gillett et al., 2021) so that a negative SAM phase enhances subsidence over subtropical Australia into the warmer months (Hendon et al., 2014). The IOD and ENSO teleconnection pathways over the Indian Ocean toward Australia also change from winter to spring (Cai et al., 2011a). This change may relate to the strength of the winter STJ, as it should prevent direct propagation of Rossby waves between the tropics and extratropics (e.g. Hoskins and Ambrizzi, 1993). McIntosh and Hendon (2018) proposed that transient eddy-feedbacks generate a secondary wave source south of the winter STJ in response to IOD forcing. In spring, the STJ weakens sufficiently to allow for direct Rossby wave propagation from the tropical Indian Ocean. However, McKay et

al. (2021) suggested that the STJ may not weaken sufficiently in September to allow direct Rossby wave propagation, and that teleconnection pathways may be different on a monthly timescale as a result.

Teleconnections driven by large-scale remote modes of variability can precondition Australia toward hotter spring conditions (e.g. Hurrell et al., 2009), but cannot guarantee a hot month or season will eventuate. Even the strongest El Niño events may not result in the canonical dry and warm conditions expected (van Rensch et al., 2019; Hauser et al., 2020). Further, differences in how those modes of variability influence Australia between winter-spring-summer and the differences between spring-average atmospheric circulation highlight that there is more to understand in how maximum temperatures evolve through spring months. Filling the gap between weather and seasonal time-scales is an ongoing area of research that can lead to improved sub-seasonal forecasting (Meehl et al., 2021). Given the increasing likelihood of future extreme heat events occurring through spring, it is imperative to understand any differences that may exist in how heat develops, and links to varying influences from the extratropics to tropics. As such, this paper aims to identify differences in how the tropics and extratropics influence anomalously high maximum temperature formation through the months of spring. The reanalysis datasets, Rossby wave and statistical analysis methods are described in Section 3.3. An overview of how Australian spring maximum temperatures are related to circulation and large-scale variability is in Section 3.4. In Section 3.5 the variation of these relationships through the months of spring are assessed. Section 3.6 describes how the drivers influence the mechanisms that promote high monthly maximum temperature. Discussion and conclusions are provided in Section 3.7

### 3.3 Methods and data

#### 3.3.1 Indices and datasets

All circulation variables for September, October, November monthly-averaged data are taken from the ECMWF's Reanalysis 5 (ERA5) (Hersbach et al., 2020) available from the Copernicus Climate Change Service (C3S, 2017) on a 0.25° grid. Here, we use data from 1979 to 2019. Low-level circulation is diagnosed using 850hPa horizontal wind and mean sea level pressure (MSLP). Mid-tropospheric vertical motion is represented by 500hPa velocity. Upper-level circulation is represented by 200hPa geopotential height (200Z). 200hPa horizontal winds are used for Rossby wave analysis. Similar results were found using ERA-Interim reanalysis (Dee et al, 2011) and the JRA-55 from the Japan Meteorological Agency (2013) (not shown).

Australian monthly-averaged daily maximum temperature data for 1979 to 2019 is taken from the Australian Water Availability Project (AWAP) (Jones et al., 2009) analyses, available on a 0.05° resolution grid.

Monthly sea surface temperature (SST) is taken from NOAA Extended Reconstructed Sea Surface Temperature (ERSST V5; Huang et al., 2017)

The impact of SAM on Australia's climate shows some sensitivity to the method used to calculate the SAM index (e.g. Risbey et al., 2009a). To ensure consistency between the other indices and circulation variables, we calculate SAM as the difference between the standardized zonal means of ERA5 MSLP anomalies at 60°S and 40°S (Gong and Wang, 1999).

The tropical TPI (Timbal and Hendon, 2011) is defined as the difference in SST averaged over a parallelogram located over the Maritime Continent (0°-20S, 90°-140E at the equator shifted to 110°-160°E at 20°S) from SST averaged and summed over two regions in the tropical Indian Ocean (10°N to 20°S, 55° to 90°E) and tropical Pacific Ocean (a trapezium that extends from 15°N to 15°S, 150°E to 140°W in the north and 180°E to 140°W in the south). ENSO is described using the Niño3.4 index (averaged SST anomalies over 5°N-5°S, 170°E-120°W) and the IOD using the dipole mode index (DMI; the difference between the SST anomalies averaged over 10°S-10°N, 50°-70°E and 10°S-0°, 90°-110°E; Saji et al., 1999).

To highlight the influence of interannual variability, the 1981-2010 climatological mean is removed from each month

All data are linearly detrended before analysis.

### 3.3.2 Rossby wave analysis

We use wave activity flux (WAF) at 200hPa to trace Rossby wave group propagation and to identify source and decay regions that influence the atmospheric circulation patterns. Following Takaya and Nakamura (2001), we calculate WAF as:

$$WAF = p \cos \phi \left\{ \begin{aligned} & \frac{U}{a^2 \cos^2 \phi} \left[ \left( \frac{\partial \psi'}{\partial \lambda} \right)^2 - \psi' \frac{\partial^2 \psi'}{\partial \lambda^2} \right] \\ & + \frac{V}{a^2 \cos \phi} \left[ \frac{\partial \psi'}{\partial \lambda} \frac{\partial \psi'}{\partial \phi} - \psi' \frac{\partial^2 \psi'}{\partial \lambda \partial \phi} \right] \frac{U}{a^2 \cos \phi} \left[ \frac{\partial \psi'}{\partial \lambda} \frac{\partial \psi'}{\partial \phi} - \psi' \frac{\partial^2 \psi'}{\partial \lambda \partial \phi} \right] \\ & + \frac{V}{a^2} \left[ \left( \frac{\partial \psi'}{\partial \phi} \right)^2 - \psi' \frac{\partial^2 \psi'}{\partial \phi^2} \right] \end{aligned} \right\}$$

where  $p$  is the pressure (200hPa) scaled against 1000hPa,  $U$  and  $V$  are the climatological zonal and meridional wind speed magnitudes,  $a$  is the radius of the earth,  $(\phi, \lambda)$  are latitude and longitude,  $\psi' =$

$Z' / f$  is the quasi-geostrophic perturbation streamfunction,  $Z'$  is the 200hPa geopotential height anomaly obtained through regression onto maximum temperature or climate driver indices,  $f = 2\Omega \sin\phi$  is the Coriolis parameter with the Earth's rotation  $\Omega$ . WAF is not plotted within  $10^\circ$  of the equator.

WAF is parallel to the direction of quasi-stationary Rossby wave group velocity, and regions of divergence or convergence of WAF correspond to zones of Rossby wave sources or sinks respectively.

Total stationary Rossby wave wavenumber (e.g., Hoskins and Karoly 1981) is defined as:

$$K_S = \sqrt{\frac{\beta - U_{yy}}{U}}$$

where  $\beta - U_{yy}$  is the meridional gradient of mean-state absolute vorticity at 200hPa. WAF should refract toward regions of higher  $K_S$  and either reflect or evanesce on regions of  $K_S < 0$ , such as in the STJ where the curvature of the flow ( $U_{yy}$ ) can become larger than the planetary vorticity gradient ( $\beta$ ) (e.g Barnes and Hartmann, 2012; X. Li et al., 2015 a,b)

### 3.3.3 Statistical analysis

Linear, partial, and multi-linear regression and Spearman's ranked correlation are used to assess the relationships between Australian maximum temperature, atmospheric circulation and the tropics and extratropics. Due to the large decorrelation length scales, Australian-average maximum temperature variability is representative of all but far north Australia's spring and spring-monthly maximum temperatures (Fig. 3-1). Statistical significance is calculated at the 95% confidence level using Student's (1908) t-test using 39 (41 years - 2) degrees of freedom. Pattern correlation is used to compare regression patterns.

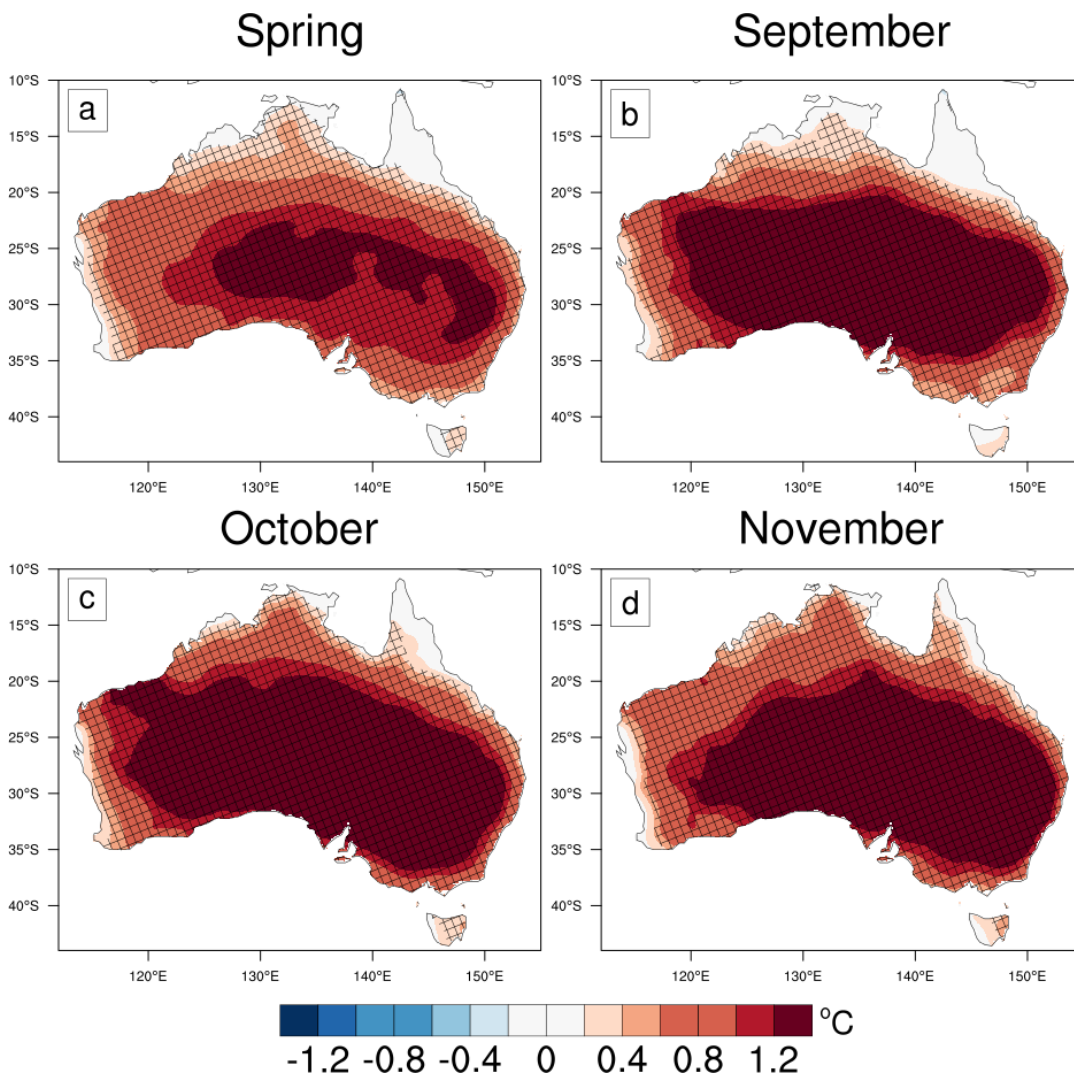


**Figure 3-1 Australian-averaged maximum temperature regressed onto gridded maximum temperature**

*Australian weighted area-averaged maximum temperature linearly regressed onto gridded Australian maximum temperature for spring (a), September (b), October (c) and November (d) over the years 1979 to 2019. Anomalies are relative to a 1981 to 2010 climatology. All variables were detrended, and the area-averaged maximum temperature time series was standardised before regression. Hashing shows where the regression was statistically significant at the 95% confidence level using a two-sided Student's *t*-test with 39 independent samples.*

### 3.4 Results

#### 3.4.1 SON maximum temperatures, circulation patterns and associations with drivers

We start by giving an overview of the spring-seasonal relationships between average Australian austral spring maximum temperature and lower- and upper-level atmospheric circulation (Fig. 3-2a,b). Barotropic cyclones appear to the southwest and southeast of Australia, occurring in both the lower- and upper-level circulation regressions (Fig. 3-2a-b) and noted during recent extreme spring heat events (Gallant and Lewis, 2016; Hope et al., 2016; McKay et al., 2021). Weak anomalous anticyclonic low-level winds are found over

Australia, as well as sinking motion across the eastern half of the continent. An upper-level anticyclone sits over southern Australia, with the wave activity flux predominantly indicating Rossby wave propagation from the subtropical Indian Ocean, through the anticyclone and into the subtropical Pacific Ocean.

We now compare the atmospheric patterns associated with spring maximum temperature to those associated with large scale modes of variability. The spring-average atmospheric circulation patterns associated with the remote drivers of variability are calculated via linear regression onto each standardised index. Note that the TPI and SAM indices have been multiplied by negative one to present positive associations with high temperatures. The pattern for SAM ( $x-1$ ) shows elongated barotropic low and high anomalies lie in the middle and high latitudes respectively (Fig. 3-2c-d), with upper-level cyclonic nodes to the southeast and southwest of Australia. Negative SAM is associated with high maximum temperatures through much of subtropical, and particularly eastern, Australia (Fig. 3-2e).

The tropical modes, represented by Niño3.4 (Fig 3-2i-k), the DMI (Fig. 3-2 l-n), and tropical TPI ( $x-1$ ) (Fig 3-2f-h)) are also associated with spring Australian maximum temperature anomalies. Each mode generates an apparent Rossby wave pattern that arcs from the tropical Indian Ocean to promote anomalous high geopotential height south of Australia, consistent with earlier studies (e.g. Cai et al., 2011a; Timbal and Hendon, 2011; McIntosh and Hendon, 2018). Each regression also shares anomalous high surface pressure over Australia, sinking motion in the east, cyclonic nodes to the southwest and east of Australia, and elongated upper-level cyclones in the subtropical Indian Ocean. These similarities are likely the result of the strong co-variability between the IOD and ENSO (e.g. Meyers et al., 2007; Risbey et al., 2009a). However, the IOD has a stronger low-level cyclone to the southeast and a poleward extension of the subtropical Indian Ocean cyclone that sets a subtly different wave train from around 50°S, 60°E that is poleward of that generated by ENSO. The positive IOD is also associated with high maximum temperatures across a broader region of southern and western Australian than is El Niño. The tropical TPI ( $x-1$ ) is a blend of both Niño3.4 and DMI circulation patterns and has a strong relationship with Australian spring maximum temperatures across all but northern Australia.

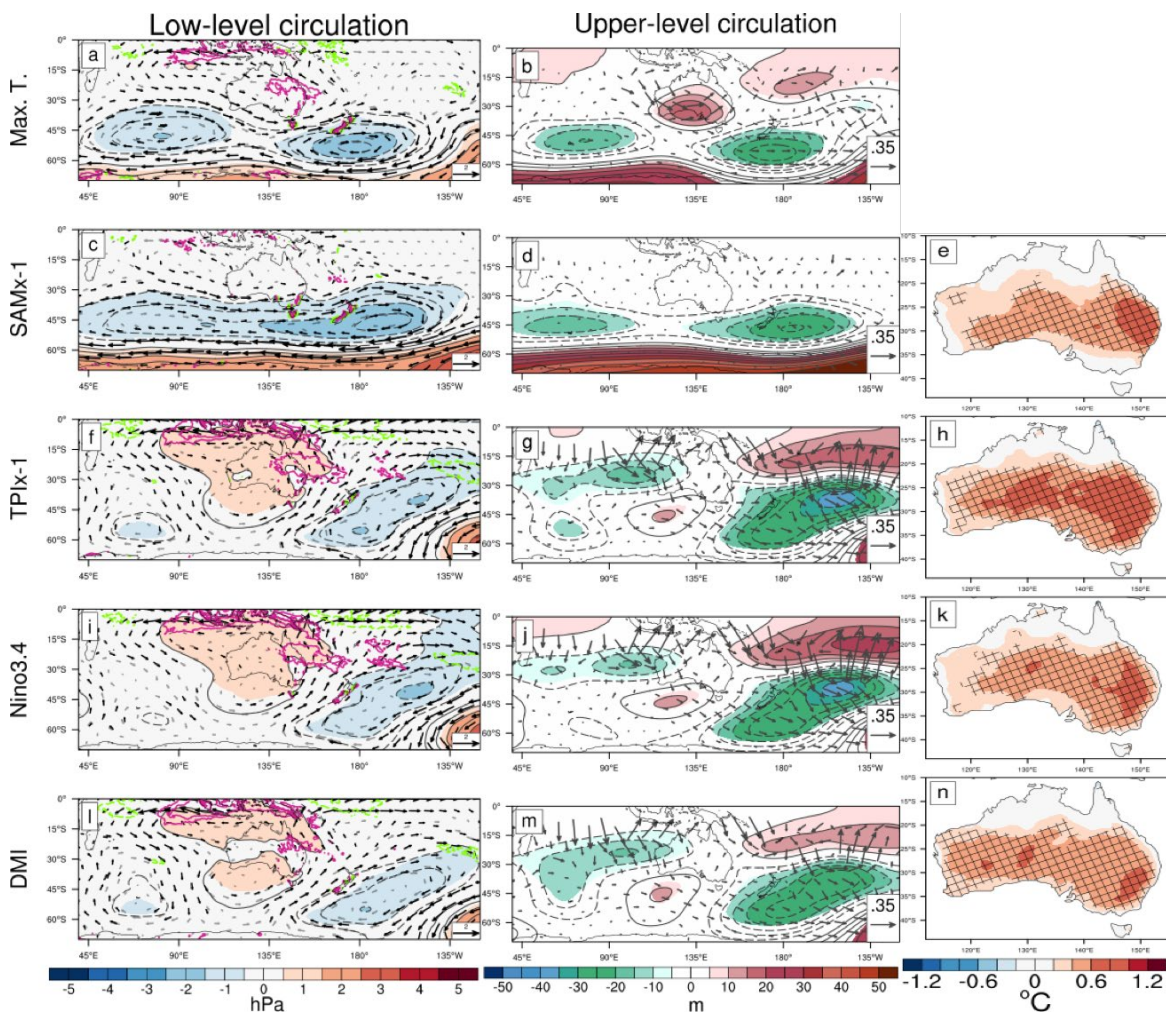


**Figure 3-2 SON circulation and maximum temperature linear regressions onto circulation and gridded maximum temperature**

Linear regressions of spring standardised weighted area-averaged Australian maximum temperature (a-b), SAMx-1 (c-e), tropical TPIx-1 (f-h), Niño3.4 (i-j) and DMI (j-n) onto low-level circulation (left column), upper-level circulation (middle column) and Australian maximum temperatures (right column). Low-level circulation is represented by anomalous mean sea level pressure (hPa) (black and filled contours), 850hPa wind vectors ( $\text{ms}^{-1}$ ) and 500hPa omega ( $\text{hPa s}^{-1}$ ) contours from  $-0.02$  to  $0.02 \text{ hPa s}^{-1}$  in steps of  $0.01 \text{ hPa s}^{-1}$  (magenta contours are positive; downward motion) and cyan contours are negative; upward motion, and the zero contour is not plotted). Upper-level circulation is represented by 200hPa geopotential height (black and filled contours and wave activity flux vectors ( $\text{m}^2 \text{s}^{-2}$ )).

Filled contours, bold wind vectors, cross-hatching, and all vertical motion contours are significant at the 95% confidence level using a Student's t-test with 39 independent samples.

Given the similarities and connections between ENSO and IOD teleconnections, we use the tropical TPI to represent the large-scale influence of the tropics. SAM is used to represent the influence of the extratropics. Statistical models of Australian weighted area-averaged spring maximum temperatures reconstructed through multilinear regression using either Niño3.4, DMI and, SAM or the tropical TPI and SAM as the predictors explains 32% and 34% of maximum temperature variability respectively (Fig 3-3).

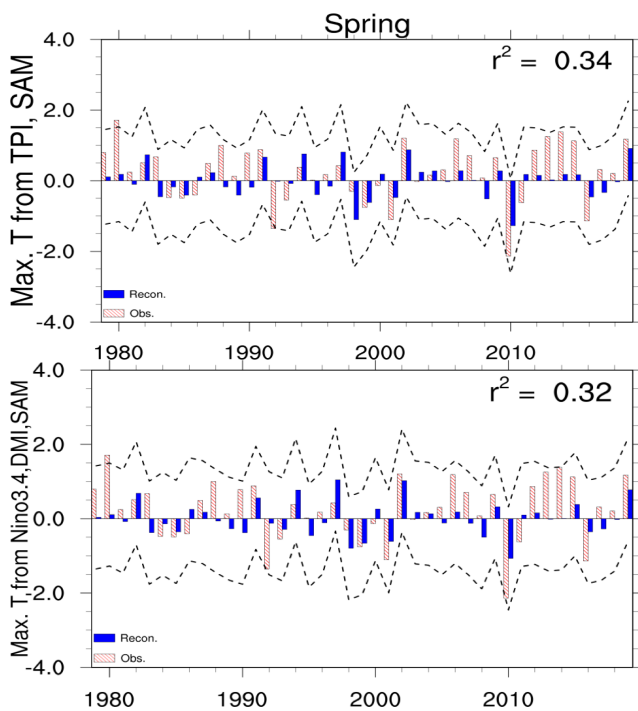


**Figure 3-3 Time series of observed and statistically reconstructed spring maximum temperature**

Spring (SON) Australian-averaged maximum temperature statistically reconstructed using the tropical TPI and SAM (top) and Niño3.4, DMI and SAM bottom) (blue bars) between 1979 to 2019. The red dashed bars show the observed temperature anomaly for each month. The dotted line shows the 95% confidence interval. The percent variance explained ( $r^2$ ) for each month is in the top right of each figure.

We next compare the atmospheric circulation associated with monthly high maximum temperatures to that with the large-scale modes of variability through the individual months of spring. To ensure that we are assessing the influence of the tropics and extratropics separately, we use multi-linear regression onto the monthly circulation variables.

### 3.4.2 Monthly circulation patterns and associations with drivers

The regression of monthly Australian maximum temperature onto the lower- and upper-level atmospheric circulation is displayed in Figures 3-4a-c and 3-5a-c respectively for September, October and November. The multi-linear regression onto the standardised monthly indices of SAM ( $x-1$ ) (Figs. 3-4d-f and 3-4d-f) and tropical TPI ( $x-1$ ) (Figs. 3-5h-i and 3-5h-i). At first glance, these monthly circulation patterns are broadly similar to the spring-average regression patterns. However, the details of the circulation patterns change as the months progress, suggesting that different processes are important for heat development through spring.

The most obvious change in atmospheric circulation through the months is in the anomalous low-level flow across Australia, particularly generated by the barotropic cyclones southwest (SWC) or southeast (SEC) of Australia (boxes in Fig. 3-4a-b). Weak anomalous low-level anticyclonic flow around the Tasman Sea (box in Fig. 3-4c) also contributes to the anomalous northerly flow over eastern Australia in November in particular (Fig. 3-4c). Tasman Sea anticyclonic blocking patterns have previously been linked to anomalously warm conditions (Marshall et al., 2014), but here appear to only contribute to high maximum temperatures in November. The SWC and SEC vary in geographic shape and strength through the months. The SWC dominates in September but weakens through October and November, whereas, the SEC is missing in

September but is strong in October and November. Similar cyclones appear in the monthly SAM (x-1) regressions (Figs. 3-5 d-f, 3d-f) and the Australian-region MSLP correlates strongly with that associated with high Australian temperature (top-right of Fig. 3-5d-f). Rather than cyclones in September and October the TPI (x-1) is associated with a barotropic anticyclone south of Australia that directs anomalous southerly low-level wind across eastern Australia (Figs. 3-5 h-i); a pattern that would be associated with cooler conditions. The September and October TPI (x-1) MSLP patterns actually anti-correlate with that associated with high Australian maximum temperatures (top-right Fig. 3-5 g-i). It is not until November that we see a barotropic cyclone to the southeast of Australia associated with the TPI (x-1). So, for the majority of spring negative TPI-forced low-level atmospheric circulation appears to counter high maximum temperatures, despite the overall positive relationship in spring (Fig. 3-2h).

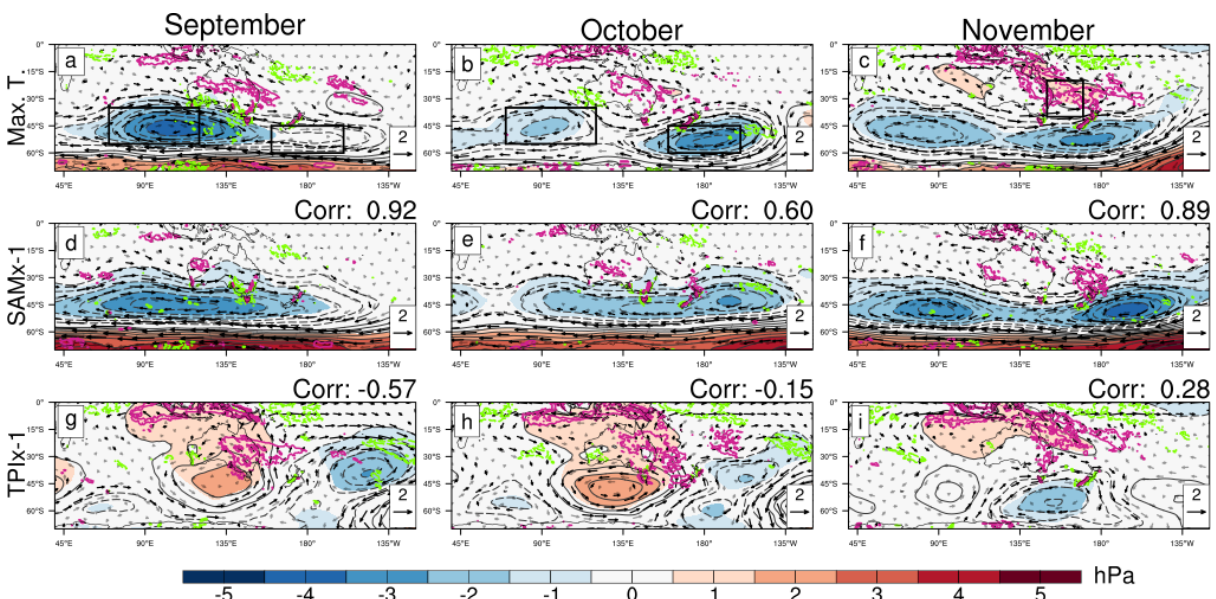


**Figure 3-4 Spring-monthly regressions of maximum temperature onto with low-level circulation**

Regressions onto low-level circulation, as in Fig. 3-2, except for September (left column), October (middle column) and November (right column). Standardised area-averaged Australian maximum temperature is linearly regressed onto low-level circulation (a-c) and SAMx-1 (d-f) and tropical TPIx-1 (g-i) are multi-linear regressions onto low-level circulation.

Pattern correlation between the maximum temperature MSLP regressions and the SAM and tropical TPI regressions calculated over 5°S-70°S; 70°E-170°E are written in the top right of each SAM or tropical TPI regression.

The boxes (a-c) show key low-level circulation features identified as being important for maximum temperature development: The southwest cyclone (SWC) 35°S-55°S; 70°-120°E; southeast cyclone (SEC) 45°S-60°S; 160°-200°E and Tasman Sea high (TSH) 20°S-40°S; 150°-170°E.

The anomalous southern Australian upper-anticyclone (SAA) from the spring pattern is also associated with high maximum temperature in each of the individual spring months (Fig. 3-5a-c), but its location shifts eastward across Australia through spring. The boxed region was chosen to match earlier studies (Gallant

and Lewis, 2016; McKay et al., 2021), but best matches the November position, likely contributing to the stronger relationship between heat and SAA in this month (McKay et al., 2021; see also section 7). The anticyclone in later spring appears to form part of a wave train from a cyclone to the northwest of Australia toward the southeast cyclone. While the monthly TPI regressions have anticyclones in September and October (Fig. 3-3g-h), they are located too far south relative to Australia, as in the spring-average regression. The regressions onto SAM ( $x-1$ ) (Fig 3-3 d-f) have weak anticyclones over western Australia that are not statistically significant. It is not until November that both SAM and TPI ( $x-1$ ) (Figs. 3-3 f,i) have an anticyclone over central-east southern Australia. Both the upper- level SAM and TPI ( $x-1$ ) regressions correlate moderately with the maximum temperature regression in November, and the SAM and TPI ( $x-1$ ) anticyclones may form part of the same wave train associated with maximum temperatures. However, the SAM and TPI ( $x-1$ ) anticyclones are weaker and too far east relative to that associated with high maximum temperatures, such that they may not contribute strongly to the SAA formation. We explore this idea further in section 7.

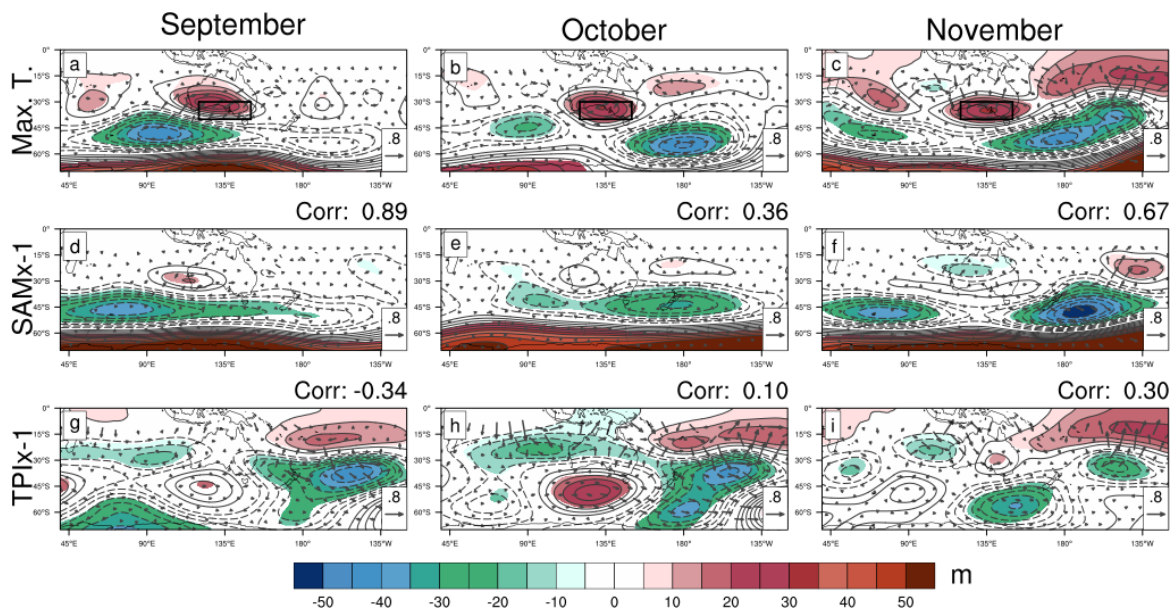


**Figure 3-5** As with Fig 3-4 but for upper-level circulation

The Australian-region pattern correlation between the maximum temperature Z200 regressions and SAM $x-1$  and TPI $x-1$  are in the top right of each figure. Boxed area (a-c) highlights the southern Australian anticyclone (SAA; 30°-40°S, 120°-150°E) that is linked with high maximum temperatures. Vectors are wave activity flux.

While the SAA is not well explained by SAM or TPI ( $x-1$ ) through spring, much of the statistically significant 500hPa vertical motion associated high maximum temperatures (green and magenta contours, Fig. 3-4a-c) matches that associated with TPI (Fig. 3-4h-j) and to a lesser extent SAM (Fig. 3-4d-f). In September, sinking motion over subtropical Australia and rising motion over the southern coasts is associated with high maximum temperatures. By November, the rising motion has largely vanished and the sinking motion has shifted to be over eastern Australia. It was expected that the SAA would generate some of the sinking

motion associated with high maximum temperature, however, this vertical motion does not correlate strongly with any of the key circulation features examined here (Table 3-1).

	SAA	SAA NS	SAA NT	SWC	SWC NS	SWC NT	SEC	SEC NS	SEC NT	TSH	TSH NS	TSH NT
<b>September</b>												
W500	0.26	0.26	0.26	0.38	0.19	<b>0.45</b>	-0.04	-0.13	0.29	0.10	0.24	-0.02
V850	<b>0.44</b>	<b>0.44</b>	0.44	<b>0.69</b>	<b>0.74</b>	<b>0.69</b>	-0.21	-0.27	<b>0.69</b>	<b>0.47</b>	<b>0.58</b>	<b>0.50</b>
U850	0.19	0.19	0.20	<b>0.65</b>	0.30	<b>0.63</b>	<b>0.37</b>	0.20	<b>0.66</b>	<b>-0.37</b>	-0.14	<b>-0.34</b>
<b>October</b>												
W500	0.31	<b>0.36</b>	0.27	0.14	-0.05	0.25	<b>0.45</b>	<b>0.37</b>	0.05	0.24	<b>0.39</b>	0.02
V850	<b>0.52</b>	<b>0.53</b>	<b>0.52</b>	<b>0.59</b>	<b>0.62</b>	<b>0.59</b>	0.05	0.03	<b>0.59</b>	<b>0.59</b>	<b>0.65</b>	<b>0.63</b>
U850	0.02	0.09	0.04	<b>0.63</b>	<b>0.45</b>	<b>0.59</b>	<b>0.57</b>	<b>0.46</b>	<b>0.65</b>	<b>-0.34</b>	-0.18	-0.26
<b>November</b>												
W500	<b>0.32</b>	0.27	0.25	0.24	-0.07	<b>0.31</b>	<b>0.35</b>	0.17	0.02	0.14	0.09	0.09
V850	<b>0.52</b>	<b>0.50</b>	<b>0.55</b>	<b>0.55</b>	<b>0.52</b>	<b>0.52</b>	0.01	-0.11	<b>0.56</b>	<b>0.63</b>	<b>0.61</b>	<b>0.65</b>
U850	0.08	0.02	0.01	<b>0.39</b>	0.06	<b>0.45</b>	<b>0.50</b>	0.30	0.18	-0.03	-0.1	-0.08

**Table 3-1 Correlation and partial correlations between circulation features and dynamical heat mechanisms**

*Spearman's ranked correlation coefficients of weighted area-averaged dynamical heat mechanisms (W500: anomalous subtropical 500hPa vertical motion; U850 and V850: 850hPa horizontal and meridional wind anomalies) correlated with key circulation features (SAA: southern-Australian anticyclone; SWC: southwest cyclone; SEC: southeast cyclone; TSH: Tasman Sea High) identified in main text. Partial correlations where either negative SAM or negative TPI were first linearly regressed out of the circulation feature timeseries are marked as |NS and |NT respectively. Correlations that are statistically significant at the 95% confidence level using a Student's t-test with 39 degrees of freedom are in bold.*

Changes in wave activity flux in Fig. 3-5a-c help explain some of the changes in the broad scale circulation changes through spring. In September, WAF predominantly diverges from the southwest cyclone toward the southern Australian anticyclone. In October, a component of WAF also diverges from the eastern tropical Indian Ocean region. By November, the tropical-component dominates the WAF and forms part of a very different pattern to the previous two months; continuous WAF follows a wave train that appears to propagate from the far southwest Indian Ocean. This wave joins with a wave out of the tropical Indian Ocean, as indicated by the tropical-origin WAF, to then continue through the southern Australian anticyclone. The latter part of this wave train is similar to the IOD teleconnection highlighted by Cai et al. (2011) in spring. The WAF associated with SAM and TPI (x-1) (Fig. 2-5d-i) also diverges from the extratropics toward the respective anticyclones in September and October. While a broad region of low height in the subtropical Indian Ocean is associated with the TPI, it does not appear to generate WAF that diverges into the extratropics. It is not until November that WAF associated with the TPI (x-1), and weakly with SAM (x-1), appears to diverge directly from the cyclone in the eastern subtropical Indian Ocean, indicating a wave that joins the anticyclone over southeastern Australia.

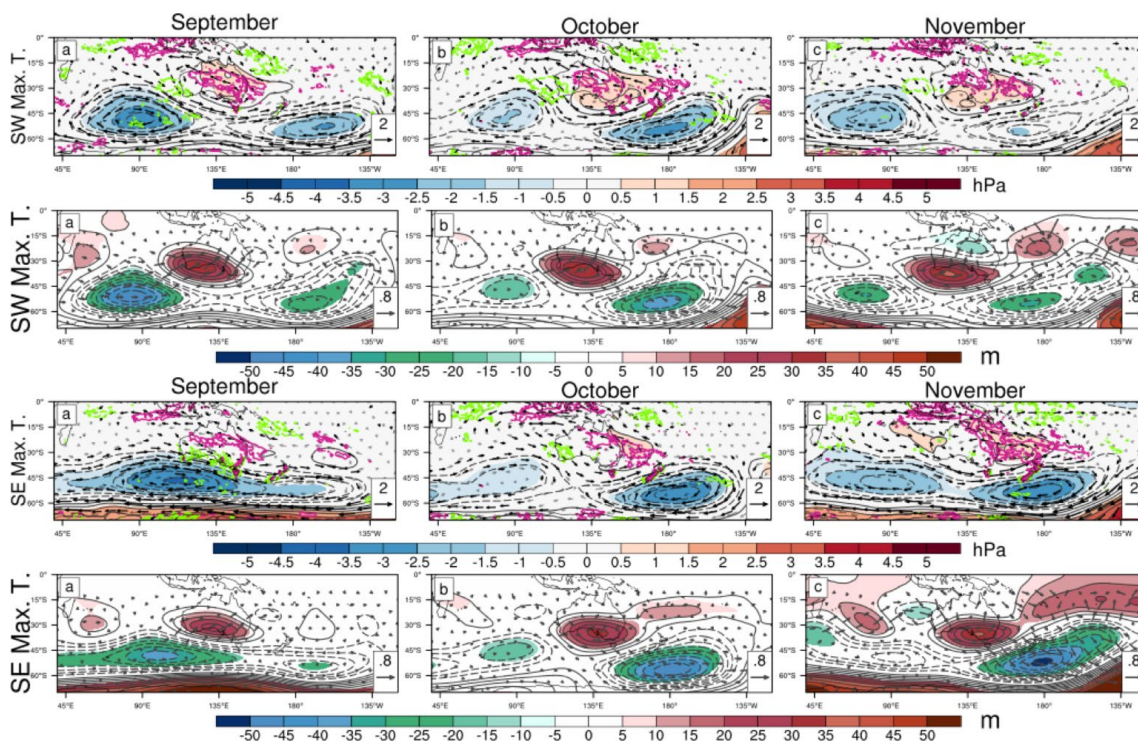


**Figure 3-6 Regional Australian maximum temperature regressions onto atmospheric circulation**

Low-level (rows 1 and 3) and upper-level (rows 2 and 4) circulation regressed onto weighted area-averaged maximum temperature averaged over southwest (SW: 25°S-36°S, 110-125°E) and southeast (SE: 25°S-45°S, 135-155°E) Australia. Low-level circulation is represented by anomalous mean sea level pressure (hPa) (black and filled contours), 850hPa wind vectors ( $\text{m s}^{-1}$ ) and 500hPa omega ( $\text{hPa s}^{-1}$ ) contours from  $-0.02$  to  $0.02 \text{ hPa s}^{-1}$  in steps of  $0.01 \text{ hPa s}^{-1}$  (magenta contours are positive (downward motion) and cyan contours are negative (upward motion); zero contour not plotted). Upper-level circulation is represented by 200hPa geopotential height (black and filled contours and wave activity flux vectors ( $\text{m}^2 \text{s}^{-2}$ )). Filled contours, bold wind vectors, cross-hatching, and all vertical motion contours are significant at the 95% confidence level using a Student's *t*-test with 39 independent samples.

Overall, these results suggest that the circulation associated with maximum temperature shifts from extratropical to tropical forcing as spring progresses. This is supported by how well SAM appears to project onto the atmospheric circulation associated with maximum temperatures in September, and how the TPI projects more strongly later in spring. The change in WAF associated with this change suggests that there may be some kind of weakening barrier between the tropics and extratropics that influences the Rossby wave propagation.

We find qualitatively similar results if we perform the linear regressions using maximum temperature averaged over sub-regions of Australia, for example southwest or southeast Australia (Fig. 3-6). Differences in atmospheric circulation between Australia-wide or southwest- or southeast- averaged maximum temperature regressions are generally limited to a slight westward or eastward shift of the circulation pattern respectively.

### 3.4.3 Connection between subtropical jet and atmospheric circulation

We next explore how the subtropical jet may be influencing the WAF through the spring months.

The subtropical jet (STJ) peaks in strength in winter and weakens through spring to have broken down by summer (e.g. see figure 9, Ceppi and Hartmann, 2013). This gradual breakdown of the STJ coincides with a decrease in the area with total stationary wavenumber less than zero over southern Australia (Fig. 3-7), and may provide an explanation for the growing relationship with the tropics and Australian maximum temperature by November.

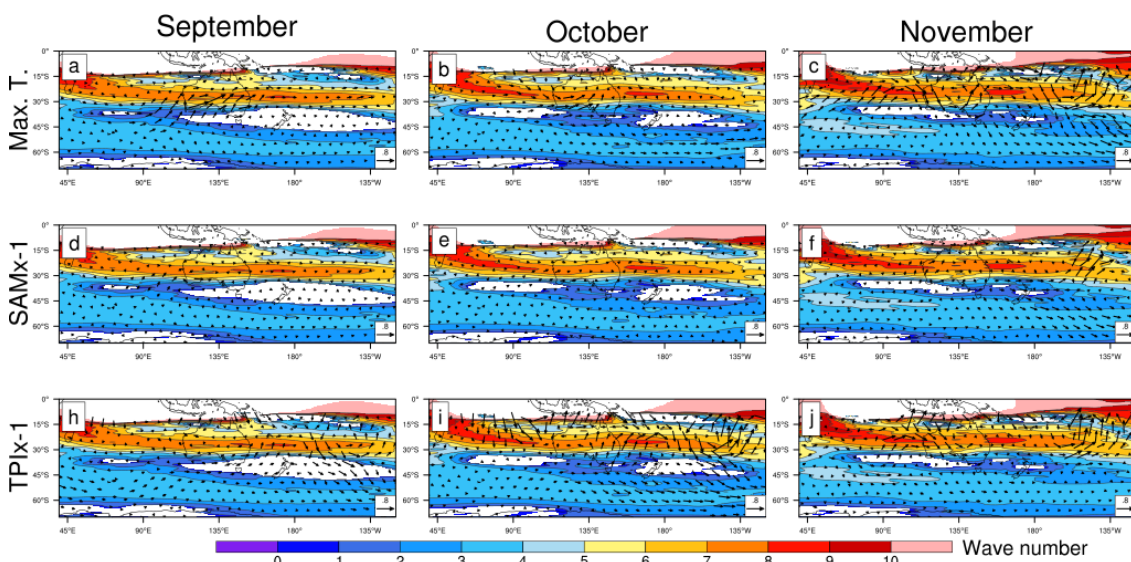


**Figure 3-7 Climatological monthly total wave number and wave activity flux**

*Total climatological wave number (Ks) calculated using 1981-2010 climatological wind for September, October and November. Vectors are the wave activity flux repeated from Fig. 3-3*

We expect wave activity flux to propagate toward and along regions of high wave number, but not cross regions where wave number is undefined, and hence, this gives an indication of where Rossby waves may or may not propagate. The wave activity flux vectors from the maximum temperature, TPI and SAM (x-1) regressions in figure 3-5 are overlaid in figure 3-7 on the monthly climatological Ks associated with the zonal winds. In September, the WAF associated with high maximum temperature (Fig. 3-5a) diverges from the region of the southwest cyclone. As such, the WAF indicates waves propagate through a region of low

total stationary Rossby wave wavenumber,  $K_s$ , over southwest Australia and are then directed along the STJ waveguide (e.g. Ambrizzi et al., 1995) (i.e. from high to low latitudes). As the jet weakens in October (Fig. 3-7b) a portion of WAF also diverges from the tropical Indian Ocean to dissipate on the jet's equatorward flank, but mostly propagates from west to east along the STJ waveguide. WAF in November (Fig. 3-7c) is even more distinctive in showing Rossby waves that propagate along the jet waveguide from a region near Africa, upstream of the figure's western edge, with further contributions from the tropical Indian Ocean. However, there is no WAF pointing out of the SWC.

The increase in WAF associated with the tropical TPI (Fig. 3-7h-j) indicates an increase in wave propagation out of the tropical Indian Ocean through spring that coincides with the STJ decay. In September and October weak WAF diverging from the central southern Indian Ocean indicates wave trains follow the eddy-driven jet waveguide (region of locally higher wave number around 50°S). This high latitude wave train suggests the secondary wave source proposed by McIntosh and Hendon (2018) may be important in early spring. The tendency for TPI-associated WAF to follow this trajectory may explain why the barotropic anticyclone associated with the TPI is further poleward than in the regression onto Australian maximum temperature. By October more increased WAF diverges from the tropical Indian Ocean to be guided along the region of high  $K_s$ . By November WAF diverges out of the extratropical Indian Ocean along the high  $K_s$  region, similar to the maximum temperature-WAF. This increase in tropical-origin WAF is consistent with increased wave trains propagating out of the tropical Indian Ocean associated with the TPI. WAF generated by SAM (Fig. 3-7d-f) also converges toward the STJ waveguide in each month.

Limits around linear Rossby wave theory (e.g. Liu & Alexander, 2007) may explain why some wave activity flux cross the region of imaginary wavenumber associated with the STJ. However, the majority of WAF associated with Australian maximum temperature, or with the tropics or extratropics does indicate wave trains divert to propagate along the jet, as expected. While the breakdown of the STJ through spring may help explain the change in teleconnection pathways of the TPI toward Australia, the STJ consistently acts as a waveguide toward Australia.

We now look more closely into how the drivers, circulation features, and heat mechanisms relate to each other and how that results in higher Australian maximum temperatures.

#### 3.4.4 Mechanisms and drivers of monthly maximum temperatures through spring

As with the atmospheric circulation regressions, the relationships between Australian maximum temperature and SAM and TPI ( $x-1$ ) evolve through the spring months. In September, negative SAM (Fig. 3-8a) is associated with a broad area of high maximum temperature over subtropical Australia, that contracts in October and November (Figs. 3-8 b-c). Conversely, the relationship with negative TPI and maximum

temperature is weaker early in spring, with statistically significant high temperatures confined to the west and east, and cool temperatures in the far north in September (Fig. 3-8d). The TPI's relationship with high maximum temperature broadens and strengthens in October and covers the majority of Australia by November (Figs. 3-8 e-f). Overall, these monthly relationships give the impression of a transition from extratropical to tropical drivers becoming more influential over Australian temperatures that is broadly consistent with the apparent change in atmospheric circulation through spring.

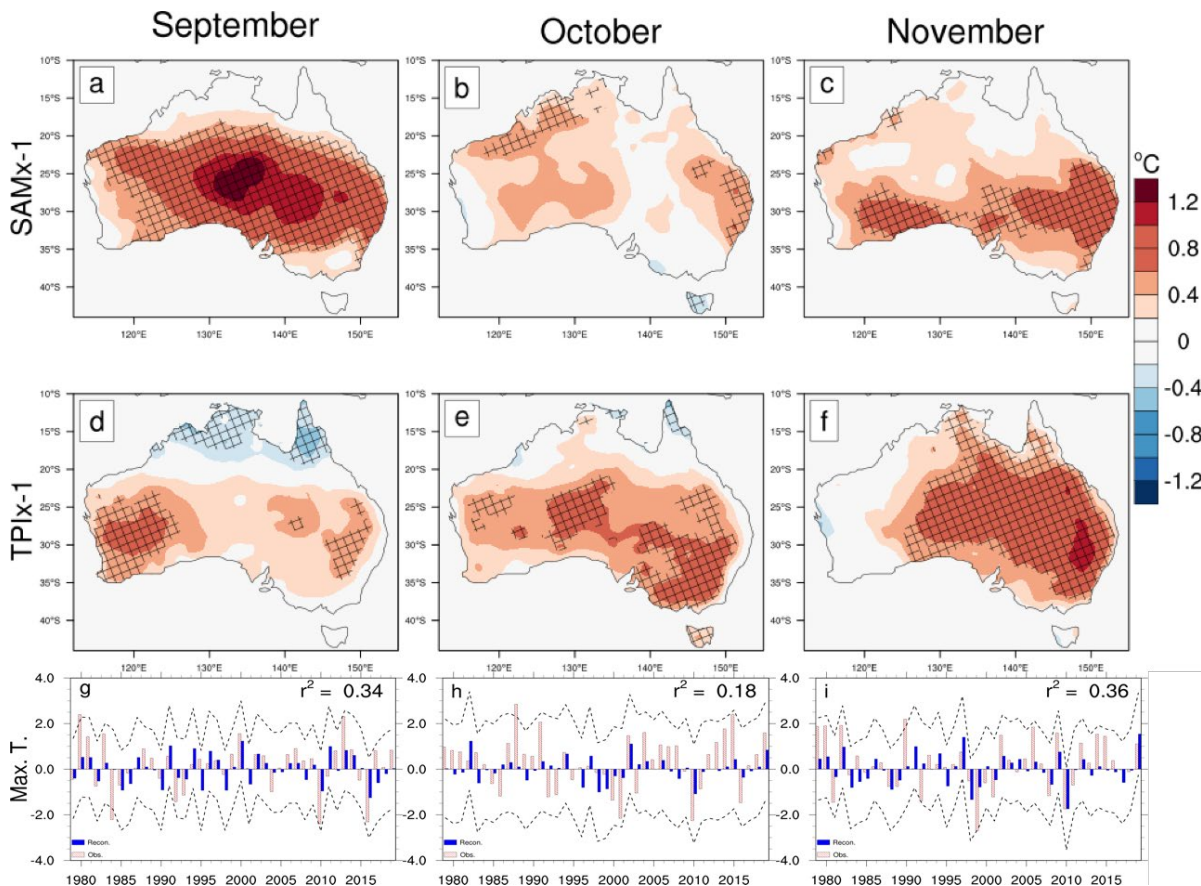


**Figure 3-8 Spring monthly extratropical and tropical regressions to maximum temperature and statistical time series reconstruction**

Multilinear regression coefficients ( $^{\circ}\text{C}$ ) of Australian maximum temperature regressed onto standardised timeseries of the SAMx-1 (a – c) and the tropical TPI x-1 (d – f) for September, October and November over the years 1979 to 2019. Reconstructions (blue bars) of September, October and November (i-k) Australian area-averaged maximum temperature from standardised time series of SAM and tropical TPI indices. Observed values are in red hashing. The dashed line shows the 95% prediction interval computed as  $\pm 1.96$  standard error and the variance explained ( $r^2$ ) of the model is in the top right of each figure.

Using the standardised SAM and TPI time series as predictors in a regression model to reconstruct the monthly Australian-averaged maximum temperature anomalies (Figs. 3-8 g-i) explains only between 18 and 36% Australian maximum temperature variance ( $r^2$ ) through spring. The model does not substantially improve if it is calculated over southeast or southwest Australia, or if using Niño3.4 or DMI as predictors instead of the tropical TPI (Fig. 3-9).

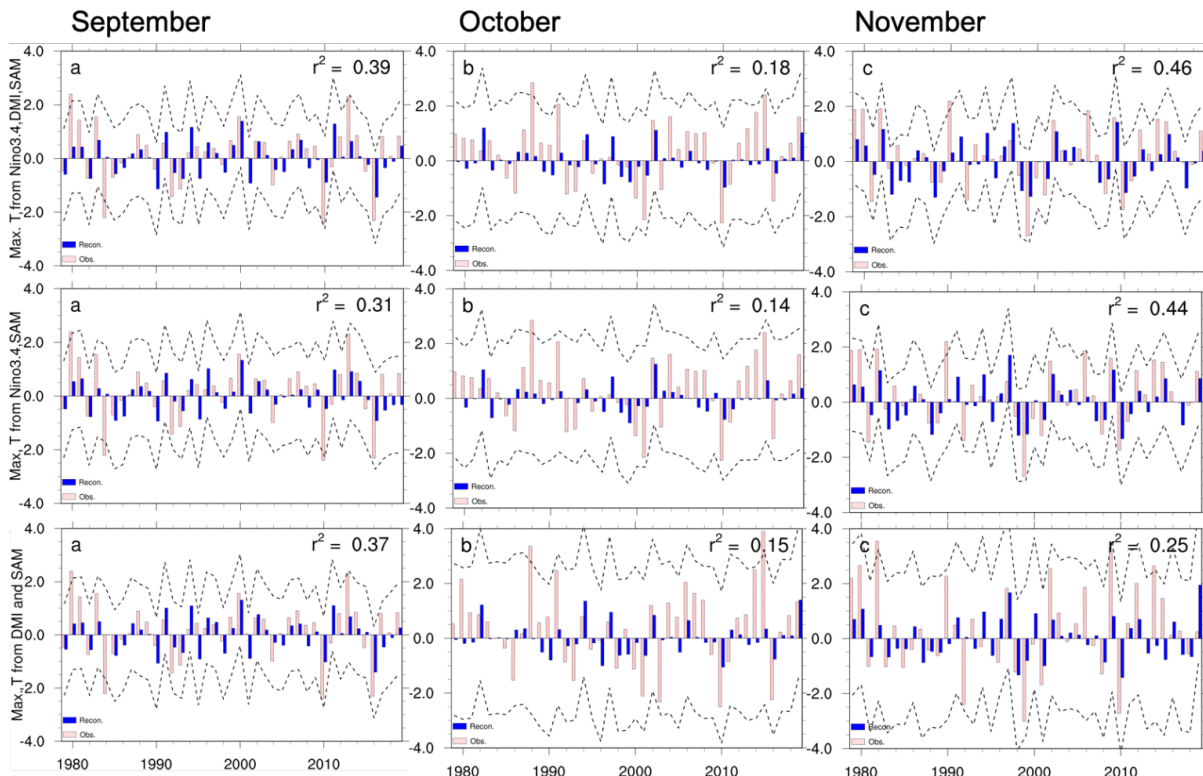


**Figure 3-9** As with Fig 3-8 g-i, but reconstructed with different combinations of climate modes of variability

Australian weighted area-averaged maximum temperature statistically reconstructed using different combinations of Niño3.4, DMI and SAM for September, October and November (blue bars) between 1979 to 2019. The red dashed lines show the observed temperature anomaly for each month. The dotted line shows the 95% confidence interval. The percent variance explained ( $r^2$ ) for each month is in the top right of each figure.

To explore how the atmospheric circulation relates to some of the mechanisms that develop heat through spring, we first compose indices of the key circulation features discussed in section 4. Weighted area-averages of mean-sea level pressure anomalies (multiplied by negative one) over the southwest and southeast cyclones (SWC and SEC) and anomalous 200hPa geopotential height over the southern Australian anticyclone (SAA) for each spring month. See Figs. 3-4 a,b and 3-5 a-c for regions. Creating a statistical model using multiple linear regression of Australian-averaged monthly spring maximum temperatures these circulation features as predictors (Fig. 3-10a-c) explains consistently higher maximum temperature variance (around 60%) than did the model from the indices of tropical and extratropical large-scale modes of variability. Further, despite the changes in the features' geographic shape, strength and position across the spring months in Fig. 3-4, the majority of maximum temperature across Australia is well explained by at least one of these features at all times through spring (Fig. 3-11). We next explore how these MSLP or 200hPa geopotential height features relate to the anomalous low-level westerly or northerly winds and vertical motion and how that relates to high maximum temperature development.

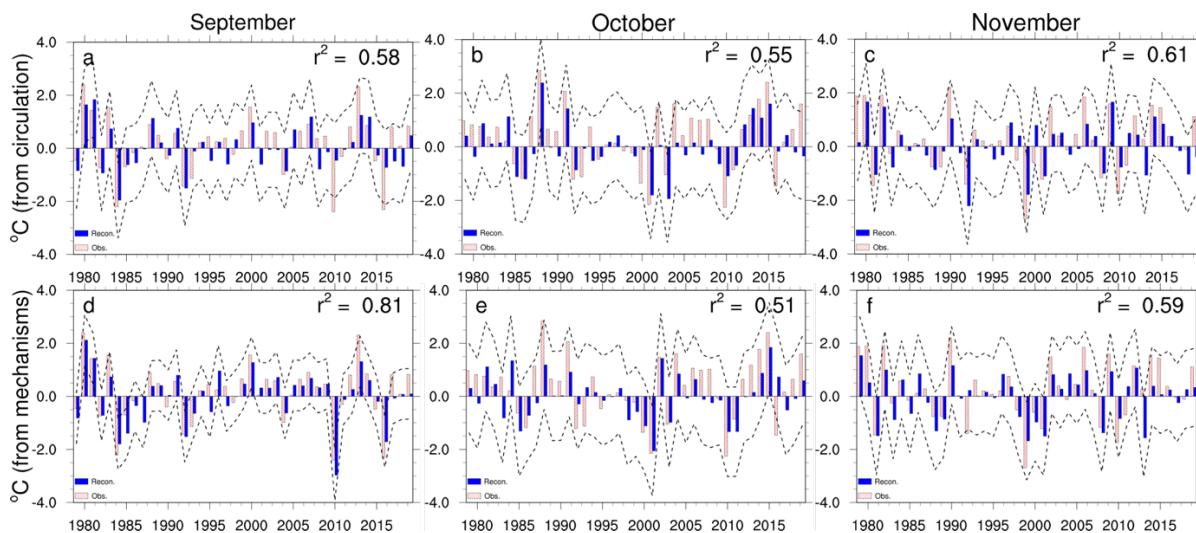


**Figure 3-10** As in Fig. 3-8(g-i) but from circulation features and heat mechanisms

Australian maximum temperature is reconstructed using time series of key circulation features (south-west low, south-east low and southern Australian anticyclone) identified in figures 1 and 2 as predictors in the top row (a-c) and area-averaged dynamical heat mechanism components (850hPa zonal wind and meridional wind (multiplied by -1) and 500hPa vertical motion; see text for region averaged over) as predictors in the bottom row (d-e) for September, October, and November.

Following van Rensch et al (2019), indices of three dynamical heat mechanisms were created by weighted area-averaging of westerly and northerly wind (meridional wind multiplied by -1) anomalies over a region around southern Australia (25°S-45°S, 105°-155°E), and 500hPa vertical motion anomalies (omega; positive is sinking motion) averaged over subtropical Australia (15°S-25°S, 120°-155°E). Regions were selected based on the areas of highest statistical significance between atmospheric circulation and Australian maximum temperature in Fig. 3-4a-c. Again, a statistical model of Australian-averaged maximum temperatures that uses these mechanisms as the predictors explains a higher proportion of maximum temperature variance through spring than does the model using SAM or the tropical TPI (Fig. 3-8 d-e). The percent variance explained is much higher in September (about 80%), before dropping to around 55% in October-November. The decrease in the percent variance explained appears to be primarily associated with how strongly the anomalous westerly winds correlate with maximum temperature over southern Australia; strong positive relationship with anomalous westerly wind in September changes to insignificant or negative in October and November (Fig. 3-12). There is also an increase in negative correlation between maximum temperatures and anomalous northerly winds in north-eastern Australia (Fig. 3-12 d-e) that will partly offset the increasing positive relationship further south. These changing relationships between dynamical mechanisms and maximum temperature through spring are linked with the changing relationships with the circulation features (Table 3-1) through spring. Overall, however, the three dynamical heat mechanisms explain much of Australia's monthly spring maximum temperature variability.

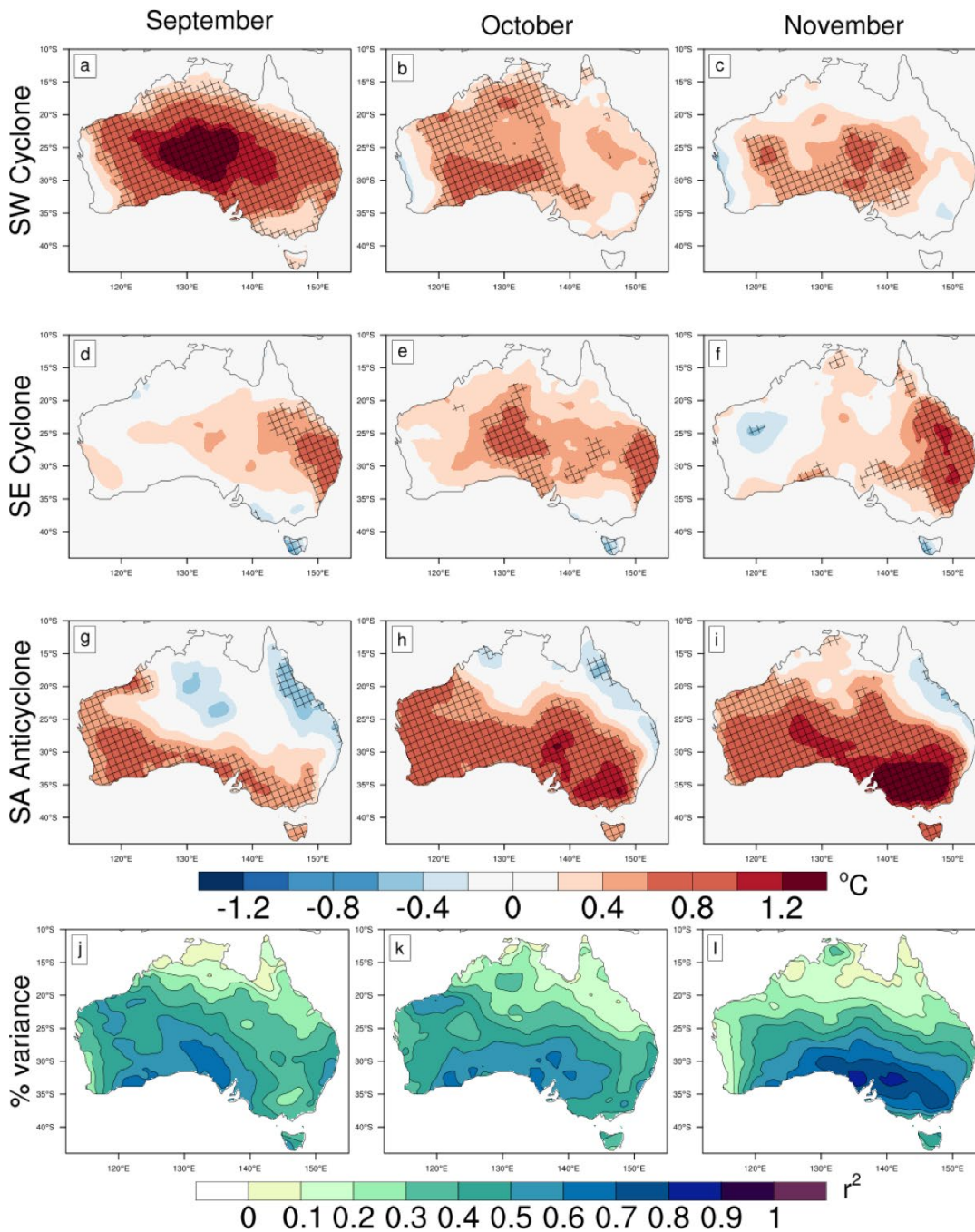


**Figure 3-11 MLR of circulation features onto Australian maximum temperature**  
 Multi-linear regression coefficients of standardised indices southwest-cyclone, southeast cyclone and southern Australian anticyclone onto Australian maximum temperatures calculated over 1979 to 2019 for September, October and November (a-i) and percent Australian maximum temperature variance explained ( $r^2$ ) by SWC, SEC and SAA (j-l). Anomalies are relative to a 1981 to 2010 climatology. All variables were detrended, and the weighted area-averaged maximum temperature time series was standardised before regression. Hashing shows where the regression was statistically significant at the 95% confidence level using a two-sided Student's *t*-test with 39 independent samples.

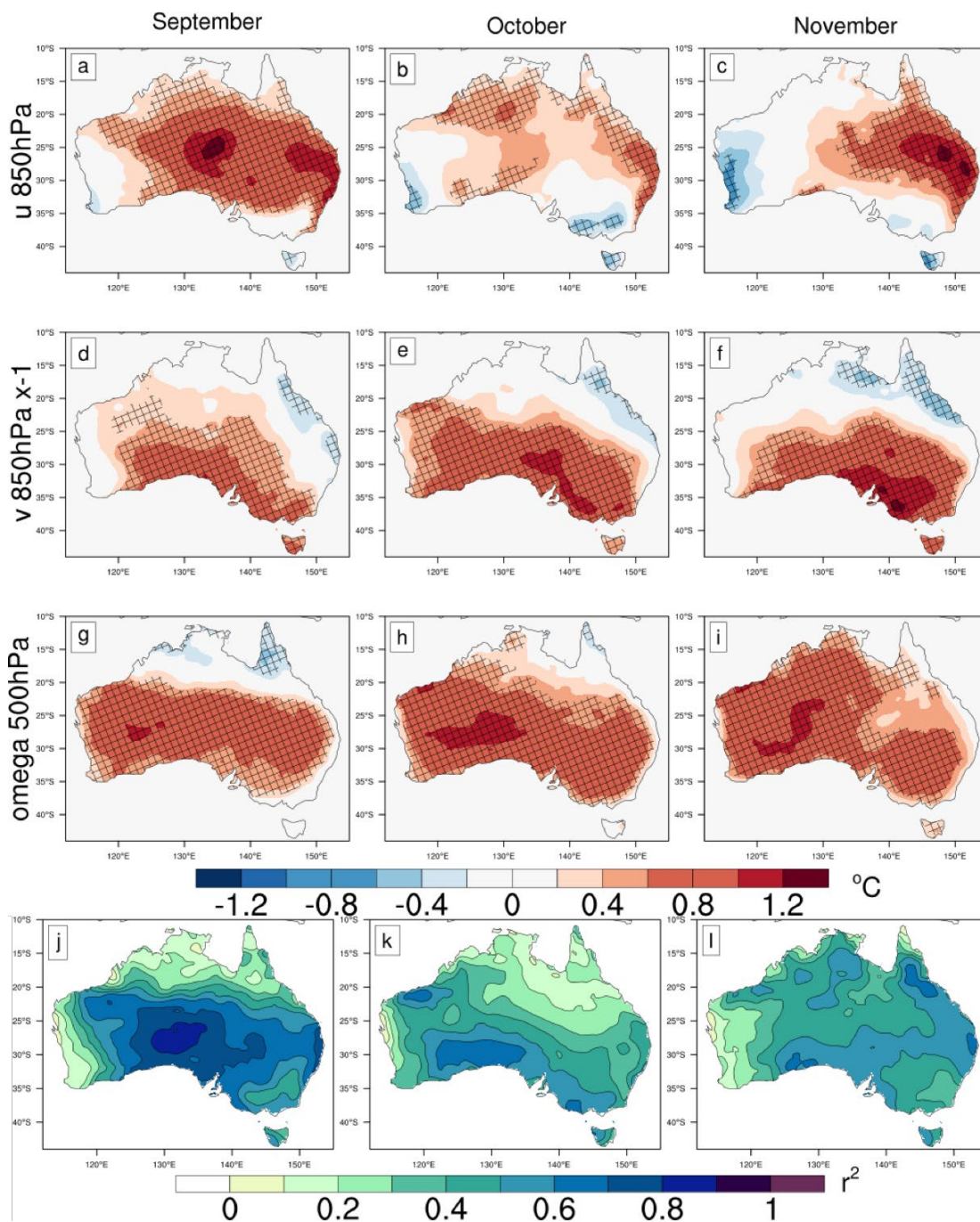


**Figure 3-12 As with Fig. 3-11, but regressed onto dynamical heat mechanisms**

Southern Australian-averaged 850hPa horizontal wind ( $u_{850hPa}$ ), and meridional wind ( $v_{850hPa}$ ) anomalies, multiplied by negative 1) and anomalous subtropical Australian sinking motion ( $\omega_{500hPa}$ ).

Figure 3-13 summarises the relationship between Australian maximum temperatures, circulation features, dynamical heat mechanisms and climate drivers through the spring months. The correlation between the SEC and Australian maximum temperature is strongest in September and rapidly decreases through October and November, while simultaneously the correlations with the SWC and particularly the SAA increase. As expected from Fig. 3-4, the SEC and SWC are more closely linked with the extratropics. Linearly regressing out the SAM component from time series of the SWC and SEC reduces the correlation strength

with Australian maximum temperature (Fig. 3-8a), particularly in September. Conversely, linearly removing the tropical TPI slightly increases the correlation between the cyclones and temperature, with the partial-correlation only weakening in November. As SAM is strongly related to the barotropic cyclones it is also strongly related to how temperature changes with the westerly wind. Linearly removing SAM from the westerly wind time series nearly halves the correlation with maximum temperature in September, and weakens the correlation in October and November (Fig. 3-13b). Conversely, linearly removing the tropical TPI actually increases the correlation slightly with the westerly wind in September and October, but decreases the correlation in November.

The relationships with anomalous northerly wind and sinking motion and Australian-averaged maximum temperature do not change as dramatically with the removal of SAM or the TPI. Northerly wind is not strongly influenced by the tropics or extratropics in September or October, but the correlation strengthens and weakens in November with the removal of the TPI and SAM, respectively. While removing SAM and TPI from the SAA had relatively little influence on the correlation with Australian maximum temperatures, removing SAM from sinking motion in September and both TPI and SAM in October and November reduced the correlation. Overall, it appears that the heat mechanisms associated with high maximum temperatures in spring are influenced differently by the different influence of the extratropics and tropics on the local atmospheric circulation features through spring.

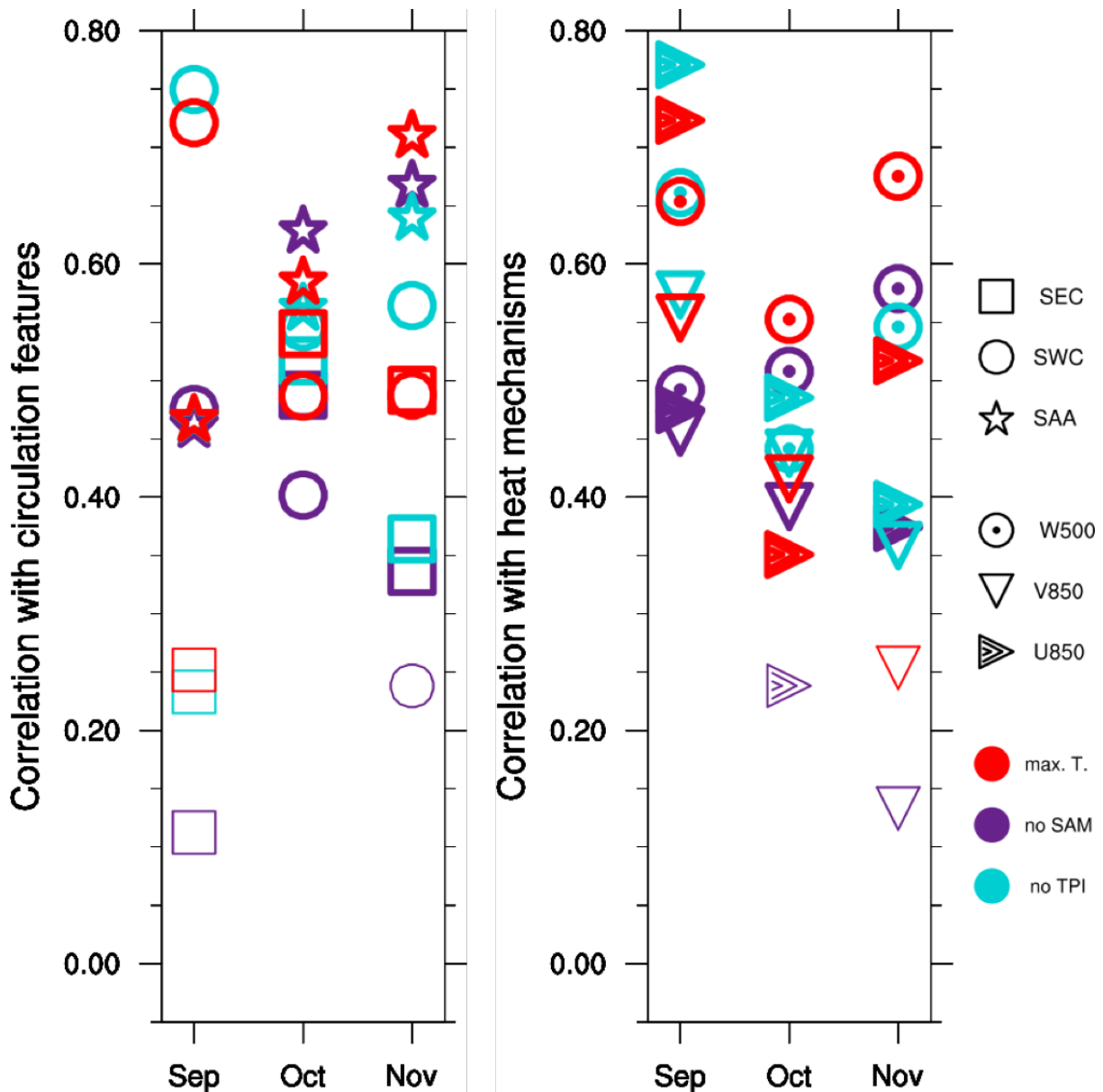


**Figure 3-13 Monthly correlations between circulation features and heat mechanisms**  
 Correlations between Australian area-averaged maximum temperature (red) between key atmospheric circulation features (left figure) and dynamical heat mechanisms (right figure) for September, October and November. The purple and turquoise show partial correlations of the same, but with SAM and the tropical TPI linearly removed. Bold lines show the correlation was statistically significant at the 95% confidence level using a Student's *t*-test with 39 samples.

### 3.5 Discussion and conclusions

The sources of the atmospheric circulation pattern associated with high monthly-maximum temperatures in Australia appear to change from primarily extratropical in early spring to tropical forcing in late spring. Examination of three dynamical heat mechanisms (anomalous low-level winds broken into westerly and northerly components, and anomalous mid-tropospheric sinking motion) indicates that this shift may be due to a change in how heat develops. In early spring, the low-level wind plays a greater role in maximum temperatures, advecting relatively warmer air from the oceans over the cold land-mass. This wind

correlates strongly with the extratropics (here, SAM) as SAM projects strongly onto the southwest and southeast cyclones that direct a lot of the low-level flow around Australia. Conversely, the atmospheric circulation associated with the TPI ( $x-1$ ) acts to counter the low-level flow that drives higher temperatures. Thus, in early spring we have a closer association with heat production and the extratropics. By late spring, the circulation patterns associated with high temperature have changed and the wind does not correlate as strongly. As such adiabatic sinking over subtropical Australia has a proportionally stronger correlation with high temperatures. Both SAM and TPI ( $x-1$ ) regressions show sinking motion in the subtropics through spring, but it is the TPI that better matches the sinking motion over eastern Australia in November. Hence, the apparent change from extratropical to tropical forcing in the circulation pattern is because the tropics promotes more of the heat developing mechanisms later in spring. However, much of the atmospheric patterns associated with heat through spring are explained by neither the tropical TPI nor SAM.

The subtropical jet appears to play a greater role in Australian spring heat by acting as a wave guide (Hoskins and Ambrizzi, 1993) that directs quasi-stationary Rossby waves toward Australia, rather than as a block that limits direct propagation of Rossby waves from the tropical Indian Ocean to the southern hemisphere extratropics (e.g. Simpkins et al., 2014; Li et al., 2015 a,b). While wave activity flux only appears to indicate wave propagation occurs directly out of the tropical Indian Ocean later in spring, this analysis does not suggest that the tropical Indian Ocean is not a wave source in early spring. Indeed, the results are broadly consistent with IOD-forced wave trains identified in the literature (Cai et al., 2011; McIntosh and Hendon, 2018; Wang et al., 2019). In particular, the secondary wave source in the high latitudes of the Indian Ocean proposed by McIntosh and Hendon (2018) may be key for promoting the TPI-forced atmospheric circulation in early spring, though this is beyond the scope of this study to confirm. As the subtropical jet did not act as a barrier preventing the tropical Indian Ocean's influence on Australia's maximum temperature, we argue instead that the apparent change in forcing through spring was more related to the origins of three of the dynamical heat mechanisms behind that heat. Consistent with this idea, wave activity flux calculated by first regressing 200Z onto the three dynamical heat mechanisms (Fig. 3-14) also indicates waves change extratropical or tropical forcing through spring, that then propagates along the jet wave guide toward Australia.

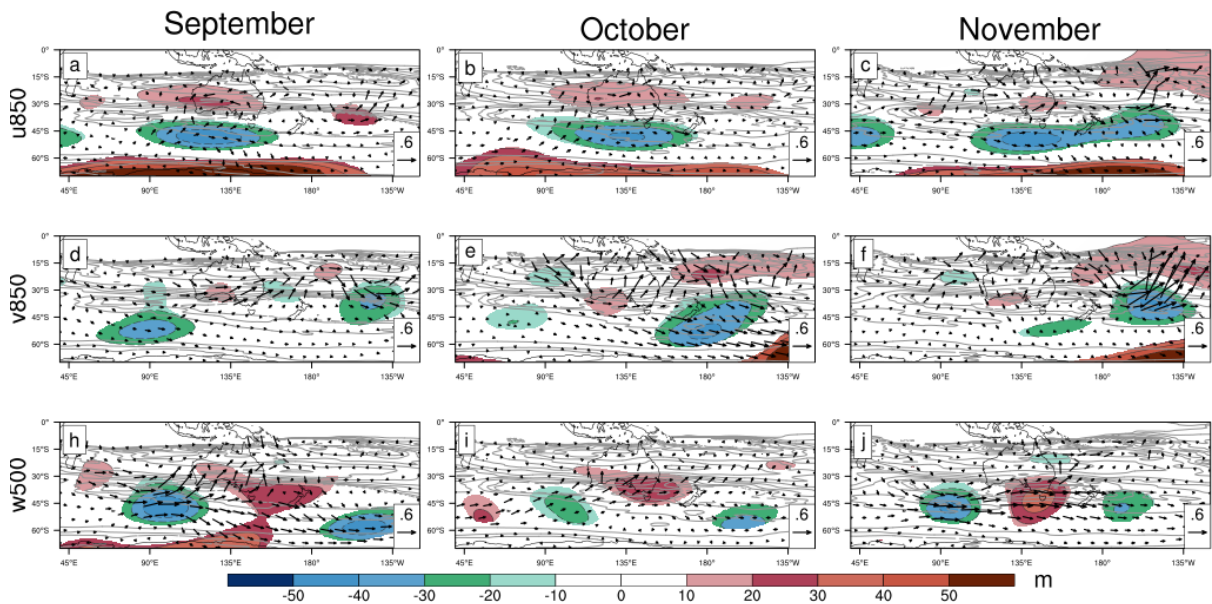


**Figure 3-14 Upper-level circulation regressions onto dynamical heat mechanisms**

*Linear regressions of standardised time series of the three dynamical heat mechanisms (anomalous low-level zonal and meridional wind, and sinking motion) onto upper-level circulation (200hPa geopotential height (filled contours) and wave activity flux vectors ( $m^2s^{-2}$ )). The grey contours show the monthly climatological total wave number (repeated from Fig. 3-7). Only 200hPa geopotential height regression coefficients that were statistically significant at the 95% confidence level (calculated using a Student's t-test with 39 samples) are shown.*

Area-averaged anomalous low-level wind and vertical motion were used to understand how the atmospheric circulation relates to Australia-wide maximum temperatures, but do not form a complete picture of spring temperature development in Australia. Statistical models using these mechanisms explain much, but not all, of the maximum temperature variance over Australia. Further, it was not always clear how the atmospheric circulation features influenced those heat mechanisms. In particular, the southern Australian anticyclone and 500hPa subtropical-Australian sinking motion, while important for heat, appear to be largely uncorrelated with the other circulation features and mechanisms. Greater insight into how remote forcing of the atmospheric circulation results in high Australian temperatures could be gained by including other heat mechanisms in future analyses, including: insolation (Lim et al., 2019a), land-surface feedbacks linked to antecedent moisture (e.g. Arblaster et al., 2014; Hirsch and King, 2020), and changes to synoptic weather systems (Cai et al., 2011a; Hauser et al., 2020). Antecedent moisture in particular is an important area for future research. Curiously, including the preceding month's Australian-averaged rainfall as a predictor in addition to the three dynamical mechanisms only improved the statistical model of Australian maximum temperature later in spring (Fig. 3-15). How each of these mechanisms relates to the others, and geographic changes across Australia should also be considered. The combination of poleward advection of adiabatically warmed air after it descended anticyclonically over the Tasman Sea has been identified as a key mechanism for summer heatwaves in southeast Australia (e.g. Quinting and Reeder, 2017). This combination of mechanisms may generate heat through spring, particularly in the east and in

November. The connection with rising motion over southern Australia has also not been examined, and may indicate the importance of air being diabatically warmed in association with storminess just to Australia's south, before advecting and descending toward Australia. While the three dynamical heat mechanisms were simple, the complex relationships between all of the mechanisms meant that the three used in this analysis were broadly representative of a large portion of how heat develops through spring.

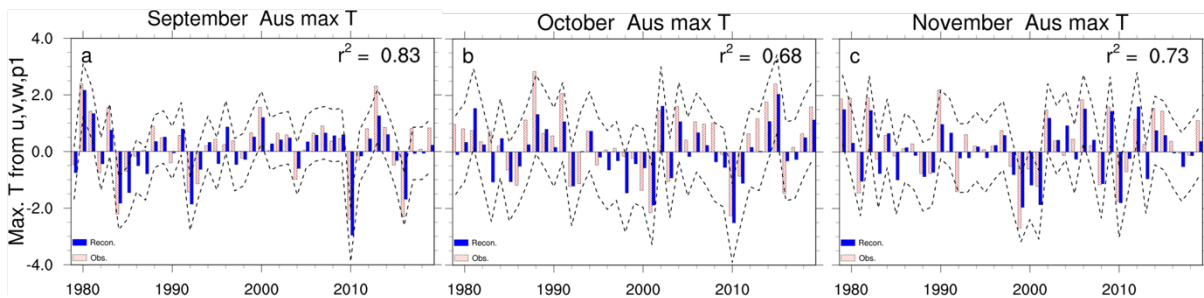


**Figure 3-15** As in Fig. 3-10 d-f but with antecedent moisture included as a predictor

*Antecedent moisture (p1) is represented by the preceding month's Australian-averaged rainfall) from AWAP.*

We used the TPI to represent tropical variability relevant to Australia's maximum temperature, but other indices or drivers may highlight different Rossby wave pathways or heat mechanisms. Reconstructing Australian maximum temperature time series with more commonly used indices for the IOD and ENSO did not change the effectiveness of the statistical models overall (not shown). However, it did suggest that the IOD had greater influence on Australia's maximum temperature in early spring than does ENSO, consistent with the seasonal-length studies of (Jones and Trewin, 2000; Saji et al., 2005). As such, we may expect different monthly Rossby wave pathways to Australia associated with the IOD in early spring, giving greater influence from the tropical Indian Ocean at this time. The MJO generates Rossby wave trains from the western Pacific that promote low minimum temperatures in Australia during winter (Wang and Hendon, 2020) and from the tropical Indian Ocean to promote high maximum temperatures in Australia in spring (personal communication: Wang and Hendon, 2021). The positive phase of the IOD suppresses MJO activity across the Indian Ocean (Wilson et al., 2013), possibly restricting the MJO's influence on Australia's maximum temperature at such times. However, MJO activity in the tropical Indian Ocean has recently been found to counter the wetting influence of La Niña during spring (Lim et al., 2021c). As such the MJO may be an important factor for spring maximum temperatures when the tropical SSTs are not otherwise conducive for high temperatures, but is beyond the scope of this study.

As the trend toward higher Australian spring temperatures is projected to continue into the future a better understanding of what drives maximum temperatures over the months of spring is critical for better prediction and better preparation to adapt to a warming climate. A combination of extreme values in

remote drivers of variability, including extreme positive IOD, central-Pacific El Niño, and sustained negative SAM associated with very strong sudden stratospheric warming, exacerbated already dry and hot conditions in spring 2019 to promote one of Australia's deadliest fire seasons (Watterson, 2020; Lim et al., 2021a; Abram et al., 2021, Marshall et al. 2021b). Further, projected trends toward positive IOD (Cai et al., 2014c; Abram et al., 2020) or toward negative TPI (Timbal and Hendon, 2011) may contribute to higher maximum temperatures in the future, particularly in later spring when the tropics exert greater influence on Australia's dynamical heat mechanisms. As we have shown just how different the atmospheric circulation and heat mechanisms can be through a season in Australia, other regions and seasons could also benefit from similar analysis, particular as the world continues to warm (e.g. Collins, et al., 2013).

## 4. Tropical Indian Ocean Influence on Australian Spring Circulation and Maximum Temperatures in Numerical Dynamical Forecast Models

### 4.1 Introduction

The previous chapters explored Australian spring (SON) temperatures on month to three-month time scales and identified several drivers, atmospheric circulation features, and mechanisms that contribute to anomalously high temperatures through spring. The remote modes of variability, El Niño Southern Oscillation (ENSO), positive Indian Ocean Dipole (IOD), negative Southern Annular Mode (SAM), phases 2 and 3 of the Madden Julian Oscillation (MJO) have been linked with hotter and drier spring conditions in Australia consistent with the earlier literature (e.g. Nicholls et al., 1997; Power et al., 1999; Jones & Trewin, 2000; Saji et al., 2005; Hendon et al., 2007; Meyers et al., 2007; Risbey et al., 2009a; Wheeler et al., 2009; Marshall et al., 2012; Min et al., 2013; White et al., 2014; Watterson, 2020; as detailed in earlier chapters). In both the literature and the earlier chapters, the atmospheric circulation driven by tropical Indian Ocean variability appears to be an important factor in Australian spring maximum temperatures. This chapter aims to quantify just how important the tropical Indian Ocean is to Australia's spring climate by addressing the third research question: What is the influence of the tropical Indian Ocean SSTs on Australian maximum spring temperature development?

Isolating the role of the tropical Indian Ocean in Australia's spring maximum temperature variability is non-trivial. The dipole mode index (DMI) of the IOD (Saji et al., 1999), used here to represent the tropical Indian Ocean SST variability, has previously been found to promote Rossby wave teleconnections that influence Australia's spring rainfall (e.g. Cai et al., 2011a; McIntosh & Hendon, 2018) and temperature (e.g. Saji et al., 2005). However, ENSO co-varies strongly with the IOD in spring, (Meyers et al., 2007; Risbey et al., 2009a; Min et al., 2013). As such, it is difficult to separate the independent contributions of the tropical Indian Ocean to Australia's spring climate from those of the tropical Pacific Ocean, particularly in observations. A commonly used method, and one used in the previous chapter, is to statistically remove the observed ENSO time series from the IOD through partial linear regression (e.g. Cai et al., 2011a). However, this method may overly penalise the IOD (or similarly, ENSO) as it removes components of the IOD that are independent from, but vary by coincidence with, ENSO variability (e.g. Cai et al., 2011a; Liguori et al., in review). To further complicate matters, all tropical ocean basins interact and feedback on each other, promoting and sustaining global teleconnections as a result (Li, X. et al., 2016; Cai et al., 2019). As such, the independent contributions of the tropical Indian Ocean to Australia's climate could be masked by variability in the other oceans, or mistakenly attributed to the tropical Indian Ocean when other ocean regions play a more significant role.

Modelling studies of various types are often used to separate the role of tropical Indian Ocean variability in the global climate from that of the other ocean basins. Stochastic models forced entirely by ENSO variability downplay the importance of the tropical Indian Ocean as they replicate much of the observed IOD variability (Dommenget & Jansen, 2009; Stuecker et al., 2017; Zhao et al., 2019; Liguori, et al., in review). However, these models often fail to predict IOD events in the absence of strong ENSO forcing, so some component of the tropical Indian Ocean is likely internally driven (Stuecker et al., 2017), and may play a role in the global climate. Further, general circulation model (GCM) simulations of ENSO and its teleconnections are often improved if realistically varying Indian Ocean conditions are included. This improvement implies that the tropical Indian Ocean feeds back onto the Pacific, increasing its importance to global climate variability (Yu et al., 2002; Wu & Kirtman, 2004; Wang, H. et al., 2019). These improvements are particularly evident if the IOD event is extreme (Luo et al., 2010), or if conditions in the Pacific Ocean are otherwise unfavourable for ENSO development (Lim & Hendon, 2017). Other modelling studies have highlighted the role of the tropical Indian Ocean in mitigating and modulating the impacts of anthropogenic warming to atmospheric teleconnections (Luo et al., 2012; Wang, H. et al., 2019; Dhame et al., 2020). Overall, dynamical modelling studies suggest that the tropical Indian Ocean plays some important part of the global climate.

Dynamical models also allow us to ‘physically’ remove competing ocean basin’s influence on the climate from that of the tropical Indian Ocean (e.g. Liguori et al., in review). However, uncertainty remains in how strong a role the latter plays in Australia’s spring-season climate. Differences in experiment design, models, and model biases result in conflicting estimates of whether the tropical Indian Ocean plays an important (e.g. Dhame et al., 2020) or lesser (e.g. Liguori et al., in review) role in Australia’s and the globe’s climate. Regardless of these conflicting outcomes, dynamical modelling can progress our understanding of the relative role of the Indian Ocean SST variability on Australia’s spring climate beyond what is possible using observations alone.

Indian Ocean model biases in particular contribute to the difficulties in isolating the relative role of the tropical Indian Ocean on Australia’s spring maximum temperatures. CMIP5 and CMIP6 models tend to overestimate IOD magnitude and its impacts and poorly simulate the ENSO-IOD relationship (e.g. Cai & Cowan, 2013; Li, G. et al., 2015; 2016; McKenna et al., 2020). While IOD simulation biases persist into models configured for seasonal prediction (e.g. Shi et al., 2012; Liu et al., 2017), these models have the advantage of relatively short run times that can limit the divergence from initial conditions that are strongly constrained by ocean, atmosphere and land observations (e.g. Wang et al., 2021). Further, the peak in IOD strength during spring corresponds to a peak in potential IOD predictability and forecast skill (Liu et al., 2017; Zhao et al., 2019), such that seasonal prediction models are well suited for understanding the relative role of the tropical Indian Ocean in spring. However, IOD predictability may be limited by how seasonal

prediction models simulate the west and east poles of the DMI. The western region of the tropical Indian Ocean is largely driven by an ENSO-atmospheric bridge mechanism, whereas, the eastern IOD pole appears more driven by internal Indian Ocean dynamics (Zhao & Hendon, 2009; Shi et al., 2012; Sooraj et al., 2012; Lee et al., in review). Regardless, as model biases will restrict any study, the benefits offered by seasonal prediction models make them more appropriate for understanding the relative influence of the tropical Indian Ocean on Australia's spring maximum temperatures.

We primarily use the seasonal prediction system POAMA, as introduced in section 1.5, in this chapter. POAMA simulates the IOD variability well, despite its relatively coarse resolution (Shi et al., 2012), and has good IOD prediction skill at up to three month's lead time (Zhao & Hendon, 2009). However, in contrast to most models, POAMA underestimates the magnitude of the IOD (Zhao & Hendon, 2009) and tends to underestimate the teleconnection from the IOD in favour of ENSO (White et al., 2014; chapter 2). These biases may be associated with poor simulation of Indian monsoon trough strength (Deoras et al., 2021) or because of a cold sea surface temperature (SST) bias in the tropical Indian and west-to-central tropical Pacific Oceans (Lim et al., 2009). However, experiments using POAMA have successfully explored the impact of rising carbon dioxide on observed extreme climate events (e.g. Hope et al., 2016; 2018; Wang et al., 2021); compared the roles of land, SST, and atmosphere in the observed heat of September 2013 (Arblaster et al., 2014); and explored the sensitivity to altered ocean initial conditions (Zhao et al., 2016; Lim & Hendon, 2015; Lim et al., 2017, 2019). POAMA has also been run with ocean initial conditions set to the 2016 negative IOD event to isolate its role from internal tropical Pacific variability in the development of the weak 2016 La Niña (Lim & Hendon, 2017). Overall, POAMA has demonstrated use as a model for experimentation and for IOD prediction, making it appropriate for understanding the relative contributions of the tropical Indian Ocean on Australia's spring maximum temperatures.

Given the difficulties associated with using both observations and models in isolating the relative role of the tropical Indian Ocean in Australian maximum temperatures we use seasonal prediction models across three complementary approaches to address the final research question. In chapter 2 we noted that POAMA has a strong reliance on tropical Pacific Ocean variability. As such, we start by comparing the POAMA hindcast relationships with the IOD with those in the hindcasts of three additional models downloaded from the Subseasonal to Seasonal (S2S) database (Vitart et al., 2017) (section 4.3.1). As strong tropical forcing can lead to stronger predictability (e.g. Kumar et al., 2013; Liu et al., 2017), we next run experiments using POAMA with increased IOD magnitude to identify the influence that event strength has on southern hemisphere teleconnections (section 4.3.2). Finally, we run an additional set of experiments using POAMA with ocean variability isolated to specific domains across the Indian, Pacific and Southern Oceans (section 4.3.3).

While our aim is to understand the relative role of the tropical Indian Ocean in Australia's climate compared to all global oceans, the strong co-variability between the IOD and ENSO remains a key issue. As such, while it is not the sole relationship discussed in this chapter, we focus primarily on untangling the ENSO-IOD relationship through each approach.

The remainder of this chapter is structured as follows: We give a description of the datasets and common analysis methods in section 4.2. The results in section three are broken into three parts, each with a detailed description of the section-specific methods, results and a discussion. The chapter concludes in section four with a discussion that synthesises the results.

## 4.2 Datasets and methods overview

This section describes the models, reanalysis datasets, and variables used in the results sections of this chapter.

### 4.2.1 Observational data

We focus on the response to changes in the ocean to atmospheric teleconnections and consequent Australian spring maximum temperature. Atmospheric circulation is represented by mean-sea level pressure (MSLP) and 200hPa geopotential height (Z200). As spring maximum temperatures and precipitation are strongly correlated (e.g. Hope & Watterson, 2018) we also look at the spring-averaged daily precipitation for greater insight, and to contrast with previous studies.

We use September-October-November monthly averaged MSLP and Z200 data from ECMWF's Reanalysis 5 (ERA5) (Hersbach et al., 2021) available from the Copernicus Climate Change Service (C3S, 2017) on a 0.25° grid to represent the observed atmospheric circulation.

Australian spring maximum temperature and precipitation are calculated from monthly-averaged maximum temperature and monthly-total precipitation data from the Australian Water Availability Project (AWAP; Jones et al., 2009), on a 0.05° resolution grid. The spring-total precipitation data (mm) was divided by 91 days (mm/day) for easier comparison with the POAMA output. Sea surface temperature data from Reynolds Optimum-Interpolation dataset (Reynolds et al., 2002) are used to calculate indices of tropical variability.

Variability in the tropical Indian Ocean is represented by the IOD as described by the dipole mode index (DMI: the difference between the SST anomalies averaged in the west-pole: 10°S-10°N, 50°-70°E, and east-

pole: 10°S-0°, 90°-110°E; Saji et al., 1999). Tropical variability in the Pacific is represented by ENSO and described using the Niño3.4 index (averaged SST anomalies over 5°N-5°S, 170°E-120°W).

All reanalysis anomalies are calculated against a 1981-2010 climatology period.

#### 4.2.2 Subseasonal-to-seasonal (S2S) models

For comparison with the POAMA data, hindcasts of MSLP, Z200, SST, and maximum temperature and precipitation data from three other seasonal prediction models were downloaded from the Subseasonal to Seasonal (S2S) Prediction Project Database (Vitart et al., 2017; <https://apps.ecmwf.int/datasets/>). The S2S database includes hindcasts from 11 different centres, each with different forecast lengths (up to 60 days), hindcast period, horizontal resolution, ensemble size, forecast frequency, atmosphere-ocean coupling, and initialisation methods. We chose three of the available S2S models based on two criteria:

1. Minimum hindcast length (60 days) to reconstruct spring month forecasts with a one-month leadtime (described in section 4.2.4 below), and
2. Maximum number of IOD events in the models' hindcast periods common to the POAMA experiments (table 4-3).

We also briefly compare with the recently updated version of the Australian Bureau of Meteorology's new seasonal prediction system: ACCESS-S2 (Hudson et al., 2017; see also <http://www.bom.gov.au/research/projects/ACCESS-S/>).

Refer to table 4-1 for an overview of the S2S, POAMA, and ACCESS-S2 models used in this study.

The three S2S models used in this study are the HMCR (Hydrometeorological Centre of Russia), KMA (Korea Meteorological Administration) and United Kingdom Met Office (UKMO) models.

The HMCR model (Tolsykh et al 2010 a [Russian]); see <https://confluence.ecmwf.int/display/S2S/HMCR+model+description> for model summary) differs from the other models as it is not coupled to an ocean model. Instead, HMCR SSTs are initialised with observed SST conditions, with the SST anomaly slowly relaxed toward climatology (Mikhail Tolsykh; personal communication). The HMCR has the longest hindcast (1985 – 2010) and has been shown to have reasonable subseasonal prediction of atmospheric variables in both the Northern and Southern Hemispheres (Tolstykh et al., 2010b).

The KMA and UKMO models are based on different versions of the UK seasonal prediction system, GloSea. The KMA is based on GLoSea5 (MacLachlan et al., 2015; see Won et al, (2015) for KMA implementation and <https://confluence.ecmwf.int/display/S2S/KMA+model+description> for details), which has improved sub-

seasonal forecasting skill (Machlachlan et al., 2015) and improved model physics over the previous versions (Walters et al., 2017). The KMA model has the shortest hindcast period (1990 to 2010). The UKMO (see <https://confluence.ecmwf.int/display/S2S/UKMO+model+description>) hindcast covers 1993 to 2016 and is based on GloSea6. GloSea6 is similar to the previous generation of GloSea with an upgraded version of the Global Coupled Atmosphere Model (GC3.2 instead of GC2), that has been shown to improve simulation of the tropospheric and stratospheric temperature structure and significantly reduce warm SST bias in the Southern Ocean (Walters et al., 2017).

We also make brief comparisons in the section 4.3.3 with SST variability ACCESS-S2, the recent upgrade to the Bureau of Meteorology's seasonal prediction system that has an extended hindcast, compared to ACCESS-S1 (Hudson et. al., 2017), from 1981 to 2018. ACCESS-S2 is based on the same GloSea family as the KMA and UKMO models.

All S2S anomalies are calculated against a climatology over each respective hindcast period, as listed in Table 1, aside from ACCESS-S2 which are relative to a 1981-2010 climatology period.

#### 4.2.3 POAMA system (version A)

As in chapter 2, much of this chapter focuses on the use of POAMA (version 2) (Cottrill et al., 2013; Hudson et al., 2013). POAMA is described in detail in this chapter to provide the background necessary to understand the experimental results.

Recall that POAMA is composed of three sub-versions (A, B, and C). For experiments we are limited to version A, which has no flux correction (Cottrill et al., 2013).

The atmospheric component of POAMA 2 is the BoM Atmospheric Model version 3 (BAM3; Colman et al., 2005) and has triangular truncation resolution T47 (about 250km) at 17 vertical levels. The land-surface scheme is a simple bucket model for soil moisture with three levels (Manabe and Holloway 1975; Hudson et al., 2011). The ocean model component is the Australian Community Ocean Model version 2 (ACOM; Schiller et al. 2002) with 25 levels and zonal resolution of 2° and meridional resolution ranging from 0.5° at the equator to 1.5° at the poles. The atmosphere and ocean models are coupled by the Ocean Atmosphere Sea Ice Soil (OASIS) software (Valcke et al., 2000). The sea-ice extent and atmospheric ozone levels are prescribed to their seasonal climatological cycle, while the default carbon dioxide level is set at 345ppm. Refer to summary in table 4-1).

We compare the experiment results against version A of the POAMA ensemble-mean hindcast.

All POAMA experiments and ensemble-mean anomalies are calculated against a 1981-2010 climatology period.

#### 4.2.4 Reconstructed and seasonal forecasts of spring

The aim of this chapter is to highlight the role of the oceans in Australia's spring maximum temperature across the different forecast models. As such, we analyse forecasts at a one-month lead time to allow for the memory of the atmospheric initial conditions to lapse, while the ocean conditions are likely to persist (Lim and Hendon, 2015; Park et al., 2017; Vitart et al., 2017).

Further, we know from the previous chapter that the months of spring vary both in temperature mechanisms and tropical or extratropical ocean forcing, and we want to include ocean initial conditions that capture this progression through spring. As such, we reconstruct spring forecasts (in 4.3.1 and 4.3.2) using forecasts for each individual month in spring (e.g. Kumar et al., 2013). Specifically, we average three one-month forecasts that were initialised nearest available dates of August 1 for the month of September, September 1 for October, and October 1 for November. All but the HMCR model were initialised on the first of each month. The HMCR hindcasts of September and October were initialised earlier (30<sup>th</sup> of July and 27<sup>th</sup> of August respectively), resulting in slightly shorter months, however, this is not expected to significantly impact the HMCR results.

In contrast, we use a seasonal spring forecast in section 4.3.3, which is the August 1 forecast for the September-October-November period.

	Model Version	Hindcast range	Hindcast period	Initialisation dates	Atmospheric Resolution	Ocean Resolution	Sea-ice	Ensemble size	Land-surface	Initial conditions
<b>UKMO</b>	GloSea6 – GC3.2	60 days	1993 – 2016	Aug-01 Sep-01 Oct-01	N216 L85 (0.83° x 0.56°)	0.25° L75 (NEMO ocean model)	Global Sea Ice 8.1: CICE 5.1.2	7	JULES <sup>1</sup>	ERA-Interim <sup>2</sup> and NEMOVAR <sup>3</sup>
<b>HMCR</b>	RUMS	61 days	1990 – 2015	Jul-30 Aug-27 Oct-01	L28 (1.1°x1.4°)	N/A (not coupled)	Persistence and climatology	10	Not perturbed	Quasi-assimilation of ERA-Interim <sup>2</sup>
<b>KMA</b>	GloSea5 – GC2	60 days	1991 – 2010	Aug-01 Sep-01 Oct-01	N216 L85 (0.83° x 0.56°)	0.25° L75 (NEMO ocean model)	Global Sea Ice 8.1: CICE 5.1.2	3	JULES <sup>1</sup>	ERA-Interim <sup>2</sup> and NEMOVAR <sup>3</sup>
<b>POAMA</b>	P24A	5 months	1981 – 2013	Aug-01 Sep-01 Oct-01	T47 (~250km)	2° zonal 0.5° meridional	Climatology	11	3-level bucket	ERA-Interim <sup>2</sup> and PEODAS
<b>ACCESS-S2</b>	GloSea5-GC2	5 months	1981 - 2018	Aug-01 Sep-01 Oct-01	N216 (~60km)	0.25°	Global Sea Ice 8.1: CICE 5.1.2	3	JULES <sup>1</sup>	ERA-Interim and NEMOVAR <sup>3</sup>

**Table 4-1 Summary of Models**

S2S model data (Vitart et al., 2017) adapted from <https://confluence.ecmwf.int/display/S2S/Models>, with additional information about the POAMA (version A) from (Cottrill et al., 2013; Hudson et al., 2013) and ACCESS-S2 (Hudson et al., 2017)

Note: The HMCR, UKMO and KMA hindcasts were produced at the same time as the real-time forecasts. Hindcast versions are all from 2020. BoM and ACCESS-S2 hindcasts are produced once during the lifetime of a given model version.

1. Best et al. (2011) 2. Dee et al. (2011) 3. Mogensen et al. (2009)

### 4.3 S2S hindcast tropical Indian Ocean relationships

We start by exploring the relationship between the IOD and the atmosphere, and Australia's spring climate across the different S2S models.

#### 4.3.1 Regression analysis

We use linear regression analysis to understand how the S2S models simulate the relative influence of the tropical Indian Ocean on the spring atmospheric circulation, and Australian maximum temperature and precipitation response. Reconstructed lead-1 spring SST, MSLP, Z200, Australian maximum temperature and precipitation fields are first calculated over each hindcast. Time series of DMI and Niño3.4 are then calculated over each model's hindcast period. Linear regression and partial linear regression (with an estimate of the influence of the ENSO linearly removed) are calculated onto each of the atmospheric and land variables over the years available in each of the models and reanalysis.

Due to the limited hindcast periods of the S2S models we estimate the regressions and 90% statistical significance level in the models with bootstrapping using 1000 samples, rather than a t-test used in other sections and in the reanalysis comparison.

Values presented are for the ensemble-mean of each model.

All variables are linearly detrended before analysis and DMI and Niño3.4 time series are standardised before calculating the regressions.

#### 4.3.2 Comparison with reanalysis

We start by revisiting the spring relationship between the IOD and the atmospheric circulation, with and without ENSO's influence in reanalysis (Fig. 4-1). The linear regression with the spring DMI (Fig. 4-1a,b) is repeated from the previous chapter to more easily compare it to the regression with DMI when the Niño3.4 time series is linearly removed (Fig. 4-1c,d). Positive IOD and El Niño are associated with positive values of the DMI and Niño3.4 indices respectively. As such, these regressions indicate positive IOD-like responses to DMI SSTs, albeit assuming linearity. Without ENSO's influence, the atmospheric circulation near and west of Australia weakens and loses some statistical significance but, generally, there are few geographic changes. The barotropic cyclones southwest and southeast of Australia remain, as does the cyclone to Australia's northwest. However, the barotropic anticyclone south of Australia shifts further poleward relative to the full regression, and the high MSLP over Australia vanishes. A Pacific South American (PSA)-like pattern (a wave-train that arcs poleward from anomalous height in the tropical Pacific Ocean to the

southeast cyclone to curve toward South America) is absent with ENSO's removal, as expected (e.g. Karoly, 1989; Irving & Simmonds, 2016).

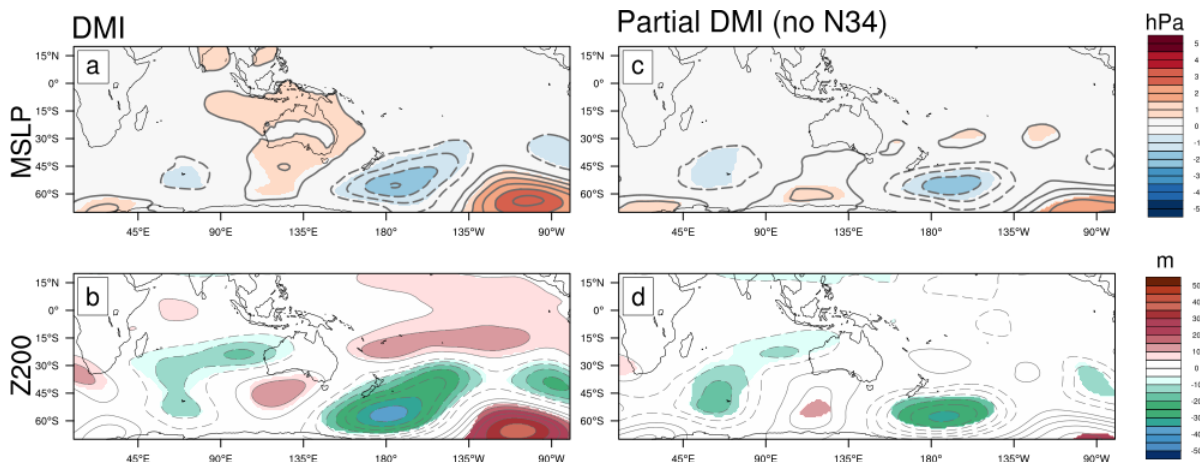


**Figure 4-1 Observed (ERA5) spring relationship between the IOD and partial IOD to the atmospheric circulation**

Mean-sea level pressure (MSLP in hPa; a,c) and 200hPa geopotential height (Z200 in m; b,d) linearly regressed onto the Dipole Mode Index (left column) and partial DMI (where the Niño3.4 index was first linearly removed from the time series) (right column) over the years 1981 to 2018. All fields were linearly detrended and the DMI and partial DMI time series were standardised before regressions were calculated. Anomalies were calculated against a 1981 to 2010 climatology from reanalysis data. Filled contours denote the regression was statistically significant at the 90% confidence level (to match the significance level used in model analyses) using a Student's t-test with 36 (38 years - 2) independent samples.

These circulation anomalies are consistent with previously reported teleconnection pathways from the tropical Indian Ocean. In particular, the apparent Rossby wave trains that arc from the southwest and northwest cyclones to join across Australia and propagate toward the southeast cyclone (e.g. Cai et al., 2011a; McIntosh and Hendon, 2018). We can compare these reanalysis pathways to those calculated in the model hindcasts as a measure of how well the models simulate the relationship between the tropical Indian Ocean and the atmospheric circulation.

The relationships between the observed IOD and maximum temperature and precipitation are generally consistent with earlier literature and the previous chapter (Fig. 4- 2). Anomalous high maximum temperature extends across the majority of Australia in association with the IOD, with dry conditions everywhere east of 130°S (Fig. 4- 2a,b). Removing ENSO weakens the statistical significance of the relationships, with the strongest relationships found in the southeast of Australia (Fig. 4-2c,d). The weakened relationship between both precipitation and maximum temperature contrasts with earlier findings that suggested that the IOD's influence extended to the southwest (e.g. Risbey et al., 2009a; Min et al., 2013). These different relationships may be due to the different time periods used in the regression

analysis of earlier studies. As the model hindcasts each cover different periods, there may be differences across the regressions that are unrelated to model skill.

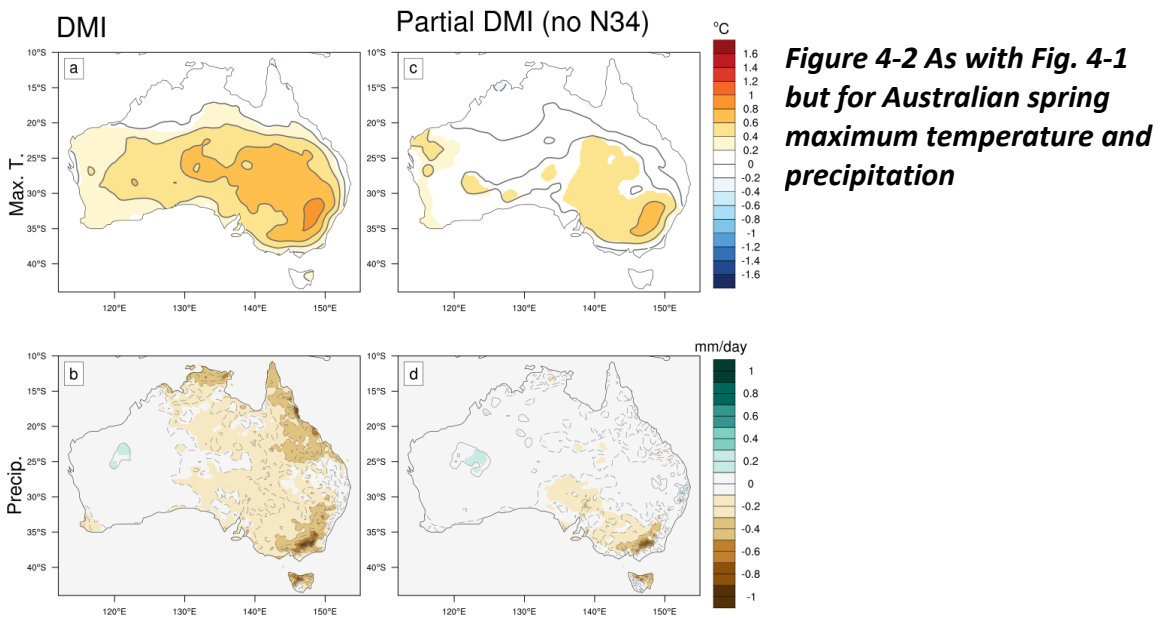


**Figure 4-2 As with Fig. 4-1 but for Australian spring maximum temperature and precipitation**

#### 4.3.3 Relationships to the IOD in the S2S Models

The S2S reconstructed spring forecasts reproduce the relationship between the DMI and atmospheric circulation with different levels of fidelity (Fig. 4- 3). While the HMCR captures the apparent wave train from upper-cyclone west of Australia to the anticyclone over southern Australia reasonably well, it does not capture the southwest low anomaly or surface pressure pattern around Australia (Fig. 4- 3a, b) found in reanalysis (Fig. 4-1a,b). Conversely, the UKMO (Fig. 4-3 c,d) captures the barotropic lows southwest and southeast of Australia, the broad high MSLP over Australia, and the apparent Rossby wave train. The KMA also broadly captures this upper-level wave train (Fig. 4- 3f), though the anticyclone over southern Australia is weak and elongated relative to both the UKMO and the reanalysis patterns. While the wavetrain in POAMA (Fig. 4- 3g,h) includes a statistically significant height anomaly over southern Australia, the MSLP and 200Z height patterns over the Indian Ocean (Fig. 4- 3g,h) do not match reanalysis. All models, except for the HMCR, simulate a PSA-like pattern, suggesting the models simulate the IOD-ENSO relationship.

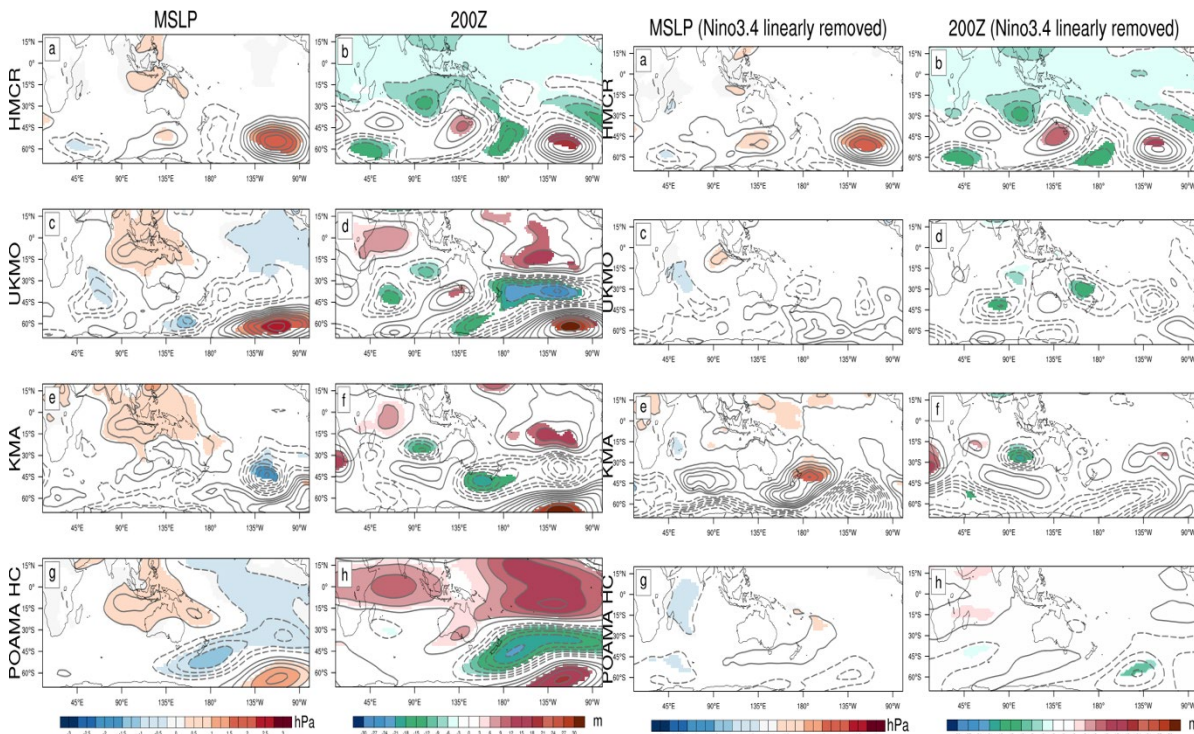


**Figure 4-4 Bootstrap estimates of linear regressions of S2S model reconstructed spring MSLP (left column; hPa) and 200hPa geopotential height (right column; m) in S2S models: HMCR (a, b); UKMO (c, d); KMA (e, f) and POAMA Hindcast (verA) (g,h). All fields were linearly detrended before calculation. Anomalies were calculated against each model's available hindcast period. Filled contours show statistical significance at the 90% confidence level calculated by bootstrapping with 1000 bootstrap samples.**

**Figure 4-4 As in Fig. 4-3, but with Niño3.4 first linearly removed.**

Despite the accurate reconstructed spring IOD regressions, linearly removing the ENSO signal from the DMI time series results in dramatically different atmospheric circulation responses in all but the HMCR model (Fig. 4-4). The lack of change between the HMCR regressions (Fig. 4-3a,b compared to Fig. 4-4a,b)), suggests only a weak ENSO-IOD relationship in this model, which is supported by relatively weak correlation between model DMI and Niño3.4 (table 4-2). This weak relationship may be the consequence of relaxing the SST anomalies toward climatology producing weaker Niño3.4 and DMI values, but contrasts with reports that the HMCR simulates the seasonal anomalies associated with ENSO well (Tolstyk et al., 2014). While removing ENSO from the DMI regressions in the other models does remove the PSA-like pattern (Fig. 4-4 c-f), the remainder of the atmospheric circulation differs from what we expected from reanalysis (Fig. 4-1c,d). In the UKMO (Fig. 4-4d) the upper-level wave train from the tropical Indian Ocean across southern Australia persists but it is much weaker and the overall pattern is distorted relative to reanalysis. In the KMA regression, the wave train is entirely absent without ENSO (Fig. 4-4f), and has anomalous high MSLP

nodes southwest and southeast of Australia instead of low MSLP (Fig. 4-4e). The differences between the UKMO and KMA regressions may reflect the improvements in GLoSea6 (UKMO) compared to GLoSea5 (KMA) (Williams et al., 2018). The partial regression over the reconstructed POAMA hindcast (Fig. 4- 4 g,h) is also far weaker than in reanalysis, consistent the findings from chapter 2. However, there is a weak upper-level wave train from the western Indian Ocean north of Madagascar that then propagates along the polar jet to Australia that was absent in the UKMO and KMA regressions.

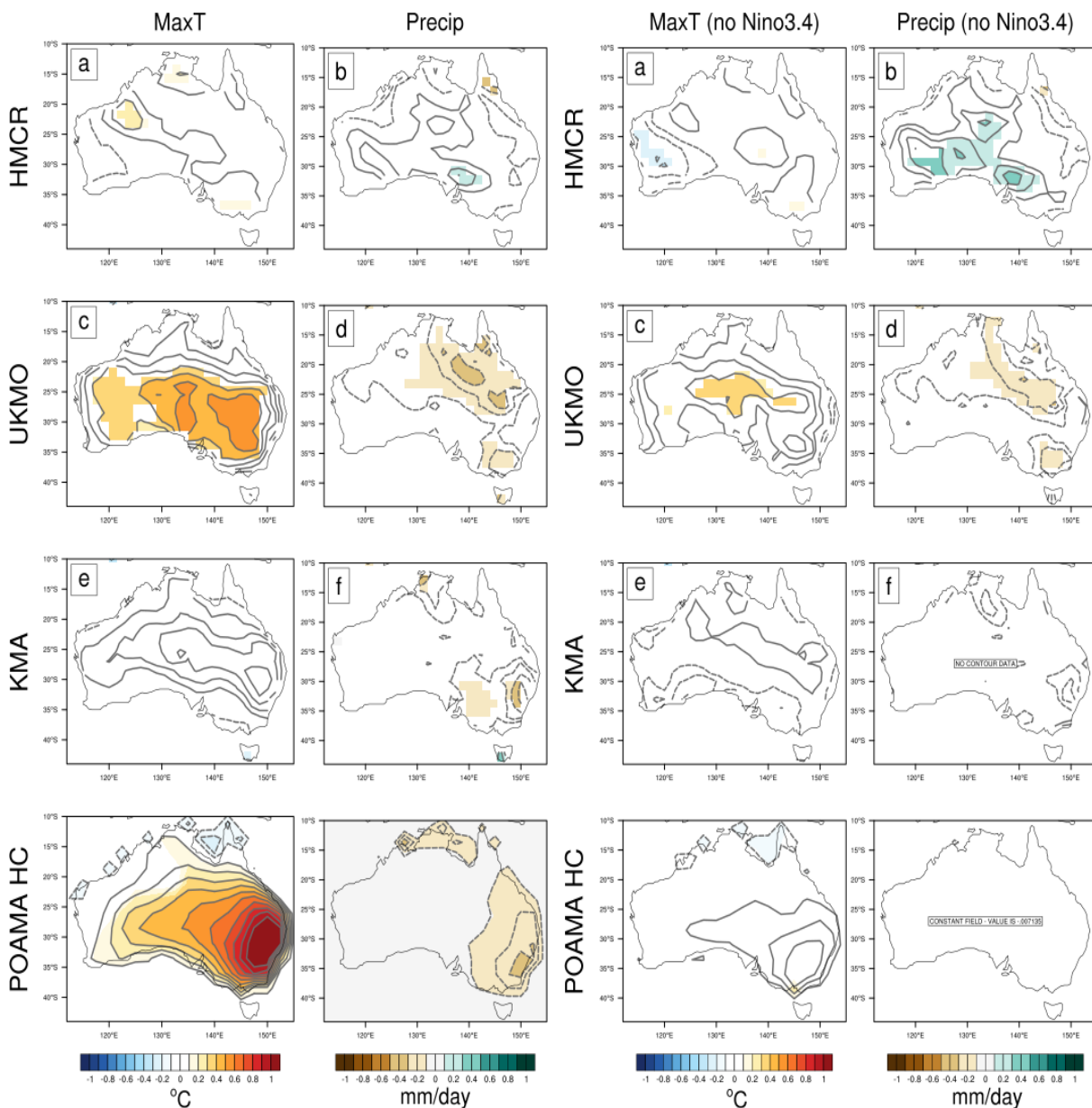


**Figure 4-6 As with Fig. 4-3 but for reconstructed spring maximum temperature (°C) and precipitation (mm/day).**

**Figure 4-6 As in Fig. 4-5, but with Niño3.4 first linearly removed.**

The reconstructed spring forecast relationships between the DMI and Australian maximum temperature and precipitation are consistent with the regressions onto the atmospheric circulation. The HMCR regression has weak warm maximum temperature anomalies but unrealistic wet precipitation anomalies

associated with the IOD (Fig. 4- 5 a,b). Neither maximum temperature nor precipitation regressions change when ENSO is removed (Fig. 4-6a,b). Broadly, the other models simulate the high temperature and low precipitation anomalies associated with positive IOD. The UKMO again performs best, with anomalous high maximum temperatures and below average rainfall across much of the Australian continent (Fig. 4-5c, d). These anomalies weaken when ENSO is removed (Fig. 4- 6 c,d) rather than contract south or southeastward as expected from reanalysis (Fig. 4-2c,d) and previous literature (e.g. Risbey et al., 2009a; Min et al., 2013). The relationships simulated by the KMA (Fig. 4- 5e,f) are weaker than in the UKMO, and all but absent when ENSO is removed. The maximum temperature and precipitation relationships in POAMA are strong but focussed in the southeast of Australia (Fig. 4- 5h,i), and, like the KMA, largely disappear with ENSO removed.

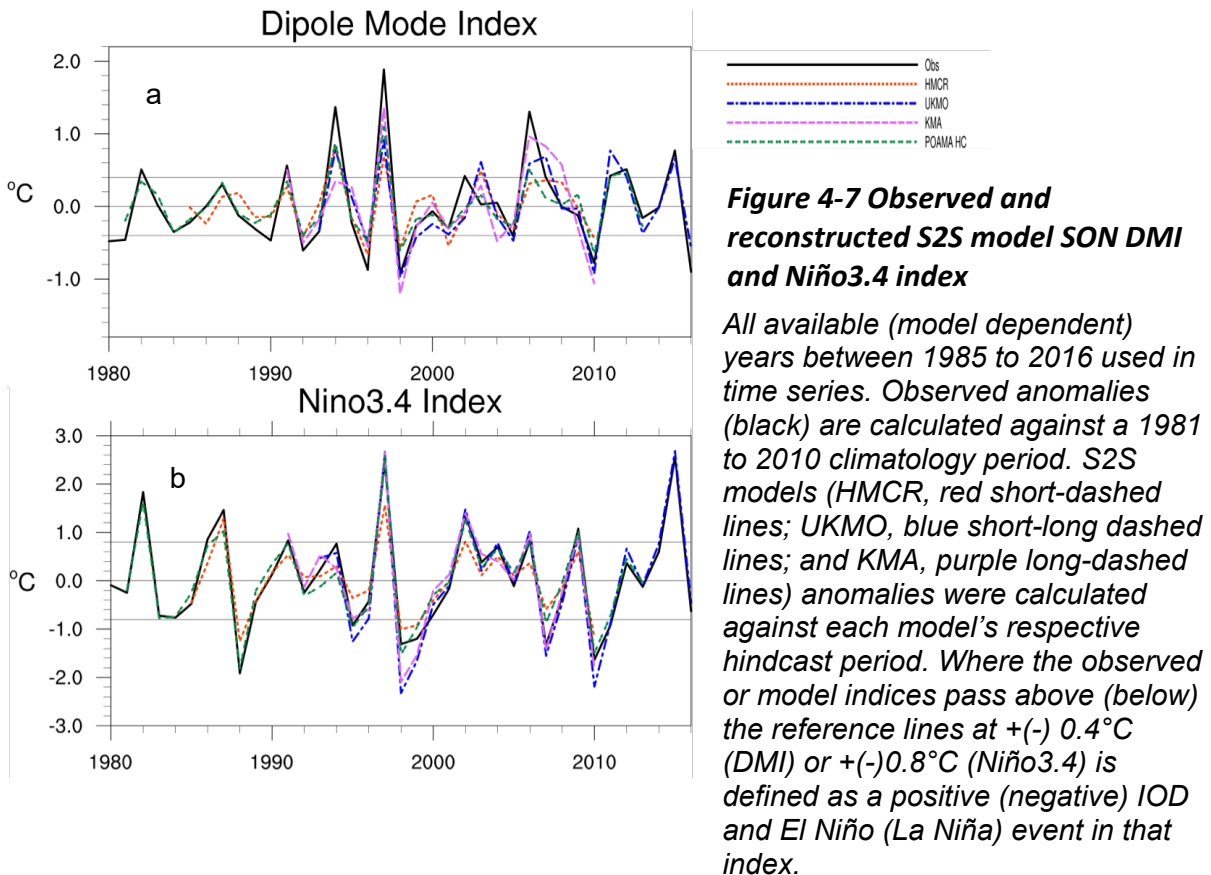
	West- vs east- pole	DMI vs Niño3.4	Partial west- pole vs Niño3.4	Partial east- pole vs Niño3.4	Period
Observations	-0.29	0.64	0.46	-0.34	1981 - 2018
HMCR	0.04	0.34	0.07	-0.36	1990 - 2015
UKMO	0.19	0.54	0.56	-0.35	1993 - 2016
KMA	0.00	0.57	0.13	-0.57	1991 - 2010
POAMA (ver. A)	-0.11	0.63	0.36	-0.48	1981- 2013

**Table 4-2 IOD, ENSO correlations in S2S models and observations**

*Pearson correlation coefficients of spring DMI poles, DMI, and Niño3.4 indices and partial correlation of east- and west-IOD poles (with opposing pole first linearly removed; e.g. Lim et al., 2017). Values are for spring-average observations and lead-1 reconstructed spring hindcasts. Correlations were calculated across different periods, as noted in the table.*

The impression from these S2S model regressions is that they, like POAMA, have overly strong atmosphere and land relationships to ENSO variability compared to that with IOD variability. While the much-reduced anomaly strength in the partial regressions may suggest ENSO and IOD correlate too strongly in these models, we see that all but POAMA have ENSO-IOD correlations that are slightly weaker than observed (table 4-2; Fig. 4-7), consistent with Shi et al., (2012). Further, regressions of Niño3.4, with the DMI linearly removed, onto the atmospheric circulation are very similar to regressions with the full Niño3.4 index (not shown). This lack of change suggests that the IOD has little to do with the ENSO relationship to the

atmospheric circulation in these models, in contrast to what is expected from observational studies (e.g. Cai et al., 2011a). As such, it appears that the models do not associate the IOD with the atmospheric circulation or Australia's spring temperature and precipitation at all, and instead attribute these variables to ENSO.



We may better understand the strong ENSO-forcing by examining the relationships and behaviour of the lead-one model IOD and ENSO SST anomalies. The models' reconstructed spring Niño3.4 (Fig. 4-7b) index follows the observed index closely, whereas the reconstructed DMI values (Fig. 4-7a) tend to be lower in magnitude or partly out of phase with the observations. A relatively weaker IOD may result in a weaker atmospheric response in the models (e.g. Hoskins & Karoly, 1981) that is compensated for by the stronger ENSO signal in the Pacific, producing the dominating relationship of ENSO with the reconstructed spring atmosphere and land conditions. We may learn more about how ENSO appears to dominate the models by exploring the relationships between the IOD poles and between ENSO.

There are few consistent errors or successes across the models in how they relate the DMI poles to each other or ENSO. Lack of consistency means it is difficult to find one single explanation for the strong relationship to ENSO, but may help us understand individual model biases in how they simulate the IOD teleconnections. In observations, ENSO correlates more strongly, and even forces, the west-pole of the IOD much more than it does the east-pole (e.g. Zhao & Hendon, 2008; Li et al., 2012; Lim et al., 2017; Lee et al., 2021). Only the UKMO simulated a partial correlation with Niño3.4 that was stronger with the west-pole than the east-pole (table 4-2). However, the UKMO also produced weaker than observed DMI values.

Unlike the observed negative correlation, the UKMO west- and east-poles are weakly positively correlated, suggesting that the poles tend to have same-sign SST anomalies, resulting in a generally weaker DMI. The HMCR and KMA simulate effectively zero correlation between west- and east-poles, and very weak partial correlations between the west-pole and Niño3.4. Instead, the DMI HMCR (weak correlation) and KMA (moderate correlation) relationship to ENSO appears to occur via the east-pole, contrasting with the observed relationship. While the POAMA hindcast better simulates the partial correlation between west-pole and ENSO, it also appears to gain more of its ENSO-IOD relationship through an overly strong connection to its east-pole. Some differences in correlation strengths may be due to the different hindcast periods and natural decadal variability in the ENSO-IOD relationship (Lim et al., 2017). However, the number of inconsistencies between correlations suggest problems with how the models simulate Indian Ocean processes. We explore this idea next by examining how the DMI pole and Niño3.4 SSTs evolve through each model hindcast.

The evolution of the daily west-pole (Fig. 4- 8), east-pole (Fig. 4- 9), and Niño3.4 (Fig. 4- 10) SST anomalies (relative to model daily climatology) through each two-month initialisation are shown for each model hindcast. Each initialisation is coloured red (for positive IOD or El Niño events), blue (for negative IOD or La Niña events), or grey (for neutral). An IOD (ENSO) event was determined if the model's reconstructed spring DMI (Niño3.4) was more than 0.4°C (0.8°C) from climatology. How the different pole- or Niño3.4-region SSTs evolve in response to a developing IOD or ENSO event may help us understand the reconstructed spring atmosphere and temperature regressions.

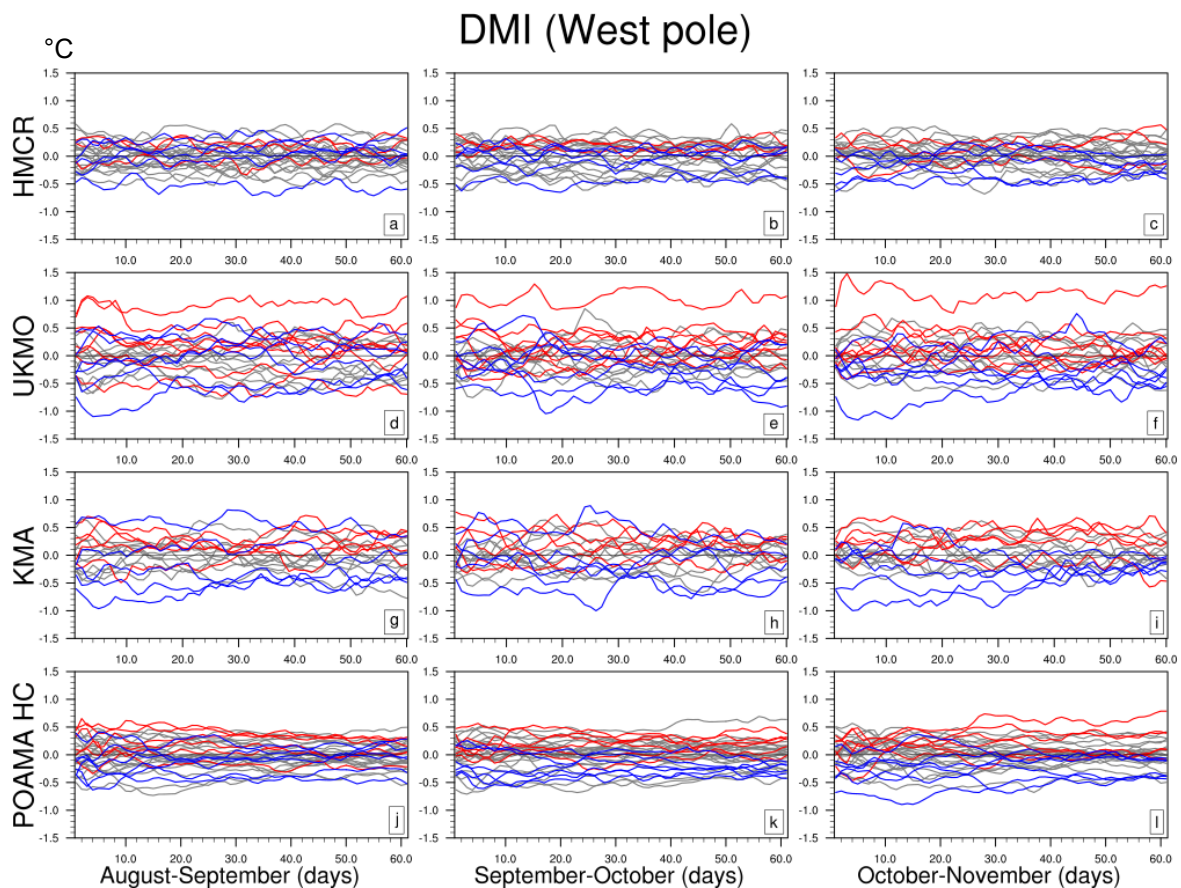


**Figure 4-8 HMCR, UKMO, KMA, POAMA (ver. A) HC daily west-pole of the DMI**  
 Daily index values in °C for the two months of each hindcast initialisation from August (left), September (middle) and October (right). Positive (red lines) and negative (blue lines) IOD years, are defined by the reconstructed SON DMI being above 0.4°C or below -0.4°C (see Fig. 4-7 for S2S model reconstructed SON DMI time series). Neutral years are in grey. Anomalies are relative to a daily climatology period calculated over each model's hindcast. The horizontal line at 0°C shows where the DMI anomalies go to zero. For comparison, observed monthly-averaged values are: 0.32°C (August), 0.22°C (September), 0.37°C (October), and 0.37°C (November) for positive IOD events and -0.16°C (August), -0.19°C (September), -0.14°C (October), and -0.05°C (November) for negative IOD events where events were defined by [www.bom.gov.au](http://www.bom.gov.au) between 1981 to 2018.

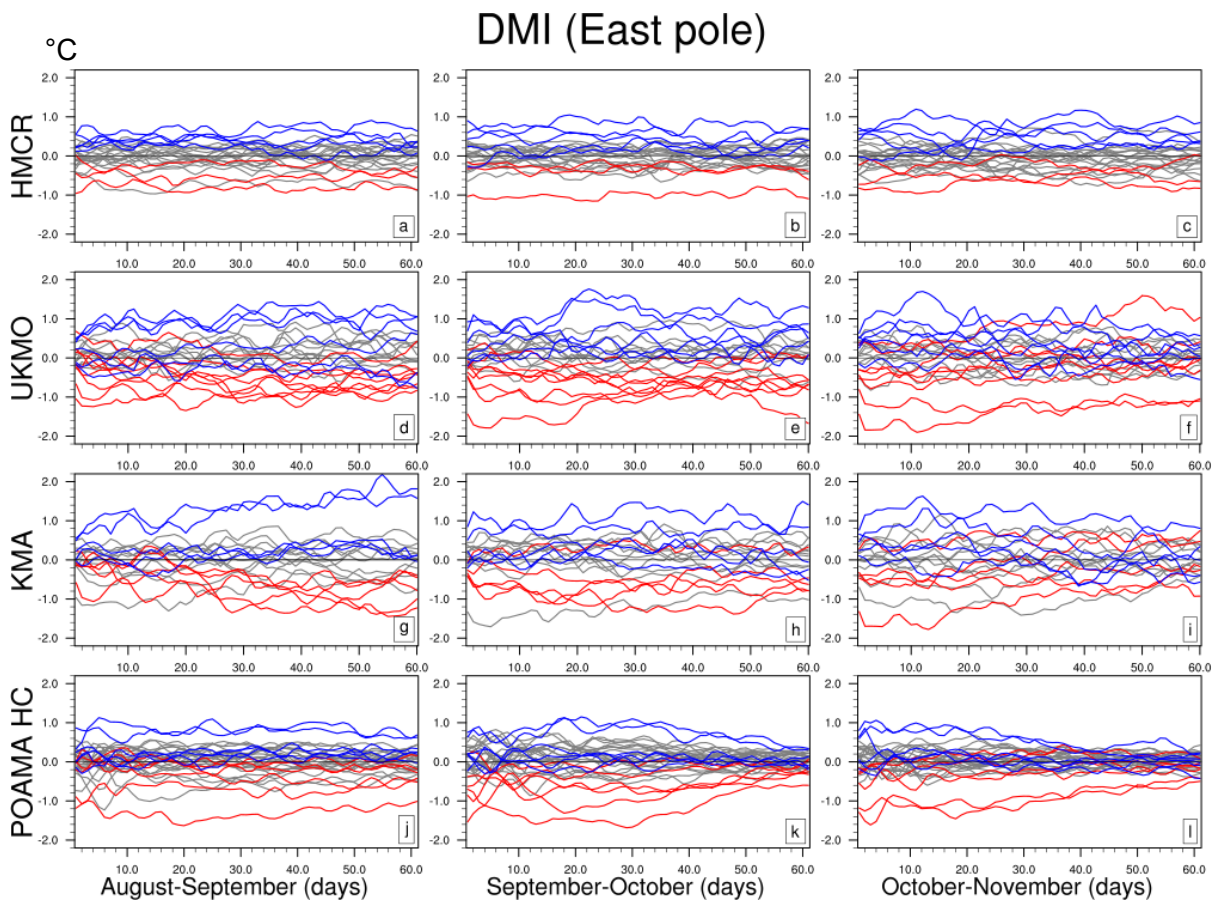


**Figure 4-9** As in Fig. 4-6 but for the east-pole of the DMI

For comparison, observed monthly-averaged values are:  $-0.41^{\circ}\text{C}$  (August),  $-0.63^{\circ}\text{C}$  (September),  $-0.65^{\circ}\text{C}$  (October), and  $-0.44^{\circ}\text{C}$  (November) for positive IOD events and  $0.47^{\circ}\text{C}$  (August),  $0.57^{\circ}\text{C}$  (September),  $0.53^{\circ}\text{C}$  (October), and  $0.34^{\circ}\text{C}$  (November) for negative IOD events where events were defined by [www.bom.gov.au](http://www.bom.gov.au) between 1981 to 2018.

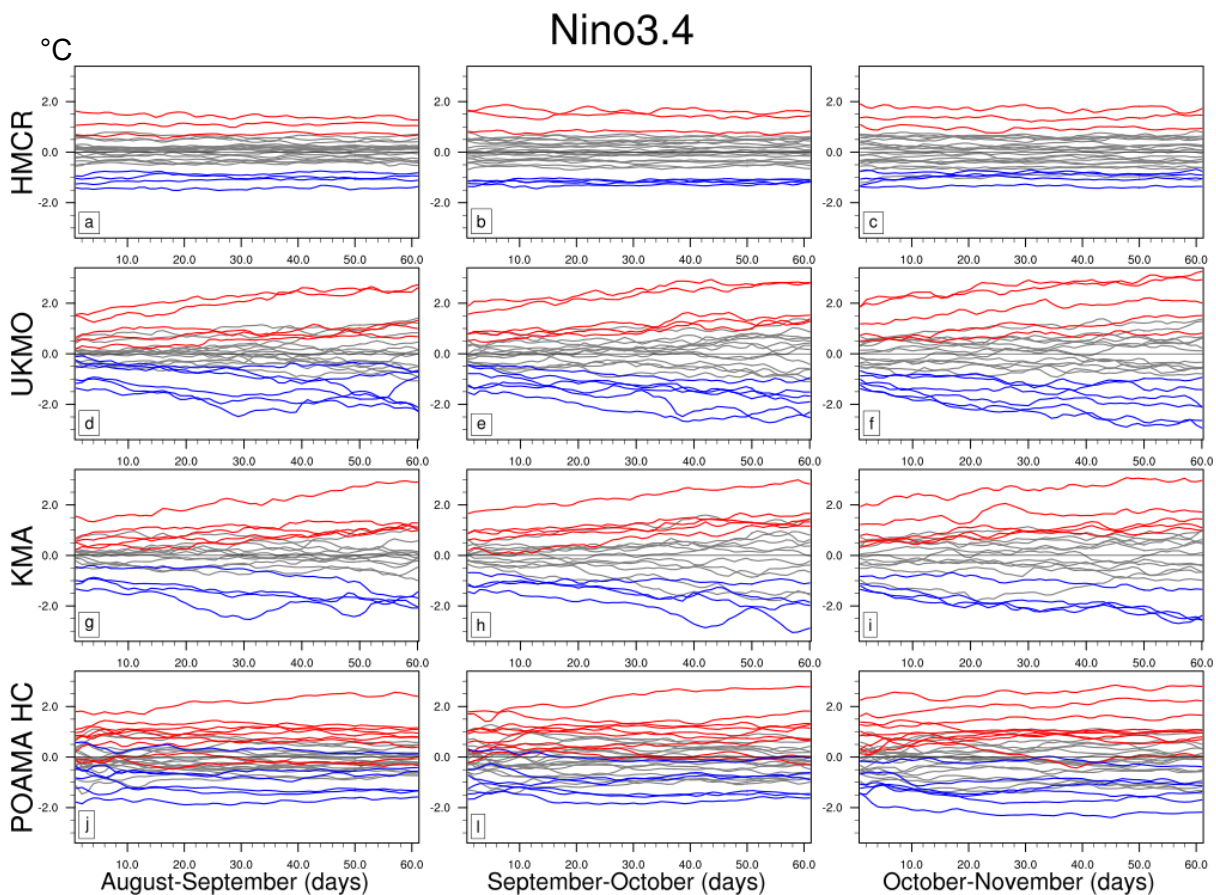


**Figure 4-10 As in Fig. 4-6 but for Niño3.4 SSTs**

*For comparison, observed monthly-averaged values are: 1.01°C (August), 1.08°C (September), 1.34°C (October), and 1.62°C (November) for El Niño events and -0.87°C (August), -0.95°C (September), -1.24°C (October), and -1.27°C (November) for La Niña events where events were defined by [www.bom.gov.au](http://www.bom.gov.au) between 1981 to 2018.*

As expected from the unrealistic correlations in table 4-2, the daily SST anomalies in the west- and east-poles and Niño3.4 regions behave differently in response to the IOD or ENSO events. There is little distinction between the west-pole SSTs across the IOD-types across most of the models (Fig. 4-8a-i), whereas the POAMA hindcast west-pole SSTs (Fig. 4-8j-l) tend to be positive (negative), if low in magnitude, during positive (negative) IOD events. The east-poles, in contrast, have generally negative (positive) SST anomalies during positive (negative) IOD across the models (Fig. 4-9). The greater distinction between IOD event types suggests that the east-pole may be the determining factor in whether a model's reconstructed spring IOD is positive, negative, or neutral. Aside from small day-to-day variations, the weaker HMCR (Fig. 4-9a-c) and the stronger UKMO east-pole values (Fig. 4-9d-f) tend to hold constant through each two-month run. The KMA (Fig. 4-9 g-i) is similar to the UKMO but has some growth of east-pole anomalies in the August initialisation and decay in the November initialisation. The POAMA hindcast (Fig. 4-9j-l) decreases the east-pole anomaly magnitudes toward the end of each hindcast run, with decay occurring earlier in each successive initialization through spring. ENSO event Niño3.4 SST anomalies seldom overlap with neutral values, with clear distinction between El Niño and La Niña in each model run (Fig. 4-10). The HMCR

and POAMA hindcasts (Fig. 4-10a-c;j-l) maintain constant Niño3.4 SST anomaly magnitude through each run. The UKMO and KMA (Fig. 4- 10 d-i), conversely, show rapid Niño3.4 growth, with approximately four months' equivalent observed monthly-mean growth (not shown, equal to around 0.5°C) occurring over the 60 days of each hindcast.

While there are just as many differences in how the models simulate the daily SST anomalies as there were differences between the observed and model IOD pole and ENSO correlations, we can suggest that the ENSO SST anomalies may grow to dominate the IOD SSTs in the models. Both the unrealistically rapid Niño3.4 growth in the UKMO and KMA models, and the unrealistically early east-pole decline in the POAMA hindcast would result in reconstructed forecast ENSO events becoming far stronger than a comparable IOD event. As such, the overly strong relationship to ENSO in the linear regressions may partly be explained by the strength of SST anomalies in the tropical Pacific Ocean compared to the tropical Indian Ocean in the models.

#### 4.3.4 S2S Summary

Spring reconstructions from the S2S hindcast show realistic atmospheric, and Australian maximum temperature and precipitation teleconnections to the IOD. However, with the exception of the HMCR, these teleconnections breakdown with the removal of ENSO. The HMCR simulated the atmospheric regression with the DMI, but poorly captures the relationships with ENSO and Australian maximum temperature and precipitation. In contrast, it appears that the UKMO, KMA, and POAMA models over-represent the influence of ENSO variability at the cost of the relationship with the tropical Indian Ocean, consistent with the results using the POAMA hindcast in chapter 2. The SSTs in the models evolve differently in the tropical Pacific and Indian Oceans such that ENSO SSTs are much stronger than a comparable IOD by the start of each lead-1 month of the spring reconstructed hindcasts. Overall, the SST evolution in the models results in the reconstructed spring IODs being generally weaker than observed. Further, relative to both observations and each other, the models simulated the ENSO to IOD east- and west-pole relationships differently. In general, however, each model had overly strong ENSO-east pole correlations. An overly strong ENSO could promote stronger Walker circulation changes that unrealistically strengthen the link to the east-pole via an atmospheric-bridge mechanism (e.g. Klein et al., 1999), further dominating the atmospheric and subsequent teleconnections.

The weaker than observed IOD strength contrasts with the majority of coupled models (Cai & Cowan, 2013; Weller & Cai, 2013b; Li, G. et al., 2015; McKenna et al., 2020). As some of core models used in the seasonal prediction systems described here are the same as some CMIP models, the contrast in results may be due to the different configurations for free-running climate mode compared to those for seasonal prediction. Firstly, some tuning may occur when configuring systems for seasonal prediction (e.g. Park et al., 2017) that

may bias the models toward ENSO as it is the strongest sources of prediction skill (e.g. Merryfield et al., 2020; Meehl et al., 2021). Secondly, and possibly more likely in the seasonal model context, the evolution of the SSTs in the tropical Indian Ocean compared to the tropical Pacific suggests that the latter has a stronger ‘memory’ for ocean initial conditions. As such, the anomalies in the Pacific Ocean persist longer than those in the Indian Ocean, resulting in stronger ENSO at lead-1 for an initially comparable IOD. However, the second argument better explains the IOD pole decay in POAMA than the Niño3.4 growth in the UKMO or KMA, or the weak but steady SSTs in the HMCR. Finally, recall that partial regression analysis may overly penalise the IOD or ENSO (e.g. Cai et al., 2011a; Liguori et al., in review) giving an over-estimation of ENSO’s influence in comparison with the IOD in the models. While this method is unrelated to the overly strong ENSO SST anomalies at lead-1, it may have coloured our interpretation of how those strong ENSO SSTs related to the Australian spring maximum temperatures. As such, we may find clearer results by running POAMA experiments that specifically highlight or isolate tropical Indian Ocean variability.

#### 4.4 Indian Ocean Dipole experiments

As mentioned in the introduction, as strong tropical forcing can lead to stronger predictability (e.g Kumar et al., 2013; Liu et al., 2017), we next run experiments using POAMA with increased IOD magnitude to identify the influence that IOD event strength has on southern hemisphere teleconnections.

The first set of POAMA experiments are designed around composites of three strong positive and three strong negative IOD events that occurred within the POAMA hindcast period (Table 2). Events were defined by the Bureau of Meteorology (see <http://www.bom.gov.au/climate/iod/>) and were chosen based on strength. Ideally, events that coincided with an El Niño or La Niña in the Pacific Ocean were to be avoided (<http://www.bom.gov.au/climate/enso/enlist/>), however, given these restrictions and the high co-variability between ENSO and IOD, few IOD events met these criteria. One of the strongest positive IODs used in these experiments coincided with a strong El Niño (1997). The influence of this El Niño on the initial conditions and experiment results is discussed in Section 3.22.

Positive IOD	1997*	1994*	2012
Negative IOD	1981	1992	1996

**Table 4-3 IOD events used in POAMA experiments**

Positive and negative IOD from <http://www.bom.gov.au/climate/iod/> where a DMI threshold value of +/- 0.4°C define positive or negative IOD events respectively. \*Coincides with El Nino.

#### 4.4.1 Comparison of reanalysis and POAMA hindcast composites

As there is some asymmetry between positive and negative IOD events (e.g. Cai et al., 2012; Lim et al., 2021c) we start by looking at composites of the spring IOD events in reanalysis and the POAMA hindcast (version A) to form a baseline of comparison for the experiments. The reanalysis atmospheric circulation in the positive IOD composites (Fig. 4-11 a,c) is similar to that found in the regression onto the DMI (Fig. 4-1). The atmospheric circulation in the negative IOD composite (Fig. 4- 11 b,d) is generally the opposite sign of that in the positive IOD composite. However, there is no corresponding anticyclone northwest of Australia, and instead, the upper-level wave train appears to form further west over South Africa and propagates only in the extratropics (Fig. 4-11d). The barotropic cyclone south of Australia is also deeper and closer to Australia than the corresponding barotropic anticyclone.

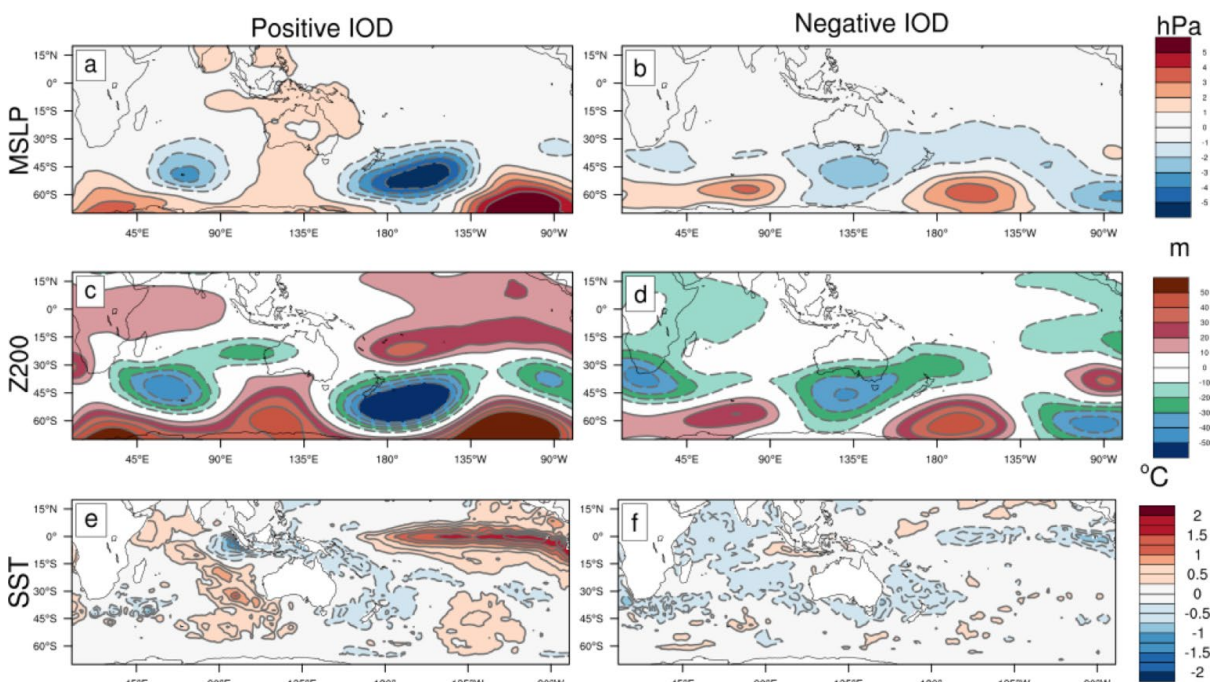


**Figure 4-11 Observed IOD composite atmospheric circulation and SST**

Spring composites of the three positive IOD events (left column) and three negative IOD events (right column) used in the IOD experiments. Atmospheric circulation is represented by mean sea level pressure (a, b; in hPa) and 200hPa geopotential height (c,d; in m) from ERA-5 reanalysis. Sea-surface temperature composite (e, f) in °C is from Reynold's OI dataset. Anomalies are relative to a 1981-2010 climatology period. Note: due to small sample size of each composite there is no statistical significance calculated for these figures.

The atmospheric circulation in the POAMA hindcast positive IOD composites (Fig. 4- 12 a,c) is similar to that in the hindcast IOD linear regression (Fig. 4-3 g,h) and does a poor job of simulating the atmospheric circulation over the Indian Ocean, consistent with chapter 2. In particular, the wave train in the Indian Ocean is very weak. Unlike reanalysis, the negative IOD composite differs significantly from the positive IOD composite as it lacks the extratropical wave train and instead has an elongated barotropic cyclone south of Australia (Fig. 4-12b,d).

The SST anomalies in the positive IOD composites are stronger than in the negative IOD composites in both reanalysis (Fig. 4-11 e,f) and the POAMA hindcast (Fig. 4-12 e,f). In particular, the cold anomaly near the Java-Sumatra upwelling region (e.g. Meyers et al., 2007; Zhao & Hendon, 2009; Sooraj et al., 2012; Lee et al., 2021) is stronger in the reanalysis and POAMA positive IOD composite than the corresponding warm anomaly in the negative IOD composite in reanalysis and absent in the POAMA composite. In both reanalysis and POAMA, the western cold anomaly in the negative IOD composite (Figs. 4-11,4-12 f) covers a broader area than the corresponding warm anomaly in the positive IOD composite (Figs. 4-11e, 4-12e), though, the anomalies in POAMA are weaker than in reanalysis. A strong warm anomaly in the tropical Pacific is evidence of the inclusion of the 1997 El Niño in the positive IOD composites (Figs. 4-11f,4-12f). The tropical Pacific SST anomaly appears stronger in magnitude than the SST anomalies in the tropical Indian Ocean (Figs. 4-11,4--12f). In contrast, there is a weak Pacific cold anomaly in the negative IOD composite.

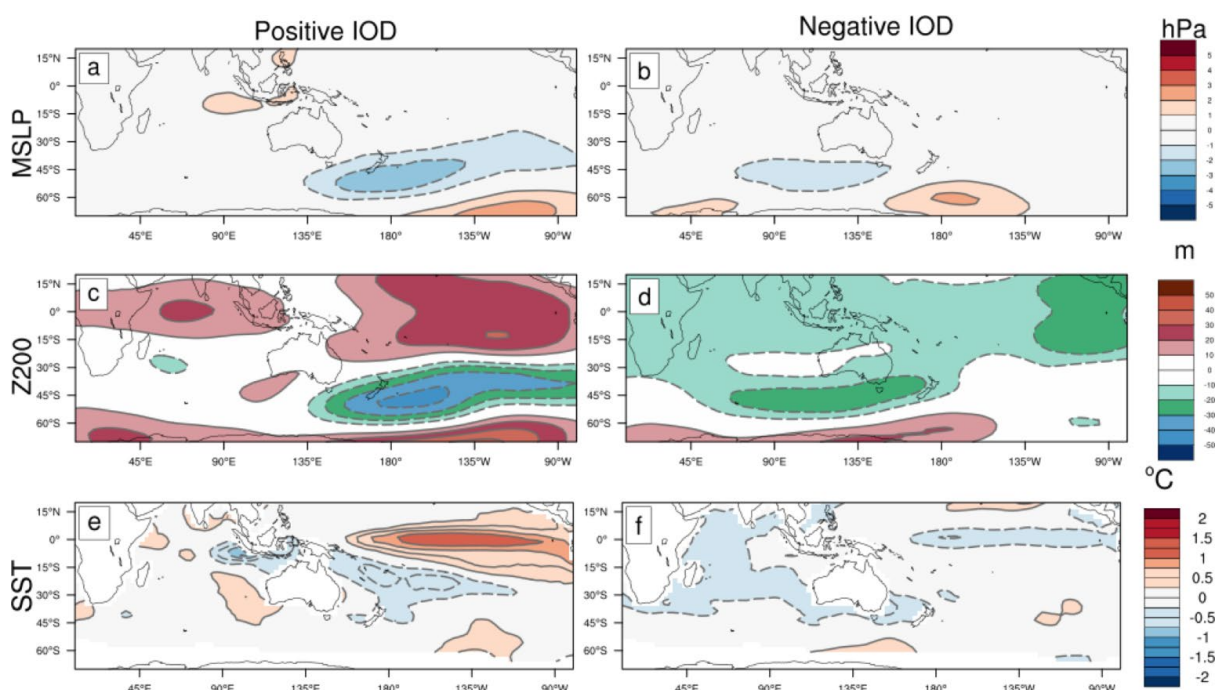


**Figure 4-12** As in Fig. 4-11 but for POAMA (version A) hindcast  
 Anomalies were calculated against a 1981 to 2010 climatology from reanalysis data.

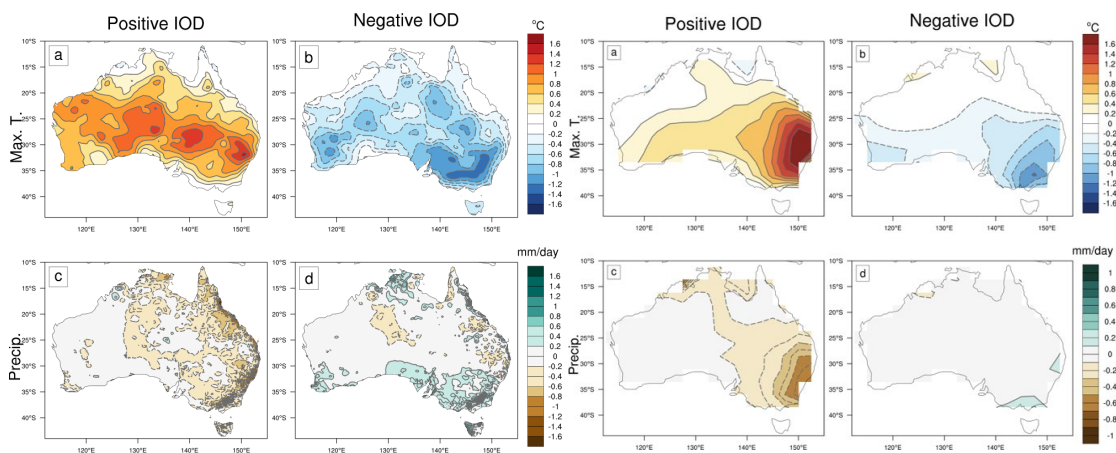


**Figure 4-14** As in Fig. 4-12, but for composite anomalies of Australian maximum temperature (°C) and precipitation (mm/day) from the AWAP dataset.

**Figure 4-14** As in Fig. 4-12 but for lead-1 reconstructed spring POAMA hindcast (ver. A).

The observed and POAMA hindcast IOD composite maximum temperature and precipitation anomalies are generally symmetric and similar to the patterns found in the linear regressions (Figs. 4-2,4-5g,h). The majority of Australia is anomalously hot (cold) in the observed positive (negative) IOD composites (Fig. 4-13 a, b). Temperature anomalies are more confined to the south and southeast in POAMA (Fig. 4-14a,b). Both the observed and hindcast dry anomalies in the positive IOD composites spread across the central-east Australia (Figs. 4-13,4-14c), while wet anomalies are more confined to the southeast, particularly in the POAMA hindcast (Figs. 4-13,4-14d).

#### 4.4.2 IOD experiment design

We run two types of IOD composite experiments that broadly follow the methods of Lim & Hendon (2017) and Lim et al. (2019b): realistic (1x composite values) and enhanced IOD (4x) for both positive and negative IOD cases. The 1x composite experiments use ocean initial conditions generated from global 3D ocean temperature, salinity and mixing height taken from August 1, September 1, and October 1 of each of the negative and positive IOD events (6 initialisation dates in total; see table 4-4). As strong tropical forcing can lead to stronger predictability (e.g Kumar et al., 2013; Liu et al 2017), we hypothesise that for POAMA to generate a strong IOD-like response in the atmosphere and Australian temperature fields, it must have a stronger IOD signal to compensate for the strong reliance on the tropical Pacific noted in chapter 2. As such, the enhanced IOD composite experiment ocean initial conditions are set by multiplying the positive and negative IOD composites by a factor of 4 (arbitrarily chosen) within the Indian Ocean domain only (See black line in Fig. 4-15 for region), with the remaining ocean conditions the same as the 1x composite experiments. A climatology experiment was run with 3D ocean initial conditions set to a 1981-2010 climatology, and used as the reference for the IOD composite experiments. See table 4-4 for a summary of the IOD composite initial conditions.

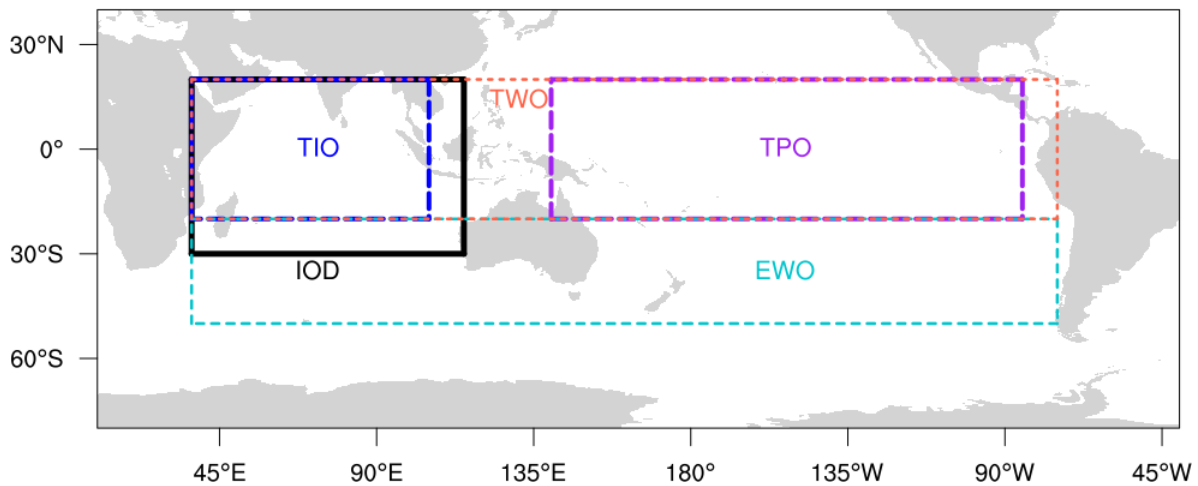


**Figure 4-15 Experiment ocean initial condition boundaries**

*Indian Ocean Dipole (black line; IOD) experiment: 20°N-30°S, 37°-115°E; tropical Indian Ocean (blue long-dashed line, TIO) experiment: 20°N-20°S, 37°-105°E; tropical Pacific Ocean (purple long-dashed line, TPO) experiment: 20°N-20°S, 140°-275°E; whole tropical Ocean (red short-dashed line; TWO): experiment: 20°N-20°S, 37°-285°E; and whole extratropical Ocean (turquoise short-dashed line; EWO) experiment: 20°-50°S, 37°-285°E.*

Each experiment has a 30-member ensemble generated by initialising the atmospheric model and its land-surface scheme with initial conditions drawn from 30 different states taken from August 1, September 1, and October 1 dates across 1981-2010. August - October composite ocean initial conditions are the same for each corresponding August - October initialisation of each ensemble member. Each one-month forecast is run at a one month lead-time before combining into a 30-member reconstructed spring forecast (described in section 4.2.4) for each IOD experiment case. The scrambled ensemble should further ensure that the memory of the atmospheric and land initial conditions are lost, increasing the influence from the ocean initial conditions (e.g. Arblaster et al., 2014; Lim and Hendon, 2015).

	<b>Ocean Initial Conditions</b>	<b>Atmosphere and land initial conditions</b>	<b>CO<sub>2</sub></b>	<b>ozone</b>
<b>Climatology</b>	Climatology 1981 – 2010	30 different conditions drawn from: August 1 1981 – 2010 September 1 1981 – 2010 October 1 1981 – 2010	345 ppm	Monthly climatology
<b>1x positive IOD composite</b>	1994, 1997, 2012 composite ocean conditions			
<b>Enhanced positive IOD</b>	4 x positive IOD composite ocean anomaly in Indian Ocean, 1 x anomaly elsewhere.			
<b>1x negative IOD composite</b>	1981, 1992, 1996 composite ocean conditions			
<b>Enhanced negative IOD composite</b>	4 x negative IOD composite anomaly in Indian Ocean, 1 x anomaly elsewhere			

**Table 4-4 IOD experiment ICs for August1, September 1, October 1 initialisations.**

#### 4.4.3 IOD experiment results

The lead-1 reconstructed spring SST anomalies (Fig. 4-16; relative to the climatology experiment) capture the expected positive (negative) IOD patterns: cold (warm) anomalies in the east, and warm (cold) anomalies in the west tropical Indian Ocean. As with the reconstructed POAMA hindcast composites (Fig. 4-12 e,f), the warm east Indian Ocean in the 1x negative IOD anomaly (Fig. 4-16b) is far weaker than the corresponding cold 1x positive IOD anomaly (Fig. 4-16a), and weaker than the warm anomaly in observations (Fig. 4-10f). The impact of enhancing the ocean initial conditions in the Indian Ocean domain is stark, with a strong warm anomaly extending from the west tropical Indian Ocean to Australia in the 4x positive IOD experiment (Fig. 4-16c) and a broad cold anomaly covering the majority of the Indian Ocean in the 4x negative IOD experiment (Fig. 4-16d). The SST anomalies in the east tropical Indian Ocean are similarly enhanced; in particular, the warm anomaly in the 4x negative IOD experiment is clearly visible, stronger, and covering a greater geographic extent than in the 1x negative IOD experiment or reanalysis. Consistent with the SST anomaly maps, the average DMI values are weaker in the 1x IOD experiments and POAMA hindcast than the average reanalysis values, but far stronger than reanalysis in the 4x IOD experiments (table 4-5).

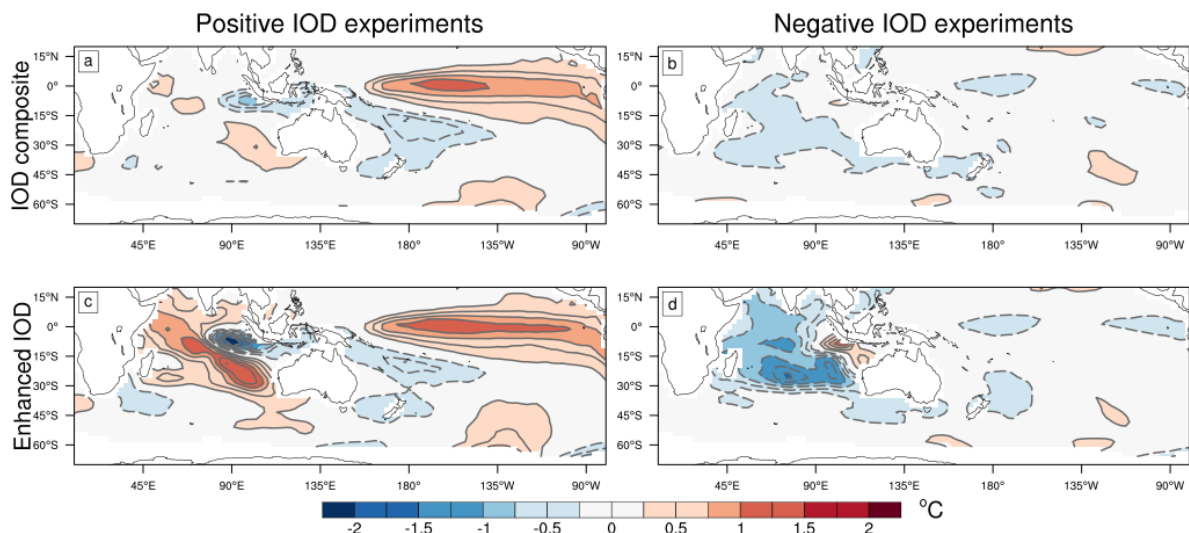


**Figure 4-16 Reconstructed spring SST anomalies from POAMA IOD experiments**  
 SST anomalies ( $^{\circ}\text{C}$ ; relative to the climatology experiment) in the positive (left column) and negative (right column) IOD experiments for single composite anomaly (a,b) and enhanced IOD anomaly (c,d).

The warm tongue in the tropical Pacific Ocean SST anomalies is evidence of the inclusion of the 1997 El Niño in both 1x and 4x positive IOD initial conditions (Fig. 4- 16a,b). Interestingly, the tropical Pacific El Niño signal is stronger in the enhanced positive IOD experiment than the 1x composite (Fig. 4- 16a,c), despite the ocean initial conditions only being enhanced in the Indian Ocean domain. In contrast, there is only a very slight broadening of the tropical Pacific SST anomalies in the enhanced negative IOD composite compared to the 1x negative IOD (Fig. 4-16 b,d). The strengthening of the anomaly in the tropical Pacific in response to the enhanced positive IOD is consistent with literature that argues that the tropical Indian Ocean feedbacks onto ENSO (e.g. Shinoda et al., 2004; Izumo et al., 2010; Luo et al., 2010; Lim & Hendon, 2017; Cai et al., 2019; Wang, H. et al., 2019). We next explore how these strengthened IODs influence the atmospheric circulation forecasts.

	Positive IOD			Negative IOD		
	West pole	East Pole	DMI	West Pole	East Pole	DMI
observed	0.36	-0.90	1.26	-0.37	0.27	-0.65
POAMA hindcast	0.23	-0.59	0.82	-0.32	0.04	-0.36
1x IOD experiment	0.21	-0.55	0.76	-0.25	0.07	-0.31
4x IOD experiment	0.79	-1.01	1.81	-0.85	0.31	-1.16

**Table 4-5 Average values for IOD experiments**

*Average spring west-pole, east-pole, and DMI values calculated over the three positive and three negative IOD events in observations and the lead-1 reconstructed POAMA hindcast (top two rows), or lead-1 ensemble average for the IOD experiments (bottom two rows).*

The reconstructed spring forecast atmospheric circulation anomalies are displayed in figure 4-17. The 1x positive (Fig. 4-17 a,b) and 1x negative IOD (Fig. 4-17 e,f) experiments broadly match the circulation anomalies in the POAMA hindcast (Fig. 4-12), as expected from the similar ocean initial conditions and reconstructed spring SST anomalies. However, there are some differences between the hindcast and 1x IOD experiments: the circulation anomalies are generally stronger in magnitude in the experiments; the elongated cyclone in the 1x negative IOD composite is longer and has two local minima southwest and southeast of Australia; and the 1x positive IOD experiment upper-level wave train over the Indian Ocean toward the anticyclone over Australia is shifted eastward relative to the weak wave train in the hindcast. These differences are likely due the different ways the hindcast and experiment composites were produced: the hindcast was run first, with the observed atmosphere and land conditions, and then composited, while the inverse is true for the experiment; and anomalies were calculated against the 1981-2010 hindcast climatology, rather than relative to a climatological ocean experiment. Despite these small differences, the 1x IOD experiments have similar shortfalls as the hindcast in their ability to represent the atmospheric circulation over the Indian Ocean.

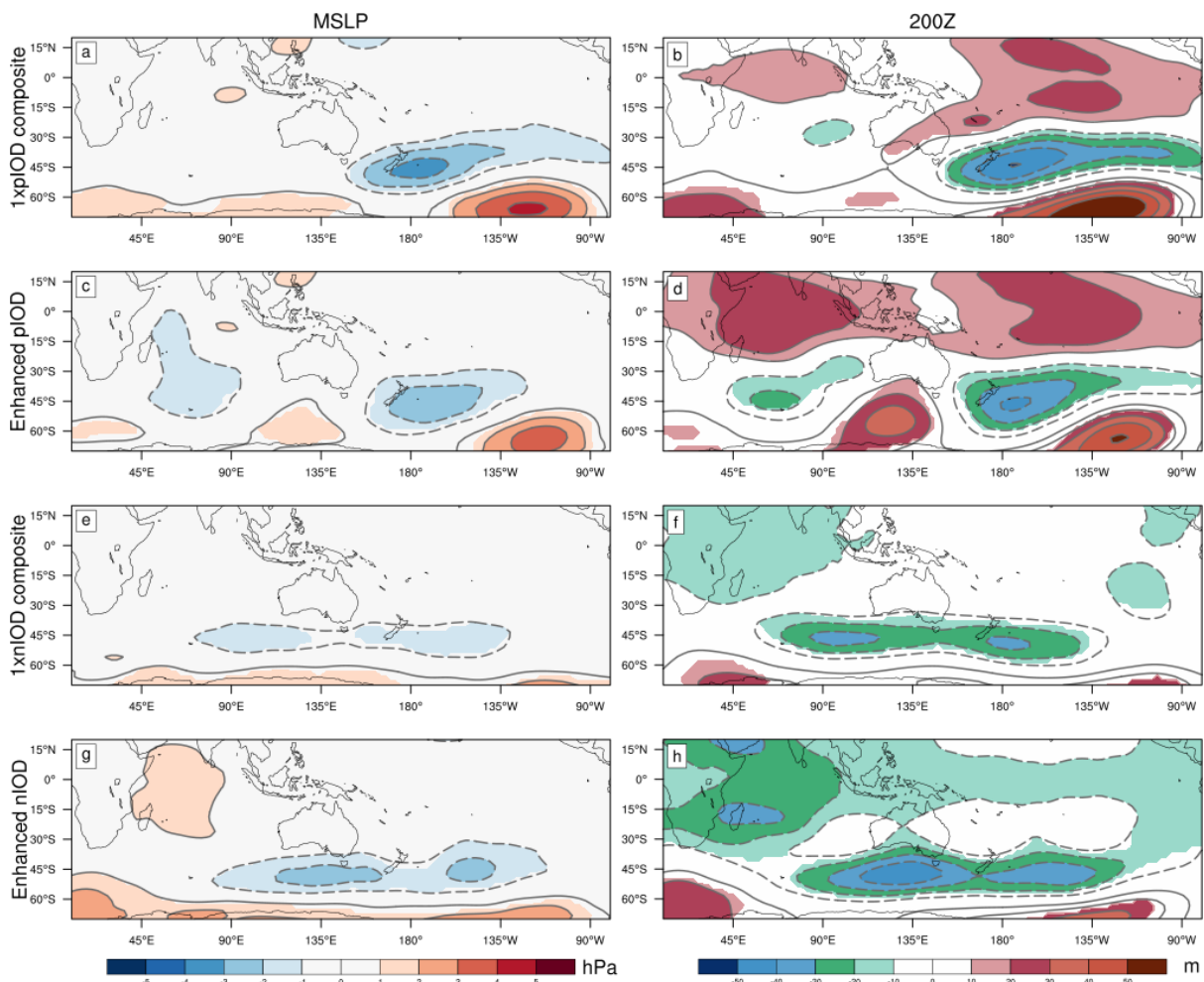


**Figure 4-17 IOD experiment lead-1 reconstructed spring forecast atmospheric circulation anomalies (relative to climatology experiment)**

Atmospheric circulation anomalies (left column: mean sea level pressure in hPa; right column 200hPa geopotential height in m) response to IOD experiments. Each figure is the anomaly relative to the ocean climatology experiment: a-b: single positive IOD composite; c-d: enhanced positive IOD; e-f: single negative IOD composite; enhanced negative IOD. Filled contours show where the experiment was statistically different from the climatology run at the 90% confidence level calculated using a Student's t-test with 28 (30-2) independent samples.

Enhancing the IOD SSTs does represent an improvement in the reconstructed spring atmospheric circulation compared to the hindcast or 1x IOD experiments. In particular, the enhanced positive IOD experiment (Fig. 4- 17 d,c) replicates the observed positive IOD composite atmospheric circulation pattern well, including over the Indian Ocean, as barotropic cyclones are now found both southwest and southeast of Australia. Further, a second upper-level cyclone is now northwest of Australia and forms part of a clearer Rossby wave path that arcs through a deeper southern Australian anticyclone and into the barotropic cyclone to Australia's southeast. The enhanced negative IOD experiment (Fig. 4- 17 g, h) does not show as strong an improvement over the 1x negative IOD composite. In particular, the enhanced negative IOD composite lacks the expected barotropic highs southwest and southeast of Australia. However, in a step closer to the reanalysis composite, the enhanced negative IOD experiment barotropic cyclone is contracted

relative to the elongated cyclone in the 1x experiment, and is now centred south of Australia. It is unclear whether the poorer response in the negative IOD experiments is due to POAMA not simulating an important dynamic or thermodynamic process, or because of the relatively weaker initial ocean conditions. To better highlight the impact of enhancing the Indian Ocean initial conditions on the negative and positive IOD forecasts, we next directly compare the two sets of experiments.

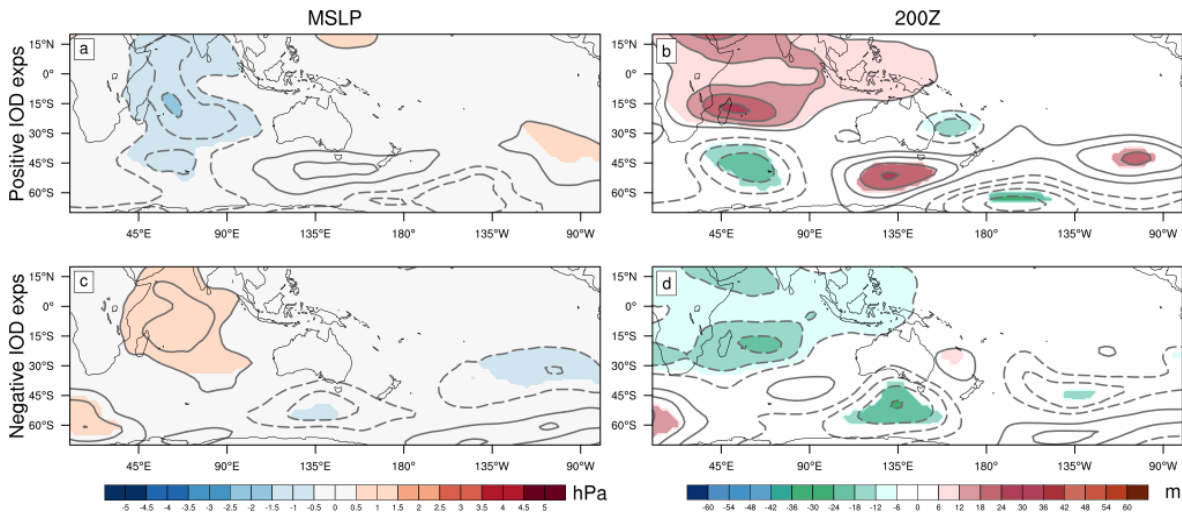


**Figure 4-18** As with Fig. 4-17, but differences are between the enhanced IOD and single composite anomalies experiments

Positive IOD experiment differences (a,b) and negative IOD experiment differences (c,d).

The difference between the enhanced and 1x composite positive and negative IOD reconstructed spring forecast atmospheric circulation is in figure 4-18. Anomalous low (high) MSLP and high (low) Z200 across the tropical Indian Ocean in the positive (Fig. 4-18a, c) (negative; Fig. 4-18 b, d) composites may be an exaggerated baroclinic response to the unrealistic ocean initial conditions. The responses in the extratropics, however, appear to be consistent with positive and negative IOD-like responses. In particular, the barotropic anticyclone in the positive IOD experiments, and cyclone south of Australia in the negative IOD experiments highlight the improvements in the experiments between enhanced and 1x composites. While the apparent Rossby Wave trains leading to the anticyclone and cyclone do not match the reanalysis (Fig. 4- 11), the different paths taken between the tropical Indian Ocean and Australia may be how POAMA simulates the asymmetry between IOD teleconnection pathways (Cai et al., 2012). Overall, the differences between the atmospheric circulation in the 1x and enhanced IOD composite experiments are consistent with POAMA simulating responses to the IOD, rather than ENSO. As such, it seems that enhancing the IOD signal results in an improved atmospheric circulation response.

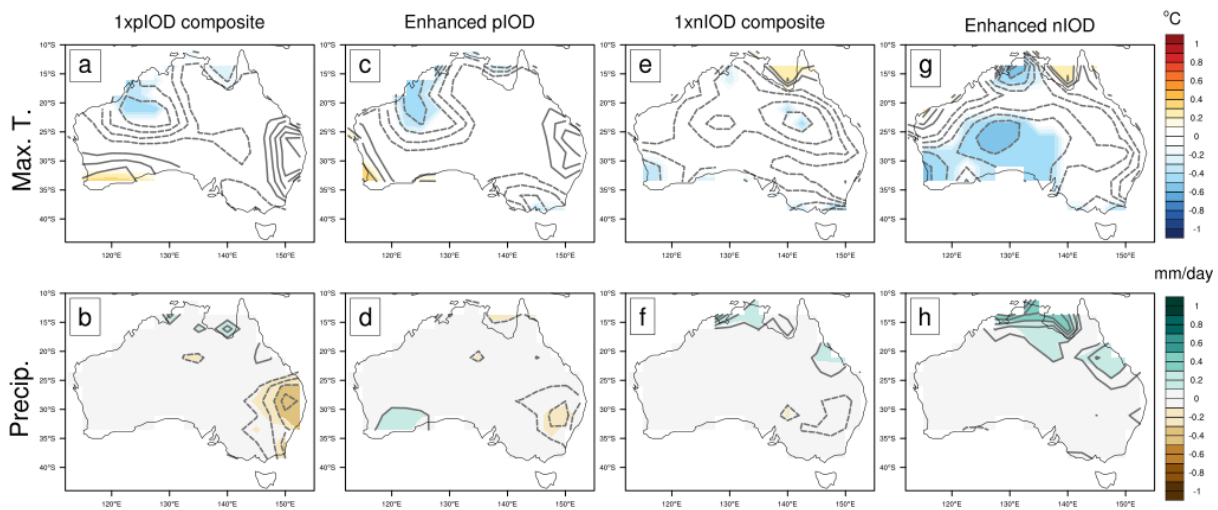


**Figure 4-19 As with Fig. 4-17, but for maximum temperature (°C) and precipitation (mm/day)**

In contrast to the atmospheric circulation patterns, in both 1x and enhanced experiments, the reconstructed Australian spring maximum temperature and precipitation anomalies (Fig. 4-19) are generally not statistically different from the climatology experiment, and do not match the spatial pattern in the reanalysis (Fig. 4-12) nor the POAMA hindcast composites (Fig. 4-13). In particular, the positive IOD experiments are generally (not statistically significantly) colder than the climatology experiment (Fig. 4-19 a,c), everywhere but the southwest and far east coast of Australia. Enhancing the positive IOD signal only weakens the southwest and east-coast warm anomalies (Fig. 4-19c), worsening the spring reconstructed forecast. There is a dry anomaly near the east coast in the 1x positive IOD experiment (Fig. 4-19b), similar to the hindcast, but again strengthening the positive IOD results in a weaker dry anomaly (Fig. 4-19d). In contrast, the negative IOD maximum temperature anomalies (Fig. 4-19 e,g) are an improvement towards the reanalysis compared to the hindcast, as cold anomalies extend across Australia. Enhancing the negative IOD further strengthens the cold anomaly in the southwest (Fig. 4-19e,g). However, these cold anomalies do not correspond to wet anomalies in the south, and wet conditions only found in the far north of Australia (Fig. 4-19 f,h). Overall, these experiments represent a decrease in skill relative to the POAMA hindcast, with the only improvement associated with the maximum temperature in the enhanced negative IOD experiment.

It is not clear why enhancing the IOD signal improves the atmospheric circulation response, but not the surface temperature and precipitation responses in Australia. The poor response in the experiments suggests that the Indian Ocean-atmosphere interactions may not be as relevant to Australia's spring maximum temperature and precipitation as expected, and other factors may be more important. One of the key differences between the hindcast composite and the 1x IOD experiments is the use of realistic land initial conditions in the hindcast, but scrambled conditions in the experiments. Land initial conditions do not decay as quickly as atmosphere initial conditions in forecasts (Dirmeyer, 2003; Meehl et al., 2020). As

such, using scrambled land initial conditions may have overridden any improvement from the atmospheric circulation. Antecedent land conditions have previously been identified via scrambled land experiments as crucial in the development of the extreme maximum temperatures observed in September 2013 (Arblaster et al., 2014), and may be a key factor in spring heat generally. However, scrambled land conditions do not explain the poor precipitation response or the further degradation in skill between the enhanced IOD experiment compared to the 1x composite experiment. As the evolution of the SST anomalies through the hindcasts helped us understand the ENSO-IOD relationships in the S2S models, we next explore how the SST responses in the experiments differ between the east pole and the west pole of the IOD.

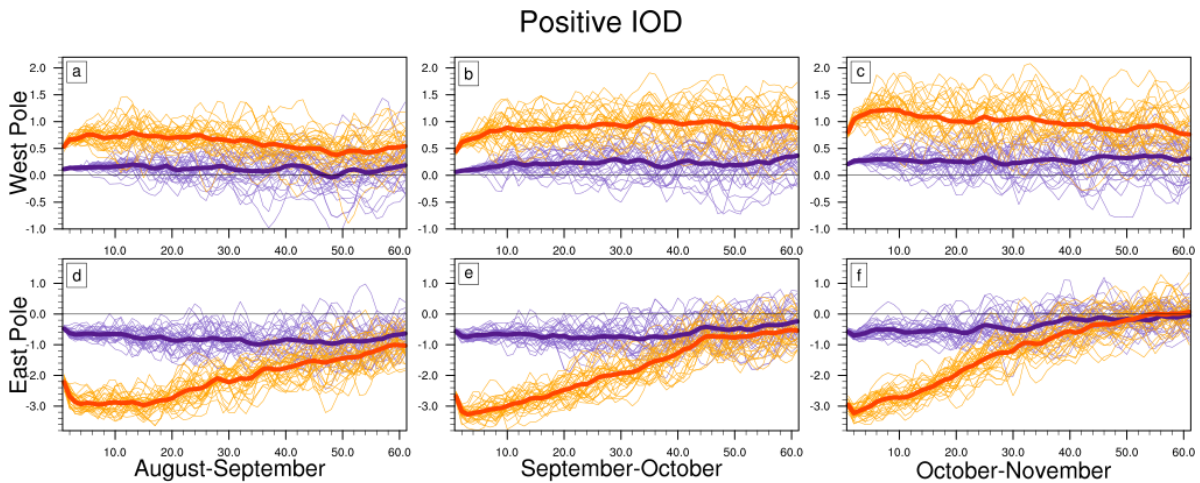


**Figure 4-21 Ensemble-member daily west- and east-pole indices from the positive IOD experiments**

West-pole (a-c) and east-pole (d-f) daily values over the first two months of the positive IOD experiments. Purple lines are DMI values from the single positive IOD composite experiment and orange lines are from the enhanced positive IOD composite experiment. The bold lines are the ensemble-mean values of each experiment. SST anomalies are relative to the corresponding daily-values of climatology experiment.

Note: East and west poles have different ranges.

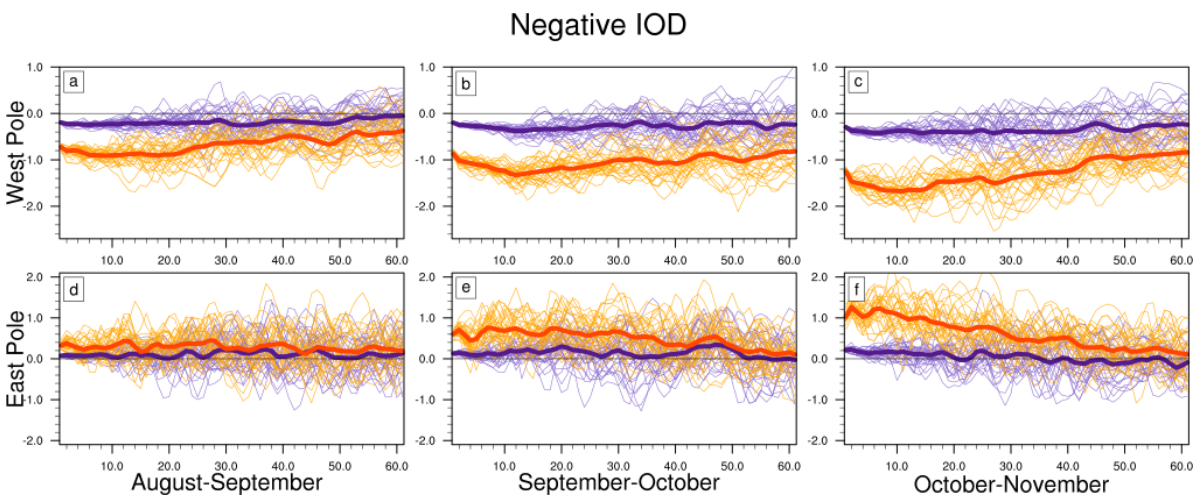


**Figure 4-21 As with Fig. 4-20, but for negative IOD experiments**

Note: Different ranges for the east and west poles.

The daily SST anomalies evolve differently in both the west and east DMI poles across the different IOD experiments. Daily DMI pole values are calculated for each ensemble member (relative to daily SST values from the climatology experiment) over the two months of each positive (Fig. 4-20) and negative IOD (Fig. 4-21) experiment. 1x (purple lines) and enhanced IOD (orange lines) ensemble members in each case begin to overlap soon after initialisation, with overlap beginning earlier if the initial DMI-pole anomaly was weak. In particular, there is little distinction between the 1x and enhanced negative IOD ensemble member east-poles within days of the August 1 initialisation (Fig. 4-21d). There is rapid change in the experiment ensemble-mean values (bold lines) in the first few days of each case, particularly when the initial pole magnitude is high, implying some model shock to the ocean initial conditions. After the shock eases, the 1x and enhanced IOD west-pole values (Figs. 4-20,4-21 a-c) remain near-constant, decaying slowly through the remainder of the two month runs. Conversely, the enhanced IOD experiment east-pole values (Figs. 4-20,4-21 d-e) quickly decay to be near-identical to the 1x experiment values by around day 40 (i.e. 10 days into the months used in the spring composite). The decay is particularly obvious in the enhanced positive IOD experiments (Fig. 4-20 d-f).

As the western Indian Ocean is more strongly linked with ENSO via atmospheric bridging (e.g. Shi et al., 2012), the relatively constant west-pole values may reflect a stabilising influence from remote tropical Pacific SSTs. However, as there is no clear difference in west-pole behaviour between positive IOD (with El Niño signal in the Pacific) and negative IOD (no La Niña) other factors may be more important, consistent with the weak west-pole-ENSO relationships in section 4.3.1. The eastern tropical Indian Ocean has a stronger internally-driven component (Shi et al., 2012; Lee et al., 2021), so the declining east-pole values may be how POAMA simulates internal ocean processes that restore the enhanced east-pole values toward the comparatively realistic 1x composite values. However, as the POAMA hindcast has an overly strong east-pole-ENSO relationship (table 4-2), the strong restoration to 1x composite values may be due to the ENSO forcing we expected for the west-pole. By the end of each two-month run, we see a switch from the east-pole being higher in magnitude to the west-pole being higher. This reversal in strength through the runs explains why the reconstructed spring west- and east-poles are closer in magnitude than observed and contributes to an overall strong positive IOD DMI value (table 4-5). Conversely, the daily west-pole values in the negative IOD experiments start at higher magnitudes relative to their east-pole counterparts, and dominate the reconstructed spring DMI value, more so than in observations (table 4-5).

The change in relative strengths between the west and east poles through each run may explain some aspects of the reconstructed spring atmospheric circulation patterns. The rapid decay of the tropical SSTs in the east-pole may induce a weaker atmospheric response (e.g. Hoskins & Karoly, 1981) toward the end of the positive IOD experiment run-time. However, the similarity in atmospheric teleconnections between the enhanced positive IOD experiment and the reanalysis composite (Figs. 4-11c-d vs. 4-17c-d) suggests any

weakening of the Rossby wave is slight. Branstator (2014) argued that a season-average extratropical Rossby wave teleconnection is the combined result of all daily tropical heating anomalies. As such, the wave pattern in the enhanced positive IOD experiment may be the average of an early-run unrealistically strong Rossby wave, a later-run unrealistically weak Rossby wave, and more consistent contributions from the stable west-pole. The asymmetry in the positive and negative IOD Rossby wave teleconnections (Fig. 4-18b,d; Cai et al., 2011a, 2012; Weller & Cai, 2013a) may be linked with a stronger initial zonal SST gradient between the west and east IOD poles in the positive IOD than in the negative IOD experiments. The east-pole SST anomaly is weaker in the negative IOD experiments, even when enhanced, and the enhanced value only just exceeds the observed value (table 4-5). As the east-pole magnitude is always lower relative to that in the positive IOD experiments it may not be a strong enough Rossby wave source in POAMA. Instead, the west-pole may act as the sole Rossby wave source, resulting in the wave train from near-Madagascar in Fig. 4-18d. However, as the enhanced negative IOD east-pole value is similar to the observed value, other factors, such as the strength or direction of the zonal SST gradient between the IOD poles, may be more important for realistic wave train initiation.

It is less clear how the differences in the model evolutions of west and east poles could induce the unrealistic maximum temperature and precipitation responses. We expect SSTs closer to Australia, (e.g. the east-pole), to have a greater impact on Australian spring climate (e.g. Watterson, 2010; Timbal & Hendon, 2011; van Rensch et al., 2019). This region could provide a moisture source for enhanced rainfall (e.g. Holgate et al., 2020a) that would change the land-surface heat balance and result in cooler spring conditions (e.g. Hope & Watterson, 2018; Hirsch & King, 2020). As such, changes in the east-pole SST could translate to different reconstructed spring maximum temperature and rainfall responses in Australia, even with improved atmospheric circulation forecasts. The rapid decay of the cold anomaly in the enhanced positive IOD may translate to weakening warming and drying in Australia through each run, resulting in a weak spring forecast overall. However, we would still expect warmer and drier conditions of similar magnitude and geographic coverage in both the enhanced and 1x positive IOD experiment, which is not the case (Fig. 4-19a-d). Warm east-pole anomalies in the negative IOD may lead to wetter and drier conditions in the reconstructed spring forecasts. The east-pole anomalies in the September and October initialisations of the enhanced negative IOD are stronger than those in the 1x negative IOD (Fig. 4-21e,f), and may have contributed to the cold anomaly in Australia's southwest in the reconstructed spring forecast (Fig. 4-19g), however, there are no corresponding wet anomalies (Fig. 4-19h). As such, the poor maximum temperature and precipitation in the IOD experiments relative to the POAMA hindcast composite remains unexplained.

#### 4.4.4 IOD experiment summary

We have shown that we can produce a better SON atmospheric circulation forecast in POAMA with an enhanced signal from the tropical Indian Ocean in the lead-1 initial conditions. The improvement was

stronger in the positive IOD case, which is likely a result of the stronger SST signal during these events. This improved atmospheric circulation forecast, however, did not correspond to a more realistic maximum temperature or precipitation response in Australia. It is unclear what causes this lack of improvement, though it does appear that POAMA treats the west and east DMI poles differently. The east-pole anomalies decay more quickly, resulting in a weaker reconstructed spring IOD, even when initially enhanced. The inclusion of the 1997 El Niño in the positive IOD initial conditions complicated the analysis and comparison with the negative IOD experiment and made it more difficult to isolate the role of the tropical Indian Ocean. However, the results are consistent with the tropical Indian Ocean playing an important role in the southern hemisphere spring atmospheric circulation.

We next try to refine these model results by comparing them to a second set of experiments with variability restricted to specific ocean domains.

## 4.5 Confined ocean variability experiments

In this final set of POAMA experiments, we use a seasonal forecast (August 1 initialisation for September-October-November rather than forecasts for each month) to avoid any potential contamination by the land-surface conditions (as noted in 3.2) and to ensure the ocean signal dominates the results.

### 4.5.1 Ocean variability experiment design

We use the same POAMA seasonal forecast system as in Section 3.2 to produce four-month forecasts from August 1 00UTC for each year from 1981 to 2018. Monthly time-varying observed levels of carbon dioxide are specified (from NOAA Mauna Loa observatory), as compared to the standard hindcast where a fixed 1985 value of 345 ppm was used. We create an ensemble of five members using perturbed atmosphere and land initial conditions (ICs) from 1981-2018. The ocean initial conditions in *specified domains* are similarly taken from 1981 to 2018, but ocean ICs are set to 1981 to 2010 climatology elsewhere.

We run four different experiments where ocean initial conditions vary between experiments in the tropical Indian Ocean (TIO), tropical Pacific Ocean (TPO), combined or 'whole' tropical Indian and Pacific Oceans (TWO) and combined or 'whole' extratropical Indian and Pacific Oceans (EWO) (See figure 15 for domain boundaries). The hypothesis is that this will allow us to quantitatively assess the relative impact of the tropical Indian Ocean variability over the past few decades. We note, however, that the oceans are free to evolve according to internal model dynamics after initialisation and will have some influence on the experiment outcome, despite starting from a climatological average.

We assess the outcome of these experiments by repeating the linear regression analysis from 3.1. Anomalies are calculated over a 1981-2010 climatology period within each experiment. The seasonal-spring DMI and Niño3.4 indices are standardised and all fields are linearly detrended before regression analysis. Statistical significance is assessed with a Student's t-test assuming 36 (38-2) independent samples.

Values presented are the ensemble-mean of each experiment.

	<b>Ocean Initial Conditions</b>	<b>Atmosphere and land initial conditions</b>	<b>CO<sub>2</sub></b>	<b>Ozone</b>	<b>Ensemble size</b>
<b>Tropical Indian Ocean (TIO)</b>	Initial conditions from August 1 1981-2018 for 20°N-20°S, 37°-105°E Climatology elsewhere	38 different conditions drawn from August 1 1981 – 2018	Varying August-average from 1981 to 2018	Monthly climatology	5
<b>Tropical Pacific Ocean (TPO)</b>	Initial conditions from August 1 1981-2018 for 20°N-20°S, 140°-275°E Climatology elsewhere				
<b>Combined Tropical Indian to Pacific (TWO)</b>	Initial conditions from August 1 1981-2018 for 20°N-20°S, 37°-285°E Climatology elsewhere				
<b>Combined Extratropical Indo-Pacific Ocean (EWO)</b>	Initial conditions from August 1 1981-2018 for 20°-50°S, 37°-285°E Climatology elsewhere				

**Table 4-6 Confined ocean variability experiment initial conditions**

1. Monthly CO<sub>2</sub> levels are from Mauna Loa observatory (<https://gml.noaa.gov/ccgg/trends/>)

#### 4.5.2 Ocean variability experiment results

The seasonal forecast SST anomalies regressed onto the DMI, with and without ENSO's influence, are presented in Fig. 4-22. Surprisingly, despite ocean conditions only varying in the tropical Indian Ocean

domain in the TIO experiment, the positive IOD-like SST anomalies in the tropical Indian Ocean (Fig. 4-22a) are weaker than in the other experiments. This weak regression can be partly explained by the TIO domain excluding part of the DMI east-pole by 5° longitude (Fig. 4-15). As the eastern tropical Indian Ocean has the strongest variability (e.g. Lee et al., 2021), this oversight in experimental design may reduce both the IOD strength and atmospheric circulation responses in the TIO experiment. Further, as we have seen earlier in this chapter, the ocean anomalies in the Indian Ocean tend to decay faster in POAMA than in other basins, also weakening the seasonal spring regression. Strong El Niño SST anomalies in the TPO, TWO and EWO (Fig. 4-22b-d) all vanish with the removal of ENSO, leaving only weaker IOD-like SST conditions in the tropical Indian Ocean in all experiments (Fig. 4-22e-h). Curiously, despite tropical ocean initial conditions being held constant in the EWO experiment (Fig. 4-22d), the seasonal spring SST anomalies in the tropics are nearly identical to those in the TPO and TWO regressions. However, there are small cold SST anomalies in the high latitudes in the partial regression in the EWO (Fig. 4-22h) experiments that are absent in the other experiments, suggesting that these similarities may be driven by internal model ENSO-dynamics.

Consistent with the regressions onto the SST, the regression in the TIO experiment (Fig. 4-23 a, b) are far weaker than in the other experiments (Fig. 4-23 c-h) or POAMA hindcast regression (Fig. 4-3 g-h). A very weak, and not statistically significant, barotropic wave train can be found in the TIO experiment from an upper-cyclone west of Australia, anticyclone south of Australia, and cyclone south of New Zealand. The wave train appears to continue to propagate over the southern Pacific Ocean. In contrast, the regressions in the other experiments have deep MSLP and 200Z anomalies but are dominated by an unrealistically strong and spatially-broadened PSA-like pattern, with little activity over the Indian Ocean. In particular, these experiments fail to capture the weak wave train found in the TIO experiments, and appear to be exaggerated examples of the POAMA hindcast regressions onto the IOD (Fig. 4-3 g-h).

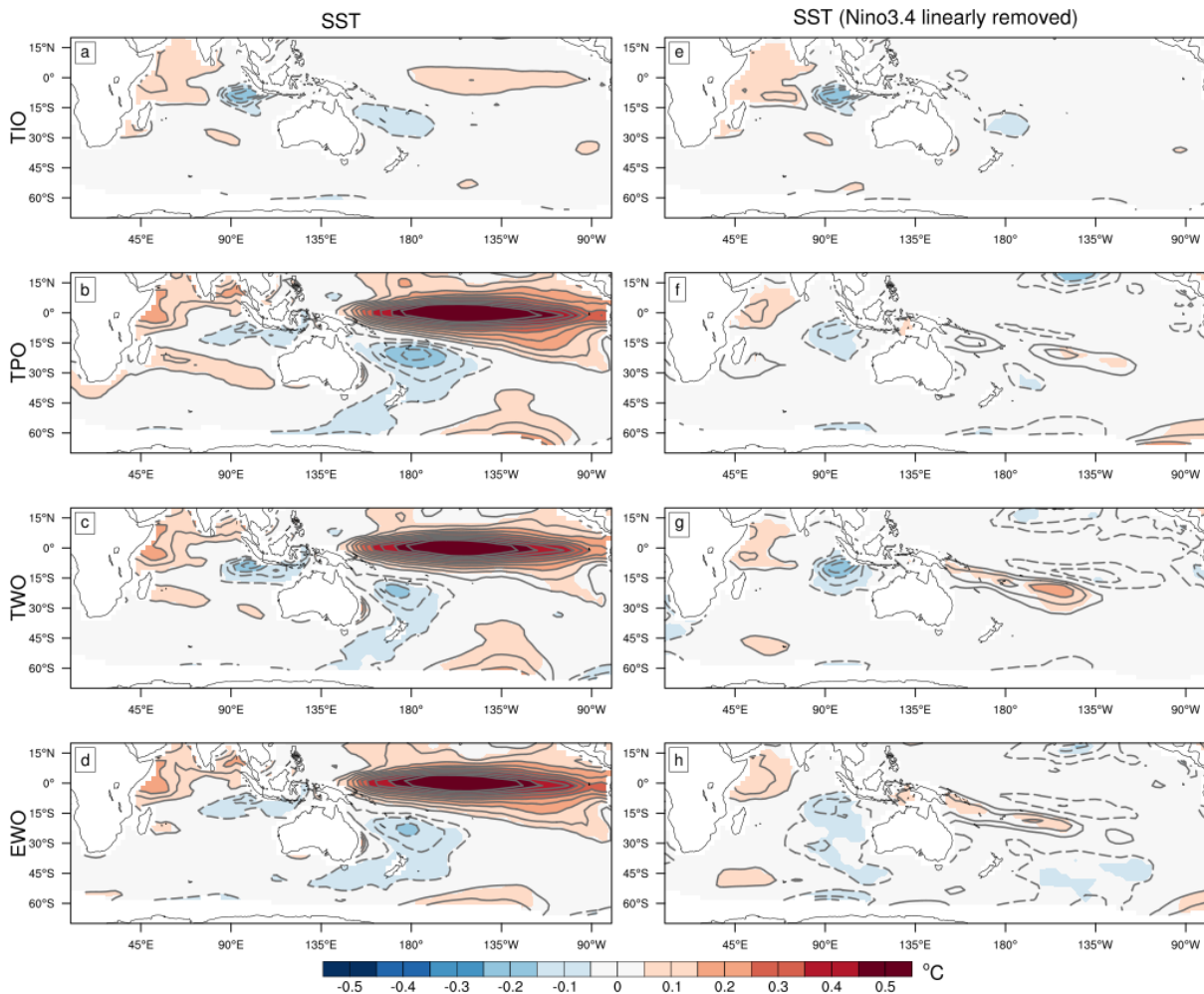


**Figure 4-22 Confined-variability experiment lead-1 seasonal-spring SST regressions onto DMI and partial DMI**

August 1-initialised seasonal-spring forecast DMI (a-d) and partial DMI (Niño3.4 linearly removed) regressed onto SST anomalies in the tropical Indian Ocean (TIO: a,b), tropical Pacific Ocean (TPO: c,d), combined tropical ocean (TWO: e,f) and combined extratropical ocean (EWO: g,h) POAMA experiments over the years 1981 to 2018. Anomalies are relative to a 1981-2010 climatology calculated per experiment. Filled contours show where the regression was statistically significant at the 90% confidence level, calculated with a Student's t-test using 36 (38-2) independent samples.

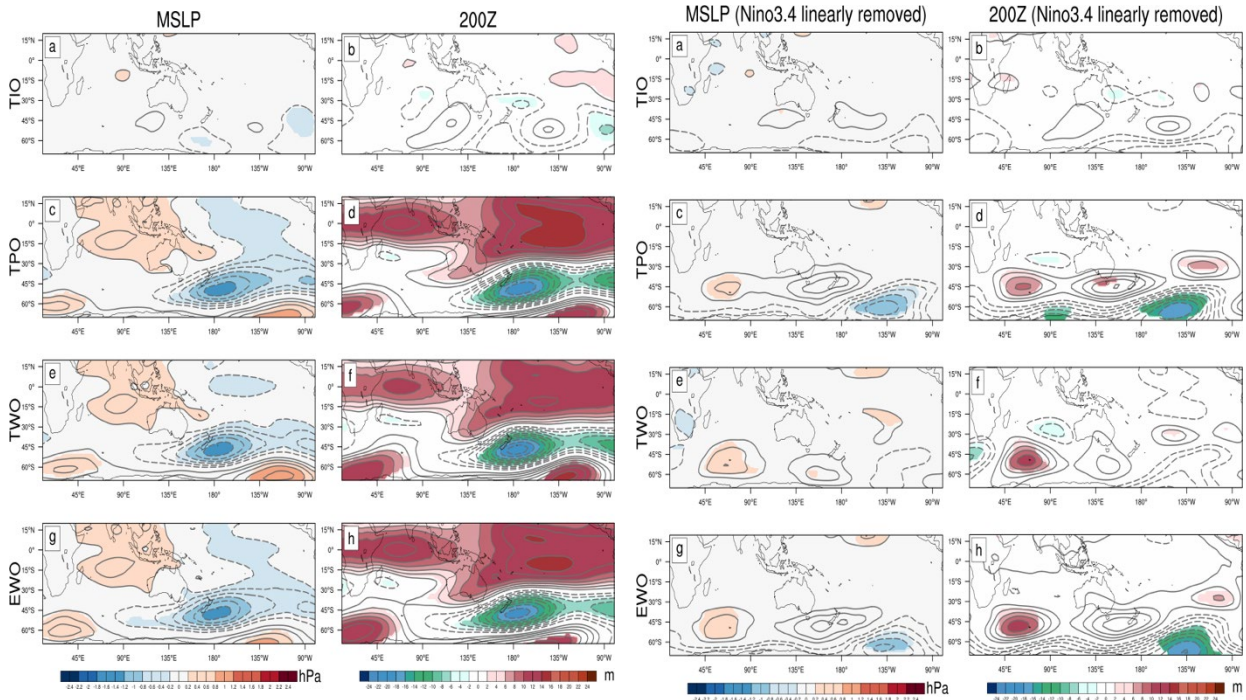


**Figure 4-24** As in Fig. 4-22 but for seasonal spring DMI regressed onto circulation anomalies.

**Figure 4-24** As in Fig. 4-23 but with seasonal Niño3.4 index first linearly removed.

MSLP (left; hPa); 200hPa geopotential height (right; m).

Linearly removing ENSO from the IOD regressions (Fig. 4-24) reveals a more IOD-like teleconnection in all the experiments. The partial regressions in the TIO are further weakened, though still has an anomalous barotropic anticyclone south of Australia (Fig. 4-24a,b). The TPO and TWO experiments (Fig. 4-24c-f) show an apparent Rossby wave from an upper-level cyclone in the eastern tropical Indian Ocean to an anticyclone south of Australia and cyclone south of New Zealand. The EWO (Fig. 4-24 g,h) has a similar wave train, but lacks the upper-level cyclone in the tropical Indian Ocean across Australia. The EWO, TWO, and TPO all have anomalously high MSLP in the southern Indian Ocean where we would expect low MSLP. Overall, the tropical Pacific Ocean continues to dominate the POAMA atmospheric circulation response, but it does seem that isolating the tropical Indian Ocean variability extracts the teleconnections from the tropical Indian Ocean in POAMA, but only weakly.

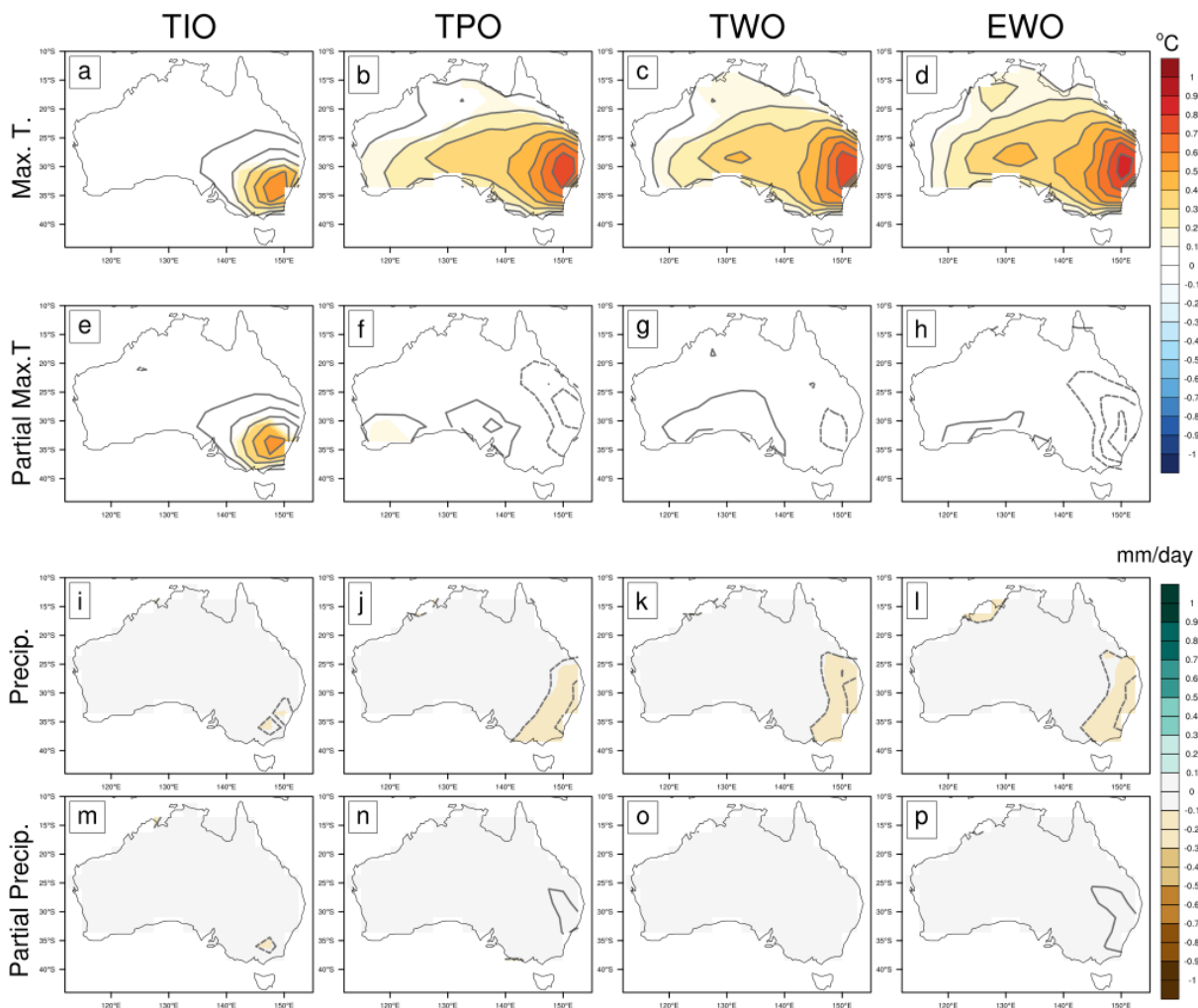


**Figure 4-25** As in Fig. 4-22 but for maximum temperature ( $^{\circ}\text{C}$ ) and precipitation ( $\text{mm/day}$ )

Similar to the hindcast regression (Fig. 4-5 g,h), anomalously high spring maximum temperature and low precipitation associated with the IOD are confined to the southeast of Australia in each experiment (Fig. 4-25), contrasting with the more widespread anomalies in reanalysis (Fig. 4-2a,b). Consistent with the weak atmospheric regressions, the TIO maximum temperature and precipitation anomalies (Fig. 4-25a,j) are weaker than those in the other experiments. Removing Niño3.4 from the regression only weakens the response from the TIO experiment (Fig. 4-25 e,m) but switches the sign of the (no longer statistically significant) maximum temperature and precipitation response in the east in the other experiments (Fig. 4-25 f-h; n-p). However, there are now weak and not statistically significant warm anomalies found in the central-south and southwest (e.g. Risbey et al., 2009a) in the TPO and TWO experiments that are absent in the hindcast partial regression (Fig. 4-6 g,h) and TIO experiment. We next explore how the ENSO and IOD SSTs across the experiments help explain the atmospheric and Australian land teleconnections.

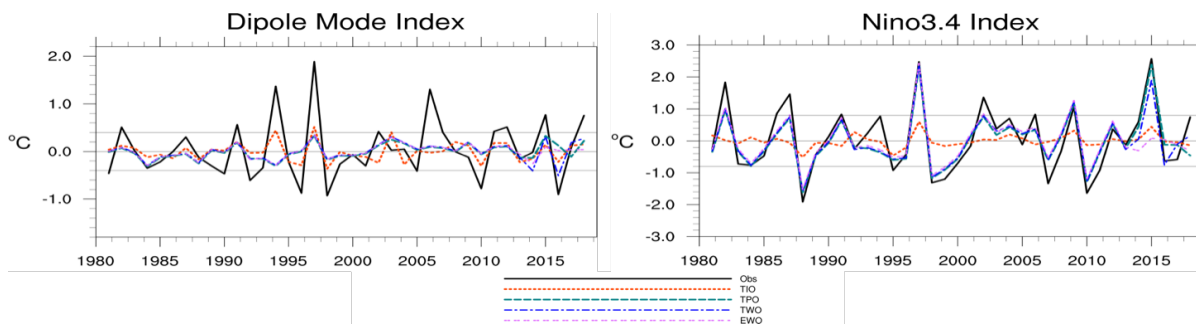


**Figure 4-26 Lead-1 seasonal spring DMI and Niño3.4 time series for the different constrained variability experiments**

*DMI and Niño3.4 are for August-1 spring-season forecasts from the tropical Indian Ocean (TIO; red short-dashed lines), tropical Pacific Ocean (TPO; green long-dashed lines), combined tropical ocean (TWO; blue short-long dashed lines) and combined extratropical ocean (EWO; purple double-dash lines) POAMA experiments over the years 1981 to 2018. Anomalies are relative to an in-experiment 1981-2010 climatology.*

The seasonal spring DMI time series for the ocean variability experiments are shown in Fig. 4-26. The TIO, and to a lesser extent the TWO, match the observed IOD variability, as peaks and troughs in the DMI generally match the observed peaks and troughs. However, all experiments significantly underestimate the observed DMI magnitude. All but the TIO experiment reproduced the variability and magnitude of the observed spring Niño3.4 index. A weak DMI time series in the TIO experiments is consistent with the weak regressions onto the atmospheric circulation and Australian maximum temperature. However, as the corresponding Niño3.4 has such weak variability, by design, even the unrealistically weak IOD is stronger than ENSO in these experiments, helping explain the IOD-like teleconnections (Fig. 4-23b). Conversely Niño3.4 variability and strength far exceed that of the IOD in the other experiments. We next explore the differences in the daily west- and east-pole, and Niño3.4 region SST evolution across the experiments to better understand how IOD and ENSO signals can persist in the full and partial regressions, even as the Indian or Pacific Ocean variability is constrained.

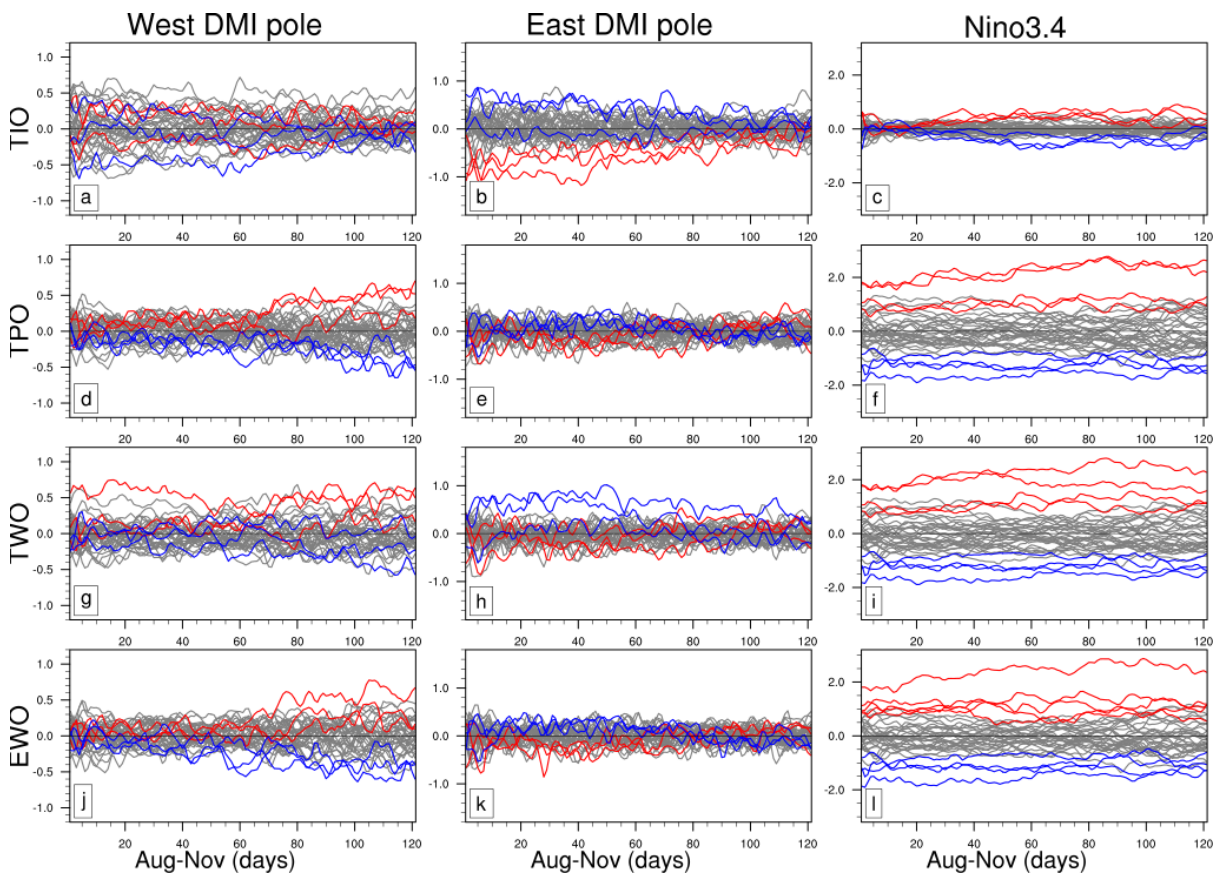


**Figure 4-27 Daily values of west- and east- DMI poles and Niño3.4 indices from the confined variability experiments**  
 Values are for each day of each August-initialisation of the tropical Indian Ocean (TIO; a-c), tropical Pacific Ocean (TPO; d-f), combined tropical ocean (TWO; g-h) and combined extratropical ocean (EWO; j-l) experiments from 1981 to 2018. Red and blue lines are model-experiment positive IOD/El Niño and negative IOD/La Niña springs. Here, IOD events were defined as the top and bottom 10% model-experiment seasonal forecast DMI index values per experiment. ENSO events were defined in the same way for the TIO experiment, and as when the seasonal forecast Niño3.4 index was greater (below) + (-) 0.8°C in the other experiments. All neutral years are in grey. Anomalies are relative to a model-experiment 1981-2010 climatology period. The horizontal line at 0°C shows where the DMI and Niño3.4 indices anomalies go to zero.

The evolution of the SST anomalies in the west- and east- poles of the IOD, and the Niño3.4 region through each experiment initialisation is displayed in fig. 4-27. As in section 4.3.1, positive IOD and El Niño events are coloured red, negative IOD and La Niña are coloured blue, and neutral springs are coloured grey. Here, however, positive and negative IOD events are defined as the top and bottom 10% experiment seasonal spring DMI time series respectively. As all but the TIO experiment simulated the observed Niño3.4 timeseries, ENSO events are described using the threshold of +/- 0.8°C, as in section 4.3.1. El Niño and La Niña events in the TIO experiment are defined as the top and bottom 10% of Niño3.4 years, respectively.

All experiment daily SST anomalies (Fig. 4-27) are weaker in magnitude than the corresponding S2S anomalies (Figs. 4-8 to 4-10), with the exception of the TPO, TWO, and EPO Niño3.4 anomalies. There is

little distinction between IOD events in the west-pole values (Fig. 4-27 a,d,g,j). However, the TPO and EWO, and to a lesser extent the TWO, west-pole anomalies begin to gain magnitude from around day-70 in both positive and negative IOD events, suggesting feedback from the other ocean basins, and likely the Pacific Ocean in particular. The TIO and TWO east-pole values (Fig. 4-27b,h) show greater spread between ‘negative’ and ‘positive’ IOD years than in the west-pole (Fig. 4-27, a,g), suggesting again that the east-pole is important for determining IOD strength. However, there is overlap between daily east-pole values for IOD-events and neutral spring years in these experiments and the east-pole values decay toward zero from around day 80. The daily Niño3.4 indices show strong and clear distinction between ENSO events in all but the TIO experiment (Fig. 4-27 f,i,l), consistent with the strong atmospheric anomalies in the IOD regressions. Interestingly, there is weak growth of Niño3.4 SSTs through spring in the TIO experiment (Fig. 4-27c), possibly suggesting some feedback of the tropical Indian Ocean onto the Pacific Ocean, as found in the enhanced IOD experiments (Fig. 4-16). Overall, the tropical Pacific Ocean remains dominant in POAMA, particularly once the east-pole anomalies decay in the TIO and TWO experiments. As such, the teleconnections have relatively stronger influence from the tropical Pacific Ocean, resulting in a stronger relationship to ENSO in the model experiments.

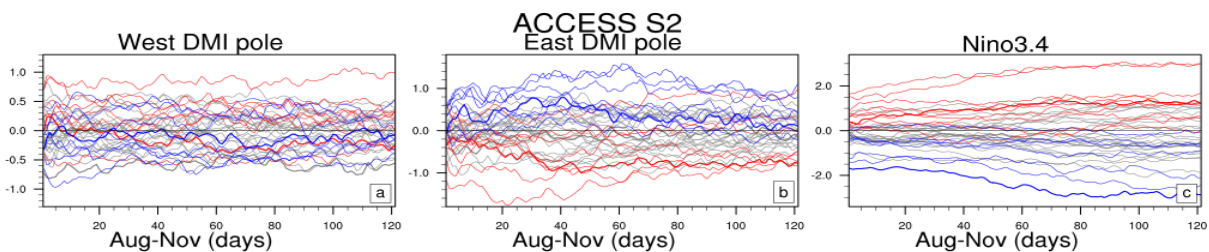


**Figure 4-28 As with Fig. 4-27 but for the ACCESS-S2 hindcast (from 1981 to 2018)**

*The daily ACCESS-S2 values are composed of a three-member ensemble, and SST anomalies were calculated against a daily climatology. Red and blue lines show all positive IOD/El Niño and negative IOD/La Niña as defined by the Australian Bureau of Meteorology (see: <http://www.bom.gov.au/climate> )*

IOD events decay abruptly around monsoon onset, usually around December (e.g. Meyers et al., 2007), so, while we expect east- and west-pole SST anomalies to decay quickly, it seems that POAMA may be ending IOD events prematurely. For comparison, the west- and east- pole SST and Niño3.4 SSTs from the latest generation of the Australian seasonal forecast system, ACCESS-S2 (table 4-1; Hudson et. al., 2017) are in figure 28. These IOD pole values do not decay prematurely. However, ACCESS-S2 does appear to rapidly grow the Niño3.4 index, introducing a similar issue as seen in the UKMO and KMA models in section 4.3.1. As ACCESS-S2 uses ocean data from the same GloSea model-family as the UKMO and KMA, this change in how ENSO may dominate the IOD is not unexpected, but will need to be considered in future work using ACCESS-S.

### 4.5.3 Ocean variability experiment summary

In this section, we attempted to understand the relative influence of the tropical Indian Ocean on Australia's maximum temperatures by re-running the POAMA hindcast with ocean variability confined to certain domains in initial conditions. These experiments suggest that the tropical Indian Ocean only drives a very small part of the atmospheric teleconnections that lead to anomalous high maximum temperatures in Australia in spring. However, the relative strength and maintenance of the Niño3.4 SSTs in POAMA compared to the decay in the west- and east- IOD poles (as well as some experiment design issues), make it difficult to dismiss the Indian Ocean. Further, while the TIO experiments did only produce weak atmospheric circulation associated with the IOD, the teleconnection pattern from the tropical Indian Ocean was significantly closer to the reanalysis than in the other experiments. Also, including the tropical Indian Ocean in the combined tropical experiment did produce more distinct high and low patterns in the partial regression, suggesting a step closer toward the reanalysis pattern. At least some of this improvement may be due to the the east-pole region being included in its entirety, in contrast to the incomplete region in the TIO experiment. While the SSTs north of Australia and through the Maritime Continent in the TWO experiment likely also contributed to the improved responses (Watterson, 2010; Hendon et al., 2010; Timbal & Hendon, 2011; van Rensch et al., 2019), the results are consistent with the tropical Indian Ocean contributing to the forecast atmospheric and Australian anomalies.

The strength of the Indian Ocean variability compared to that of the Pacific Ocean may be another factor impacting the efficacy of the TIO experiment. The observed SST standard deviation across the tropical Indian Ocean basin is dwarfed by the ENSO signal in the Pacific but is stronger than in the POAMA hindcast (not shown). As such, it would not be difficult for tropical anomalies in the Pacific to dominate over those in the Indian Ocean in POAMA. Selecting a region for the TIO experiment that reduced the east-pole anomaly likely further weakened the Indian Ocean signal in the experiment. Combined with the biases found here in how POAMA simulates the west and east DMI poles compared to how it maintains the ENSO anomaly, it is not surprising that these experiments did not result in a strong Indian Ocean signal.

## 4.6 Discussion and chapter conclusion

We have shown through analysis of hindcasts and two experiments using seasonal prediction systems that the tropical Indian Ocean plays a relatively small, though arguably important, role in Australian maximum spring temperature development. The tropical Pacific Ocean, represented by ENSO, particularly dominates the tropical Indian Ocean signal, represented by the IOD, in each of the three approaches used in this chapter. As ENSO is the strongest driver of interannual variability in Australia (e.g. Meyers et al., 2007; Risbey et al., 2009a) and the strongest source of predictability (Merryfield et al., 2020; Meehl et al., 2021) the ENSO dominance may not be surprising. Recent coupled and uncoupled model simulations using

CESMv1.1 by Liguori et al. (in review) with suppressed variability in either the tropical Pacific or Indian Ocean regions suggest that the tropical Pacific Ocean's influence on Australia's rainfall far exceeds that of the tropical Indian's. However, while the tropical Indian Ocean's role in Australia's spring climate may not be as strong as initially expected, it also cannot be dismissed. First, ENSO SSTs tend to be too strong relative to the IOD in the seasonal prediction models, suggesting that they overestimate ENSO's influence on the climate. Second, enhancing or isolating the tropical Indian Ocean signal in the different POAMA experiments resulted in more realistic atmospheric teleconnections, if not Australian spring forecasts. Finally, the experiments with enhanced and isolated tropical Indian Ocean initial conditions appear to feedback on and enhance the ENSO signal in the Pacific Ocean. Indian Ocean feedbacks may improve predictability of both ENSO and IOD events (Klein et al., 1999; Ashok et al., 2001; Yu et al., 2002; Kug, 2005; Shinoda et al., 2004; Luo et al., 2010; Lim & Hendon, 2017; Stuecker et al., 2017; Guo et al., 2018; Wang, H. et al., 2019). Overall ENSO may be the primary driving force behind the broad strokes of the spring atmospheric circulation and Australia's maximum temperature variability, but the tropical Indian Ocean is key to the details. Results are summarised in table 4-7 and figure 4-29.

The use of one-month lead seasonal prediction systems in this chapter was chosen to highlight the role of the ocean but may have underestimated the contribution of the tropical Indian Ocean in the spring atmospheric circulation and Australia's maximum temperatures. In general, coupled models tend to overestimate the strength and variability of the IOD (e.g. Cai & Cowan, 2013; McKenna et al., 2020), contrasting with our results. However, as we are using seasonal forecasts for our analysis, the memory of the observation-based initial conditions in the tropical Indian Ocean appears to decay very quickly, compared to those in the tropical Pacific, such that the IOD strength and variability are reduced in the lead-1 forecast output. Hence, we do not find as strong a relationship in these models as may be found in observations or other model experiments. Uncoupled or partially coupled models with SSTs restored to observed or climatological conditions at each time step may provide the benefits of realistic tropical Indian Ocean conditions without the unrealistic decay or growth in initial conditions. Such model studies have previously been used to understand the relationships between the Indian, Pacific and Southern Ocean to Antarctic sea-ice (e.g. Purich et al., 2019, 2021; Purich & England, 2019) or the tropical Indian Ocean on Australian summer rainfall (Taschetto et al., 2011). Further, running prescribed SST atmosphere-only models can result in a cleaner estimate of the Indian Ocean's influence on the climate without ocean-atmosphere feedbacks. While earlier studies have successfully run experiments with POAMA at lead times ranging from zero-to several months it is unclear whether similarly decaying Indian Ocean conditions were a factor in their results (e.g. Lim & Hendon, 2017; Lim et al., 2019b). While our findings do agree with those of Liguori et al., (in review) it is important to recall that the CESM model poorly represents the ENSO-IOD relationship (Wiener, et al., 2019), which needs to be considered, just as the under-represented IOD variability needs to be considered in interpreting our results.

r-values	Observed	S2S				Indian Ocean Variability			
		HMCR	UK	KMA	PHC	TIO	TPO	TWO	EWO
Partial DMI vs E-W pole OLR	0.61	N/A	N/A	N/A	0.58	0.70	0.33	0.31	0.25
Partial DMI vs Z200 S of Aus.	0.20	0.30	0.02	0.06	0.17	0.01	0.18	0.12	0.20
Partial Niño3.4 vs Z200 S of Aus.	-0.02	-0.28	0.17	0.17	-0.18	0.14	0.33	0.43	0.32
E-W pole OLR vs Z200 S of Aus.	0.35	N/A	N/A	N/A	-0.07	0.03	0.61	0.61	0.57
Z200 S of Aus. vs Aus. Max. T	0.29	0.06	0.43	0.24	0.21	0.14	-0.30	0.34	0.27
Partial DMI vs Aus. Max. T	0.27	-0.18	-0.10	0.17	0.08	0.14	0.01	0.04	-0.02
Partial Niño3.4 vs Aus. Max. T.	0.17	0.03	0.35	0.37	0.47	0.05	0.44	0.44	0.53

**Table 4-7 Correlation between indices in Fig. 4-29**

**Figure 4-29 Chapter summary of relationships in observations and models**

Scatter plot of SON variables from observations (1<sup>st</sup> column), S2S models (2<sup>nd</sup> column), IOD-experiment ensemble members (3<sup>rd</sup> column), and Indian Ocean variability experiment ensemble members (4<sup>th</sup> column).

1<sup>st</sup> row: Partial (Niño3.4 index linearly removed) DMI vs OLR east-west pole gradient. OLR gradient was calculated by subtracting OLR averaged over the DMI east pole (0°S to 10°S; 90°E to 110°E) from that averaged over the DMI west pole (10°N to 10°S; 50°E to 70°E).

2<sup>nd</sup> row: Partial (Niño3.4 index linearly removed) DMI vs 200hPa geopotential height averaged over a region south of Australia (30°S to 60°S; 120°E to 150°E) to match the Rossby wave node.

3<sup>rd</sup> row: Partial (DMI linearly removed) Niño3.4 vs 200hPa geopotential height averaged over a region south of Australia

4<sup>th</sup> row: East-west pole gradient OLR vs 200hPa geopotential height averaged over a region south of Australia

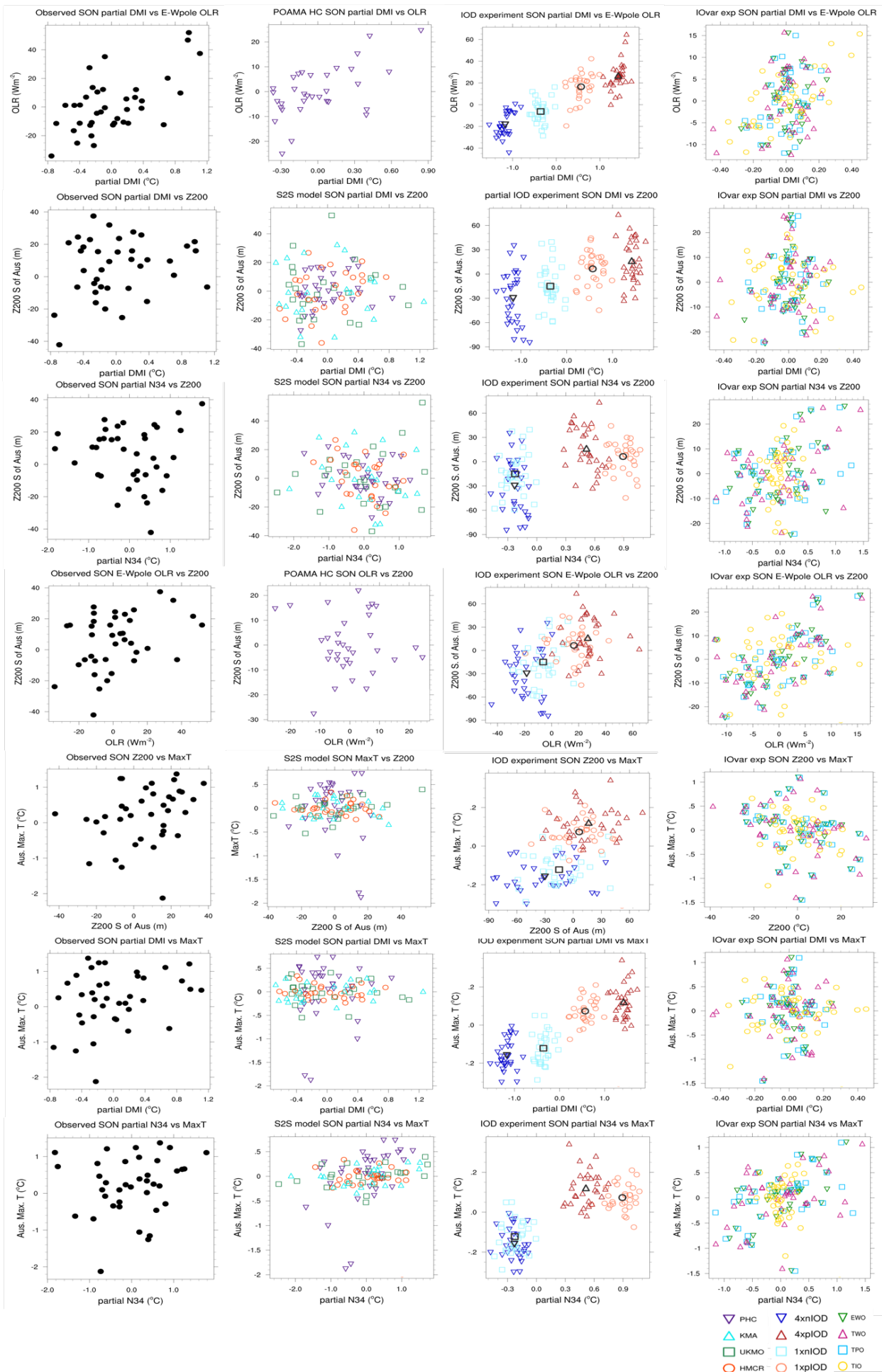
5<sup>th</sup> row: 200hPa geopotential height south of Australia vs Australian-averaged maximum temperature

6<sup>th</sup> row: Partial (Niño3.4 index linearly removed) DMI vs Australian-averaged maximum temperature.

7<sup>th</sup> row: Partial (DMI linearly removed) Niño3.4 vs Australian-averaged maximum temperature.

Note: OLR data was not available for the S2S models due to database outage between February 2022-June 2022

Observed values are in black, experiment values are identified in legend in bottom right of the figure.



The relationships found in this chapter between the tropical Indian Ocean, the atmosphere, and Australia's spring maximum temperature in the observations and models are summarised in Fig. 4-29. Starting with the observed relationships (left column), there is a clear and strong baroclinic (i.e. warm SST generates increased convection and a negative OLR anomaly) relationship between OLR and the partial IOD suggests that the tropical Indian Ocean, even in the absence of ENSO-forcing, is driving anomalous atmospheric convection over this region. The strong relationship between this OLR anomaly and the 200hPa geopotential height averaged south of Australia suggests that the tropical Indian Ocean is at least a key factor in generating this wave train. Further, as this height anomaly correlates well with Australian maximum temperature, these figures are consistent with the tropical Indian Ocean being a key factor in Australian spring maximum temperatures. The models and model experiments broadly simulate the relationships between the tropical Indian Ocean, the height anomaly south of Australia, and spring maximum temperatures in Australia. However, with ENSO removed the teleconnection correlations weaken considerably, suggesting that, in the models, ENSO is the main driver and the tropical Indian Ocean forcing is too weak, relative to observations.

The overly weak IOD at one-month lead time was the largest constraint in this study, but how that weakness manifested in the DMI poles and their relationships to ENSO suggest starting points for future work. The ocean-atmosphere coupling in the Indian Ocean involves complicated feedbacks between the South-Asian monsoon easterly winds and ocean upwelling near Java-Sumatra (e.g. Meyers et al., 2007) that can contribute to model biases (e.g. Cai & Cowan, 2013; Weller & Cai, 2013b; Li, G. et al., 2015). Here, the relationships between ENSO and the east- and west- poles were generally not well simulated in the seasonal prediction models, suggesting they have similar issues. Exploring how these models simulate the Indian and Pacific Ocean thermocline, particularly through the experiments, as well as changes to the Walker Circulation and atmospheric bridging from Pacific to Indian (e.g. Klein et al., 1999) could both improve our understanding of why the IOD strength decays relative to that of ENSO. Comparing these forecast model results with similar experiments in uncoupled models with prescribed SSTs would also be beneficial. Overall, the use of a seasonal prediction system in our experiments suggests that they can struggle to simulate the strength of the IOD teleconnection to Australia due to fast decay of the IOD and consequent dominance of ENSO. However, the apparent improvement in the atmospheric circulation in response to enhanced IOD suggests a potential avenue for improvements in future generations of seasonal prediction systems, such as the new ACCESS-S model.

## 5 Thesis Conclusions and Discussion

This thesis aimed to understand the drivers of atmospheric circulation associated with anomalously high maximum temperatures in Australia in spring. This aim was addressed through the use of reanalyses and seasonal hindcasts of the recent decades. Drivers that promoted different atmospheric circulation configurations, and the consequent Australian maximum temperature in these datasets were compared across three spring heat events, linear regression analysis over spring-month and -season time scales, and two sets of dynamical model experiments.

As the overall thesis was structured around three research questions, this chapter begins by describing how these questions were addressed, before summarising the overall thesis findings. The chapter concludes with a discussion of the broader implications of the thesis' results, the caveats to these findings, and the potential extensions of this research.

### 5.1 Addressing the research questions

The first research question (RQ 1) asked: What drove the atmospheric circulation that contributed to three of Australia's most extreme spring heat events in observations and POAMA?

RQ1 was addressed in chapter 2 by comparing the atmospheric circulation of three different spring anomalous heat events (September 2013, October-November 2014, and October 2015) in reanalysis to that in the best and worst performing POAMA ensemble members. On top of the previously identified contribution of the background warming trend to the heat (e.g. Arblaster et al., 2014; Hope et al., 2015, 2016; Gallant and Lewis 2016), we identified several important drivers of the heat across these events: barotropic cyclones southwest or southeast of Australia; Tasman Sea anticyclonic blocking; a quasi-stationary Rossby wave that propagated from the tropical Indian Ocean to promote anticyclonic upper-height anomaly over southern Australia. Further, there were indications that the atmospheric circulation associated with heat has more forcing from the extratropics in early spring and more forcing from the tropics in later spring, possibly in association with the seasonal subtropical jet decay.

The second research question (RQ2) asked: How do the remote drivers of variability and dynamical mechanisms that promote anomalous Australian maximum temperature vary across the months of spring?

RQ2 was addressed in chapter 3 through the use of linear regression analysis of monthly reanalysis data, and led to more generalised findings around how the atmospheric dynamics and mechanisms associated with Australian surface heat change through spring than were possible in the previous chapter. Barotropic cyclones southwest or southeast of Australia, and an upper-level anticyclone over southern Australia were confirmed as key atmospheric circulation features associated with spring high maximum temperature. The relative importance and configuration of these features changes through spring, and appear more related with the extratropics in early spring and the tropics in later spring. However, rather than this change in

apparent forcing being related to the subtropical jet decay as was initially hypothesised, it appears the true reason is more subtle. The dynamical mechanisms that promote heat in Australia, such as subsidence and advection, also change from September to November, and it is these mechanisms that project more onto extratropical or tropical forcing. So, the subtropical jet decay may be more coincidental with the apparent transition to greater tropical forcing, rather than causal. Instead, the subtropical jet may have a greater role in Australia's climate as a waveguide, helping guide Rossby waves initiated remotely toward Australia.

The third, and final, research question (RQ3) asked: What is the influence of the tropical Indian Ocean on Australian maximum spring temperature development?

RQ3 was addressed in chapter 4 through the analysis of several sub-seasonal model hindcasts and two sets of experiments using POAMA that were designed to isolate the tropical Indian Ocean. The tropical Indian Ocean appears to play some role in Australian spring maximum temperature variability, though the findings in this chapter suggests that this role is minor, particularly relative to the tropical Pacific Ocean. However, the IOD signal quickly weakens in the seasonal prediction models, relative to the ENSO signal, such that ENSO may have an overly strong influence on the forecasts. As such, the role of the tropical Indian Ocean in Australia's spring maximum temperatures may be larger in reality than identified here. In particular, enhancing the IOD signal in POAMA did produce a more realistic atmospheric circulation teleconnection, suggesting that it may be possible to compensate for the unrealistic decay of the Indian Ocean initial conditions in this model. As such, compensating for ocean initial condition decay may lead to improved sub- seasonal and seasonal forecasts, as well as a more realistic estimation of the relative influence of the tropical Indian Ocean on the climate.

## 5.2 Thesis synthesis

The research in this thesis has advanced the understanding of the drivers that promote anomalous high spring maximum temperatures in Australia. Previously, studies tended to focus on remote drivers and dynamics of Australian spring rainfall variability (e.g. Risbey et al., 2009a; Cai et al., 2011a; Hendon et al., 2014; McIntosh & Hendon, 2017), with maximum temperature studies generally limited to statistical relationships (e.g. Saji et al., 2005; Hendon et al., 2007; Min et al., 2013). Consistent with these earlier studies, this thesis has confirmed that the main drivers of climate variability in Australia; ENSO, the IOD, and SAM (e.g. Risbey et al., 2009a), are linked with Australian maximum temperature, but explain a relatively low percentage of variability through spring (e.g. Saji et al., 2005). Instead, dynamical mechanisms, such as low-level advection or subsidence, can more completely explain anomalous high maximum temperatures. Further, how these mechanisms promote heat changes through spring, and the corresponding configuration of the atmospheric changes too.

The formation of the atmospheric circulation associated with anomalous high maximum temperatures over Australia was understood through the use of Rossby wave theory. Comparing wave trains associated with Australian maximum temperature to those propagating from the extratropics and tropics improved our overall understanding of the regions that promote the atmospheric circulation associated with anomalous high temperatures through spring. In particular, quasi-stationary Rossby waves driven by convection over the tropical Indian Ocean appear important for driving the atmospheric circulation associated with high maximum temperatures. While it remains unclear to what extent the tropical diabatic heating associated with these waves is driven by internal Indian Ocean processes or remotely by the tropical Pacific and other ocean basins, it is clear that the tropical Indian Ocean is important for Australia's spring maximum temperatures.

This thesis made novel use of seasonal prediction systems, primarily POAMA, to add depth to the research beyond what is possible from reanalysis alone. Seasonal prediction systems have several advantages over general climate models, including using observation-based initial conditions such that their hindcasts and forecasts are estimates of real-world climate events. As such, the POAMA hindcast ensemble-members and POAMA experiments were used to test Australia's spring climate in 'alternate realities'. Using POAMA in this way contributed to this thesis' findings around the components of the atmospheric circulation that are important for Australian maximum temperature generation, and the importance of the tropical Indian Ocean in driving that circulation. This method also led to unexpected findings around biases in the POAMA system. The atmospheric circulation over the Indian Ocean is not well represented in POAMA and the 'memory' of the Indian Ocean initial conditions is lost more quickly than those of the Pacific Ocean, contributing to the overly strong relationship with ENSO noted by earlier research (White et al., 2014). Improving these aspects in future generations of seasonal prediction systems may lead to improvements in sub- to seasonal forecasts. While these findings are useful for improving future forecast systems, they did limit POAMA's overall effectiveness in understanding the atmospheric circulation of Australian maximum temperature. Limitations around the use of seasonal prediction systems are discussed in section 5.3.3.

### 5.3 Implications, caveats and future work

We conclude this thesis with a discussion centred around four themes relevant through this thesis: heat mechanisms and remote drivers of variability, linear Rossby wave theory, dynamical modelling, and the ongoing impacts of anthropogenic climate change. These themes highlight areas where our work was either limited by scope or experimental design or where our work could lead to in future research.

### 5.3.1 Other heat drivers and mechanisms not considered

We considered only a subset of the tropical remote drivers of variability that influence Australia's spring climate. We focussed on the tropical Indian and Pacific Oceans, as the IOD and ENSO are Australia's strongest climate drivers (e.g. Meyers et al., 2007; Risbey et al., 2009a). But the Niño3.4, DMI, and tropical TPI indices may miss nuances in how these ocean basins interact with Australia's climate. ENSO and IOD skewness (e.g. Cai et al., 2012), ENSO flavour (e.g. central or east Pacific El Niño (e.g. Santoso et al., 2019), east- versus west- IOD poles (Ummenhofer et al., 2009b) may all produce different climate impacts. We neglected the potential influence of the tropical Atlantic Ocean, despite it generating Rossby waves that propagate along the eddy-driven jet to pass just south of Australia before reaching Antarctica (Li, X., et al., 2014; 2015a,b; Simpkins et al., 2014), and knowing the Atlantic interacts with other ocean basins (Li, X. et al., 2016). Indeed, inter-ocean basin interactions could be considered more closely in future work (Li, X. et al., 2016; Cai et al., 2019), particularly as the results from chapter 4 were consistent with the tropical Indian Ocean feeding back onto the tropical Pacific. SSTs nearer to Australia may be as important for spring climate as remote tropical SSTs (van Rensch et al., 2019). Future work could explore whether local SST-moisture sources (e.g. Holgate et al., 2020a) could counter otherwise heat-promoting circulation by increasing antecedent moisture and changing to the surface heat balance (e.g. Loughran et al., 2019). Finally, the MJO-forced Rossby wave teleconnections to Australia (Wang and Hendon, 2020) and MJO-interference with large-scale drivers' influence on Australia's spring rainfall (Lim et al., 2021b) highlight just how important the MJO could be to Australia's spring climate. In particular, understanding the dynamics of if or how different MJO phases interact with different IOD and ENSO phases could improve sub-seasonal predictability (e.g. Merryweather, et al., 2020; Meehl et al., 2021). Arguably, the tropical indices used in this thesis captured some of the variability mentioned here (e.g. the DMI poles overlap with certain MJO phases; the tropical TPI includes SSTs north of Australia), but, future work could benefit from detailed assessment of the different tropical influences on Australia's spring maximum temperatures.

The different modes of variability act over different time scales, and these time scales could influence the results from this thesis. SAM decorrelation occurs within two weeks (Hendon et al., 2007; Marshall et al., 2012) and while ENSO (e.g., Zhou and Yu 2004; L'Heureux and Thompson, 2006) and anomalous stratospheric warming or cooling (e.g., Seviour et al. 2014; Byrne and Shepherd 2018; Lim et al., 2019b) push SAM to maintain a certain phase, this predominantly occurs from late spring, when we argued that the extratropics are relatively less important. Sudden stratospheric warming (SSW) events, via the associated negative SAM-like conditions, have been linked with extreme heat from October into early summer (e.g. Lim et al., 2019b; 2021a), are also worth further investigation in their own right. As well as zonally aligned SAM, the meridional variations in the high-latitudes described by zonal wave three (ZW3) may be modulated by the tropics (e.g. Goyal et al., 2021), and have potential implications for Australia's spring climate. On longer time scales, inter-decadal processes, such as the Inter-decadal Pacific Oscillation

(IPO) modulate the strengths, spatial patterns, and climatic impacts of ENSO, IOD, and SAM (Zhao et al., 2016; Lim et al., 2017). In particular, the cold phase of the IPO may strengthen the ENSO and IOD influence on Australia’s rainfall (Power et al., 1999; Lim et al., 2017) and promote positive SAM (Yang et al., 2020). Our analysis period included two phases of the IPO, potentially influencing the shape of the regression patterns in chapter 3 (e.g. Lim et al., 2017). The interactions with the different drivers on different time scales may help explain some of the disconnection between circulation patterns associated with heat and what we found in association with the drivers.

We identified several key atmospheric circulation features associated with heat, and, while the remote drivers help nudge the atmosphere toward this configuration neither the drivers nor the key features explain the full circulation required to support high temperature development. The subtropical ridge (STR) has also been linked with high spring maximum temperatures (Pepler et al., 2018), and we can expect the STR to project onto the circulation features discussed in this thesis. Further, the ridge location marches poleward through spring (Drosowsky, 2005; Cai et al., 2011b; Timbal & Drosowsky, 2013; Maher & Sherwood, 2014). As such, future work could explore how the STR location relates to the apparent transition from extratropical to tropical forcing of heat generating mechanisms in Australia through spring.

The subtropical ridge and subtropical jet (STJ) are dynamically linked by the Hadley Cell (e.g. Maher & Sherwood, 2014), and the STJ may also be an area for further research. Preliminary investigation (not shown) using an Indo-Pacific-region subtropical jet index (Gillett et al., 2021) suggests that a weaker STJ correlates with higher maximum temperatures through spring, particularly in November. A simple scale-analysis of the zonal geographic wind,  $u_g$  (equation 1), suggests that these results are consistent with this thesis’ findings associated with anomalously high geopotential height,  $\partial z$ , over southern Australia. As the Coriolis parameter,  $f$ , and meridional gradient  $\partial y$  are negative in the Southern Hemisphere we get an easterly wind (i.e. negative wind speed anomaly or weaker jet).

$$u_g = \frac{-g}{f} \frac{\partial z}{\partial y} \text{ (equation 5.1)}$$

This scale-analysis is expected if we picture the anomalous wind flow around the anticyclone: easterly on its equatorward flank and westerly on its poleward flank. These results are consistent with Risbey et al. (2009b), who linked wetter synoptic conditions across southeast Australia in winter, and by extension, cooler conditions in spring, with a stronger local STJ. Conversely, other studies have found an increase in winter rainfall with a weaker jet (Lim & Hendon, 2015; Maher & Sherwood, 2014). This contrast in results may be explained by differences in STJ definition, particularly as considering zonal wind-intensity only (as in the latter two studies) neglects how the flow may distort meridionally around synoptic or seasonal height anomalies. The careful interpretation of these contrasting results present a cautionary note in the use of indices to represent large-scale circulation features and regional responses, something that is relevant to

the findings through this thesis. Overall, further investigation into how the subtropical jet influences maximum temperatures over Australia, as well as how it interacts with other features like the subtropical ridge or southern anticyclone, is an important area for future research.

Creating indices to represent the Australian maximum temperature variability and dynamical heat mechanisms was useful for our analysis but we lose information when variables are averaged spatially and temporally. As we descend in scale from the large-scale remote drivers to heat generating mechanisms, local geographic scale becomes more important. For example, high maximum temperature is more closely related to northerly advection and the Tasman Sea high pressure system if averaged over the southeast Australia than Australia-wide, consistent with previous studies (e.g. Marshall et al., 2014). Further, the SON climate of far north Australia is subject to different patterns of atmospheric circulation and heat generation mechanisms that were not investigated through this thesis. As the majority of the maximum temperature variability in SON occurs in the central to southeast of Australia (Fig. 1-2b) the results through this thesis are more representative of extratropical variability. A more detailed analysis could explore the tropical mechanisms of heat, as well as southeast and southwest regional aspects of extratropical Australian heat generation through spring.

Temporal averaging to a monthly or seasonal time-scale also loses information about how maximum temperatures develop through spring. We can only make assumptions about how the key atmospheric circulation features associated with heat relate to changes in synoptic systems, such as cold fronts, cut-off lows, and blocking highs. For example, are the barotropic cyclones southwest and southeast of Australia associated with high maximum temperature because they reflect a greater tendency for fronts and lows to propagate away from the continent or for some other reason? Would we see the expected stronger relationship between anomalous anticyclones over Australia and sinking motion (e.g. Hope et al., 2015; Pfahl et al., 2015; Gallant & Lewis, 2016; Suarez-Gutierrez et al., 2020) if we looked at synoptic time scales rather than monthly averages? Further studies based on composites of synoptic weather during spring (e.g. Hauser et al., 2020) could address these questions.

This thesis considered only three heat mechanisms with limited interactions, and was confined to spring periods only. Increased insolation, low antecedent soil moisture and land-surface feedbacks, changes to synoptic weather systems (Cai et al., 2011a; Arblaster et al., 2014; Lim et al., 2019b; Hirsch and King, 2020; Hauser et al., 2020) are just some additional heat mechanisms that, in conjunction with different levels of wind or adiabatic motion can result in anomalous heat. Preliminary investigation shows a strong relationship with high spring maximum temperature and low rainfall in the preceding months or seasons (e.g. Hirsch & King, 2020) that could be further explored. In particular, we have found indications that the relationship with antecedent rainfall to maximum temperature varies not just through spring, but through

the year too. Further research could benefit in repeating and extending the analysis from this thesis to explore how the heat mechanisms interact with each other, the broad scale circulation and the remote drivers of variability not just in spring, but in all months and seasons of the year.

### 5.3.2 Limits to Rossby wave theory

Linear Rossby wave theory (e.g. Hoskins and Karoly, 1981) is useful for understanding the steady-state response to tropical forcing relevant to Australia, but comes with several restrictions. We assume that patterns of monthly height anomalies are stationary or quasi-stationary Rossby waves (i.e. that the frequency is zero). For this to be accurate, the phase speed needs to be about equal magnitude to the speed of the background flow. Scale analysis of Rossby wave phase speed shows that 30-day oscillations (i.e. the monthly-averages used in this thesis) in the mid-latitudes have non-stationary characteristics (Yang and Hoskins, 1996). However, Yang and Hoskins (1996) noted that even non-stationary Rossby waves have some of the stationary wave characteristics, including being directed along subtropical and eddy-driven jet wave guides (Yang and Hoskins 1996; Rudeva & Simmonds, 2021). A similar assumption, noted in 5.3.1, is that the quasi-stationary Rossby waves made by the height patterns are somewhat representative of the synoptic weather (transient waves) through that month. Further analysis based on daily data, such as composites through spring months (e.g. Hauser et al., 2020) or model experiments (e.g. Branstator, 2014) could not only help connect the synoptic time scales to monthly, but avoid some of the issues surrounding linear Rossby wave theory (Branstator, 2014).

Application of linear Rossby wave theory leads to several very useful Rossby wave analysis tools, however, these tools are also limited by the assumptions underpinning theory. We used wave activity flux (WAF) extensively through this thesis, but WAF is strongly influenced by the background flow. We calculated WAF against the 1981-2010 climatological wind (e.g. McIntosh and Hendon, 2018; Wang et al., 2019), but our results could differ if calculated against different climatological periods. Rossby wave tracing (Hoskins and Karoly, 1981), another wave analysis tool, follows wave propagation between latitudes of reflection or dissipation, and could be used to verify the robustness of our WAF results. However, both WAF and ray tracing require that background flow be slowly varying compared to the wave propagation (Wentzel–Kramers–Brillouin approximation for linearization), which breaks down near jets. This breakdown in theory may explain why some WAF propagates through the jet waveguides in chapter 3 (e.g. Gillet et al., in review) and also suggests that ray tracing is not an appropriate tool for analysis near jets (Wirth, 2020). Another option for further investigation is to use Rossby wave source (Sadashmukh and Hoskins, 1988; Qin and Robinson, 1993) to explore how the tropics and extratropics evolve as sources of teleconnection patterns to Australia. Early work in this thesis (not shown) found that the tropical Indian Ocean does grow as a source of Rossby waves through spring, particularly when interacting with the subtropical jet west of Australia (Li et al 2014; Wang et al 2019). However, this analysis did not help explain how this source

resulted in extratropical impacts, as the majority of waves from these sources should have been reflected back into the tropics (Li, X. et al., 2014; 2015a,b; Simpkins et al., 2014). Further analysis could benefit from the use of Rossby wave source diagnostics, along with cautious use of ray tracing.

The subtropical jet has been highlighted by linear Rossby wave theory both as a barrier between the tropics and extratropics, a possible secondary wave source, and, in particular, a waveguide. As the jet weakened through spring we could have expected not only a weakening barrier, but a less effective waveguide. However, jet waveguide strength may increase smoothly with increasing jet wind speed and decreasing meridionally jet width (Wirth, 2020). As such, WAF associated with high maximum temperature propagated along the subtropical jet waveguide, even as the region of wavenumber,  $K_s$ , less than zero shrank. Through spring, the subtropical jet waveguide, as well as the eddy-driven jet waveguide to the south, directed WAF toward Australia associated with high maximum temperature, heat mechanisms, and tropical and extratropical forcing. The eddy-driven jet waveguide directs quasi-stationary Rossby waves from the tropical Atlantic to the Amundsen Sea (Li, X. et al., 2014; 2015a,b; Simpkins et al., 2014), as well as directing synoptic-scale Rossby waves that lead to Australian summer and spring heatwaves (Risbey et al., 2018). As such, jet waveguides appear to be important components of Australia's spring climate and could be explored further. However, linear wave theory may be inappropriate for understanding the subtropical jet's role as a waveguide through spring. Linear theory both breaks down near jets and rigidly states a jet either is or is not a waveguide (Ambrizzi et al., 1995; Wirth, 2020). As such, defining the waveguide region with potential vorticity gradients (e.g. Wirth, 2020), rather than total wavenumber, or analysis of synoptic Rossby waves (e.g. Rudeva and Simmonds, 2021) may provide better insight into how the subtropical jet waveguide relates to Australian maximum temperature.

Despite the subtropical jet's apparent importance as a waveguide, it should still prevent much of Rossby wave propagation from the tropical Indian Ocean into the extratropics. Breakdowns in linear Rossby wave theory may explain some of the tropical to extratropical propagation through the jet (e.g. Wirth, 2020; Gillet et al., in review), but not all of it. The increase in tropical Indian Ocean-WAF through spring may simply be the result of tropical SST anomalies peaking in late spring (e.g. Meyers et al., 2007) to create a stronger forcing impact, or again be related to the subtropical jet decay. The eddy-feedback secondary wave source suggested by McIntosh and Hendon (2018) may provide an alternative mechanism for this decay as the resulting height anomalies are proportional to jet wind strength (Hoskins et al., 1983). So, the secondary source could weaken through spring with the jet, and potentially produce different atmospheric flow by November. However, recent work by Gillet et al (in review) using model experiments with a diabatic heat source suggests that this secondary source mechanism is not necessary and the majority of Rossby wave propagation from the tropical Indian Ocean occurs via waves that tunnel underneath the jet, or propagate around and through the jet. While it is not immediately clear how tunnelling would explain the

change in tropical-origin WAF through spring, extending their analysis beyond winter may help explain the atmospheric dynamics linking the tropics and Australia's spring climate. Improving understanding of the subtropical jet is an important area of future work. Overall, while this thesis addressed many questions around the atmospheric dynamics impacting Australian temperatures during spring, there are still some facets that are beyond the scope of this thesis to address and could be the topic of further work.

### 5.3.3 Restrictions associated with numerical modelling

This thesis used the POAMA seasonal forecasting system as the main analysis tool as it has many benefits, as described in chapters 1, 2 and 4, but has also been identified as having many limitations. POAMA has good predictive skill in spring (Lim et al., 2009; Hudson et al., 2013), a long history as an experimental model (Lim et al., 2015; 2016a; 2019b; Lim & Hendon, 2017; Hope et al., 2016, 2018; Zhao et al., 2016), and simulates the IOD variability and teleconnections well, even in comparison to higher resolution S2S models (Zhao & Hendon 2009; Li et al., 2012). However, POAMA remains an older and lower-resolution model that is biased toward ENSO variability, with model physics that had not been updated since the early 2000s (Hudson et al., 2013; 2017). These limitations in POAMA impacted the strength of some of the results in this thesis. To what extent is the weaker relationship between the tropical Indian Ocean and Australia's maximum temperature due to the overly strong relationship between the atmosphere and ENSO in POAMA (chapter 4)? How much is realistic? Addressing these questions requires more research with more sophisticated models.

Many of the issues with POAMA, and the other S2S models, revolved around how Indian Ocean processes were simulated, suggesting that this is an important area for model improvement. Correcting or compensating for the relatively poor memory for Indian Ocean initial conditions in seasonal prediction systems compared to those in the Pacific Ocean is a clear starting point. Further work could explore whether enhancing Indian Ocean initial conditions in a portion of ensemble members could compensate for the rapid initial condition decay to produce an overall better forecast. Another option is to explore the importance of ENSO in maintaining the strength of anomalies in the Indian Ocean by examining how quickly IOD pole anomalies, or anomalies in the subsurface ocean, decay during ENSO events compared to neutral years. The seasonal prediction systems used in this thesis had ENSO-IOD-pole relationships that differed from observations in different ways. Better model resolution around the east- or west- IOD poles, has been identified as a way to improve the representation of the IOD in models (Liu et al., 2017), and could potentially lead to better simulation of the ENSO-IOD relationships and teleconnections. As ACCESS-S includes improved model physics, resolution, and reduced biases (Hudson et al., 2017), repeating the POAMA experiment in ACCESS-S could result in a clearer picture of the relative role of the tropical Indian Ocean. However, using ACCESS-S for experimentation is hampered by its significantly larger computation and storage costs. Further, ACCESS-S may also have biases in how it simulates the IOD (Lim et al., 2016b)

and have overly strong growth of ENSO-SSTs (chapter 4). In general, modelling the processes in the Indian Ocean remains a difficult topic that requires further research before a full understanding of its role in Australia's spring climate can be reached.

All dynamical models are subject to biases that can influence how they simulate tropical Indian Ocean teleconnections. The majority of CMIP5 models tend to overestimate IOD magnitude (Cai & Cowan, 2013; Li, G. et al., 2015;2016) and variance (Weller & Cai, 2013b), and under-estimate the observed positive IOD skew (Weller & Cai, 2013a). Biases in both the IOD and ENSO persist into the latest generation of CMIP6 models (McKenna et al., 2020). These biases occur due to a range of processes, including overly strong Bjerkness feedback in the east tropical Indian Ocean that results from an unrealistically sloped thermocline (Cai & Cowan, 2013; Weller & Cai, 2013b; Li, G. et al., 2016) or biases in simulating the South Asian monsoon that are potentially important for IOD initiation (Ashok et al., 2001) and IOD strength (Li, G. et al., 2015). Improving these processes may require refining model physics and initialisation schemes, and higher ocean resolution (Liu et al., 2017), though the latter does not necessarily result in improved IOD simulations (Shi et al., 2012). Another option is to use models with large ensembles (Kay et al., 2015) and multi-model means (e.g. Liu et al., 2017; Deser et al., 2020). However, care is required when using multiple models from the same model-family or with common biases (e.g. Abramowitz, 2010; Li, G., 2016; Abramowitz et al., 2019). The UKMO, KMA and ACCESS-S2 seasonal prediction systems each had Niño3.4 SSTs that grew faster than expected from observations, and resulted in overly strong ENSO events compared to IOD. This common result may be due to these models all being based on GloSea, despite differences in model generations or configurations (e.g. ACCESS-S uses a burst, rather than lagged, ensemble initiation method; Hudson et al., 2013; 2017; Maclachlan et al., 2015). Overall, accurately simulating the Indian Ocean and the resulting teleconnections remains an ongoing challenge in all models.

While many of the issues and findings from using POAMA are specific to seasonal forecasting systems, there is potential to extend some benefits to the more general circulation models mentioned above, as well as future generations of seasonal prediction systems. In particular, enhancing the Indian Ocean anomalies in POAMA beyond realistic observations did increase the strength of the simulated teleconnection, suggesting a possible, if rough, bias-correction method. The elongated cyclones south of Australia, which are a known bias in POAMA (Marshall et al., 2012) and were an issue in its simulation of the heat events in chapter 2, were effectively removed in the enhanced positive IOD experiments. Further work refining this bias-correction method could result in improved simulation of the Indian Ocean and its teleconnections. Accurate simulation of the Indian Ocean is relevant not just to Australian, but African and Asian climates (e.g. Saji et al., 2005; Risbey et al., 2009a; Hirons & Turner, 2018), and inter-ocean basin interactions (Cai et al., 2019). As such, any model improvements have positive and deep societal impacts, even if the model remains imperfect. After all, while "all models are wrong, some are useful" (George Box).

While sub-seasonal and seasonal prediction was not a direct theme of this thesis, it often ran parallel to our methods and findings. In particular, we argued that the shift toward greater direct influence of the tropics on Australia's maximum temperatures in later spring could lead to better temperature predictability. While this shift is related more to a change in the dynamical mechanisms related to heat, rather than a direct increase in tropical forcing, it is worth further investigation. A study of how predictable each of those heat mechanisms is across the different S2S models through spring in association with different extratropical or tropical forcing could be very useful for the Australian and broader community. Improving the apparent biases in how the S2S models, POAMA, and ACCESS-S simulate ENSO and the IOD teleconnections could also improve Australian sub-seasonal forecasting. ENSO is the strongest source of potential predictability (e.g. Merryfield et al., 2020; Meehl et al., 2021), so seasonal prediction models may be tuned to ENSO variability to gain much of their skill. However, to move beyond first order approximations of Australia's local atmospheric circulation and spring maximum temperature, it is important to be able to simulate the impact of the tropical Indian Ocean as well.

#### 5.3.4 Impact of anthropogenic climate change

This thesis focussed on drivers and influences of natural variability on Australia's spring maximum temperatures, but the story of high temperatures is incomplete without considering the impact of anthropogenic climate change. The increase in heat from the background warming trend was a significant factor in each of the spring heat events discussed in chapter two (e.g. Arblaster et al., 2014; Hope et al., 2015; 2016; Gallant and Lewis 2016). The probability of breaking heat records and reaching new high temperature extremes is likely to increase in the future (Power & Delage, 2019; Fischer et al., 2021). We argued in the introduction that understanding the dynamics of how heat develops in the present climate is critical to being able to assess and constrain future projections. However, climate change has already impacted today's temperatures and is already a part of what drives high temperatures in Australia in spring.

Further, the teleconnections that underpinned much of this thesis, that is, how maximum temperature is driven by the tropical Indian and Pacific Oceans, and SAM, are also subject to change due to anthropogenic climate change. Positive IOD event frequency increased during the late 20<sup>th</sup> century (Abram et al., 2008; Cai et al., 2013) and may have contributed to the observed decrease in rainfall in southeast Australia (Cai et al., 2014a). While model biases remain an issue (e.g. McKenna et al., 2020), the projection toward a positive IOD-like mean state (Cai et al., 2013) is consistent with this observed increase in positive IODs. As such, there is potential for more extreme positive IODs than the 2019 extreme event (Cai et al., 2014c; Abram et al., 2020) that could result in drier and hotter Australian springs. SAM has no observed trend in spring (e.g. Fogt & Marshall, 2020), but there are indications that the ENSO-SAM relationship in late spring may be weakening (Lim et al., 2019b), and that ENSO variability could be increasing (e.g. Cai et al., 2021).

Additionally, the large-scale circulation may also be changing. The subtropical ridge has been intensifying in the Australian sector, contributing to the decrease in rainfall and increase in maximum temperature from winter to spring (Timbal & Drosowsky, 2013; Pepler et al., 2018). Overall, Australian maximum temperature variability in winter to summer may increase significantly in future years (IPCC Atlas; Gutiérrez et al., in press) such that our current understanding of how the remote drivers of variability and large-scale atmospheric circulation may be insufficient to explain future spring heat extremes. As such, we need to improve our understanding of how anthropogenic forces influence remote drivers of variability to better understand how high maximum temperature develops in spring, now and in the future.

## 5.4 Thesis conclusion

Australia recorded a relatively wet and mild spring through 2021

(<http://www.bom.gov.au/climate/current/season/aus/summary.shtml> issued December 1, 2021), likely in association with observed La Niña, negative IOD, and positive SAM conditions

(<http://www.bom.gov.au/climate/enso/> issued December 7, 2021). As such, the remote drivers of variability may have buffered the background warming trend, preventing the more extreme heat of other recent springs from developing this year. However, the combination of the roll of the dice that is natural variability and the warming associated with anthropogenic climate change means that we can expect extreme heat to return in future springs. This thesis has shown that both remote drivers and the atmospheric circulation are important for understanding spring heat variability, and highlighted that improvements in simulation of tropical to extratropical teleconnections are critically needed for better seasonal forecasts of anomalous high maximum temperatures. When extreme spring heat does return, we hope that the findings from this thesis help contribute to better preparation for extreme conditions.

## 6 References

- Abram, N. J., Gagan, M. K., Cole, J. E., Hantoro, W. S., & Mudelsee, M. (2008). Recent intensification of tropical climate variability in the Indian Ocean. *Nature Geoscience*, *1*(12), 849–853. <https://doi.org/10.1038/ngeo357>
- Abram, N. J., Wright, N. M., Ellis, B., Dixon, B. C., Wurtzel, J. B., England, M. H., Ummenhofer, C. C., Philibosian, B., Cahyarini, S. Y., Yu, T.-L., Shen, C.-C., Cheng, H., Edwards, R. L., & Heslop, D. (2020). Coupling of Indo-Pacific climate variability over the last millennium. *Nature*, *579*(7799), 385–392. <https://doi.org/10.1038/s41586-020-2084-4>
- Abram, N. J., Henley, B. J., Sen Gupta, A., Lippmann, T. J. R., Clarke, H., Dowdy, A. J., Sharples, J. J., Nolan, R. H., Zhang, T., Wooster, M. J., Wurtzel, J. B., Meissner, K. J., Pitman, A. J., Ukkola, A. M., Murphy, B. P., Tapper, N. J., & Boer, M. M. (2021). Connections of climate change and variability to large and extreme forest fires in southeast Australia. *Communications Earth & Environment*, *2*(1), 8. <https://doi.org/10.1038/s43247-020-00065-8>
- Abramowitz, G. (2010). Model independence in multi-model ensemble prediction. *Australian Meteorological and Oceanographic Journal*, *59*(1SP), 3–6. <https://doi.org/10.22499/2.5901.002>
- Abramowitz, G., Herger, N., Gutmann, E., Hammerling, D., Knutti, R., Leduc, M., Lorenz, R., Pincus, R., & Schmidt, G. A. (2019). ESD Reviews: Model dependence in multi-model climate ensembles: weighting, sub-selection and out-of-sample testing. *Earth System Dynamics*, *10*(1), 91–105. <https://doi.org/10.5194/esd-10-91-2019>
- Alexander, L. V., & Arblaster, J. M. (2009). Assessing trends in observed and modelled climate extremes over Australia in relation to future projections. *International Journal of Climatology*, *29*(3), 417–435. <https://doi.org/10.1002/joc.1730>
- Alexander, L. V., & Arblaster, J. M. (2017). Historical and projected trends in temperature and precipitation extremes in Australia in observations and CMIP5. *Weather and Climate Extremes*, *15*, 34–56. <https://doi.org/10.1016/j.wace.2017.02.001>
- Ambrizzi, T., Hoskins, B. J., & Hsu, H.-H. (1995). Rossby wave propagation and teleconnection patterns in austral winter. *Journal of the Atmospheric Sciences*, *52*(21), 3661–3672. [https://doi.org/10.1175/1520-0469\(1995\)052<3661:RWPATP>2.0.CO;2](https://doi.org/10.1175/1520-0469(1995)052<3661:RWPATP>2.0.CO;2)
- Australian Bureau of Meteorology. 2013. ‘Special Climate Statement 46 - Australia’s Warmest September on Record’. *Special Climate Statement*, no. October.
- 2014. ‘Special Climate Statement 50 – Australia’s Warmest Spring on Record’, no. December.
- . 2016. ‘Australia’s Warmest Autumn on Record. Special Climate Statement 52.’ 52 (December): 25

- Arblaster, J., Meehl, G. & Moore, A. (2002), Interdecadal modulation of Australian rainfall. *Climate Dynamics* 18, 519-531.
- Arblaster, J., Lim, E.-P., Hendon, H., Trewin, B., Wheeler, M., Liu, G., & Braganza, K. (2014). UNDERSTANDING AUSTRALIA'S HOTTEST SEPTEMBER ON RECORD. *Bulletin of the American Meteorological Society*, 95(9), S37–S41.
- Ashok, K., Guan, Z., & Yamagata, T. (2001). Impact of the Indian Ocean dipole on the relationship between the Indian monsoon rainfall and ENSO. *Geophysical Research Letters*, 28(23), 4499–4502. <https://doi.org/10.1029/2001GL013294>
- Bals-Elsholz, T. M., Atallah, E. H., Bosart, L. F., Wasula, T. A., Cempa, M. J., & Lupo, A. R. (2001). The Wintertime Southern Hemisphere Split Jet: Structure, Variability, and Evolution. *JOURNAL OF CLIMATE*, 14, 25.
- Barnes, E. A., and Hartmann, D. L. (2012). Detection of Rossby wave breaking and its response to shifts of the midlatitude jet with climate change: WAVE BREAKING AND CLIMATE CHANGE. *Journal of Geophysical Research: Atmospheres*, 117(D9), n/a-n/a. <https://doi.org/10.1029/2012JD017469>
- Best, M. J., Pryor, M., Clark, D. B., Rooney, G. G., Essery, R. . L. H., Ménard, C. B., Edwards, J. M., Hendry, M. A., Porson, A., Gedney, N., Mercado, L. M., Sitch, S., Blyth, E., Boucher, O., Cox, P. M., Grimmond, C. S. B., & Harding, R. J. (2011). The Joint UK Land Environment Simulator (JULES), model description – Part 1: Energy and water fluxes. *Geoscientific Model Development*, 4(3), 677–699. <https://doi.org/10.5194/gmd-4-677-2011>
- Black, M. T., & Karoly, D. J. (2017). SOUTHERN AUSTRALIA'S WARMEST OCTOBER ON RECORD: THE ROLE OF ENSO AND CLIMATE CHANGE [in “Explaining Extremes of 2015 from a Climate Perspective”]. *Bulletin of the American Meteorological Society*, 98(12), S1–S157. <https://doi.org/10.1175/BAMS-D-17-0118.1>
- Boschat, G., Pezza, A., Simmonds, I., Perkins, S., Cowan, T., & Purich, A. (2015). Large scale and sub-regional connections in the lead up to summer heat wave and extreme rainfall events in eastern Australia. *Climate Dynamics*, 44(7–8), 1823–1840. <https://doi.org/10.1007/s00382-014-2214-5>
- Branstator, G. (1983), Horizontal energy propagation in a barotropic atmosphere with meridional and zonal structure, *J. Atmos. Sci.*, 40, 1689–1708.
- Branstator, G. (2014). Long-Lived Response of the Midlatitude Circulation and Storm Tracks to Pulses of Tropical Heating. *Journal of Climate*, 27(23), 8809–8826. <https://doi.org/10.1175/JCLI-D-14-00312.1>
- Brunet, G., Shapiro, M., Hoskins, B., Moncrieff, M., Dole, R., Kiladis, G. N., Kirtman, B., Lorenc, A., Mills, B., Morss, R., Polavarapu, S., Rogers, D., Schaake, J., & Shukla, J. (2010). Collaboration of the Weather and Climate Communities to Advance Subseasonal-to-Seasonal Prediction. *Bulletin of the American Meteorological Society*, 91(10), 1397–1406. <https://doi.org/10.1175/2010BAMS3013.1>

- Byrne N. J., Shepherd TG (2018) Seasonal persistence of circulation anomalies in the Southern Hemisphere stratosphere and its implications for the troposphere. *J Clim* 31:3467–3483. doi: 10.1175/JCLI-D-17-0557.1
- Cai, W., van Rensch, P., Cowan, T., & Hendon, H. H. (2011a). Teleconnection Pathways of ENSO and the IOD and the Mechanisms for Impacts on Australian Rainfall. *Journal of Climate*, 24(15), 3910–3923. <https://doi.org/10.1175/2011JCLI4129.1>
- Cai, W., van Rensch, P., & Cowan, T. (2011b). Influence of Global-Scale Variability on the Subtropical Ridge over Southeast Australia. *Journal of Climate*, 24(23), 6035–6053. <https://doi.org/10.1175/2011JCLI4149.1>
- Cai, W., and P. van Rensch (2012), The 2011 south-east Queensland extreme summer rainfall: A confirmation of a negative Pacific Decadal Oscillation phase? *Geophys. Res. Lett.*, 39, L08702.
- Cai, W., van Rensch, P., Cowan, T., & Hendon, H. H. (2012). An Asymmetry in the IOD and ENSO Teleconnection Pathway and Its Impact on Australian Climate. *Journal of Climate*, 25(18), 6318–6329. <https://doi.org/10.1175/JCLI-D-11-00501.1>
- Cai, W., & Cowan, T. (2013). Why is the amplitude of the Indian Ocean Dipole overly large in CMIP3 and CMIP5 climate models?: MODEL IOD BIASES. *Geophysical Research Letters*, 40(6), 1200–1205. <https://doi.org/10.1002/grl.50208>
- Cai, W., Zheng, X.-T., Weller, E., Collins, M., Cowan, T., Lengaigne, M., Yu, W., & Yamagata, T. (2013). Projected response of the Indian Ocean Dipole to greenhouse warming. *Nature Geoscience*, 6(12), 999–1007. <https://doi.org/10.1038/ngeo2009>
- Cai, W., Purich, A., Cowan, T., van Rensch, P., & Weller, E. (2014a). Did Climate Change–Induced Rainfall Trends Contribute to the Australian Millennium Drought? *Journal of Climate*, 27(9), 3145–3168. <https://doi.org/10.1175/JCLI-D-13-00322.1>
- Cai, W., Borlace, S., Lengaigne, M., van Rensch, P., Collins, M., Vecchi, G., Timmermann, A., Santoso, A., McPhaden, M. J., Wu, L., England, M. H., Wang, G., Guilyardi, E., & Jin, F.-F. (2014b). Increasing frequency of extreme El Niño events due to greenhouse warming. *Nature Climate Change*, 4(2), 111–116. <https://doi.org/10.1038/nclimate2100>
- Cai, W., Santoso, A., Wang, G., Weller, E., Wu, L., Ashok, K., Masumoto, Y., & Yamagata, T. (2014c). Increased frequency of extreme Indian Ocean Dipole events due to greenhouse warming. *Nature*, 510(7504), 254–258. <https://doi.org/10.1038/nature13327>
- Cai, W., Wu, L., Lengaigne, M., Li, T., McGregor, S., Kug, J.-S., Yu, J.-Y., Stuecker, M. F., Santoso, A., Li, X., Ham, Y.-G., Chikamoto, Y., Ng, B., McPhaden, M. J., Du, Y., Dommenges, D., Jia, F., Kajtar, J. B., Keenlyside, N., ... Chang, P. (2019). Pantropical climate interactions. *Science*, 363(6430), eaav4236. <https://doi.org/10.1126/science.aav4236>
- Cai, W., Santoso, A., Collins, M., Dewitte, B., Karamperidou, C., Kug, J.-S., Lengaigne, M.,

- McPhaden, M. J., Stuecker, M. F., Taschetto, A. S., Timmermann, A., Wu, L., Yeh, S.-W., Wang, G., Ng, B., Jia, F., Yang, Y., Ying, J., Zheng, X.-T., ... Zhong, W. (2021). Changing El Niño–Southern Oscillation in a warming climate. *Nature Reviews Earth & Environment*, 2(9), 628–644. <https://doi.org/10.1038/s43017-021-00199-z>
- Ceppi, P., & Hartmann, D. L. (2013). On the Speed of the Eddy-Driven Jet and the Width of the Hadley Cell in the Southern Hemisphere. *Journal of Climate*, 26(10), 3450–3465. <https://doi.org/10.1175/JCLI-D-12-00414.1>
- Chung, C. T. Y., & Power, S. B. (2016). Modelled impact of global warming on ENSO-driven precipitation changes in the tropical Pacific. *Climate Dynamics*, 47(3–4), 1303–1323. <https://doi.org/10.1007/s00382-015-2902-9>
- Collins, M., Knutti, R., Arblaster, J., Dufresne, J.-L., Fichet, T., Friedlingstein, P., Gao, X., Gutowski, W. J., Johns, T., Krinner, G., Shongwe, M., Tebaldi, C., Weaver, A. J., Wehner, M. F., Allen, M. R., Andrews, T., Beyerle, U., Bitz, C. M., Bony, S., & Booth, B. B. B. (2013). Long-term Climate Change: Projections, Commitments and Irreversibility. *Climate Change 2013 - The Physical Science Basis: Contribution of Working Group I to the Fifth Assessment Report of the Intergovernmental Panel on Climate Change*, 1029–1136.
- Colman, R., and Coauthors, 2005: BMRC Atmospheric model (BAM) version 3.0: Comparison with mean climatology. BMRC Research Rep. 108, 23 pp.
- Cottrill, A., Hendon, H. H., Lim, E.-P., Langford, S., Shelton, K., Charles, A., McClymont, D., Jones, D., & Kuleshov, Y. (2013). Seasonal Forecasting in the Pacific Using the Coupled Model POAMA-2. *Weather and Forecasting*, 28(3), 668–680. <https://doi.org/10.1175/WAF-D-12-00072.1>
- Cowan, T., van Rensch, P., Purich, A., and Cai W., 2013. ‘The Association of Tropical and Extratropical Climate Modes to Atmospheric Blocking across Southeastern Australia’. *Journal of Climate* 26 (19): 7555–69. <https://doi.org/10.1175/JCLI-D-12-00781.1>
- CSIRO (Commonwealth Scientific and Industrial Research Organisation) (2020) State of the Climate 2020, <http://www.bom.gov.au/state-of-the-climate/documents/State-of-the-Climite-2020.pdf>
- Cullen, B. R., Johnson, I. R., Eckard, R. J., Lodge, G. M., Walker, R. G., Rawnsley, R. P., & McCaskill, M. R. (2009). Climate change effects on pasture systems in south-eastern Australia. *Crop and Pasture Science*, 60(10), 933. <https://doi.org/10.1071/CP09019>
- Dee, D. P., Uppala S. M., Simmons A. J., Berrisford P., Poli P., Kobayashi S., Andrae U., et al. 2011. ‘The ERA-Interim Reanalysis: Configuration and Performance of the Data Assimilation System’. *Quarterly Journal of the Royal Meteorological Society* 137 (656): 553–97. <https://doi.org/10.1002/qj.828>.

- Deoras, A., Hunt, K. M. R., & Turner, A. G. (2021). Comparison of the Prediction of Indian Monsoon Low Pressure Systems by Subseasonal-to-Seasonal Prediction Models. *Weather and Forecasting*, 36(3), 859–877. <https://doi.org/10.1175/WAF-D-20-0081.1>
- Deser, C., Lehner, F., Rodgers, K. B., Ault, T., Delworth, T. L., DiNezio, P. N., Fiore, A., Frankignoul, C., Fyfe, J. C., Horton, D. E., Kay, J. E., Knutti, R., Lovenduski, N. S., Marotzke, J., McKinnon, K. A., Minobe, S., Randerson, J., Screen, J. A., Simpson, I. R., & Ting, M. (2020). Insights from Earth system model initial-condition large ensembles and future prospects. *Nature Climate Change*, 10(4), 277–286. <https://doi.org/10.1038/s41558-020-0731-2>
- Dhame, S., Taschetto, A.S., Santoso, A. et al. Indian Ocean warming modulates global atmospheric circulation trends. *Clim Dyn* 55, 2053–2073 (2020). <https://doi.org/10.1007/s00382-020-05369-1>
- Dirmeyer, P. A. (2003). The Role of the Land Surface Background State in Climate Predictability. *JOURNAL OF HYDROMETEOROLOGY*, 4, 12.
- Dommenget, D., & Jansen, M. (2009). Predictions of Indian Ocean SST Indices with a Simple Statistical Model: A Null Hypothesis, *Journal of Climate*, 22(18), 4930-4938.
- Dong, L., Zhou, T., Dai, A. et al. The Footprint of the Inter-decadal Pacific Oscillation in Indian Ocean Sea Surface Temperatures. *Sci Rep* 6, 21251 (2016). <https://doi.org/10.1038/srep21251>
- Dowdy, A. J. (2018). Climatological Variability of Fire Weather in Australia. *Journal of Applied Meteorology and Climatology*, 57(2), 221–234. <https://doi.org/10.1175/JAMC-D-17-0167.1>
- Drosowsky, W. (2005). The latitude of the subtropical ridge over Eastern Australia: The L index revisited. *International Journal of Climatology*, 25(10), 1291–1299. <https://doi.org/10.1002/joc.1196>
- Eyring, V., N.P. Gillett, K.M. Achuta Rao, R. Barimalala, M. Barreiro Parrillo, N. Bellouin, C. Cassou, P.J. Durack, Y. Kosaka, S. McGregor, S. Min, O. Morgenstern, and Y. Sun, 2021: Human Influence on the Climate System. In *Climate Change 2021: The Physical Science Basis. Contribution of Working Group I to the Sixth Assessment Report of the Intergovernmental Panel on Climate Change* [Masson-Delmotte, V., P. Zhai, A. Pirani, S.L. Connors, C. Péan, S. Berger, N. Caud, Y. Chen, L. Goldfarb, M.I. Gomis, M. Huang, K. Leitzell, E. Lonnoy, J.B.R. Matthews, T.K. Maycock, T. Waterfield, O. Yelekçi, R. Yu, and B. Zhou (eds.)]. Cambridge University Press. In Press.
- Fawcett, R. J. B., Trewin B. C., Braganza K., Smalley R. J., Jovanovic B., and Jones D. A. n.d. 'On the Sensitivity of Australian Temperature Trends and Variability to Analysis Methods and Observation Networks', 66.
- Fischer, E.M., Sippel, S. & Knutti, R. Increasing probability of record-shattering climate extremes. *Nat. Clim. Chang.* 11, 689–695 (2021). <https://doi.org/10.1038/s41558-021-01092-9>
- Fogt, R. L., & Marshall, G. J. (2020). The Southern Annular Mode: Variability, trends, and climate

- impacts across the Southern Hemisphere. *WIREs Climate Change*, 11(4).  
<https://doi.org/10.1002/wcc.652>
- Gallant, A. J. E., & Lewis, S. C. (2016). Stochastic and anthropogenic influences on repeated record-breaking temperature extremes in Australian spring of 2013 and 2014: CAUSES OF REPEATED TEMPERATURE RECORDS. *Geophysical Research Letters*, 43(5), 2182–2191.  
<https://doi.org/10.1002/2016GL067740>
- Gillett, Z. E., Hendon, H. H., Arblaster, J. M., & Lim, E.-P. (2021). Tropical and Extratropical Influences on the Variability of the Southern Hemisphere Wintertime Subtropical Jet. *Journal of Climate*, 34(10), 4009–4022. <https://doi.org/10.1175/JCLI-D-20-0460.1>
- Gillet, Z. E., Hendon H. H., Arblaster, J. M., Fuchs, D., Lin, H., On the Dynamics of Indian Ocean Teleconnections into the Southern Hemisphere during winter, under review
- Gong, D. Y., and S. W. Wang (1999), Definition of Antarctic oscillation index, *Geophys. Res. Lett.*, 26, 459–462.
- Goyal, R., Jucker, M., Sen Gupta, A., Hendon, H. H., & England, M. H. (2021). Zonal wave 3 pattern in the Southern Hemisphere generated by tropical convection. *Nature Geoscience*.  
<https://doi.org/10.1038/s41561-021-00811-3>
- Guo, F., Liu, Q., Yang, J., & Fan, L. (2018). Three types of Indian Ocean Basin modes. *Climate Dynamics*, 51(11–12), 4357–4370. <https://doi.org/10.1007/s00382-017-3676-z>
- Gutiérrez, J.M., R.G. Jones, G.T. Narisma, L.M. Alves, M. Amjad, I.V. Gorodetskaya, M. Grose, N.A.B. Klutse, S. Krakovska, J. Li, D. Martínez-Castro, L.O. Mearns, S.H. Mernild, T. Ngo-Duc, B. van den Hurk, and J.-H. Yoon, 2021: Atlas. In *Climate Change 2021: The Physical Science Basis. Contribution of Working Group I to the Sixth Assessment Report of the Intergovernmental Panel on Climate Change* [Masson-Delmotte, V., P. Zhai, A. Pirani, S.L. Connors, C. Péan, S. Berger, N. Caud, Y. Chen, L. Goldfarb, M.I. Gomis, M. Huang, K. Leitzell, E. Lonnoy, J.B.R. Matthews, T.K. Maycock, T. Waterfield, O. Yelekçi, R. Yu, and B. Zhou (eds.)]. Cambridge University Press. In Press. Interactive Atlas available from Available from <http://interactive-atlas.ipcc.ch/>
- Hauser, S., Grams, C. M., Reeder, M. J., McGregor, S., Fink, A. H., & Quinting, J. F. (2020). A weather system perspective on winter–spring rainfall variability in southeastern Australia during El Niño. *Quarterly Journal of the Royal Meteorological Society*, qj.3808.  
<https://doi.org/10.1002/qj.3808>
- Hendon, H. H., Thompson, D. W. J., & Wheeler, M. C. (2007). Australian Rainfall and Surface Temperature Variations Associated with the Southern Hemisphere Annular Mode. *Journal of Climate*, 20(11), 2452–2467. <https://doi.org/10.1175/JCLI4134.1>
- Hendon, H. H., Lim, E.-P., & Nguyen, H. (2014). Seasonal Variations of Subtropical Precipitation Associated with the Southern Annular Mode. *Journal of Climate*, 27(9), 3446–3460.  
<https://doi.org/10.1175/JCLI-D-13-00550.1>

- Henley, B. J., J. Gergis, D. J. Karoly, S. Power, J. Kennedy, and C. K. Folland, 2015: A Tripole Index for the Interdecadal Pacific Oscillation. *Clim. Dyn.*, 45, 3077–3090, doi:10.1007/s00382-015-2525-1.
- Hersbach, H., Bell, B., Berrisford, P., Hirahara, S., Horányi, A., Muñoz-Sabater, J., Nicolas, J., Peubey, C., Radu, R., Schepers, D., Simmons, A., Soci, C., Abdalla, S., Abellan, X., Balsamo, G., Bechtold, P., Biavati, G., Bidlot, J., Bonavita, M., ... Thépaut, J. (2020). The ERA5 global reanalysis. *Quarterly Journal of the Royal Meteorological Society*, 146(730), 1999–2049. <https://doi.org/10.1002/qj.3803>
- Hirons, L., & Turner, A. (2018). The Impact of Indian Ocean Mean-State Biases in Climate Models on the Representation of the East African Short Rains. *Journal of Climate*, 31(16), 6611–6631. <https://doi.org/10.1175/JCLI-D-17-0804.1>
- Hirsch, A. L., & King, M. J. (2020). Atmospheric and Land Surface Contributions to Heatwaves: An Australian Perspective. *Journal of Geophysical Research: Atmospheres*, 125(17). <https://doi.org/10.1029/2020JD033223>
- Holgate, C. M., Evans, J. P., van Dijk, A. I. J. M., Pitman, A. J., & Di Virgilio, G. (2020a). Australian Precipitation Recycling and Evaporative Source Regions. *Journal of Climate*, 33(20), 8721–8735. <https://doi.org/10.1175/JCLI-D-19-0926.1>
- Holgate, C. M., Van Dijk, A. I. J. M., Evans, J. P., and Pitman, A. J. (2020b). Local and Remote Drivers of Southeast Australian Drought. *Geophysical Research Letters*, 47(18). <https://doi.org/10.1029/2020GL090238>
- Hope, P, Timbal B., and Fawcett R. 2009. 'Associations between Rainfall Variability in the Southwest and Southeast of Australia and Their Evolution through Time'. *International Journal of Climatology*, n/a-n/a. <https://doi.org/10.1002/joc.1964>.
- Hope, P, Lim E-P, Wang G., Hendon H. H., and Arblaster J. M. 2015. 'Contributors to the Record High Temperatures Across Australia in Late Spring 2014'. *Bulletin of the American Meteorological Society* 96 (12): S149–53.
- Hope, P., Wang, G., Lim, E.-P., Hendon, H. H., & Arblaster, J. M. (2016). WHAT CAUSED THE RECORD-BREAKING HEAT ACROSS AUSTRALIA IN OCTOBER 2015? [in "Explaining Extreme Events of 2015 from a Climate Perspective"]. *Bulletin of the American Meteorological Society*, 96(12 (suppl)), S1–S172. <https://doi.org/10.1175/BAMS-D-15-00157.1>
- Hope, P., Lim, E.-P., Hendon, H., & Wang, G. (2018). The Effect of Increasing CO<sub>2</sub> on the Extreme September 2016 Rainfall Across Southeastern Australia. *Bulletin of the American Meteorological Society*, 99(1), S133–S138. <https://doi.org/10.1175/BAMS-D-17-0094.1>
- Hope, P., & Watterson, I. (2018). Persistence of cool conditions after heavy rain in Australia. *Journal of Southern Hemisphere Earth System Science*, 68(1). <https://doi.org/10.22499/3.6801.004>
- Hoskins B. J., James IN, White GH (1983) The shape, propagation and mean-flow interaction of large-scale weather systems. *J Atmos Sci* 40:1595–1612
- Hoskins, B. J., & Karoly, D. J. (1981). The Steady Linear Response of a Spherical Atmosphere

- to Thermal and Orographic Forcing. *Journal of the Atmospheric Sciences*.  
[https://doi.org/10.1175/1520-0469\(1981\)038<1179:TSLROA>2.0.CO;2](https://doi.org/10.1175/1520-0469(1981)038<1179:TSLROA>2.0.CO;2)
- Hoskins B.J., Ambrizzi T. (1993) Rossby wave propagation on a realistic longitudinally varying flow. *J Atmos Sci* 50:1661–1671
- Huang, B., Peter W. Thorne, et. al, 2017: Extended Reconstructed Sea Surface Temperature version 5 (ERSSTv5), Upgrades, validations, and intercomparisons. *J. Climate*, doi: 10.1175/JCLI-D-16-0836.1
- Hudson, D, Alves O., Hendon H. H., and Marshall A. G. (2011). ‘Bridging the Gap between Weather and Seasonal Forecasting: Intraseasonal Forecasting for Australia’. *Quarterly Journal of the Royal Meteorological Society* 137 (656): 673–89. <https://doi.org/10.1002/qj.769>.
- Hudson, D., Marshall, A. G., Yin, Y., Alves, O., & Hendon, H. H. (2013). Improving Intraseasonal Prediction with a New Ensemble Generation Strategy. *Monthly Weather Review*, 141(12), 4429–4449. <https://doi.org/10.1175/MWR-D-13-00059.1>
- Hudson, D., Marshall, A. G., Alves, O., Young, G., Jones, D., & Watkins, A. (2016). Forewarned is Forearmed: Extended-Range Forecast Guidance of Recent Extreme Heat Events in Australia. *Weather and Forecasting*, 31(3), 697–711. <https://doi.org/10.1175/WAF-D-15-0079.1>
- Hudson, D, Alves O., Hendon H. H., Lim E-P, Liu G., Luo J-J., MacLachlan C., Marshall A. G., Shi L., Wang G., Wedd R., Young G., Zhao M., Zhou X., 2017. ‘ACCESS-S1 The New Bureau of Meteorology Multi-Week to Seasonal Prediction System’. *Journal of Southern Hemisphere Earth System Science* 67 (3): 132–59.
- Hurrell, J., Meehl, G. A., Bader, D., Delworth, T. L., Kirtman, B., & Wielicki, B. (2009). A Unified Modeling Approach to Climate System Prediction. *Bulletin of the American Meteorological Society*, 90(12), 1819–1832. <https://doi.org/10.1175/2009BAMS2752.1>
- Irving, D., & Simmonds, I. (2016). A New Method for Identifying the Pacific–South American Pattern and Its Influence on Regional Climate Variability, *Journal of Climate*, 29(17), 6109–6125
- Izumo, T., et al. (2010), Influence of the state of the Indian Ocean Dipole on the following year’s El Niño Nature Geoscience, 3, 168.
- Japan Meteorological Agency/Japan (2013), JRA-55: Japanese 55-year Reanalysis, Daily 3-Hourly and 6-Hourly Data, <https://doi.org/10.5065/D6HH6H41>, Research Data Archive at the National Center for Atmospheric Research, Computational and Information Systems Laboratory, Boulder, Colo. (Updated monthly.) Accessed December 2020
- Jarvis, C., Darbyshire, R., Goodwin, I., Barlow, E. W. R., & Eckard, R. (2019). Advancement of winegrape maturity continuing for winegrowing regions in Australia with variable evidence of compression of the harvest period: Advancement of winegrape maturity. *Australian Journal of Grape and Wine Research*, 25(1), 101–108. <https://doi.org/10.1111/ajgw.12373>
- Jones, D., & Trewin, B. C. (2000). On the relationships between the El Niño–Southern Oscillation and

Australian land surface temperature. *Int. J. Climatol.*, 23.

- Jones, D., Wang W., and Fawcett R. 2009. 'High-Quality Spatial Climate Data-Sets for Australia'. *Australian Meteorological and Oceanographic Journal* 58 (04): 233–48. <https://doi.org/10.22499/2.5804.003>.
- Karoly, D. J., 1989: Southern Hemisphere circulation features associated with El Niño–Southern Oscillation events. *J. Climate*, 2, 1239–1252, doi:10.1175/1520-0442(1989)002<1239:SHCFAW>2.0.CO;2.
- Karoly, D. J., and D. G. Vincent, 1998: Meteorology of the Southern Hemisphere. *Amer. Meteor. Soc.*, 410
- Kay, J. E., Deser, C., Phillips, A., Mai, A., Hannay, C., Strand, G., Arblaster, J. M., Bates, S. C., Danabasoglu, G., Edwards, J., Holland, M., Kushner, P., Lamarque, J.-F., Lawrence, D., Lindsay, K., Middleton, A., Munoz, E., Neale, R., Oleson, K., ... Vertenstein, M. (2015). The Community Earth System Model (CESM) Large Ensemble Project: A Community Resource for Studying Climate Change in the Presence of Internal Climate Variability. *Bulletin of the American Meteorological Society*, 96(8), 1333–1349. <https://doi.org/10.1175/BAMS-D-13-00255.1>
- King, A. D., L. V. Alexander, and M. G. Donat (2013), Asymmetry in the response of eastern Australia extreme rainfall to low-frequency Pacific variability. *Geophys. Res. Lett.*, 40, 2271–2277.
- King, A.D., Pitman, A.J., Henley, B.J. et al. The role of climate variability in Australian drought. *Nat. Clim. Chang.* 10, 177–179 (2020a). <https://doi.org/10.1038/s41558-020-0718-z>
- King, A. D., Hudson, D., Lim, E., Marshall, A. G., Hendon, H. H., Lane, T. P., & Alves, O. (2020b). Sub-seasonal to seasonal prediction of rainfall extremes in Australia. *Quarterly Journal of the Royal Meteorological Society*, 146(730), 2228–2249. <https://doi.org/10.1002/qj.3789>
- Klein, S. A., Soden, B. J., & Lau, N.-C. (1999). Remote Sea Surface Temperature Variations during ENSO: Evidence for a Tropical Atmospheric Bridge. *JOURNAL OF CLIMATE*, 12, 16.
- Koch, P., Wernli, H., & Davies, H. C. (2006). An event-based jet-stream climatology and typology. *International Journal of Climatology*, 26(3), 283–301. <https://doi.org/10.1002/joc.1255>
- Kug, J.-S. (2005). Preconditions for El Niño and La Niña onsets and their relation to the Indian Ocean. *Geophysical Research Letters*, 32(5), L05706. <https://doi.org/10.1029/2004GL021674>
- Kumar, A., Chen, M., Hoerling, M., & Eischeid, J. (2013). Do extreme climate events require extreme forcings?: EXTREME CLIMATE EVENTS. *Geophysical Research Letters*, 40(13), 3440–3445. <https://doi.org/10.1002/grl.50657>
- Lee, S.-K., Lopez, H., Foltz, G., Kim, D., Larson, S., Lim, E.-P., Pujiana, K., Volkov, D., Chakravorty, S., & Gomez, F. (2021). *Java-Sumatra Niño/Niña and associated regional rainfall variability* [Preprint]. In Review. <https://doi.org/10.21203/rs.3.rs-619357/v1>
- L'Heureux, M. L., & Thompson, D. W. J. (2006). Observed Relationships between the El Niño–Southern Oscillation and the Extratropical Zonal-Mean Circulation. *Journal of Climate*, 19(2), 276–287. <https://doi.org/10.1175/JCLI3617.1>
- Li, G., Xie, S.-P., & Du, Y. (2015). Monsoon-Induced Biases of Climate Models over the Tropical Indian Ocean. *Journal of Climate*, 28(8), 3058–3072. <https://doi.org/10.1175/JCLI-D-14-00740.1>

- Li, G., Xie, S., & Du, Y. (2016). A Robust but Spurious Pattern of Climate Change in Model Projections over the Tropical Indian Ocean, *Journal of Climate*, 29(15), 5589-5608. <https://doi.org/10.1175/JCLI-D-15-0565.1>
- Li, X. David M. Holland, Edwin P. Gerber, & Changhyun Yoo. (2014). Impacts of the north and tropical Atlantic Ocean on the Antarctic Peninsula and sea ice. *Nature*, 505(7484), 538–542. <https://doi.org/10.1038/nature12945>
- Li, X., Gerber, E. P., Holland, D. M., & Yoo, C. (2015a). A Rossby Wave Bridge from the Tropical Atlantic to West Antarctica. *Journal of Climate*, 28(6), 2256–2273. <https://doi.org/10.1175/JCLI-D-14-00450.1>
- Li, X., Holland, D. M., Gerber, E. P., & Yoo, C. (2015b). Rossby Waves Mediate Impacts of Tropical Oceans on West Antarctic Atmospheric Circulation in Austral Winter. *Journal of Climate*, 28(20), 8151–8164. <https://doi.org/10.1175/JCLI-D-15-0113.1>
- Li, X., Xie, S.-P., Gille, S. T., & Yoo, C. (2016). Atlantic-induced pan-tropical climate change over the past three decades. *Nature Climate Change*, 6(3), 275–279. <https://doi.org/10.1038/nclimate2840>
- Liebmann B. and Smith C.A., (1996): Description of a Complete (Interpolated) Outgoing Longwave Radiation Dataset. *Bulletin of the American Meteorological Society*, 77, 1275-1277.
- Liguori, G., McGregor, S., Singh, M., Arblaster, J., Di Lorenzo, E., Revising ENSO and IOD contributions to Australian Precipitation, in review, *Geophysical Research Letters*
- Lim E-P, Hendon H. H., Alves O., Yin Y., Zhao M., Wang G., Hudson D., Liu G. (2009) Impact of SST bias correction on prediction of ENSO and Australian winter rainfall CAWCR Research Letters Issue 3, pages 22-29 available from <https://www.cawcr.gov.au/>
- Lim E-P, Hendon H.H., Rashid H. (2013) Seasonal predictability of the Southern Annular Mode due to its association with ENSO. *J Clim* 26:8037–8054. doi: 10.1175/JCLI-D-13-00006.1
- Lim, E.-P., & Hendon, H. H. (2015). Understanding and predicting the strong Southern Annular Mode and its impact on the record wet east Australian spring 2010. *Climate Dynamics*, 44(9–10), 2807–2824. <https://doi.org/10.1007/s00382-014-2400-5>
- Lim, E.-P., Hendon, H. H., Arblaster, J. M., Chung, C., Moise, A. F., Hope, P., Young, G., & Zhao, M. (2016a). Interaction of the recent 50 year SST trend and La Niña 2010: Amplification of the Southern Annular Mode and Australian springtime rainfall. *Climate Dynamics*, 47(7–8), 2273–2291. <https://doi.org/10.1007/s00382-015-2963-9>
- Lim, E-P, Hendon, H.H., Hudson, D., Zhao, M., Shi, L., Alves, O. and Young G. (2016b). Evaluation of the ACCESS-S1 hindcasts for prediction of Victorian seasonal rainfall. Bureau Research Report No. 19, Bureau of Meteorology Australia (available from: <http://www.bom.gov.au/research/research-reports.shtml>).
- Lim, E.-P., & Hendon, H. H. (2017). Causes and Predictability of the Negative Indian Ocean Dipole

and Its Impact on La Niña During 2016. *Scientific Reports*, 9, 11.

<https://doi.org/DOI:10.1038/s41598-017-12674-z>

- Lim, E.-P., Hendon, H. H., Zhao, M., & Yin, Y. (2017). Inter-decadal variations in the linkages between ENSO, the IOD and south-eastern Australian springtime rainfall in the past 30 years. *Climate Dynamics*, 49(1–2), 97–112. <https://doi.org/10.1007/s00382-016-3328-8>
- Lim, E. -P., Hendon, H. H., & Thompson, D. W. J. (2018). Seasonal Evolution of Stratosphere-Troposphere Coupling in the Southern Hemisphere and Implications for the Predictability of Surface Climate. *Journal of Geophysical Research: Atmospheres*, 123(21), 12,002–12,016. <https://doi.org/10.1029/2018JD029321>
- Lim, E.-P., Hendon, H. H., Boschath, G., Hudson, D., Thompson, D. W. J., Dowdy, A. J., & Arblaster, J. M. (2019a). Australian hot and dry extremes induced by weakenings of the stratospheric polar vortex. *Nature Geoscience*, 12(11), 896–901. <https://doi.org/10.1038/s41561-019-0456-x>
- Lim, E.-P., Hendon, H. H., Hope, P., Chung, C., Delage, F., & McPhaden, M. J. (2019b). Continuation of tropical Pacific Ocean temperature trend may weaken extreme El Niño and its linkage to the Southern Annular Mode. *Scientific Reports*, 9(1), 17044. <https://doi.org/10.1038/s41598-019-53371-3>
- Lim, E.-P., Hendon, H. H., Butler, A. H., Thompson, D. W. J., Lawrence, Z. D., Scaife, A. A., Shepherd, T. G., Polichtchouk, I., Nakamura, H., Kobayashi, C., Comer, R., Coy, L., Dowdy, A., Garreaud, R. D., Newman, P. A., & Wang, G. (2021a). The 2019 Southern Hemisphere Stratospheric Polar Vortex Weakening and Its Impacts. *Bulletin of the American Meteorological Society*, 102(6), E1150–E1171. <https://doi.org/10.1175/BAMS-D-20-0112.1>
- Lim, E.-P., Hendon, H. H., Shi, L., de Burgh-Day, C., Hudson, D., King, A., Trewin, B., Griffiths,., & Marshall, A. (2021b). Tropical forcing of Australian extreme low minimum temperatures in September 2019. *Climate Dynamics*. <https://doi.org/10.1007/s00382-021-05661-8>
- Lim, E.-P., Hudson, D., Wheeler, M. C., Marshall, A. G., King, A., Zhu, H., Hendon, H. H., de Burgh-Day, C., Trewin, B., Griffiths, M., Ramchurn, A., & Young, G. (2021c). Why Australia was not wet during spring 2020 despite La Niña. *Scientific Reports*, 11(1), 18423. <https://doi.org/10.1038/s41598-021-97690-w>
- Liu, Z., & Alexander, M. (2007). Atmospheric bridge, oceanic tunnel, and global climatic teleconnections. *Reviews of Geophysics*, 45(2), RG2005. <https://doi.org/10.1029/2005RG000172>
- Liu, H., Tang, Y., Chen, D., & Lian, T. (2017). Predictability of the Indian Ocean Dipole in the coupled models. *Climate Dynamics*, 48(5–6), 2005–2024. <https://doi.org/10.1007/s00382-016-3187-3>
- Loughnan, M., Tapper, N., & Loughnan, T. (2014). The Impact of “Unseasonably” Warm Spring Temperatures on Acute Myocardial Infarction Hospital Admissions in Melbourne, Australia: A City with a Temperate Climate. *Journal of Environmental and Public Health*, 2014, 1–8. <https://doi.org/10.1155/2014/483785>

- Loughran, T. F., Pitman, A. J., & Perkins-Kirkpatrick, S. E. (2019). The El Niño–Southern Oscillation’s effect on summer heatwave development mechanisms in Australia. *Climate Dynamics*, 52(9–10), 6279–6300. <https://doi.org/10.1007/s00382-018-4511-x>
- Luo, J.-J., Zhang, R., Behera, S. K., Masumoto, Y., Jin, F.-F., Lukas, R., & Yamagata, T. (2010). Interaction between El Niño and Extreme Indian Ocean Dipole. *Journal of Climate*, 23(3), 726–742. <https://doi.org/10.1175/2009JCLI3104.1>
- Luo, J. J., Sasaki, W., & Masumoto, Y. (2012). Indian Ocean warming modulates Pacific climate change. *Proceedings of the National Academy of Sciences of the United States of America*, 109(46), 18701–18706. <https://doi.org/10.1073/pnas.1210239109>
- MacLachlan, C., Arribas, A., Peterson, K. A., Maidens, A., Fereday, D., Scaife, A. A., Gordon, M., Vellinga, M., Williams, A., Comer, R. E., Camp, J., Xavier, P., & Madec, G. (2015). Global Seasonal forecast system version 5 (GloSea5): A high-resolution seasonal forecast system: GloSea5: A High-Resolution Seasonal Forecast System. *Quarterly Journal of the Royal Meteorological Society*, 141(689), 1072–1084. <https://doi.org/10.1002/qj.2396>
- Maher, P., and Sherwood, S. C. (2014). Disentangling the Multiple Sources of Large-Scale Variability in Australian Wintertime Precipitation. *Journal of Climate*, 27(17), 6377–6392. <https://doi.org/10.1175/JCLI-D-13-00659.1>
- Manabe, S., and Holloway J. L., 1975: The seasonal variation of the hydrologic cycle as simulated by a global model of the atmosphere. *J. Geophys. Res.*, 80, 1617–1649.
- Marshall, G. J. (2003). Trends in the Southern Annular Mode from Observations and Reanalyses. *JOURNAL OF CLIMATE*, 16, 10.
- Marshall, A., Hudson, D., Wheeler, M. C., Hendon, H. H., & Alves, O. (2012). Simulation and prediction of the Southern Annular Mode and its influence on Australian intra-seasonal climate in POAMA. *Climate Dynamics*, 38(11–12), 2483–2502. <https://doi.org/10.1007/s00382-011-1140-z>
- Marshall, A., Hudson, D., Wheeler, M., Alves, O., Hendon, H., Pook, M., & Risbey, J. (2014). Intra-seasonal drivers of extreme heat over Australia in observations and POAMA-2. *Climate Dynamics*, 43(7–8), 1915–1937. <https://doi.org/10.1007/s00382-013-2016-1>
- Marshall, A., Hendon, H. H., & Hudson, D. (2021a). Influence of the Madden-Julian Oscillation on multiweek prediction of Australian rainfall extremes using the ACCESS-S1 prediction system. *Journal of Southern Hemisphere Earth Systems Science*. <https://doi.org/10.1071/ES21001>
- Marshall, A. G., Gregory, P. A., de Burgh-Day, C. O., & Griffiths, M. (2021b). Subseasonal drivers of extreme fire weather in Australia and its prediction in ACCESS-S1 during spring and summer. *Climate Dynamics*. <https://doi.org/10.1007/s00382-021-05920-8>
- McIntosh, P. C., & Hendon, H. H. (2018). Understanding Rossby wave trains forced by the Indian Ocean Dipole. *Climate Dynamics*, 50(7–8), 2783–2798. <https://doi.org/10.1007/s00382-017-3771-1>

- McKay, R. C., Arblaster, J. M., Hope, P., and Lim, E.-P. (2021). Exploring atmospheric circulation leading to three anomalous Australian spring heat events. *Climate Dynamics*, 56(7–8), 2181–2198. <https://doi.org/10.1007/s00382-020-05580-0>
- McKenna, S., Santoso, A., Gupta, A. S., Taschetto, A. S., & Cai, W. (2020). Indian Ocean Dipole in CMIP5 and CMIP6: Characteristics, biases, and links to ENSO. *Scientific Reports*, 10(1), 11500. <https://doi.org/10.1038/s41598-020-68268-9>
- Meehl, G. A., Richter, J. H., Teng, H., Capotondi, A., Cobb, K., Doblas-Reyes, F., Donat, M. G., England, M. H., Fyfe, J. C., Han, W., Kim, H., Kirtman, B. P., Kushnir, Y., Lovenduski, N. S., Mann, M. E., Merryfield, W. J., Nieves, V., Pegion, K., Rosenbloom, N., ... Xie, S.-P. (2021). Initialized Earth System prediction from subseasonal to decadal timescales. *Nature Reviews Earth & Environment*. <https://doi.org/10.1038/s43017-021-00155-x>
- Merryfield, W. J., Baehr, J., Batté, L., Becker, E. J., Butler, A. H., Coelho, C. A. S., Danabasoglu, G., Dirmeyer, P. A., Doblas-Reyes, F. J., Domeisen, D. I. V., Ferranti, L., Ilynia, T., Kumar, A., Müller, W. A., Rixen, M., Robertson, A. W., Smith, D. M., Takaya, Y., Tuma, M., ... Yeager, S. (2020). Current and Emerging Developments in Subseasonal to Decadal Prediction. *Bulletin of the American Meteorological Society*, 101(6), E869–E896. <https://doi.org/10.1175/BAMS-D-19-0037.1>
- Meyers, G., McIntosh, P., Pigot, L., & Pook, M. (2007). The Years of El Niño, La Niña, and Interactions with the Tropical Indian Ocean. *Journal of Climate*, 20(13), 2872–2880. <https://doi.org/10.1175/JCLI4152.1>
- Min, S.-K., Cai, W., & Whetton, P. (2013). Influence of climate variability on seasonal extremes over Australia: SEASONAL EXTREMES OVER AUSTRALIA. *Journal of Geophysical Research: Atmospheres*, 118(2), 643–654. <https://doi.org/10.1002/jgrd.50164>
- Mogensen K, Balmaseda M, Weaver AT, Martin M, Vidard A. 2009. NEMOVAR: A variational data assimilation system for the NEMO ocean model. In ECMWF Newsletter, Walter Z. (ed.) 120: 17–21. ECMWF: Reading, UK
- Nairn, J., & Fawcett, R. (2014). The Excess Heat Factor: A Metric for Heatwave Intensity and Its Use in Classifying Heatwave Severity. *International Journal of Environmental Research and Public Health*, 12(1), 227–253. <https://doi.org/10.3390/ijerph120100227>
- Nicholls, N., 1989. Sea surface temperature and Australian winter rainfall. *J. Clim.* 2, 965–973.
- Nicholls, N., Drosowsky, W., & Lavery, B. (1997). Australian rainfall variability and change. *Weather*, 52(3), 66–72. <https://doi.org/10.1002/j.1477-8696.1997.tb06274.x>
- O'Brien, L., & Reeder, M. J. (2017). Southern Hemisphere summertime Rossby waves and weather in the Australian region: Southern Hemisphere Summertime Rossby Waves. *Quarterly Journal of the Royal Meteorological Society*, 143(707), 2374–2388. <https://doi.org/10.1002/qj.3090>
- Park, S., Kim, D.-J., Lee, S.-W., Lee, K.-W., Kim, J., Song, E.-J., & Seo, K.-H. (2017). Comparison of Extended Medium-Range Forecast Skill Between KMA Ensemble, Ocean Coupled Ensemble, and GloSea5. 9.

- Parker, T. J., Berry, G. J., & Reeder, M. J. (2013). The influence of tropical cyclones on heat waves in Southeastern Australia: TROPICAL CYCLONES AND HEAT WAVES. *Geophysical Research Letters*, 40(23), 6264–6270. <https://doi.org/10.1002/2013GL058257>
- Parker, T. J., Berry G. J., and Reeder M. J. (2014). 'The Structure and Evolution of Heat Waves in Southeastern Australia'. *Journal of Climate* 27 (15): 5768–85. <https://doi.org/10.1175/JCLI-D-13-00740.1>.
- Pepler, A., Timbal, B., Rakich, C., & Coutts-Smith, A. (2014). Indian Ocean Dipole Overrides ENSO's Influence on Cool Season Rainfall across the Eastern Seaboard of Australia. *Journal of Climate*, 27(10), 3816–3826. <https://doi.org/10.1175/JCLI-D-13-00554.1>
- Pepler, A., Ashcroft, L., & Trewin, B. (2018a). The relationship between the subtropical ridge and Australian temperatures. *Journal of Southern Hemisphere Earth System Science*, 68(1), 201–214. <https://doi.org/10.22499/3.6801.011>
- Pfahl, S., Schwierz, C., Croci-Maspoli, M., Grams, C. M., and Wernli, H. (2015). Importance of latent heat release in ascending air streams for atmospheric blocking. *Nature Geoscience*, 8(8), 610–614. <https://doi.org/10.1038/ngeo2487>
- Philip SY, Kew SF, van Oldenborgh GJ, Otto FEL, Vautard R, van der Wiel K, King AD, Lott FC, Arrighi J, Singh RP, van Aalst MK (2020) A protocol for probabilistic extreme event attribution analyses. *Adv Stat Climatol Meteorol Oceanogr* 6:177–203. <https://doi.org/10.5194/ascmo-6-177-2020>
- Plumb, R. A. 1985. 'On the Three-Dimensional Propagation of Stationary Waves'. *Journal of the Atmospheric Sciences*. [https://doi.org/10.1175/1520-0469\(1985\)042<0217:OTTDPO>2.0.CO;2](https://doi.org/10.1175/1520-0469(1985)042<0217:OTTDPO>2.0.CO;2).
- Pook, M. J., Risbey, J. S., McIntosh, P. C., Ummenhofer, C. C., Marshall, A. G., & Meyers, G. A. (2013). The Seasonal Cycle of Blocking and Associated Physical Mechanisms in the Australian Region and Relationship with Rainfall. *Monthly Weather Review*, 141(12), 4534–4553. <https://doi.org/10.1175/MWR-D-13-00040.1>
- Power, S., Tseitkin, F., Torok, S., Lavery, B., Dahni, R., and McAvaney, B. (1998). Australian temperature, Australian rainfall and the Southern Oscillation, 1910-1992: coherent variability and recent changes. *Australian Meteorological Magazine*, 47, 85–101.
- Power, S., Casey, T., Folland, C., Colman, A., & Mehta, V. (1999). Inter-decadal modulation of the impact of ENSO on Australia. *Climate Dynamics*, 15(5), 319–324. <https://doi.org/10.1007/s003820050284>
- Power, S., M. Haylock, R. Colman, and X. Wang, 2006: The predictability of interdecadal changes in ENSO activity and ENSO teleconnections. *J. Clim.*, 19, 4755–4771, doi:10.1175/JCLI3868.1.
- Power, S., Delage, F., Chung, C., Kociuba, G., & Keay, K. (2013). Robust twenty-first-century projections of El Niño and related precipitation variability. *Nature*, 502(7472), 541–545. <https://doi.org/10.1038/nature12580>
- Power, S. B., & Delage, F. P. D. (2019). Setting and smashing extreme temperature records over

- the coming century. *Nature Climate Change*, 9(7), 529–534. <https://doi.org/10.1038/s41558-019-0498-5>
- Purich, A., England, M. H., Cai, W., Chikamoto, Y., Timmermann, A., Fyfe, J. C., Frankcombe, L., Meehl, G. A., & Arblaster, J. M. (2016). Tropical Pacific SST Drivers of Recent Antarctic Sea Ice Trends, *Journal of Climate*, 29(24), 8931-8948.
- Purich, A., & England, M. H. (2019). Tropical teleconnections to Antarctic sea ice during austral spring 2016 in coupled pacemaker experiments. *Geophysical Research Letters*, 2019GL082671. <https://doi.org/10.1029/2019GL082671>
- Purich, A., Boschat, G., & Liguori, G. (2021). Assessing the impact of suppressing Southern Ocean SST variability in a coupled climate model. *Scientific Reports*, 11(1), 22069. <https://doi.org/10.1038/s41598-021-01306-2>
- Qin, J. & Robinson, W. A. On the rossby wave source and the steady linear response to tropical forcing. *J. Atmos. Sci.* 50, 1819–1823 (1993)
- Quinting, J. F., & Reeder, M. J. (2017). Southeastern Australian Heat Waves from a Trajectory Viewpoint. *Monthly Weather Review*, 145(10), 4109–4125. <https://doi.org/10.1175/MWR-D-17-0165.1>
- Reeder, M. J., Spengler, T., & Musgrave, R. (2015). Rossby waves, extreme fronts, and wildfires in southeastern Australia. *Geophysical Research Letters*, 42(6), 2015–2023. <https://doi.org/10.1002/2015GL063125>
- Reynolds, R. W., Rayner, N. A., & Smith, T. M. (2002). An Improved In Situ and Satellite SST Analysis for Climate. *JOURNAL OF CLIMATE*, 15, 17.
- Risbey, J. S., Pook, M. J., McIntosh, P. C., Wheeler, M. C., & Hendon, H. H. (2009a). On the Remote Drivers of Rainfall Variability in Australia. *Monthly Weather Review*, 137(10), 3233–3253. <https://doi.org/10.1175/2009MWR2861.1>
- Risbey, J. S., Pook, M. J., McIntosh, P. C., Ummenhofer, C. C., & Meyers, G. (2009b). Characteristics and variability of synoptic features associated with cool season rainfall in southeastern Australia. *International Journal of Climatology*, 29(11), 1595–1613. <https://doi.org/10.1002/joc.1775>
- Risbey, J. S., O’Kane, T. J., Monselesan, D. P., Franzke, C. L. E., & Horenko, I. (2018). On the Dynamics of Austral Heat Waves: DYNAMICS OF AUSTRAL HEAT WAVES. *Journal of Geophysical Research: Atmospheres*, 123(1), 38–57. <https://doi.org/10.1002/2017JD027222>
- Rudeva, I., & Simmonds, I. (2021). Midlatitude Winter Extreme Temperature Events and Connections with Anomalies in the Arctic and Tropics. *Journal of Climate*, 34(10), 3733–3749. <https://doi.org/10.1175/JCLI-D-20-0371.1>
- Saji, N. H., Goswami B. N., Vinayachandran P. N., and Yamagata T. 1999. ‘A Dipole Mode in the Tropical Indian Ocean’. *Nature* 401 (6751): 360–63. <https://doi.org/10.1038/43854>.

- Saji, N. H., and Yamagata T. 2003. 'Possible Impacts of Indian Ocean Dipole Mode Events on Global Climate'. *Climate Research* 25 (2): 151–69.
- Saji, N. H., Ambrizzi, T., & Ferraz, S. E. T. (2005). Indian Ocean Dipole mode events and austral surface air temperature anomalies. *Dynamics of Atmospheres and Oceans*, 39(1–2), 87–101. <https://doi.org/10.1016/j.dynatmoce.2004.10.015>
- Santoso, A., Hendon, H., Watkins, A., Power, S., Dommenges, D., England, M. H., Frankcombe, L., Holbrook, N. J., Holmes, R., Hope, P., Lim, E.-P., Luo, J.-J., McGregor, S., Neske, S., Nguyen, H., Pepler, A., Rashid, H., Gupta, A. S., Taschetto, A. S., ... Delage, F. (2019). Dynamics and Predictability of El Niño–Southern Oscillation: An Australian Perspective on Progress and Challenges. *Bulletin of the American Meteorological Society*, 100(3), 403–420. <https://doi.org/10.1175/BAMS-D-18-0057.1>
- Sardeshmukh, P. D., & Hoskins, B. J. (1988). The Generation of Global Rotational Flow by Steady Idealized Tropical Divergence. *Journal of the Atmospheric Sciences*, 45(7), 1228–1251. [https://doi.org/10.1175/1520-0469\(1988\)045<1228:TGOGRF>2.0.CO;2](https://doi.org/10.1175/1520-0469(1988)045<1228:TGOGRF>2.0.CO;2)
- Schiller A, Godfrey J, McIntosh P, Meyers G, Smith N, Alves O, Wang O, Fiedler R. 2002. A new version of the Australian community ocean model for seasonal climate prediction. CSIRO Marine Research Report No. 240, CSIRO: Australia.
- Seiour W.J.M., Hardiman S.C., Gray L.J., et al (2014) Skillful seasonal prediction of the Southern Annular Mode and Antarctic ozone. *J Clim* 27:7462–7474. doi: 10.1175/JCLI-D-14-00264.1
- Sharmila, S., Hendon, H.H. Mechanisms of multiyear variations of Northern Australia wet-season rainfall. *Sci Rep* 10, 5086 (2020). <https://doi.org/10.1038/s41598-020-61482-5>
- Shi, L., Hendon, H. H., Alves, O., Luo, J.-J., Balmaseda, M., & Anderson, D. (2012). How Predictable is the Indian Ocean Dipole? *Monthly Weather Review*, 140(12), 3867–3884. <https://doi.org/10.1175/MWR-D-12-00001.1>
- Shinoda, T., M. A. Alexander, and H. H. Hendon, 2004: Remote response of the Indian Ocean to interannual SST variations in the tropical Pacific. *J. Climate*, 17, 362–372.
- Shinoda, T., & Han, W. (2005). Influence of the Indian Ocean Dipole on Atmospheric Subseasonal Variability. *Journal of Climate*, 18(18), 3891–3909. <https://doi.org/10.1175/JCLI3510.1>
- Simpkins, G. R., McGregor, S., Taschetto, A. S., Ciasto, L. M., & England, M. H. (2014). Tropical Connections to Climatic Change in the Extratropical Southern Hemisphere: The Role of Atlantic SST Trends. *Journal of Climate*, 27(13), 4923–4936. <https://doi.org/10.1175/JCLI-D-13-00615.1>
- Simmonds, I. (1998). Seasonal and regional responses to changes in Australian soil moisture conditions. *Int. J. Climatol.*, 35.
- Sooraj, K. P., Annamalai, H., Kumar, A., & Wang, H. (2012). A Comprehensive Assessment of CFS Seasonal Forecasts over the Tropics\*. *Weather and Forecasting*, 27(1), 3–27. <https://doi.org/10.1175/WAF-D-11-00014.1>

- Stan, C., Straus, D. M., Frederiksen, J. S., Lin, H., Maloney, E. D., & Schumacher, C. (2017). Review of Tropical-Extratropical Teleconnections on Intraseasonal Time Scales: The Subseasonal to Seasonal (S2S) Teleconnection Sub-Project. *Reviews of Geophysics*, 55(4), 902–937. <https://doi.org/10.1002/2016RG000538>
- Stocker, T.F., Qin D., Plattner G.-K., Tignor M., Allen S.K., Boschung J., Nauels A., Xia Y., Bex V. and Midgley P.M. (eds.). 2013. *Climate Change 2013 - The Physical Science Basis. Contribution of Working Group 1 to the Fifth Assessment Report of the Intergovernmental Panel on Climate Change*. Edited by Intergovernmental Panel on Climate Change. Cambridge: Cambridge University Press. <https://doi.org/10.1017/CBO9781107415324>.
- Stone, D., Auffhammer, M., Carey, M. et al. The challenge to detect and attribute effects of climate change on human and natural systems. *Climatic Change* 121, 381–395 (2013). <https://doi.org/10.1007/s10584-013-0873-6>
- Student, (1908). The probable error of a mean, *Biometrika*, 6, 1–25.
- Stuecker, M. F., Timmermann, A., Jin, F., Chikamoto, Y., Zhang, W., Wittenberg, A. T., Widiastih, E., & Zhao, S. (2017). Revisiting ENSO/Indian Ocean Dipole phase relationships. *Geophysical Research Letters*, 44(5), 2481–2492. <https://doi.org/10.1002/2016GL072308>
- Suarez-Gutierrez, L., Müller, W. A., Li, C., and Marotzke, J. (2020). Dynamical and thermodynamical drivers of variability in European summer heat extremes. *Climate Dynamics*, 54(9–10), 4351–4366. <https://doi.org/10.1007/s00382-020-05233-2>
- Swart, N. C., Fyfe J. C., Gillett N., and Marshall G. J.. 2015. ‘Comparing Trends in the Southern Annular Mode and Surface Westerly Jet’. *Journal of Climate* 28 (22): 8840–59. <https://doi.org/10.1175/JCLI-D-15-0334.1>.
- Takaya, K., and Nakamura H. 2000. ‘A Formulation of a Wave-Activity Flux for Stationary Rossby Waves on a Zonally Varying Basic Flow’. *Geophysical Research Letters* 24 (23): 2985–88. <https://doi.org/10.1029/97GL03094>.
- Taschetto, A. S., Sen Gupta, A., Hendon, H. H., Ummenhofer, C. C., & England, M. H. (2011). The Contribution of Indian Ocean Sea Surface Temperature Anomalies on Australian Summer Rainfall during El Niño Events. *Journal of Climate*, 24(14), 3734–3747. <https://doi.org/10.1175/2011JCLI3885.1>
- Taylor, C., Cullen, B., D’Occhio, M., Rickards, L., & Eckard, R. (2018). Trends in wheat yields under representative climate futures: Implications for climate adaptation. *Agricultural Systems*, 164, 1–10. <https://doi.org/10.1016/j.agsy.2017.12.007>
- Thompson, D. W. J., & Wallace, J. M. (2000). Annular Modes in the Extratropical Circulation. Part I: Month-to-Month Variability. *JOURNAL OF CLIMATE*, 13, 17.

- Timbal, B., Power, S., Colman, R., Viviand, J., & Lirola, S. (2002). Does Soil Moisture Influence Climate Variability and Predictability over Australia? *Journal of Climate*, 15(10), 1230–1238. [https://doi.org/10.1175/1520-0442\(2002\)015<1230:dsmicv>2.0.co;2](https://doi.org/10.1175/1520-0442(2002)015<1230:dsmicv>2.0.co;2)
- Timbal, B., & Drosowsky, W. (2013). The relationship between the decline of Southeastern Australian rainfall and the strengthening of the subtropical ridge. *International Journal of Climatology*, 33(4), 1021–1034. <https://doi.org/10.1002/joc.3492>
- Timbal, B., & Hendon, H. (2011). The role of tropical modes of variability in recent rainfall deficits across the Murray-Darling Basin: TROPICAL VARIABILITY AND RAINFALL DEFICIT IN THE MDB. *Water Resources Research*, 47(12). <https://doi.org/10.1029/2010WR009834>
- Trewin, B. 2013. 'A Daily Homogenized Temperature Data Set for Australia'. *International Journal of Climatology* 33 (6): 1510–29. <https://doi.org/10.1002/joc.3530>.
- Tolstykh, M. A., Kiktev, D. B., Zaripov, R. B., Zaichenko, M. Yu., & Shashkin, V. V. (2010). Simulation of the seasonal atmospheric circulation with the new version of the semi-Lagrangian atmospheric model. *Izvestiya, Atmospheric and Oceanic Physics*, 46(2), 133–143. <https://doi.org/10.1134/S0001433810020015>
- Tolstykh M. A. Global semi-Lagrangian numerical weather prediction model, FOP, Obninsk, Moscow, Russia, pp. 111, 2010 [Russian]
- Tolstykh M.A., Diansky N.A., Gusev A.V., Kiktev D.B., 2014: Simulation of seasonal anomalies of atmospheric circulation using coupled atmosphere–ocean model. *Izvestiya, Atmospheric and Oceanic Physics*, Vol. 50, No. 2, pp. 111–121.
- Ummenhofer, C. C., England, M. H., McIntosh, P. C., Meyers, G. A., Pook, M. J., Risbey, J. S., Gupta, A. S., & Taschetto, A. S. (2009a). What causes southeast Australia's worst droughts? *Geophysical Research Letters*, 36(4), L04706. <https://doi.org/10.1029/2008GL036801>
- Ummenhofer, C. C., Sen Gupta, A., Taschetto, A. S., & England, M. H. (2009b). Modulation of Australian Precipitation by Meridional Gradients in East Indian Ocean Sea Surface Temperature. *Journal of Climate*, 22(21), 5597–5610. <https://doi.org/10.1175/2009JCLI3021.1>
- Valcke S, Terray L, Piacentini A. 2000. Oasis 2.4, Ocean atmosphere sea ice soil: user's guide. TR/CMGC/00/10, CERFACS: Toulouse. van Oldenborgh, G.J., van der Wiel, K., Kew, S. et al. Pathways and pitfalls in extreme event attribution. *Climatic Change* 166, 13 (2021). <https://doi.org/10.1007/s10584-021-03071-7>
- van Rensch, P., Arblaster, J., Gallant, A. J. E., Cai, W., Nicholls, N., & Durack, P. J. (2019). Mechanisms causing east Australian spring rainfall differences between three strong El Niño events. *Climate Dynamics*, 53(5–6), 3641–3659. <https://doi.org/10.1007/s00382-019-04732-1>
- Vance, T. R., Roberts, J. L., Plummer, C. T., Kiem, A. S., & van Ommen, T. D. (2015). Interdecadal Pacific variability and eastern Australian megadroughts over the last millennium. *Geophysical Research Letters*, 42(1), 129–137. <https://doi.org/10.1002/2014GL062447>

- Vitart, F., Ardilouze, C., Bonet, A., Brookshaw, A., Chen, M., Codorean, C., Déqué, M., Ferranti, L., Fucile, E., Fuentes, M., Hendon, H., Hodgson, J., Kang, H.-S., Kumar, A., Lin, H., Liu, G., Liu, X., Malguzzi, P., Mallas, I., ... Zhang, L. (2017). The Subseasonal to Seasonal (S2S) Prediction Project Database. *Bulletin of the American Meteorological Society*, *98*(1), 163–173.  
<https://doi.org/10.1175/BAMS-D-16-0017.1>
- Walters, D., Boutle, I., Brooks, M., Melvin, T., Stratton, R., Vosper, S., Wells, H., Williams, K., Wood, N., Allen, T., Bushell, A., Copsey, D., Earnshaw, P., Edwards, J., Gross, M., Hardiman, S., Harris, C., Heming, J., Klingaman, N., ... Xavier, P. (2017). The Met Office Unified Model Global Atmosphere 6.0/6.1 and JULES Global Land 6.0/6.1 configurations. *Geoscientific Model Development*, *10*(4), 1487–1520. <https://doi.org/10.5194/gmd-10-1487-2017>
- Wang, G., Hendon, H. H., Arblaster, J. M., Lim, E.-P., Abhik, S., & van Rensch, P. (2019). Compounding tropical and stratospheric forcing of the record low Antarctic sea-ice in 2016. *Nature Communications*, *10*(1), 13. <https://doi.org/10.1038/s41467-018-07689-7>
- Wang, G., Cai, W., Yang, K., Santoso, A., & Yamagata, T. (2020). A Unique Feature of the 2019 Extreme Positive Indian Ocean Dipole Event. *Geophysical Research Letters*, *47*(18). <https://doi.org/10.1029/2020GL088615>
- Wang, G., & Hendon, H. H. (2020). Impacts of the Madden–Julian Oscillation on wintertime Australian minimum temperatures and Southern Hemisphere circulation. *Climate Dynamics*, *55*(11–12), 3087–3099. <https://doi.org/10.1007/s00382-020-05432-x>
- Wang, G., Hope, P., Lim, E.-P., Hendon, H. H., & Arblaster, J. M. (2021). An Initialized Attribution Method for Extreme Events on Subseasonal to Seasonal Time Scales. *Journal of Climate*, *34*(4), 1453–1465. <https://doi.org/10.1175/JCLI-D-19-1021.1>
- Wang, H., Kumar, A., Murtugudde, R., Narapusetty, B., & Seip, K. L. (2019). Covariations between the Indian Ocean dipole and ENSO: A modeling study. *Climate Dynamics*, *53*(9–10), 5743–5761. <https://doi.org/10.1007/s00382-019-04895-x>
- Watterson, I. G. (2010). Relationships between southeastern Australian rainfall and sea surface temperatures examined using a climate model. *Journal of Geophysical Research*, *115*(D10), D10108. <https://doi.org/10.1029/2009JD012120>
- Watterson, I. G. (2020). Australian Rainfall Anomalies in 2018–2019 Linked to Indo-Pacific Driver Indices Using ERA5 Reanalyses. *Journal of Geophysical Research: Atmospheres*, *125*(17). <https://doi.org/10.1029/2020JD033041>
- Wiens, C.E., Dijkstra, H.A. & de Ruijter, W.P.M. The interaction between the Western Indian Ocean and ENSO in CESM. *Clim Dyn* *52*, 5153–5172 (2019). <https://doi.org/10.1007/s00382-018-4438-2>
- Weller, E., & Cai, W. (2013a). Asymmetry in the IOD and ENSO Teleconnection in a CMIP5 Model Ensemble and Its Relevance to Regional Rainfall. *Journal of Climate*, *26*(14), 5139–5149. <https://doi.org/10.1175/JCLI-D-12-00789.1>

- Weller, E., & Cai, W. (2013b). Realism of the Indian Ocean Dipole in CMIP5 Models: The Implications for Climate Projections. *Journal of Climate*, 26(17), 6649–6659. <https://doi.org/10.1175/JCLI-D-12-00807.1>
- Wheeler MC, Hendon HH (2004) An All-season real-time multivariate MJO Index: development of an index for monitoring and prediction. *Mon Weather Rev* 132:1917–1932. [https://doi.org/10.1175/1520-0493\(2004\)132<1917:AARMM I>2.0.CO;2](https://doi.org/10.1175/1520-0493(2004)132<1917:AARMM I>2.0.CO;2)
- Wheeler, M. C., Hendon, H. H., Cleland, S., Meinke, H., & Donald, A. (2009). Impacts of the Madden–Julian Oscillation on Australian Rainfall and Circulation. *Journal of Climate*, 22(6), 1482–1498. <https://doi.org/10.1175/2008JCLI2595.1>
- White, C. J., Hudson, D., & Alves, O. (2014). ENSO, the IOD and the intraseasonal prediction of heat extremes across Australia using POAMA-2. *Climate Dynamics*, 43(7–8), 1791–1810. <https://doi.org/10.1007/s00382-013-2007-2>
- Williams, K. D., Copsey, D., Blockley, E. W., Bodas-Salcedo, A., Calvert, D., Comer, R., Davis, P., Graham, T., Hewitt, H. T., Hill, R., Hyder, P., Ineson, S., Johns, T. C., Keen, A. B., Lee, R. W., Megann, A., Milton, S. F., Rae, J. G. L., Roberts, M. J., ... Xavier, P. K. (2018). The Met Office Global Coupled Model 3.0 and 3.1 (GC3.0 and GC3.1) Configurations. *Journal of Advances in Modeling Earth Systems*, 10(2), 357–380. <https://doi.org/10.1002/2017MS001115>
- Wilson, E. A., Gordon, A. L., & Kim, D. (2013). Observations of the Madden Julian Oscillation during Indian Ocean Dipole events: IOD-MJO. *Journal of Geophysical Research: Atmospheres*, 118(6), 2588–2599. <https://doi.org/10.1002/jgrd.50241>
- Winter, H. C., Tawn, J. A., & Brown, S. J. (2016). Modelling the effect of the El Niño-Southern Oscillation on extreme spatial temperature events over Australia. *The Annals of Applied Statistics*, 10(4). <https://doi.org/10.1214/16-AOAS965>
- Wirth, V. (2020). Waveguidability of idealized midlatitude jets and the limitations of ray tracing theory. *Weather and Climate Dynamics*, 1(1), 111–125. <https://doi.org/10.5194/wcd-1-111-2020>
- Won, D., Y. S. Lee, Y. H. Kang, and H. J. Ham, 2015: Operational system description of GloSea5 in KMA and verification result of 2014. KMA Technical Report, 2015-04, 142 pp.
- Wu, R., & Kirtman, B. P. (2004). Understanding the Impacts of the Indian Ocean on ENSO Variability in a Coupled GCM. *JOURNAL OF CLIMATE*, 17, 13.
- Xie, S., Hu, K., Hafner, J., Tokinaga, H., Du, Y., Huang, G., & Sampe, T. (2009). Indian Ocean Capacitor Effect on Indo–Western Pacific Climate during the Summer following El Niño, *Journal of Climate*, 22(3), 730–747.
- Yang, G., and B. Hoskins, 1996: Propagation of Rossby waves of nonzero frequency. *Journal of the Atmospheric Sciences*, 53, 2365–2378, [https://doi.org/10.1175/1520-0469\(1996\)053<2365:PORWON>2.0.CO;2](https://doi.org/10.1175/1520-0469(1996)053<2365:PORWON>2.0.CO;2).

- Yang, D., Arblaster, J. M., Meehl, G. A., England, M. H., Lim, E.-P., Bates, S., & Rosenbloom, N. (2020). Role of Tropical Variability in Driving Decadal Shifts in the Southern Hemisphere Summertime Eddy-Driven Jet. *Journal of Climate*, 33(13), 5445–5463. <https://doi.org/10.1175/JCLI-D-19-0604.1>
- Yu, J.-Y., Mechoso, C. R., McWilliams, J. C., & Arakawa, A. (2002). Impacts of the Indian Ocean on the ENSO cycle: IMPACTS OF THE INDIAN OCEAN ON THE ENSO CYCLE. *Geophysical Research Letters*, 29(8), 4614–4618. <https://doi.org/10.1029/2001GL014098>
- Zhang, L., Han, W., Karnauskas, K. B., Meehl, G. A., Hu, A., Rosenbloom, N., & Shinoda, T. (2019). Indian Ocean Warming Trend Reduces Pacific Warming Response to Anthropogenic Greenhouse Gases: An Interbasin Thermostat Mechanism. *Geophysical Research Letters*, 46(19), 10882–10890. <https://doi.org/10.1029/2019GL084088>
- Zhao, M., & Hendon, H. H. (2009). Representation and prediction of the Indian Ocean dipole in the POAMA seasonal forecast model. *Quarterly Journal of the Royal Meteorological Society*, 135(639), 337–352. <https://doi.org/10.1002/qj.370>
- Zhao, M., Hendon, H. H., Alves, O., Liu, G., & Wang, G. (2016). Weakened Eastern Pacific El Niño Predictability in the Early Twenty-First Century. *Journal of Climate*, 29(18), 6805–6822. <https://doi.org/10.1175/JCLI-D-15-0876.1>
- Zhao, S., Jin, F.F., & Stuecker, M. F. (2019). Improved predictability of the Indian Ocean Dipole using seasonally modulated ENSO forcing forecasts. *Geophysical Research Letters*, 46, 9980–9990. <https://doi.org/10.1029/2019GL084196>
- Zhou T.J., Yu R.C. (2004) Sea-surface temperature induced variability of the Southern Annular Mode in an atmospheric general circulation model. *Geophys Res Lett* 31:L24206. doi: 10.1029/2004GL021473
- Zhang, W., Mao, W., Jiang, F., Stuecker, M. F., Jin, F., & Qi, L. (2021). Tropical Indo-Pacific Compounding Thermal Conditions Drive the 2019 Australian Extreme Drought. *Geophysical Research Letters*, 48(2). <https://doi.org/10.1029/2020GL090323>